Seismic Assessment Strategies for Masonry Structures

by

Matthew J. DeJong

Bachelor of Science, Civil & Environmental Engineering (2001)
University of California at Davis

Master of Science, Civil & Environmental Engineering (2005)
Massachusetts Institute of Technology

Submitted to the Department of Architecture
in partial fulfillment of the requirements for the degree of

Doctor of Philosophy in Architecture: Building Technology

at the

MASSACHUSETTS INSTITUTE OF TECHNOLOGY

June 2009

Signature of Author . . . . . .
Department of Architecture
May 1, 2009

Certified by . . . . . .
John A. Ochsendorf
Associate Professor of Architecture
Thesis Supervisor

Accepted by . . . . . .
Julian Beinart
Professor of Architecture
Chair, Departmental Committee on Graduate Students

Thesis Supervisor . . . . . .

John A. Ochsendorf
Associate Professor
Department of Architecture, MIT

Thesis Reader . . . . . .

John T. Germaine
Senior Research Associate
Department of Civil & Environmental Engineering, MIT

Thesis Reader . . . . . .

Thomas Peacock
Associate Professor
Department of Mechanical Engineering, MIT

Seismic Assessment Strategies for Masonry Structures

by

Matthew J. DeJong

Submitted to the Department of Architecture on May 1, 2009
in partial fulfillment of the requirements for the degree of
Doctor of Philosophy in Architecture: Building Technology

ABSTRACT

Masonry structures are vulnerable to earthquakes, but their seismic assessment remains a challenge. This dissertation develops and improves several strategies to better understand the behavior of masonry structures under seismic loading, and to determine their safety. The primary focus is on historic arched or vaulted structures, but more modern unreinforced masonry structures are also considered.

Assessment strategies which employ simplified quasi-static loading to simulate seismic effects are initially addressed. New analysis methods which focus on stability or strength are presented, and the merits of these strategies are clarified. First, a new parametric graphical equilibrium method is developed which allows real-time analysis and illuminates the complex stability of vaulted masonry structures. Second, a finite element strategy for predicting brittle fracture of masonry structures is extended to incorporate non-proportional loading and shell elements. These extensions enable prediction of damage and collapse mechanisms in general, but are specifically used to predict the response of a full-scale masonry structure to quasi-static cyclic loading.

Subsequently, assessment methods based on the dynamic response of masonry structures under earthquake loading are presented. First, rigid body dynamics and an experimental testing program are used to characterize the rocking response of the masonry arch for the first time. An assessment criterion is developed which successfully predicts experimentally observed arch collapse under a variety of earthquake time histories. Second, the behavior of rocking structures is addressed in general, and clearly distinguished from typical dynamic oscillators. The rocking response is time dependent, evoking the development of a statistical method for predicting collapse. Finally, the ability of discrete element methods to predict the dynamics of masonry structures is evaluated through comparison with analytical and experimental results, and a rational method for assigning modeling parameters is proposed.

Thesis Supervisor: John A. Ochsendorf
Title: Associate Professor of Architecture

Acknowledgements

First, I thank my supervisor, Professor John Ochsendorf, for his guidance and inspiration. The impetus for this research came from his desire to understand the stability of masonry structures, an interest which I have inherited over the last four years. This research was greatly improved by his expertise, and I have thoroughly enjoyed tackling these challenging problems under his mentorship. I can not thank him enough for the opportunities he has provided me, and for truly looking out for my best interests. He has set an example which I hope to emulate in my career.

Second, I acknowledge financial support for this research provided by an MIT Presidential Fellowship, a US Fulbright Pre-Doctoral Grant, and a TU Delft Research Fellowship.

Additionally, I am pleased to acknowledge several others who contributed directly or indirectly to this research. I thank my committee members, Dr. John T. Germaine and Professor Thomas Peacock, for reviewing this work. Specifically, I thank Dr. Germaine for his assistance with the experimental aspects of this research. It has been a privilege working in the company of someone with so much experience and intuition related to physical testing, and someone who is so devoted to helping students succeed.

I am indebted to Professors Jan Rots and Max Hendriks at the Technical University of Delft, for hosting me for one year as a visiting researcher in the Netherlands. I thank them for allowing me to join them in their research regarding finite element analysis of masonry structures, a much needed complement to the rest of the work in this dissertation. Chapter 4 would not have been possible without their expertise. I am also grateful to Professor Andrei Metrikine at the Technical University of Delft, for numerous discussions related to structural dynamics and practically any other subject one could think of. Chapter 6 was inspired by these conversations, which changed the way I perceived the dynamics of rocking structures, and the world. My time working with these colleagues at Delft improved my research, but also changed me personally and encouraged me to pursue an academic career.

I am grateful for collaboration with Laura De Lorenzis of the University of Lecce, Italy, regarding the dynamics of masonry arches in Chapter 5. This effort catalyzed the experimental work on arches, for which I acknowledge the assistance of two undergraduate research students: David Lallemant, who assisted me in constructing a shake table in the Civil Engineering Laboratory, and Stuart Adams, who spent many hours testing masonry arches.

Finally, I would like to thank a few individuals who have shared the last six years at MIT with me. I thank Philippe Block, specifically for his assistance with the thrust line analysis in Chapter 3, but also for numerous conversations related to all aspects of this work. More than that, I thank him for his companionship in our PhD pursuits. I also thank JongMin Shim for his friendship and for exemplifying hard work and endurance in his studies. Most of all, I would like to thank Cara for her enduring support. Her encouragement and enthusiasm made this possible.

Contents

IV Conclusions

V Appendices

Bibliography

Part I

General Presentation

Chapter 1

Introduction

1.1 Global Context

Masonry structures comprise a majority of the global built environment. These structures exist in the form of typical houses and office buildings, but also include a wealth of invaluable structures which compose the fabric of human history. Masonry refers to "the art and craft of building and fabricating in stone, clay, brick, or concrete block" ("masonry", 2009). In this dissertation, masonry is used to refer to traditional masonry, often referred to as unreinforced masonry. The array of structures within this category is vast, ranging from historic stone structures to mortared brick structures still being constructed today.

Many masonry structures are located in seismic regions, where earthquakes have exposed their vulnerability. Recent earthquakes in Iran [2003], Pakistan [2005], and Peru [2007] have caused devastating loss of life and infrastructure. For example, the earthquake in Pakistan killed more than 80,000 people and left more than 4 million homeless (EERI 2005). The 2003 earthquake in Iran killed 30,000, the majority of whom were buried by collapsing masonry. Eighty percent of the city of Bam was flattened, including the iconic, 2500 year old citadel (Fallahi 2007).

This problem is obviously not limited to the developing world. Italy has seen significant damage to its infrastructure during recent earthquakes, including the collapse of a frescoed vault in the Basilica of St. Francis of Assisi in 1997 (Bohlen 1997). A wealth of similar damage during

recent earthquakes catalyzed an increase in seismic assessment requirements in Italy (Povoledo 2007), motivating an increase in related research in the country. Here in the United States, the re-evaluation of San Francisco's infrastructure at the 100 year anniversary of the devastating 1906 earthquake resulted in masonry structures being labeled the highest retrofit priority of all structural typologies.

Despite their prevalence and their long existence, the behavior of masonry structures under earthquake loading is still not well understood, and extremely hard to predict. The problem is challenging and it must be addressed.

1.2 Seismic Assessment of Masonry Structures

Why does it remain difficult to determine the safety of masonry structures in seismic regions? First, the majority of these structures did not benefit from modern engineering design, but instead resulted from empirical expertise. As a result, masonry assessment methods have naturally lagged far behind assessment methods for modern steel and concrete structures.

Second, the long existence of many masonry structures yields several unknowns. In most cases, geometry is difficult to determine because construction drawings do not exist, and environmental factors have resulted in material degradation, support displacements, and damage during extreme events.

Third, the basic nature of masonry remains difficult to model. Finite Element Modeling (FEM), the most widespread structural analysis tool, is tailored toward continuous structures which remain relatively connected during elasto-plastic failure under both static and dynamic loading. Masonry, on the other hand, is discontinuous by nature. Failure is brittle and individual units (e.g. stones, bricks) are often free to separate, especially during dynamic loading. While progress has been made towards modeling these behaviors using FEM, alternative methods are attractive but underdeveloped.

Finally, researchers and engineers remain divided in their emphasis on what is important: strength or stability. Certainly, the answer is a combination of the two, and largely depends on the nature of the specific structure. However, the assessment methods applied to these structures generally emphasize strength, while neglecting stability (Boothby 2001). There is need for integration of these two concepts, and an understanding for what is critically important.

These difficulties have resulted in a misunderstanding of structural behavior of masonry. In turn, this has led to unnecessary interventions, and even destructive interventions, which must be

prevented in the future. It has also made it difficult to identify which buildings are at risk of collapse.

1.3 Research Motivation and Objective

As the previous sections mentioned, there is a global need to evaluate the safety of masonry structures, and there are technical limitations which are preventing this need from being met. This context provides the general motivation for this work:

- We need a better fundamental understanding of both the static and dynamic behavior of masonry structures in order to improve assessment methods.
- We need better numerical tools to predict both the quasi-static and the dynamic response of masonry structures.

Based on these motivating factors, this dissertation aims:

> *To increase fundamental understanding of structural behavior and to develop accurate, tested analysis methods that allow appropriate assessment of masonry structures which are vulnerable to seismic loading.*

To meet this objective, a variety of methods will be applied, as outlined in §1.4. These approaches are tailored to different types of failure (strength -vs- stability), loading (quasi-static -vs- dynamic), and structures (simple -vs- complex; historic -vs- modern). Analytical, geometrical, numerical, and experimental approaches are incorporated.

This broad approach is intentional. A wide-ranging exploration of available methods is necessary to determine the most appropriate method for a given structure. Furthermore, the broad scope bridges the gap between these methods, showing how they can be complementary. This work will clarify the state of the field, and push it further in several directions.

1.4 Outline of Thesis

The approach taken to achieve the objective in §1.3 is as follows. Part I includes this introduction, which states the problem, and Chapter 2, which reviews previous research. The aim is to set the context for the contributions made in this dissertation.

Part II is focused on quasi-static assessment methods, primarily the modeling of quasi-static collapse. There is no point in modeling dynamic collapse without first addressing and understanding the quasi-static problem. Chapter 3 extends the graphical equilibrium assessment

method of Thrust Line Analysis, a method purely focused on the stability of masonry, not on strength. This simple but powerful approach, tailored towards historic vaulted masonry structures, can be used as a first order assessment method, but is also of educational value as a means of clarifying the fundamental concept of collapse due to instability.

Chapter 4, on the other hand, deals with predicting damage to masonry structures through the modeling of failure due to lack of material strength. Methods which were primarily developed to predict strength failure can give an indication of possible collapse mechanisms, but often struggle to predict collapse. In Chapter 4, a new method for modeling brittle fracture using finite element analysis is presented. This method, while applicable to brittle structures in general, is applied towards relatively modern brick structures with horizontal floor and roof diaphragms and masonry walls.

Part III is focused on dynamic collapse under earthquake loading. While Part II addressed both stability and strength, Part III will only address collapse due to instability. This is motivated by the fact that a majority of research has been devoted to the possibility of elastic resonance, which might lead to material failure but does not necessarily explain much about collapse. Less research has been devoted to the dynamic response of discrete interacting masonry blocks which are assumed to have no tensile strength (i.e. which have no mortar or unreliable mortar strength).

Part III starts with Chapter 5, an analytical and experimental investigation of the masonry arch under dynamic loading. Despite its prevalence throughout history, dynamic collapse conditions for the masonry arch have not been defined. In contrast to previous studies regarding elastic vibrations, the dry-stone arch and other vaulted masonry structures are shown to behave as rocking structures which must be treated differently than typical elastic structures.

Chapter 6, inspired by the findings in Chapter 5, is focused on the fundamental behavior of rocking structures. While numerous papers have been written on the single rocking block, certain aspects of its behavior remain undefined. Specifically, the ground motions to which rocking structures are most vulnerable are clarified.

While Chapters 5 and 6 are primarily deal with fundamental behavior and analytical assessment methods, Chapter 7 focuses on numerical modeling. It is impossible to create analytical models to predict the dynamic response of most full-scale structures, so computational power must be employed. This chapter explores discrete element modeling, first using it to predict experimental response of the arch and then applying it to larger scale structures. Additionally, a method for defining critical modeling parameters is presented.

Part IV summarizes this work and discusses avenues of future research. The conclusions justify the broad spectrum of approaches discussed throughout.

Chapter 2

Literature Review

2.1 Introduction

The safety assessment of masonry structures in seismic regions has gained significant attention in recent years. Increased computational power has changed the way all kinds of structures are assessed, allowing more degrees of freedom to be modeled. In this chapter, it is unrealistic to attempt a comprehensive overview of all methods which have been applied. Instead, the basic frameworks in which masonry structures are assessed will be introduced, to provide the context for the contributions herein. This chapter, like the dissertation, is divided into two main sections: quasi-static analysis and dynamic analysis.

Equilibrium methods, strength methods, discrete block methods, and continuum methods will be reviewed. While these methods vary dramatically in their assumptions and complexities, the question should not be "Which method is better?" Instead, realizing that all of these methods are appropriate for given applications, the questions which should be asked are "How can these methods be improved?" and "Where can new contributions be made?" The answers to these questions motivate the work in the following chapters.

2.2 Quasi-static Analysis Methods

Quasi-static analysis methods are the logical starting place, as these methods were the first to be formalized. By neglecting dynamic effects entirely, or by approximating them in a quasi-static fashion, a first-order seismic assessment is possible, often with reduced computational power, time, and therefore expense. While more approximate, these methods are powerful and practical, and remain the primary tools applied to assess masonry structures today.

Dynamic earthquake loading is typically simplified as a quasi-static loading in one of two ways. The first method is to apply a constant horizontal acceleration to the structure, which is the equivalent of applying a constant horizontal ground motion. This conservatively ignores the fact that actual ground motions only occur for a short period of time, but also neglects the possibility of resonant amplification. Thus, this method is appropriate when stability is a concern and where elastic resonance is expected to have a relatively small effect, as discussed in §2.2.1.

The second method involves applying horizontal forces distributed along the height of the structure, which are meant to approximate the effects of an earthquake. The relative magnitudes of the forces are distributed with preference towards the top of the structure, accounting for amplification caused by dynamic resonance effects (e.g. *Uniform Building Code* 1997). All of the horizontal forces can then be scaled to approximate different magnitude earthquakes, and the response of the structure can be determined. This concept has been extended into what is typically referred to as "pushover analysis" (American Society of Civil Engineers 2000). Initially, pushover analysis was developed for frame-type structures typical of steel and concrete construction. However, the technique has also been applied to masonry structures by modeling continuous wall elements directly or through use of the equivalent frame technique. This method is appropriate for strength methods, where resonance effects may play a larger role and must be accounted for, as discussed in §2.2.2.

2.2.1 Equilibrium Methods

Equilibrium methods, or stability methods, have been used for centuries (Heyman 1995, Huerta 2004). Recent studies show that some historic masonry structures were built on the edge of stability, hinting at the idea of the builder adding more mass or thickness where necessary to make the structure stand and ensure safety (Nikolinakou et al. 2005). However, this was not always the case. In the late 19th century, Antoni Gaudi used hanging mass models to develop stable forms. This design methodology takes advantage of the fact that masonry structures act

predominantly in compression. Once Gaudi had established the most efficient form in tension, he inverted that form to construct a pure compression structure.

Although Gaudi's hanging models are perhaps more well-known, the idea of pure compression structures was investigated much earlier. Hooke (1675) wrote, "As hangs the flexible line, so but inverted will stand the rigid arch." The mathematical solution to the shape of the hanging chain, the catenary, was later published by Gregory (1697), who states, "...none but the catenaria is the figure of a true legitimate arch, or fornix. And when an arch of any other figure is supported, it is because in its thickness some catenaria is included." Heyman (1998) restates this in a more general sense, "...if any thrust line can be found lying within the masonry, then the arch will stand."

Based on this foundation, Couplet made three key assumptions about the behavior of masonry in 1730: (1) masonry has no tensile strength, (2) masonry has infinite compressive strength, and (3) sliding failure between arch voussoirs does not occur (Heyman 1998). These assumptions still provide the criteria used for analysis of masonry structures, as outlined by Heyman (1966, 1995). Furthermore, these assumptions eliminate the possibility of failure due to material strength, so only failure due to instability can be assessed. Thus, methods which incorporate these assumptions are referred to as "equilibrium methods" in this thesis. Couplet's assumptions have the following consequences:

- The static analysis of masonry structures is a problem of stability which is based solely on geometry. Analysis results are independent of scale, meaning that a small scale model should behave the same as a full scale structure.
- Individual blocks are not free to slide or crush, but they are free to separate, or hinge. Hinges form when the 'thrust line' mentioned by Heyman (1998), can no longer be contained within the masonry and exits the surface of the masonry. At this point, the masonry can no longer support the applied loads, and the structure is no longer in equilibrium without hinging.
- Since stresses are not a concern, a constant horizontal acceleration can be achieved by tilting the ground surface upon which a structure rests. This concept was applied by researchers at the Institute for Lightweight Structures in Suttgart, Germany, who tilted model masonry structures until collapse to determine their resistance to lateral loading (Gaß 1990).

Equilibrium methods are primarily applied to pure compression structures. Thus, they are more appropriate for historical masonry structures, which incorporate vaults and arches to transfer loads instead of slabs and beams. Therefore, the discussion and application of

equilibrium methods will be limited to these types of structures. These methods have been implemented in two primary ways: graphically and numerically.

Graphical Equilibrium Methods

Graphical methods have long been used for the design and assessment of masonry structures (Poleni 1747, Huerta 2004). For example, Snell (1846) used graphical methods to evaluate the stability of the masonry arch. In Figure 2-1a, Snell (1846) uses the force polygon to the right of the arch to draw a thrust line (thickened) which lies entirely within the masonry, demonstrating that the arch is stable. Later, Huerta (2004) constructs three different thrust line solutions by adjusting the horizontal thrust in the same arch (Figure 2-1b). An infinite number of such thrust lines could be drawn within the thickness of the masonry due to the indeterminate nature of the problem.

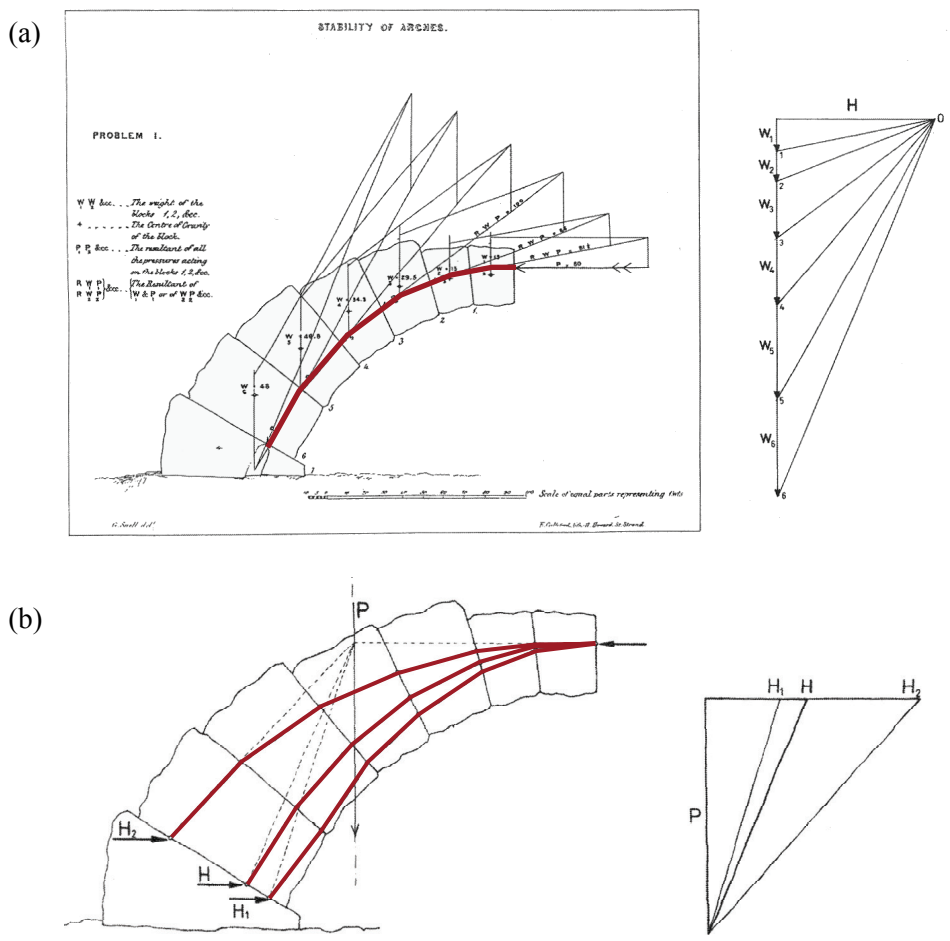

Figure 2-1: Graphical analysis of a masonry arch by (a) Snell (1846), and (b) Huerta (2004). (after Huerta 2004, thrust line thickened)

Perhaps the most widely applied method of graphical analysis is *graphic statics*, formalized by Karl Culmann (1866). In recent years, graphical methods have been largely replaced by numerical methods, especially in engineering education. However, recent work by Allen and Zalewski (2009) demonstrates that graphic statics is still a viable and powerful technique for both analysis and design.

One major drawback of graphical methods, which likely led to their reduced application, is that hand-drawn graphical constructions can be tedious and time-consuming. However, recent interactive computational geometry software can significantly reduce this negative aspect. By implementing graphic statics in a parametric computational geometry framework, Block (2005) developed a useful tool for assessment and design. Using the assumption that stability is based solely on geometry, Block (2005) developed parametric constructions for various masonry structures. These constructions are created only once, after which the geometry can be adjusted in real-time. Using this tool, a rapid first order assessment of the stability of masonry structures can be achieved, and the effect of geometrical changes such as arch thickness, buttress width, etc., can be readily evaluated. Furthermore, the visual results often lead to better understanding and clearer interpretation.

The application of graphical methods to assess the stability of arches under quasi-static seismic loading has not been attempted. Prior to the computational implementation introduced by Block (2005), this would have been prohibitively time-consuming.

Numerical Equilibrium Methods

Numerical equilibrium methods have been applied to study the stability of masonry structures under quasi-static point loads or displacements, but this section will focus on seismic assessment of arches and vaulted structures. All of these approaches apply a constant horizontal acceleration to simulate possible earthquake effects, either directly or by tilting the structure.

Oppenheim (1992) addressed the problem of the masonry arch under horizontal ground accelerations by introducing an analytical model describing the masonry arch as a single degree of freedom (SDOF) three-bar (four-hinge) mechanism (Figure 2-2). He then derived the equations of motion using Hamilton's Principle and Lagrange's equations for the SDOF system of rigid bodies. Sets of four hinge locations were assumed and the governing collapse mechanism and the corresponding minimum horizontal ground acceleration necessary to cause collapse were found through iteration.

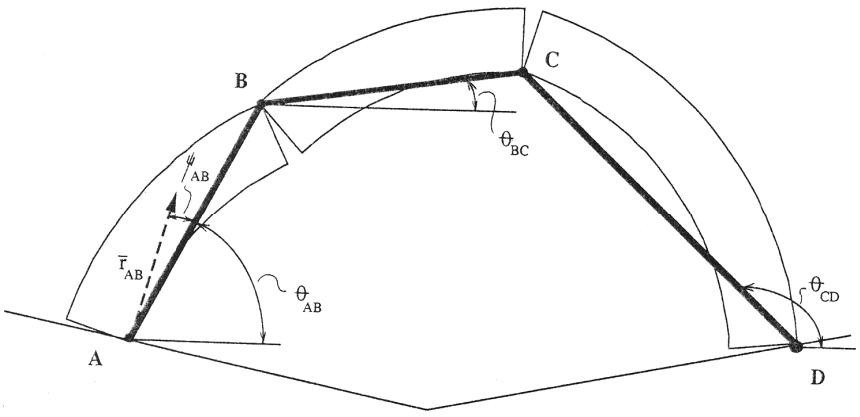

Figure 2-2: The three bar mechanism formed by a masonry arch under horizontal ground motion. (after Oppenheim 1992)

Clemente (1998) also studied the collapse of a masonry arch subjected to constant horizontal ground acceleration by assuming four hinge locations and writing the equilibrium equations in terms of virtual powers. Again by iterating through all the possible sets of hinge locations which would cause collapse, the governing horizontal ground acceleration was identified, and the corresponding collapse mechanism was found. Using this procedure, he plotted the constant horizontal acceleration required to cause collapse as well as the locations of the hinges at the point of collapse for various arch geometries. Results compare well with the results of Oppenheim (1992).

Appleton (1999) and Ochsendorf (2002) studied the same problem by using the principle of virtual work to determine the ground surface tilt which causes collapse, and the corresponding horizontal ground acceleration. Ochsendorf (2002) extended the analysis to a buttressed arch and showed the relative effect of both the arch and the buttress on the stability of the structure. Additionally, Ochsendorf developed a method for determining the cracking of a tilting buttress which can be observed during collapse. This buttress cracking results directly from the postulate that the masonry has no tensile strength, and clearly reduces the maximum allowable horizontal acceleration.

Finally, other authors have extended these ideas to address more complete structures. For example, De Luca et al. (2004) assessed the stability of an arch on buttresses in a similar fashion. Additionally, they propose the use of finite element models to determine where cracking of a masonry structure might occur, and then use equilibrium methods to determine the stability of the determined mechanism. Essentially, they include some tensile strength to determine a collapse mechanism, and then neglect the tensile strength when assessing stability. This approach leads the discussion to methods which incorporate strength.

2.2.2 Strength Methods

In some cases, it is not reasonable or desirable to make the three assumptions that are incorporated in the equilibrium methods discussed in §2.2.1, and the strength of the material needs to be included in the analysis. This could be the case for newer brick-and-mortar construction where the tensile strength of mortar is appreciable. Or it could be the case for certain structural typologies where the structure is confined or constrained so as to prevent instability without significant sliding or crushing, e.g. for the in-plane failure of masonry walls.

In general, the primary advantage of strength methods is their ability to predict or assess damage. However, once some of level of damage has been developed, it often remains a challenge for these methods to predict when the structure will collapse. The basis for strength methods is vast, ranging from micromechanical modeling of failure to macro-scale approximation of masonry properties.

Micro-mechanical Damage Models

With an emphasis on micromechanical modeling, Lourenço (1996) outlined computational strategies for masonry structures, starting with separate brick and mortar layers. This led to the development of a brick-interface model (Lourenço and Rots 1997) and an anisotropic continuum model (Lourenço and Rots 1998) for finite element analysis of masonry. Similarly, Gambarotta and Lagomarsino (1997a) proposed a brick-and-mortar damage model for seismic loading, and then applied homogenization techniques to develop a continuum model applicable to cyclic loading of masonry walls (Gambarotta and Lagomarsino 1997b). More recently, Brasile et al. (2007) built upon this work, developing more efficient iteration techniques for a similar brick-and-mortar joint model, making this complex micro-scale model more feasible (Figure 2-3).

In addition to these studies focused on the in-plane failure of brick-and-mortar walls, micro-mechanical models have been applied to assess historic masonry structures. For example, Velente (2003) used complex fracture mechanics to address the failure and reconstruction of Noto cathedral, which collapsed following an earthquake in 1996. Additionally, commercially available homogenized crack models have been widely applied to predict damage to masonry structures in seismic regions (e.g. Romano 2003). However, the material properties, geometry, and existing damage of historic structures are often poorly defined. Thus, use of these techniques should be applied tentatively, with an understanding of the limited level of accuracy which can be realistically achieved. The majority of methods in this category employ finite element software for analysis.

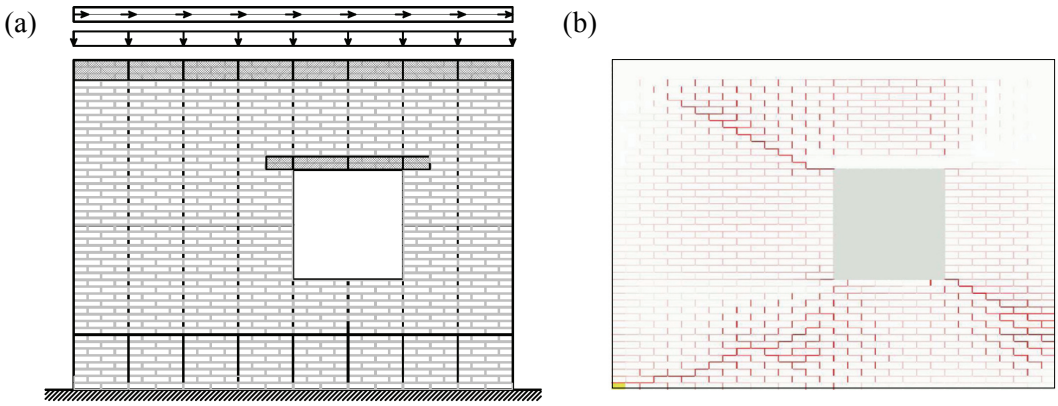

Figure 2-3: Analysis of a masonry wall under in-plane loading by Brasile et al. (2007): (a) geometry and loading, and (b) final damage distribution map. (after Brasile et al. 2007)

Macro-scale Damage Models

At the other extreme of the analysis spectrum, simplified macro-scale models are sometimes more practical for engineering applications, as these methods require less computational power or expertise. For example, *FEMA 356* (American Society of Civil Engineers 2000) outlines a pier-spring model which describes the force-deformation relationship of masonry elements or components based on macro-scale properties. Moon et al. (2006) proposed improvements to *FEMA 356* in order to account for global overturning and perpendicular wall effects. Also from the macro-scale perspective, simplified formulas for predicting rocking, shearing, and sliding capacities of wall piers have been applied (e.g. Magenes and Calvi 1997). Finally, several researchers have approximated masonry walls as equivalent frames with plastic hinges to assess wall capacity (e.g. Magenes and Della Fontana 1998, Kappos et al. 2002, Salonikios et al. 2003).

Combined Approaches

Between these two extremes, Yi et al. (2006b) applied a macro-scale interface method, where the masonry is modeled as an elastic continuum with contact elements at predefined crack locations (Figure 2-4). The strength of the material is only assessed at these contact elements. The authors used shell finite elements to predict the 3D response of a two-story masonry building under lateral loading. This approach simplifies the analysis considerably, reducing computation time and convergence problems. It is effective if probable crack locations are known with some certainty.

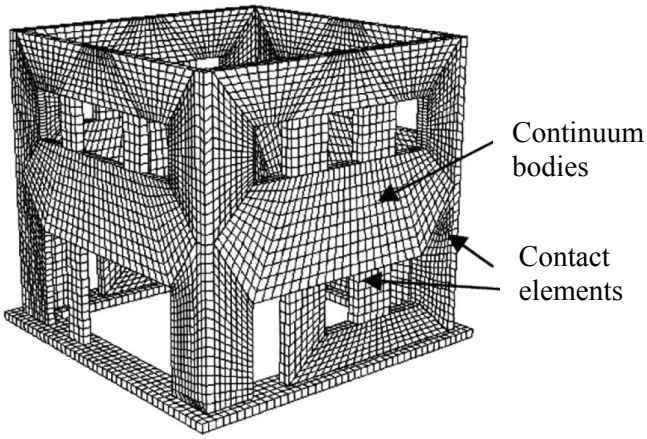

Figure 2-4: Finite element model with predefined crack locations (contact elements) used by Yi et al. (2006b) for the analysis of a masonry structure under lateral loading. (after Yi et al. 2006b)

In another combined approach, Milani et al. (2006a, 2006b) proposed a limit analysis technique based on homogenized micro-mechanical properties, and then extended the method to assess 3D masonry buildings under horizontal loads (Milani et al. 2007). While not capable of predicting a force-displacement response, the method is attractive because it incorporates both the stability of the structure and the material strength to determine collapse loads and 3D collapse mechanisms. Thus, it can assess both damage and collapse. The method has been applied to assess the seismic vulnerability of a historical masonry building, and compared to micro-mechanical finite element modeling results (Mallardo et al. 2008). Additionally, the method has been extended to assess masonry vaults under point loading (Milani et al. 2008), and it could be applied to assess their seismic capacity.

While these methods have attempted to bridge the gap between complex micro-scale analysis and simplified macro-scale analysis, there is still a need for other methods to fill this void. Methods are needed that (1) assess material failure in situations where macro-scale models are not applicable, (2) can be easily applied by the engineer, and (3) do not require extensive computational expertise.

2.3 Dynamic Analysis Methods

In this section, previous research related to the prediction of the dynamic response of masonry structures is presented. The focus will be on the dynamics of distinct interacting blocks, with the primary motivation being prediction of collapse. Analytical approaches which employ rigid body dynamics are first introduced in §2.3.1. These studies are limited to structures with

relatively few degrees of freedom, motivating the use of discrete body computational methods which are discussed in §2.3.2.

Continuum methods are often used to assess the dynamics of masonry structures, but they are beyond the scope of this dissertation. However, it must be mentioned that continuum methods are typically applied to determine the steady-state dynamic response through modal analysis. The modal response of the structure is often used to determine where stresses are highest and where cracking might occur. Thus, continuum methods can be effective in predicting locations of damage, but fall short when trying to predict collapse or the actual transient dynamic response of interacting distinct bodies. FEM tools that both incorporate dynamic resonance effects, and predict dynamic failure once cracking begins, still need to be developed.

2.3.1 Analytical Methods

Several studies have addressed the dynamic response of masonry structures through derivation of analytical equations of motion. The majority of these studies focus on the most basic rocking structure, the rocking block, but some address more complex structures like arches and portal frames.

The Rocking Block

Housner (1963) was the first to investigate systematically the dynamics of a single rigid block on a rigid base undergoing horizontal motion (Figure 2-5a). Assuming that the block rotates about its bottom corners without sliding or bouncing, Housner derived an equation of motion for rocking in each direction. At the transition between rocking in each direction, the block impacts the base as the hinge about which rocking occurs transfers from one corner to the other. The dissipation of energy during impact is approximated using conservation of angular momentum, essentially assuming plastic impact.

Using this framework, Housner determined that the natural rocking period, unlike typical oscillators, increases with the rocking angle (Figure 2-5b). Furthermore, as the rocking angle increases, the rocking period asymptotically approaches infinity. Although physically unrealistic, this occurs when the block is perfectly balanced on its corner and does not oscillate at all. Housner then investigated both rectangular and sinusoidal acceleration impulses, and determined the relationship between the impulse acceleration and duration which causes overturning. Despite numerous assumptions (small angles, slender block, no friction, no bouncing, energy dissipation, etc.), Housner's work is the basis for the plethora of rocking block studies which have followed.

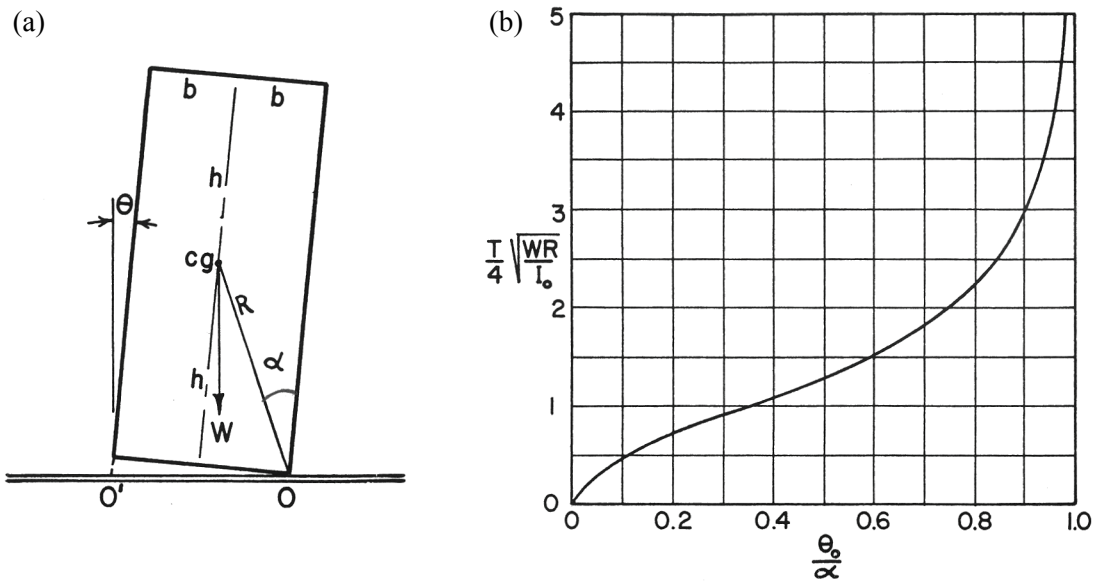

Figure 2-5: Rocking block analysis by Housner (1963): (a) definition of the rocking motion, and (b) the natural rocking period (**T**) as a function of the rocking angle θ_o. (after Housner 1963) Note: I_o is the moment of inertia of the block about point **O**.

Yim et al. (1980) approached the rocking block problem without making small angle assumptions. Instead, using a fourth order Runge-Kutta integration scheme, the non-linear equations of motion were solved numerically. Using this numerical solution procedure and simulated random earthquake ground motions, Yim et al. (1980) addressed the problem of the magnitude of the simulated earthquake necessary to cause overturning of a rigid block. Due to the random nature of the loading, the rigid block response was found to vary drastically from relatively little motion to complete overturning when subjected to the same magnitude of randomly generated horizontal ground motion. Due to this variability, the problem becomes one of probability. By repeating simulations for each of several block geometries and ground motion magnitudes, cumulative probability density functions were plotted. The probability of overturning was found to increase with an increase in slenderness ratio and magnitude of ground motion, and decrease with an increase in scale. Small variations (5%) in the restitution coefficient developed by Housner were found to have a negligible effect on the probability of overturning.

The study by Yim et al. (1980) demonstrates the difficulty in predicting the stability of a block structure when the ground acceleration (simulated earthquake motion) is randomly generated, even if the maximum magnitude of the ground acceleration is specified. However, even though the stability of a structure could not be definitively determined, clear trends were found which could be used to determine the probability of overturning. In the process, the

uncertainty involved in predicting the rocking response to earthquake motion is clearly demonstrated, and must be kept in perspective.

While Yim et al. (1980) focused on the rocking block response to randomly generated earthquake motion, Spanos and Koh (1984) focused on the rocking block response to harmonic horizontal ground acceleration. Using both the linearized and non-linear equations of motion, the stability of a rocking block subjected to harmonic ground accelerations of varying frequency and amplitude was determined. The frequencies and amplitudes for which the steady state modes of oscillation are stable were also determined. However, these steady state modes are dependent on perfectly harmonic ground motions. Yim et al. (1980) showed that a slight variation in ground motion can have a drastic effect on the rocking response. Thus, it seems unlikely that these steady-state rocking modes could be physically realized.

Following the work by Spanos and Koh (1984), numerous researchers focused on the response of rocking blocks to harmonic ground motion (e.g., Tso and Wong 1989, Hogan 1990, Yim and Lin 1991, Shenton and Jones 1991b, Lenci and Rega 2006). Although the rocking response to harmonic shaking is an interesting dynamical problem, the attention it garnered perhaps demonstrates a structural dynamics mindset rooted in the concept of the response spectra, inheriting the assumption that harmonic ground motion could illicit a resonant response.

In addition to investigating different ground motions, researchers have explored more complex block behaviors including coupled sliding, bouncing, and rocking behavior (e.g. Shenton and Jones 1991a, Augusti and Sinopoli 1992, Lipscombe 1993, Scalia and Sumbatyan 1996, Shenton 1996, Pompei et al. 1998). Including these coupled behaviors is important for short, stout blocks, but is less important for tall, slender blocks.

In contrast to these studies, Zhang and Makris (2001) applied Housner's original framework and expanded Housner's investigation of the rocking response to ground pulses, clearly defining two distinct failure modes and the corresponding failure domains for cycloidal pulses. Zhang and Makris (2001) focused their attention on the largest cycloidal impulses within an expected earthquake ground motion, reasoning that the rotational inertia generated by these impulses are the driving force of collapse rather than the harmonic response to the frequency spectra. Makris and Konstantinidis (2003) then critically evaluated the work of Priestley et al. (1978) and concluded that a rocking structure cannot be replaced by an equivalent 'typical elastic' oscillator and should not be evaluated using response spectra. Makris and Konstantinidis (2003) also highlighted fundamental differences between rocking blocks and typical elastic oscillators and proposed the rocking spectra as a unique measure of earthquake intensity.

Finally, several researchers have investigated the response of multiple block systems. For example, in an attempt to bridge the gap between single block rocking and actual masonry structures, Sinopoli and Sepe (1993) investigated the behavior of a three block frame structure subjected to horizontal ground acceleration. Similarly, Spanos et al. (2001) analyzed the dynamics of a stacked two-block structure. The derivation of the equations of motion becomes quite extensive for this two-block problem, and extending the derivation to several block systems would be intensive. The authors note that "this effort could perhaps be expedited by incorporating in the analysis concepts of the discrete elements technique" (Spanos et al. 2001), which will be discussed in §2.3.2.

The Arch

After studying the response of the arch to a constant horizontal acceleration, both Oppenheim (1992) and Clemente (1998) extended their quasi-static analyses to dynamic horizontal acceleration loading. Both authors used their quasi-static analysis to determine hinge locations and assumed that the resulting SDOF mechanism remains unchanged throughout dynamic motion. The simplification of this multiple block system to a SDOF equation of motion allows an analytical solution. Both authors applied a rectangular acceleration impulse and came to the expected conclusion that the allowable ground acceleration is highly dependent on both the duration and magnitude of the ground acceleration. The arch was found to remain standing under large ground accelerations of short durations, and as the impulse duration increases, the allowable horizontal acceleration asymptotically decreases to the quasi-static allowable horizontal acceleration. In their analyses, both authors only considered the first half-cycle of oscillation, i.e. until the arch first returns to the natural configuration.

The equations of motion derived by both authors are independent of the mass (or density) of the blocks, but are dependent on the overall scale of the structure. Oppenheim (1992) noted that the acceleration impulse necessary to cause collapse approximately increased by the square root of the arch radius. In other words, larger structures are more resistant to base accelerations than smaller ones.

Although neither Oppenheim (1992) nor Clemente (1998) verified their modeling experimentally, Appleton (1999) conducted an experimental investigation inspired by the work of Oppenheim. She constructed arches and tilted them to verify her quasi-static numerical analysis, and also tested arches under a variety of horizontal ground motions.

2.3.2 Computational Methods

Although analytical solutions provide insight regarding the nature of the dynamics of masonry structures, their complexity demonstrates the need for computational tools which can correctly address the problem of rigid block dynamics. Initially, finite element programs were the computational tools of choice for most engineers, but they are optimal for problems of elasticity and plasticity, not stability. The more recent application of Discrete Element Modeling (DEM) inherently captures the discontinuous nature of masonry.

Several different techniques for modeling the dynamic interaction of discrete blocks have been taken, all of which allow complete separation of blocks and can recognize new contacts as blocks impact each other. The way that these methods address contact between blocks can be divided into two primary categories. The first category involves methods which allow slight block interpenetration, referred to as "compliant contact." These methods employ a spring-dashpot element where contact is recognized. The Universal Distinct Element Code (UDEC) and the 3-dimesional Distinct Element Code (3DEC), both distributed commercially by Itasca (www.itascacg.com), fall into this category and will be discussed. The second category includes methods in which zero block interpenetration is allowed, referred to as "unilateral contact." These methods rigorously prevent block overlap by aligning block boundaries where contact is recognized. Non-Smooth Contact Dynamics (NSCD) falls into this category and will also be discussed.

UDEC / 3DEC

UDEC (Itasca 2004) and 3DEC (Itasca 2003) are probably the most widely applied discrete methods, and are both based on the research of Cundall (1971, 1980) and Cundall and Strack (1979). Explicit integration is used with sufficiently small time steps to ensure computational stability. Blocks can be either rigid or deformable, and joint properties and Rayleigh damping properties must be defined. Details of these programs are discussed further in Chapter 7.

UDEC has been applied to model the response of several masonry structures to ground motion (e.g. Azevedo et al. 2000, Psycharis et al. 2000, Drei and Fontana 2003). While these studies show the potential of the method to predict the collapse of masonry structures (Figure 2-6), there is little mention of modeling parameters or assumptions, and the results are not verified.

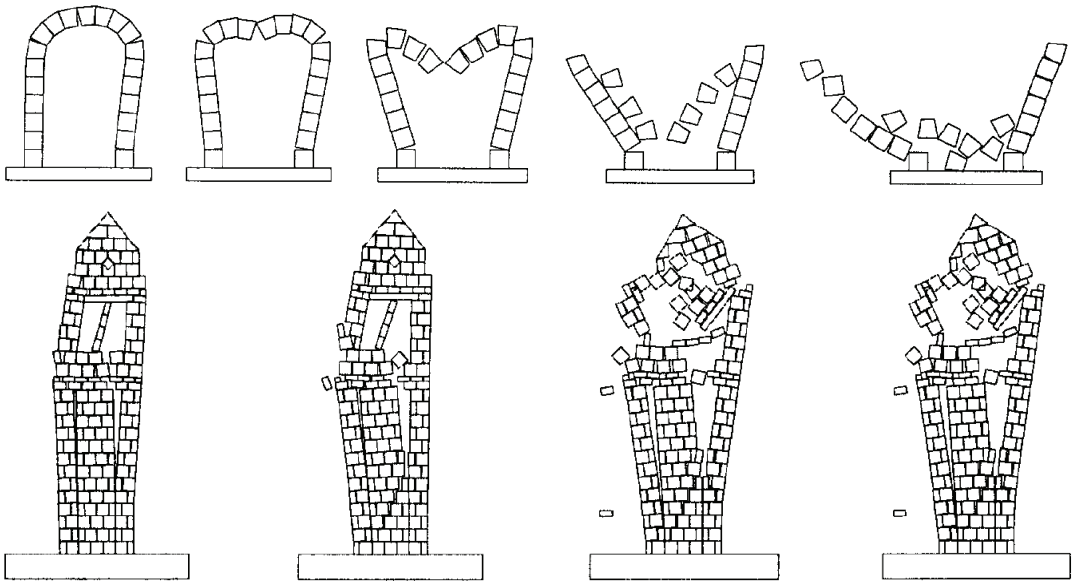

Figure 2-6: Seismic behavior and collapse patterns for two different masonry structures under seismic loading. (after Azevedo et al. 2000)

UDEC also has been used to evaluate the response of rocking blocks, and two studies in particular propose methods for defining joint and stiffness properties and compare results with experimental tests. First, Winkler et al. (1995) applied the discrete element method to simulate the response of one, two, and three stacked blocks, in an attempt to evaluate furniture overturning in an earthquake. They defined joint stiffness properties based on measured material properties of the blocks that they tested, and defined damping properties by fitting UDEC predictions to match free-rocking experiments. They focused on harmonic base motion, and found good agreement between numerical and experimental results. Second, Peña et al. (2007) used UDEC to predict the response of a single rocking block to both harmonic and earthquake ground motions. Instead of defining joint properties according to the material of the blocks tested, joint properties were defined based on an analytically derived frequency parameter of the system. Once joint properties were defined, stiffness-proportional damping properties were derived to approximate the analytical damping employed by Housner's restitution coefficient. Subsequently, the modeling parameters were improved by fitting them to free-rocking experimental results. The method resulted in an unrealistically soft joint interface, from which the block does not separate during rocking motion. Thus, continual damping is applied in order to approximate actual damping which primarily occurs at impact. After fitting, the method was effective in predicting experimental results of more complex ground motions.

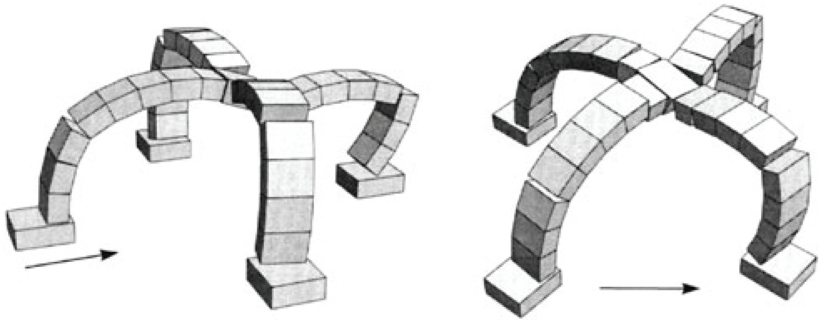

Figure 2-7: Collapse mechanisms formed by intersecting masonry arches under horizontal ground motion. (after Lemos 1998)

The response of masonry structures to ground motion has also been investigated using 3DEC. Lemos (1998) assessed the three-dimensional stability of masonry arches due to ground motion, and predicted interesting collapse mechanisms (Figure 2-7). More recently, Lemos (2007) critically evaluated numerical issues which can arise when trying to model structural dynamics using discrete elements, and mentions some difficulties involved in defining damping. Papantonopoulos et al. (2002) simulated experiments on a one-third scale replica of a Parthenon column conducted by Mouzakis et al. (2002). The authors did a sensitivity study to determine appropriate damping parameters, and concluded that 3DEC can be used with confidence to estimate the response of ancient monuments to expected earthquake motions. Subsequently, Psycharis et al. (2003) used 3DEC to assess the stability of the entire Parthenon Pronaos.

While many of these studies conclude that UDEC and 3DEC are effective in predicting results, this can only be concluded after modeling parameters are adjusted so that results do compare well. A methodical way of defining modeling parameters before analysis is still lacking. This is necessary before confidence can be placed in DEM prediction.

NSCD

Non-smooth contact dynamics involves an implicit time-stepping scheme in which blocks can be either rigid or deformable. Unilateral contact is based on the work of Moreau (1988), and ensures that blocks do not interpenetrate and contacting bodies do not attract each other, i.e. normal contact forces remain outward. Coulomb friction is included in the model. The impact between rigid blocks is taken into account using shock laws, in which the energy dissipation can theoretically be adjusted by the "dissipation index" (Moreau 1988). The NSCD method was formalized by Jean (1998), in which standard inelastic shock (Moreau 1984) is assumed.

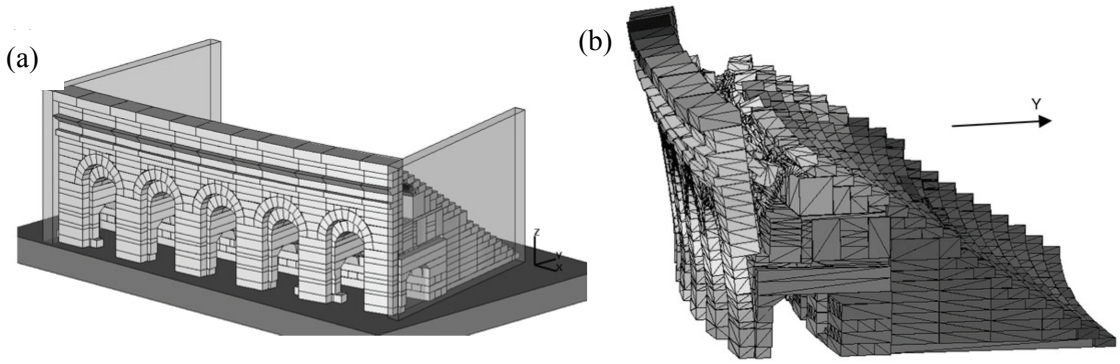

Figure 2-8: NSCD analysis of the arena in Nîmes, France by Rafiee et al. (2008b): (a) analyzed section of the arena, and (b) the collapse mechanism for ground motion in the *y*-direction. (after Rafiee et al. 2008b)

Recently, the NSCD method has been used to model the dynamics of masonry structures, including investigations of in-plane wall behavior (Chetouane 2005), dynamic arch behavior (Rafiee et al. 2008a), and analyses of full-scale masonry structures (Rafiee et al. 2008b). In all cases, the analyses depict the potential of the method to predict the complex response of block structures to earthquakes (e.g. Figure 2-8), but experimental verification of the method is still necessary. Furthermore, the sensitivity of results to the modeling parameters, particularly the dissipation index, is of interest.

2.4 Summary

This chapter has identified many of the approaches taken to assess masonry structures in seismic regions. The goal is to define what has been done and to highlight the areas in which contributions need to be made. This literature review allows the following conclusions to be drawn, and motivates the corresponding contributions of this dissertation:

- Graphical methods are appropriate for assessing the stability of pure compression structures, but hand-drawn constructions can be prohibitively tedious. Realization of graphical methods through computational geometry software has alleviated this problem, providing the framework necessary to assess the capacity of pure compression structures to resist constant horizontal ground acceleration. Models which accomplish this are developed in Chapter 3.
- There is a gap between micro-mechanical material damage models and macro-scale assessment methods for damage prediction of masonry structures. Micro-mechanical material damage models are often tailored towards research, while macro-scale models are better suited for the engineering industry. However, Sequentially Linear Analysis

(SLA) has been proposed as a simplified alternative to model damage of masonry structures which could bridge this gap (Rots 2001). This method is discussed, further developed, and applied in Chapter 4.

- While rigid body dynamics is a powerful method for analytically determining the response of rigid block structures, it becomes cumbersome for multiple block systems and is therefore reaching its practical limits. However, the simplification of arches as SDOF mechanisms holds potential for describing the dynamics of arches using analytical rigid body dynamics. Furthermore, the dynamics of arches has not been thoroughly explored experimentally. An analytical arch model is developed and compared with new experimental results in Chapter 5.
- While rocking behavior has been extensively studied, a clear investigation into the ground motions to which rocking structures are most vulnerable has not been conducted. Furthermore, while research suggests that the primary impulse within an earthquake excitation is the critical factor which causes overturning of rocking structures, the possibility that multiple impulses could act together to amplify the rocking response has not been addressed. These concepts are explored in Chapter 6.
- Discrete element models with compliant contacts (e.g. UDEC) have been effective in capturing the general dynamic behavior of masonry structures to earthquake ground motions. However, further evaluation of these methods is necessary, and a clearer understanding of modeling limitations should encourage intelligent ways in which these methods can be confidently applied. Additionally, a systematic way of defining modeling parameters is lacking. These challenges are addressed in Chapter 7.

The areas in which the contributions of this dissertation are made are summarized in Table 2.1, where the primary research studies upon which contributions are built are also cited.

Table 2.1: Primary areas of contribution and the primary work upon which these contributions are built

General Focus	Contribution	Primary Previous Work	Chapter
Quasi-Static loading:			
Stability	Graphical assessment method: Thrust Line Analysis	Block (2005)	3
Strength	Simplified micro-mechanical modeling: SLA	Rots (2001)	4
Dynamic loading:			
Stability	Experimental assessment: Arches	Appleton (1999)	5
	Rigid body dynamics: Arches	Oppenheim (1992)	5,6
	Rigid body dynamics: Rocking structures	Housner (1963)	6
	Evaluation of computational modeling: UDEC	Lemos (1998, 2007)	7

Part II

Quasi-static Analysis

Chapter 3

Thrust Line Analysis

3.1 Introduction

For assessing masonry structures in seismic regions, it is necessary to understand quasi-static collapse before moving on to dynamic collapse. This chapter focuses on a quasi-static assessment method based purely on stability. Once stability limits are determined, then assessment methods based on strength can be applied to model damage if desired, as in Chapter 4.

As discussed in §2.2.1, equilibrium methods are effective for the assessment of masonry under static loading (Heyman 1995). Under the assumptions of these methods, sliding and crushing are not possible, but stability can be assessed. The concept of a *thrust line* is used to visualize the forces within the structure. When the thrust line can no longer be contained within the masonry, the masonry can no longer support the applied loads, and the structure is no longer in equilibrium without hinging. In general, hinging does not necessarily mean that the collapse of the structure is eminent, because four hinges are necessary to form an unstable mechanism. Take for example, the arch on spreading supports. Three hinges form immediately under an applied support *displacement*, but the thrust line remains within the masonry and the structure therefore remains stable until four hinges form at the point of collapse (Ochsendorf 2006). On the other hand, applied *forces* do not cause any hinging until a four-hinge mechanism directly forms.

Although the static analysis of arched structures has been studied for centuries, Block (2005) recently developed a tool which uses graphic statics to achieve a rapid first order assessment of

the stability of various masonry structures. A parametric graphical framework allows geometry to be adjusted in real-time, allowing the effect of geometrical changes to be rapidly evaluated. All graphical constructions presented in this chapter were implemented using Cabri Geometry II Plus (www.cabri.com), a commercial geometric modeling software. For a review of graphic statics, see Zalewski and Allen (1998).

3.2 Tilt Analysis

As mentioned in Chapter 2, it is common practice in structural engineering design to simulate earthquake loading by a constant horizontal force that is some fraction of the weight of the structure in magnitude. This is equivalent to applying a constant horizontal acceleration that is some fraction of the acceleration of gravity. Such an 'equivalent static loading' does not capture all of the dynamics, but it does provide a measure of the lateral loading that the structure could withstand before collapse.

One way of implementing equivalent static analysis is by tilting the ground surface. This effectively applies a combination of vertical and horizontal acceleration to the structure. Note that in the reference frame that rotates with the structure, tilting causes the vertical acceleration to be reduced as horizontal acceleration increases. Thus, tilting is not exactly the same as only applying constant horizontal ground acceleration. However, while this would be problematic if the stresses within the structure were of interest, the assumption that crushing will not occur negates this problem. The ratio of vertical to horizontal acceleration is all that is of interest, and the fact that stresses within the structure are effectively reduced is assumed to be of secondary importance. The ratio of horizontal acceleration ($\ddot{u}_h$) to vertical acceleration ($\ddot{u}_v$) in the rotating reference frame is directly related to the angle of tilt (α):

$$\gamma = \frac{\ddot{u}_h}{\ddot{u}_v} = \tan\alpha \tag{3.1}$$

In this chapter, graphic statics is used to develop a tool to simulate structures on a tilting surface. The ground surface is tilted until the thrust line cannot be contained within the structure, i.e. until the point where it touches the exterior surface of the structure at four locations. At this point, a four-hinge mechanism would form and the structure would collapse.

Although it is trivial, the overturning collapse of a single block helps to clarify tilting thrust line analysis. The single block in Figure 3-1a is only acted upon by gravity, and therefore the thrust line is drawn vertically downward from the center of mass. In this initial state, the thrust line remains within the block until it enters the supporting ground, thus the block is stable. If the

block is tilted, the thrust line will remain within the block until the critical angle of ground tilt, α_{cr}, shown in Figure 3-1b. Just beyond this point, the thrust line exits the block before entering the support, indicating that it would overturn by rotating about a 'hinge' which would form at its bottom right corner (point *O*). At the point of overturning, the tilting angle, α, can be related to the constant horizontal ground acceleration ($\ddot{u}_g$) which would cause collapse of an un-tilted block:

$$\ddot{u}_g = \gamma; \quad where \ \gamma = \tan\alpha = B / H \tag{3.2}$$

where *B* and *H* are defined in Figure 3-1, and γ is expressed as a fraction of the earth's gravitational acceleration, *g*.

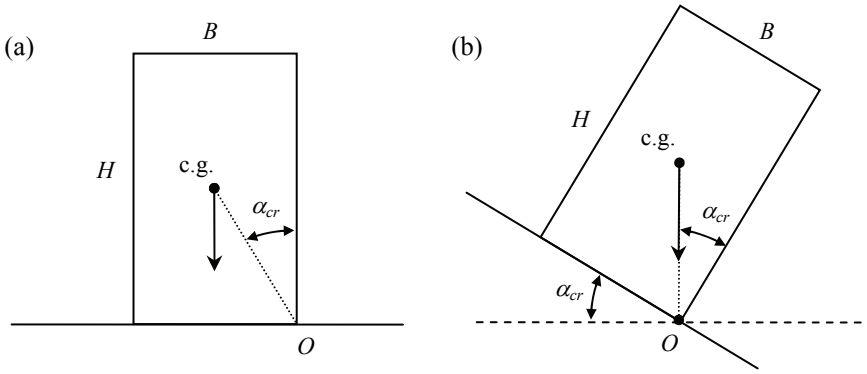

Figure 3-1: Tilting thrust line analysis of a single block.

3.3 The Arch

While the analysis of the single block clearly demonstrates hinging collapse, analysis of the masonry arch provides more interesting results which demonstrate the benefit of graphic statics. In this section, the part-circular masonry arch studied by Oppenheim (1992) is investigated. It has the following characteristics: seven voussoirs (n_A = 7), an angle of embrace (β_A) of 157.5 degrees, an arch center-line radius (R_A) of 10 m, and a thickness (t_A) of 1.5 m.

In its initial un-tilted state, one thrust line which fits within the masonry is depicted in Figure 3-2a, and therefore the arch is stable. An infinite number of similar thrust lines could also be drawn within the masonry, as mentioned in §2.2.1 (Figure 2-1). To the right of Figure 3-2a, the force polygon which is used to draw the line of thrust is shown. The force polygon is used to resolve the forces within the structure, ensuring that it is in equilibrium. Note that the thrust line and force polygon are parametrically linked, so they interact in real time.

The parametric model was created so that the structure can be tilted by clicking and dragging the appropriate point, and the thrust line can be adjusted in the same manner. In Figure 3-2b, the arch has been tilted and the thrust line adjusted to fit within the arch thickness. Again, there are an infinite number of other thrust lines which would remain within the masonry, and the arch is still stable. The corresponding force polygon (Figure 3-2b, right) indicates the rotation of the forces and the increased length of the top line of the force polygon correlates to the increased force at the left springing of the arch.

Finally, as tilting continues, a single unique thrust line is found which touches the exterior of the arch at four locations (Figure 3-3c), and collapse is imminent. Collapse would occur through formation of the four-hinge mechanism depicted in Figure 3-3d. Using thrust line analysis, the maximum allowable tilt angle was found to be 20.3 degrees ($\gamma = 0.37$ g), the same value found by Oppenheim (1992) using virtual work calculations.

While only a single arch geometry is discussed here, this graphical tool allows the geometric properties (t_A, R_A, β_A) to be updated by clicking and dragging the mouse. Thus, the effects of geometric properties on stability can be investigated both visually and quantitatively, as will be seen in the following sections.

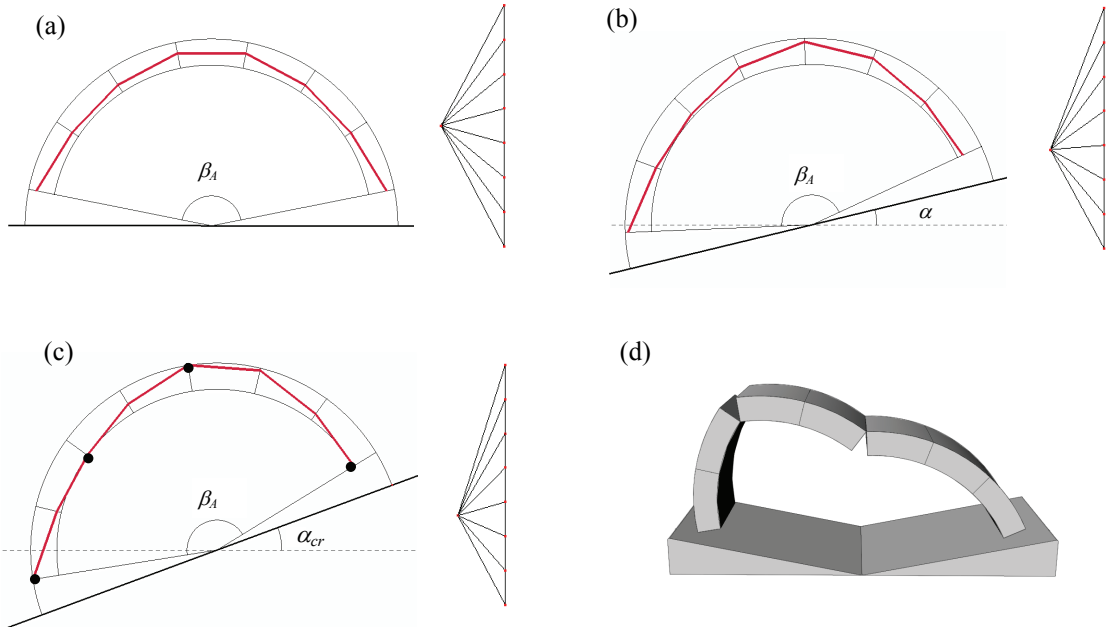

Figure 3-2: Tilting thrust line analysis of a masonry arch: (a) initial condition, (b) tilted but still stable, (c) tilted to the verge of collapse, and (d) mechanism of collapse.

3.4 The Buttressed Barrel Vault

Tilting thrust line analysis can be expanded to address a more complete structure: a barrel vault supported by continuous buttresses. In order to allow a rough comparison with the results of §3.3, a barrel vault with the same radius (10 m), and thickness (1.5 m) is investigated. However, the inclusion angle, which is taken as the angle between the intersection of the arch extrados and the buttress at each springing, is quite a bit smaller (β_A = 120 degrees). This smaller inclusion angle, typical of buttressed barrel vaults, results in much greater resistance to tilting; using tilting thrust line analysis for an arch (§3.3), the vault alone can sustain a tilt angle of α_{cr} = 42 degrees (γ = 0.91 g). The height of the extrados of the barrel vault springing and the thickness of the buttresses were initially assumed to be 1.5 and 0.33 times the vault span of 8.5 m, respectively, and were then varied independently to clarify the stability of the structure. Once the geometric construction is created, the geometry of the entire structure, the thrust line, and the tilt angle of the ground surface can all be adjusted in real-time by clicking and dragging the designated points.

For the initial geometry, tilting causes collapse through the four-hinge mechanism shown in Figure 3-3, at a tilt angle of 7.7 degrees (γ= 0.13 g). The three hinges in the arch indicate that it is in a state of minimum thrust, as would be expected. This mechanism remained approximately unchanged for the wide range of geometries subsequently investigated. It is worth noting that evidence of this type of collapse during earthquakes has been widely observed for small churches throughout the world (e.g. Figure 3-3c, after Unesco 1994).

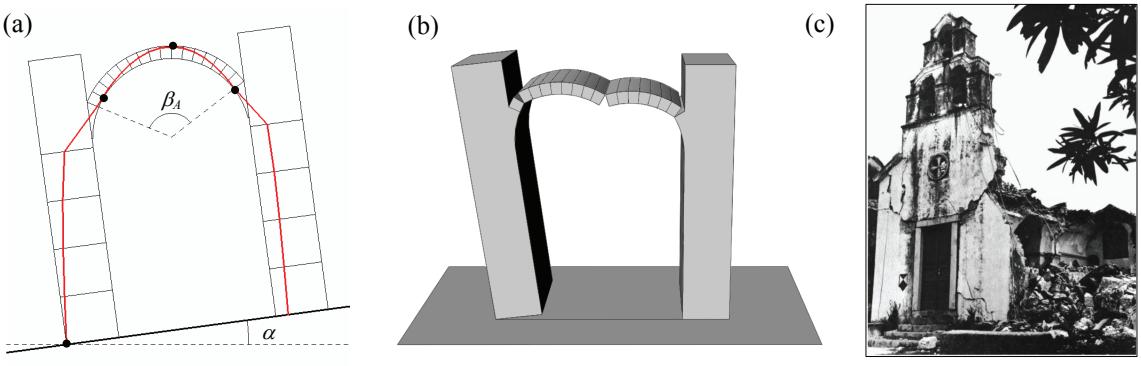

Figure 3-3: Tilting thrust line analysis of a buttressed barrel vault: (a) tilted to the verge of collapse, (b) the resulting collapse mechanism, and (c) evidence of similar collapse during the 1979 Montenegro Earthquake (after Unesco 1984).

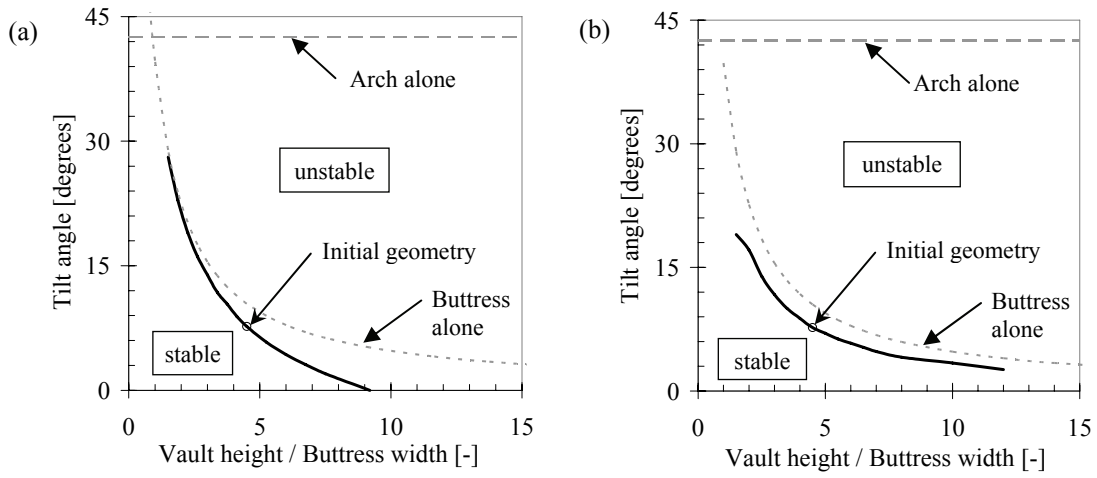

Figure 3-4: Stability curves for a buttressed barrel vault with fixed vault thickness and span: (a) fixed vault height but variable buttress width, (b) fixed buttress width but variable vault height.

For a fixed vault height but a variable buttress width, the tilt angle necessary to cause collapse is plotted in Figure 3-4a. Notice that at the lower limit, no tilt is possible above a vault height / buttress width ratio of 9.2 (vault span / buttress width = 6.1). This is because the structure is unstable in its un-tilted state for thinner buttresses. Also note that as the buttresses become unrealistically thick (vault height / buttress width ≤ 1.5, i.e. vault span / buttress width ≤ 1), the tilt capacity is quite large and will eventually reach that of the arch alone.

For a fixed buttress width but a variable vault height (and dependent buttress height), the tilt angle necessary to cause collapse is plotted in Figure 3-4b. For this case, stability increases as the vault height decreases. At the lower limit of the vault height, the results are only plotted until a slightly different collapse mechanism would form, but the limiting tilt would again eventually reach the capacity of the arch alone. At the upper limit of vault height, it is interesting to note that the tilt angle will never reach zero, as the structure will remain stable no matter how high the vault is raised. (Of course, at some point it would fail due to crushing, so that would be the governing failure mode in this theoretical case.) However, as the height increases, the stability curves for the entire structure and for the buttress alone merge and asymptotically approach zero. This behavior is expected as extremely tall, slender structures overturn rather quickly when tilted.

3.5 The Buttressed Barrel Vault with Side Aisles

Adding one more level of complexity to the structure, a buttressed barrel vault with side aisles is considered. In this case, the number of geometric parameters which could be adjusted is large, so it is useful to start by taking approximate dimensions from existing structures.

Accordingly, two structures with significantly different characteristics were selected as geometric starting points. Subsequently, their geometries were adjusted to investigate possible collapse mechanisms and to understand the effect of the side aisles on the stability of the main aisle. Again, the geometry and thrust line can be adjusted in real-time by clicking and dragging the mouse. The goal of this section is not to evaluate the safety of these specific structures, although this could be done, but instead to: 1) understand the stability and collapse of these types of structures, and 2) highlight the benefits and shortcomings of such an analysis.

The first geometry used is inspired by the Basilica of St. Mary Magdalene in Vezelay, France (Figure 3-5). The structure is assumed to be symmetric and the geometry of the main aisle and the height of the side vaults were assumed fixed, while the side aisle span and exterior buttress widths were adjusted. The overall width of the entire structure was also assumed to be fixed.

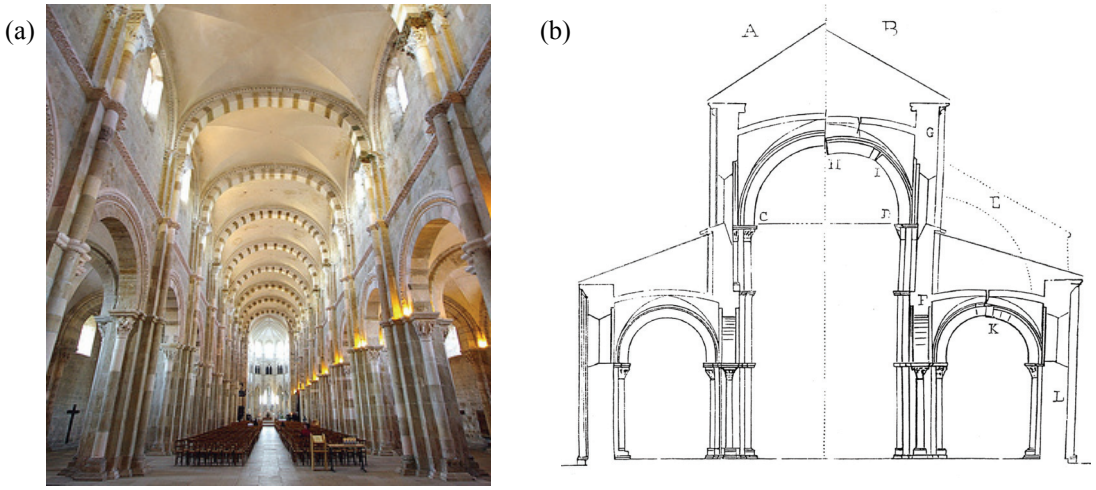

Figure 3-5: The Basilica of St. Mary Magdalene in Vezelay, France: (a) interior view of the main nave, (b) cross-section by Viollet-le-Duc (1860) depicting the original geometry on the left and the deformed geometry on the right.

The resulting horizontal acceleration necessary to cause collapse is plotted in Figure 3-6a as a function of the side aisle geometry. Three different mechanisms result. If the side aisle buttresses are too thin, then the side aisles would collapse alone, with the side aisle vault in a state of minimum thrust, providing very little additional stability to the main aisle (Mechanism 1, Figures 3-6b). As the width of the side aisle buttresses increases, they work to stabilize the main aisle, and collapse of the main and side aisle buttresses occurs simultaneously (Mechanism 2, Figures 3-6c). Finally, for wide side aisle buttresses, but correspondingly thin side aisle vaults, the side aisle vaults form a mechanism in a state of maximum thrust while the main aisle collapses in minimum thrust (Mechanism 3, Figures 3-6d). Notice that there is a side aisle geometry which maximizes

the tilt angle which can be achieved (Figure 3-6a), and therefore optimizes the relationship between the side aisle span and the buttress width.

Compared to the range of buttressed barrel vaults investigated in §3.5, the main aisle alone is not very stable (Figure 3-6a). This is expected as the side aisles are intended to support the main aisle. In this rough approximation, the side aisles approximately double the angle of tilt that the structure could withstand. It is worth noting that the side aisles are short with respect to the height of the main aisle, which limits their effectiveness in providing additional stability. While the cause of the deformations depicted by Viollet-le-Duc (1860) on the right of Figure 3-5b is unknown, the solution was to add flying buttresses on both sides of the main aisle (drawn dashed above the right side aisle in Figure 3-5b). This solution solves the problem of the limited stabilizing capacity of the short side aisles.

The second geometry used is inspired by the Church of Saint Patrocle in Colombier, France (Figure 3-7a). In this structure, the side aisles are almost as tall as the main aisle, and much taller than in the basilica in Vezelay. Taking an approximation of a cross-section of the church in Colombier from the database of Bourbonnais churches compiled at Columbia University (Murray 2009), the effect of the side-aisles on stability is again investigated using the same geometric assumptions made for Vezelay. Initially, the exterior buttresses, which were added to one side of the church well after construction (Figure 3-8a), are ignored. Subsequently, the effect of these buttresses on the stability is briefly evaluated.

The resulting horizontal acceleration at collapse is again plotted as a function of side aisle geometry in Figure 3-7b. Three primary collapse mechanisms result (Figure 3-7), which differ from those in Figure 3-6 due to the taller side aisles. For thin side aisle buttresses, the side aisles again collapse alone before the main aisle (Mechanism 1, Figure 3-7c), and again provide very little additional stability. For wider side aisle buttresses, the stability increases significantly. The higher side aisles cause all three vaults to collapse in unison, with the right side aisle in minimum thrust and the other two at intermediate states of thrust (Mechanism 2b, Figure 3-7d). This is noticeably different than the case of Vezelay, in which the right side aisle is never predicted to collapse. Last, as the side aisle buttresses get extremely wide, the side aisle arches again become the weak link. All three vaults collapse together, with the left, center and right vaults being in maximum, intermediate, and minimum states of thrust, respectively (Mechanism 3b, Figure 3-7e). Again notice that there is an optimal side aisle geometry which maximizes the stability of the entire system, and provides roughly three times the tilt capacity of the main aisle alone (Figure 3-7b). However, this would require side aisle buttresses which are extremely thick, inspiring the alternate solution of the flying buttress.

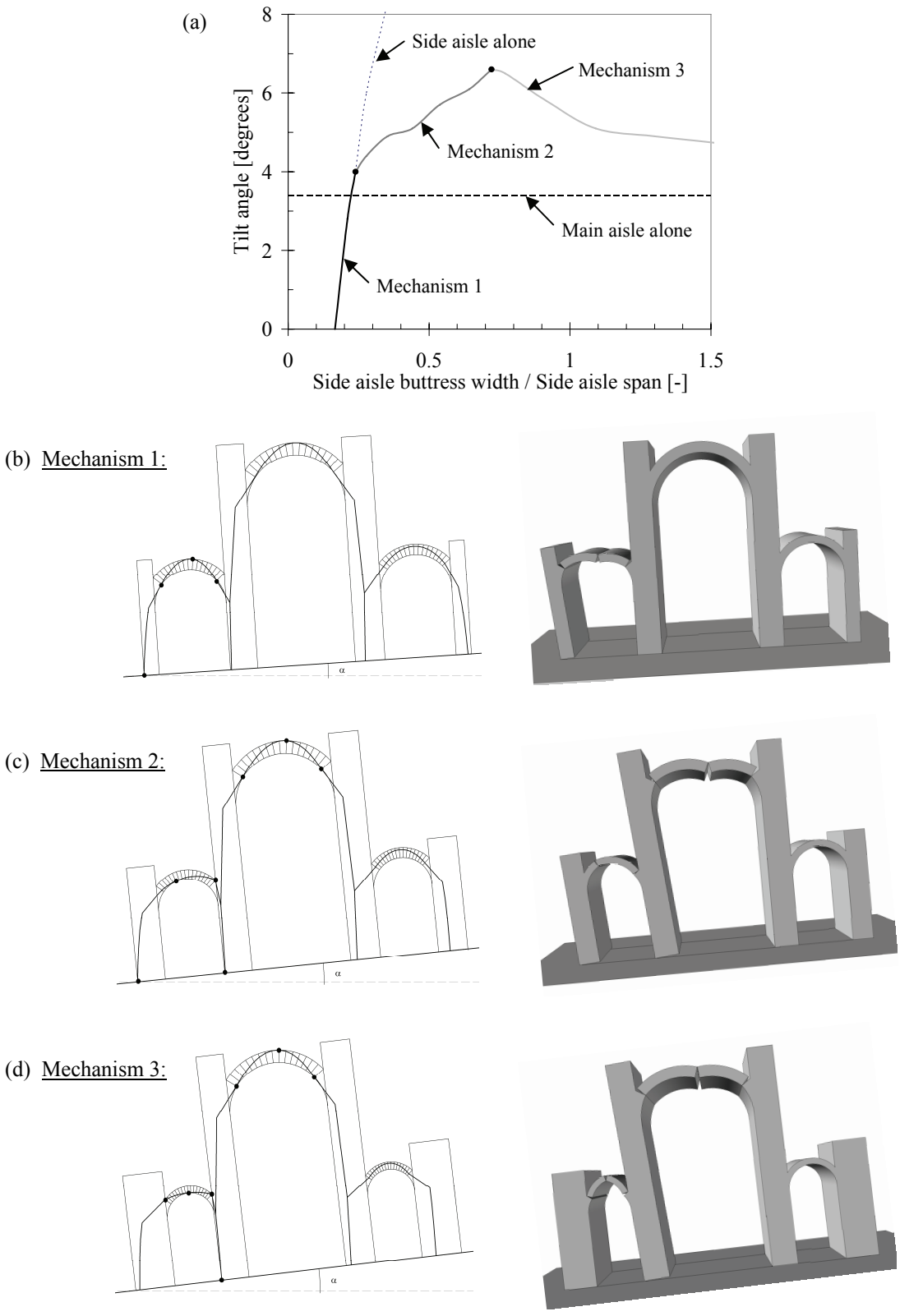

Figure 3-6: Stability results for the Basilica of St. Mary Magdalene in Vezelay, France: (a) allowable tilt angle for different side aisle geometries, and (b)-(d) the corresponding tilting thrust line analyses and collapse mechanisms.

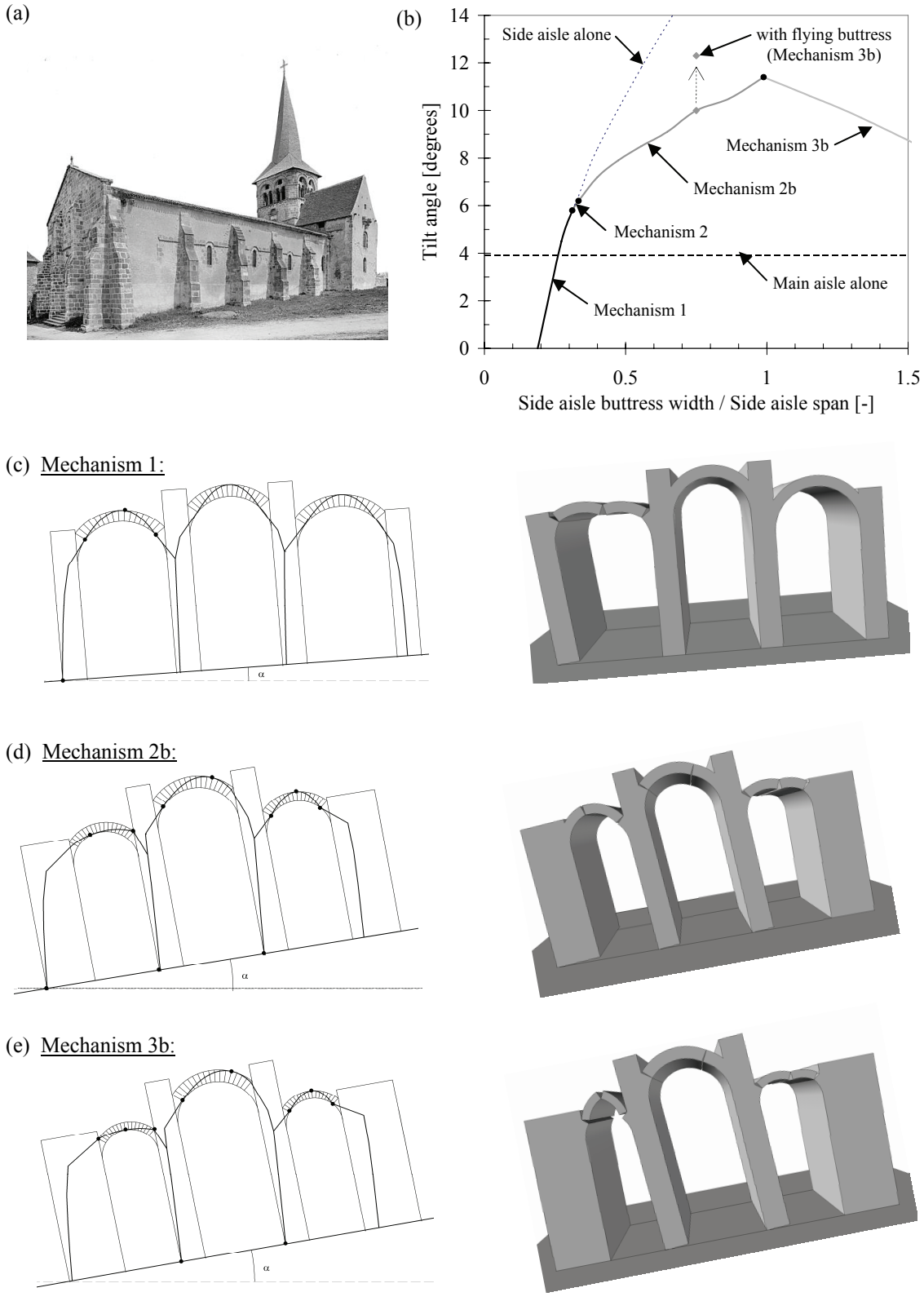

Figure 3-7: Stability results for the Church of Saint Patrocle in Colombier, France: (a) image of church, (b) allowable tilt angle for different side aisle geometries, and (c)-(e) the corresponding tilting thrust line analyses and collapse mechanisms.

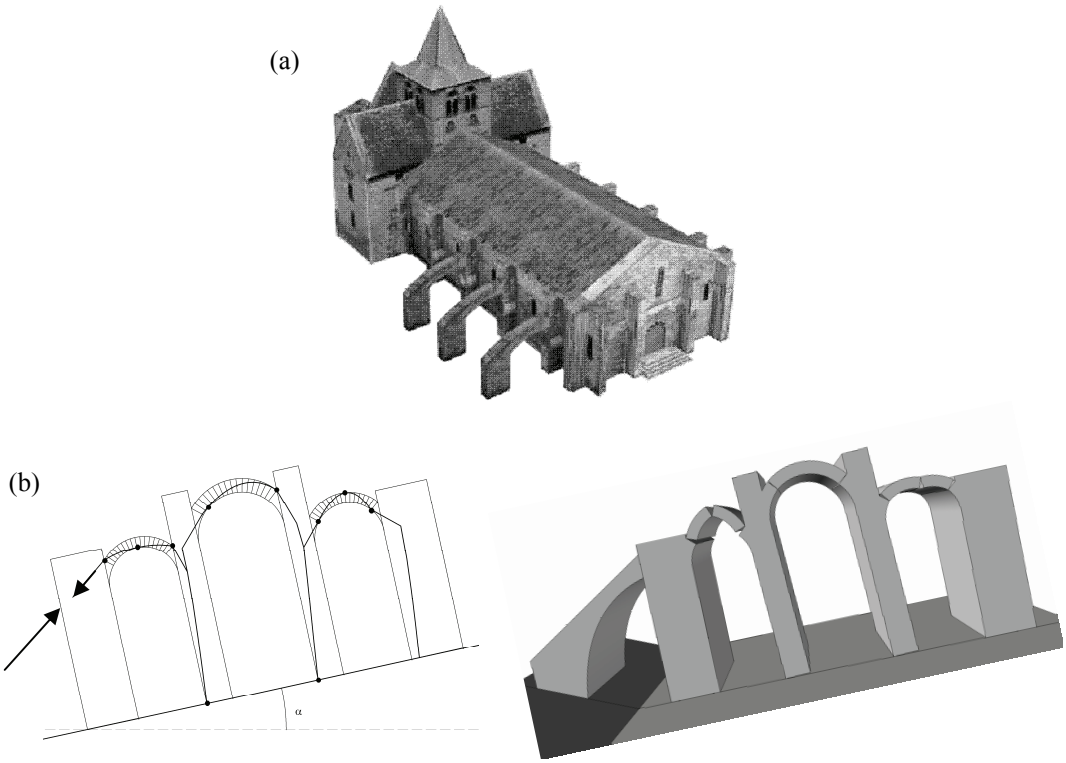

Figure 3-8: Effect of adding exterior buttresses to the Church of Saint Patrocle in Colombier, France: (a) image of the added buttresses (after Murray 2009), (b) tilting thrust line analysis and collapse mechanism with added buttresses.

The exterior flying buttresses shown in Figure 3-8a were added to one side of the church in the early 19th century (Murray 2009). An approximation of the stability of the cross-section with the buttresses is plotted as a single point in Figure 3-7b. The buttresses clearly increase the stability. The reason for this stability increase is that the added buttresses force collapse to occur through Mechanism 3b instead of Mechanism 2b (Figure 3-8b).

3.6 Discussion

The three vaulted masonry typologies investigated in §3.3, §3.4, and §3.5 clarify the behavior of vaulted structures under horizontal ground accelerations through the use of tilting thrust line analysis. The method illuminates the stability of sub-structures alone (e.g. vaults, buttresses, side aisles), as well as how the delicate interaction of the structural components effects the stability of the structure as a whole. Similar assessment would be difficult with typical structural analysis tools, and extremely difficult to demonstrate.

Vaulted structures are prolific throughout the world, and extremely detailed analyses are often times not realistic for every structure. The examples also demonstrate how such a method

could be used to rapidly assess the seismic capacity of a large number of vaulted structures of a certain type. Then more extensive analyses could be conducted on the structures which are determined to be the least safe.

Furthermore, while this chapter has emphasized the use of tilting analysis as a first order seismic assessment method, the concept is also valuable as a general stability measure of masonry structures in non-seismic regions. In the worst case, a stable structure can sustain zero tilt, signifying no factor of safety. On the other hand, a larger tilt capacity indicates increased stability, and therefore a greater factor of safety.

While this method is both instructional and effective, numerous simplifications have been made, resulting in the following limitations:

- Tilting analysis is a quasi-static assessment method which predicts the collapse of the structure under constant horizontal ground acceleration. Thus, the predicted horizontal accelerations which cause collapse are extremely conservative in that they assume an infinite duration of loading. Actual earthquake loadings are obviously of much shorter duration. For finite durations of ground acceleration, the structure could recover due to inertial effects, even if a mechanism is briefly formed due to horizontal accelerations above the predicted acceptable level. This is clearly demonstrated and investigated in Part II of this dissertation. Additionally, other effects of dynamic loading (e.g. impact and vibration displacements between blocks) are also ignored by a static analysis.
- As mentioned previously, the assumptions of limit analysis remove the possibility of local crushing and sliding. For the types of structures discussed in this chapter, these behaviors typically have a negligible effect under static loading (Ochsendorf and De Lorenzis 2008). However, for certain types of structures, they could cause results to be unconservative. For these structures, failure is typically captured with methods focused on strength rather than stability, as demonstrated in Chapter 4.
- The method presented is currently limited to two-dimensional problems. The structure should be simplified from three-dimensions to two-dimensions in a manner that ensures that results are conservative.

Despite these limitations, the method is valuable as a starting point for assessing masonry structures in seismic regions.

3.7 Summary

Equilibrium methods have a strong tradition in the analysis of masonry structures, where stability often governs. This chapter has demonstrated how these methods can be extended to provide a first order seismic assessment using graphical analysis. The primary conclusions are as follows:

- Thrust line analysis is particularly advantageous for studying numerous structures with similar geometry. Once models are constructed for a certain structural typology (as in §3.3, §3.4, and §3.5) a first order assessment of stability can be rapidly obtained. Furthermore, effects of changes in geometry can be rapidly evaluated.
- The results obtained are both qualitative and visual, giving the user a clear depiction of the collapse mechanism and a better understanding of structural behavior.
- The framework of real-time graphic statics is valuable for design, as the user can adjust the geometry and immediately get feedback on the stability of their structural form.
- The tools developed in this section are also valuable for instructional purposes, where visual depiction of results is particularly valuable.

Therefore, while more rigorous dynamic analyses should be executed for structures which are known to be in danger of collapse, this equivalent static analysis method can provide a valuable tool for identifying those structures which are in danger, as well as likely collapse mechanisms to be concerned about.

Chapter 4

Sequentially Linear Analysis*

4.1 Introduction

At the opposite end of the spectrum from equilibrium assessment methods (e.g. Chapter 3), lie analysis methods which focus on strength. These methods attempt to predict material deformations and material failure, but can have difficulty predicting collapse. Equilibrium methods, on the other hand, can predict collapse but are not capable of predicting material behavior and material failure. Thus, strength methods are particularly appropriate when attempting to predict material damage. More generally, they should be used if neglecting material deformation, tensile capacity, and compressive failure is undesirable or unconservative.

Strength methods are often appropriate when simulating the response of more modern masonry structures under simplified quasi-static earthquake loading. If these structures have some appreciable tensile capacity or are tied together with reinforced concrete or timber floor diaphragms, the likelihood of collapse due to instability is relatively low, and the tensile and compressive strengths of masonry must be accounted for in the analysis. In these cases, failure through material damage can not be neglected.

Strength methods might also be appropriate when trying to predict or explain damage in vaulted or domed structures with complex geometries. For example, consider what happens if a

* This research was conducted at the Technical University of Delft under the supervision of Professors Jan Rots and Max Hendriks.

constant horizontal acceleration were applied to a complex vault made of several layers of mortared thin tile. The collapse mechanism might not be immediately obvious, and might be difficult to predict using equilibrium methods. However, strength methods could be used to predict where damage might occur, which could inform possible collapse mechanisms. Then, equilibrium methods could be used to predict collapse.

As discussed in §2.2.2, the majority of strength methods employ Finite Element Modeling (FEM), the framework that will be used in this chapter. Modeling the fracture of brittle materials is an essential requirement for predicting damage to masonry structures, and remains a challenge using FEM due to sharp material "softening" after realization of the material strength. Nonlinear finite element analysis techniques have been adapted to deal with the sharp softening curves associated with brittle materials like masonry, but convergence difficulties still motivate alternate modeling procedures.

In this chapter, one alternate method for modeling brittle fracture, Sequentially Linear Analysis (SLA), will be discussed and further developed. The motivation for this is to fill the void between existing masonry analysis methods which focus on strength, as reviewed in §2.2.2. Specifically, the goal is to bridge the gap between simplified macro-scale analyses (e.g. linear elastic analysis, pier-spring models, equivalent frame analysis) typically employed in engineering practice and advanced non-linear finite element analyses being applied in academic research. To achieve this, the aim is to model the 3D response of masonry structures under lateral loading, while avoiding: 1) the discretization of walls into equivalent frames, 2) the *a priori* definition of crack locations, and 3) the convergence difficulties which can occur during non-linear finite element analysis.

In §4.2, SLA is reviewed. In §4.3, the SLA framework is extended to include non-proportional loading. The accuracy of this extension, which is critical to allow the inclusion of self-weight in addition to seismic loads, is verified through simulation of previous experiments involving brittle fracture. In §4.4, the framework is extended to include shell elements, for the purpose of predicting three dimensional crack patterns and possible failure mechanisms for masonry structures under seismic loading. Experiments on a full-scale masonry structure under cyclic quasi-static loading are simulated to exemplify the capabilities and limitations of the method. Finally, conclusions and findings are summarized in §4.5.

4.2 Review of Sequentially Linear Analysis

Modeling fracture through an event-by-event cracking procedure is an attractive alternative to typical FEM because modeling proceeds by imposing an increment of damage instead of an increment of displacement, force, or time. In this way, it is unnecessary to make large jumps in damage during a single load step or time step, which is usually the source of convergence problems. In other words, while nonlinear finite element analysis "skips over" portions of the structural response when brittle behavior occurs, and hopefully rejoins the response through iteration algorithms, event-by-event procedures avoid this by specifying damage directly.

For example, discrete lattice models (e.g. Herrmann et al. 1989, Schlangen 1993), which have become quite attractive for modeling fracture, impose incremental damage by breaking a single beam element in every step. Recently, Rots (2001) proposed SLA as a method to prescribe incremental damage in a continuum model. Consecutive linear finite element analyses are used to identify the critical location in the model, to which an increment of damage is applied. The procedure is similar to lattice modeling, except the constitutive relationship is discretized into saw-teeth instead of the continuum into beam elements. The resulting method effectively describes highly nonlinear behavior through a continuum model which completely avoids convergence problems.

Sequentially linear analysis was developed specifically to address the difficulty of modeling snap-back behavior (Rots and Invernizzi 2004), typical of full-scale concrete and masonry structures (Rots et al. 2006). While generally applicable for materials with non-linear softening behavior, it is particularly beneficial when brittle fracture causes convergence issues. In this study brittle behavior will be modeled with a linear softening relationship after initial tensile failure (Figure 4-1a). Compressive failure will not be considered, as tensile failure typically governs due to inherent material weakness in tension. Inclusion of compressive failure is more important for reinforced concrete structures, and has also been implemented using SLA (Rots et al. 2008).

The sequentially linear approach approximates the constitutive stress-strain relationship using a series of saw-teeth which maintain a positive tangent stiffness (Figure 4-1b). Linear analyses are repeated, each with a reduced positive stiffness, until the global analysis is complete. Thus, the negative tangent stiffness, which is characteristic of masonry softening curves and can be detrimental to convergence, is avoided entirely. Specifically, the modeling procedure is implemented as follows:

- Apply a reference proportional load, W (force or displacement), and calculate the principal stresses through linear elastic analysis.

- Determine the critical integration point as the point for which the maximum principal tensile stress, σ_t, utilizes the largest percentage of the current tensile strength, f_{ti}^{+}, and calculate the critical load multiplier: $\lambda_{crit} = f_{ti}^{+} / \sigma_t$.
- Scale the reference load proportionally using the critical load multiplier, $\lambda_{crit} * W$, and determine the current stress-strain state.
- Reduce the stiffness and strength of the critical integration point according to the saw-tooth approximation of the tensile constitutive relationship (Figure 4-1b).
- Repeat this cycle of steps continuously, updating the properties of a single integration point after each cycle.
- The non-linear response is extracted by linking consecutively the results of each cycle.

This procedure can overcome difficult convergence problems (Rots et al. 2006, Rots et al. 2008), but the analyst must take care in approximating the stress-strain relationship by a series of positive-stiffness saw-teeth. The linear tensile softening stress-strain relationship is characterized by the elastic modulus, E, tensile strength, f_t, and the fracture energy, G_f. The ultimate strain, ε_u, is calculated directly from these properties:

$$\varepsilon_u = \frac{2G_f}{f_t h} \tag{4.1}$$

where h is the crack bandwidth, i.e. the anticipated width of the zone where cracking occurs and where the constitutive relationship holds. The crack bandwidth, h, is dependent on the finite element size, shape, and integration scheme, and will be defined according to the guidelines proposed by Rots (1988).

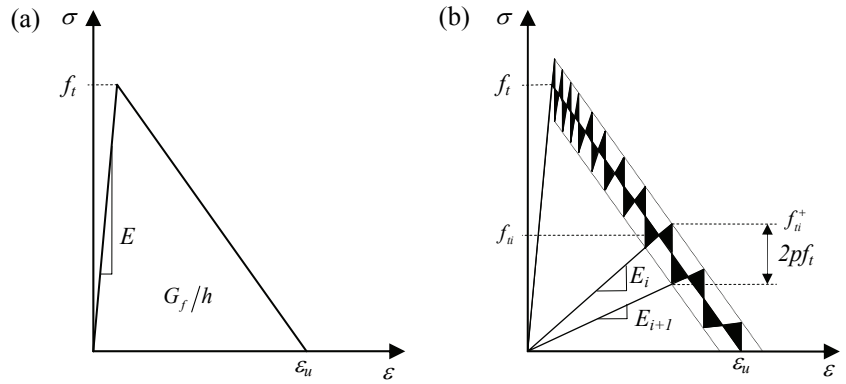

Figure 4-1: The stress-strain relationship for (a) linear softening, and (b) the consistent saw-tooth diagram.

Several saw-tooth approximations could be specified by adjusting the elasticity, maximum strain, and strength of each consecutive saw-tooth. However, the approximation must yield results that are mesh independent. Rots and Invernizzi (2004) investigated several saw-tooth approximations, and concluded that any approximation must conserve the dissipated energy, i.e. the area under the softening curve, G_f / h. Rots et al. (2008) conducted a more expansive study regarding the shape of the saw-tooth curve, and presented the "ripple" softening curve which was used in this study (Figure 4-1b).

The ripple curve is derived by defining an envelope around the softening curve of magnitude $2pf_t$ (Figure 4-1b), from which the number of teeth and the reduced strength and stiffness of each tooth are directly defined (see Rots et al. (2008) for the complete derivation). Thus, p is an input variable which modulates the fineness of the saw-tooth approximation. While a small p value provides more accurate results, this benefit must be balanced with the resulting increased computational time. In the ripple curve, the dissipated energy is conserved, as over- and under-estimation of the dissipated energy are canceled out by consecutive teeth. This is visually evident in Figure 4-1b where the pairs of black triangles, above and below the softening curve, are of equal area.

4.3 Non-proportional Loading

In this section, the SLA framework is extended to non-proportional loading, which opens the door to an array of engineering applications. This extension allows the inclusion of self-weight, which is critical when modeling full-scale structures. This is of particular interest for seismic assessment, where self-weight can not be neglected when applying a quasi-static horizontal loading as a first-order approximation of expected seismic loads.

A pre-stressed four-point bending beam example is used to clarify the procedure. Application of non-proportional loading often leads to significant stress rotations, making the material behavior in the crack parallel direction more important. As a result, an isotropic cracking model is insufficient, and a fixed direction orthotropic cracking model is introduced. Simulations of experimental tests with non-proportional loading by Nooru-Mohammed (Nooru-Mohammed 1992, Nooru-Mohammed et al. 1993) and Swartz and Taha (1991) are conducted to verify accuracy and exemplify modeling capabilities and limitations.

As described in §4.2, sequentially linear analysis relies on the identification of a critical integration point at which cracking will occur. After identification, the applied load is scaled so

that the critical point reaches its strength limit, its material properties are reduced, and the process is repeated. The same process holds true for non-proportional loading, but identification of the critical load multiplier, λ_{crit}, becomes more complex, and universal rules for the determination of λ_{crit} are more difficult to derive.

4.3.1 General Procedure for Non-proportional Loading

Non-proportional loading will be described by the application of two load cases, an initial load A and a subsequent load B, which will be superimposed. For example, load A might represent the self-weight of the structure, and load B might represent wind or earthquake loading. Cracking will be limited to occur during application of load B; the effect of this assumption will be discussed later. In general, the procedure is similar to proportional loading, but specifically is as follows:

- Apply load A, calculate the stresses, σ_A, and then remove load A.
- Apply a reference load B and calculate the stresses, σ_B.
- Calculate the load multipliers, $\lambda_{1,2}$, at which the maximum principal stress resulting from the combination of loads A and B ($\sigma_A + \lambda_{1,2}\sigma_B$) equals the current tensile strength, f_{ti}^{+}.
- Determine the critical integration point and calculate λ_{crit}.
- Apply the critical load combination by scaling the reference load B with the critical load multiplier, $\sigma_A + \lambda_{crit}\sigma_B$, and obtain the current stress-strain state.
- Remove all loads and update the stiffness and strength properties of the critical integration point according to the saw-tooth constitutive model (Figure 4.1).
- Repeat this cycle of steps continuously, updating the properties of a single integration point after each cycle.

These steps were implemented in an adapted version of DIANA (www.tnodiana.com) and are described in more detail in the following sections.

Calculation of the Load Multiplier, λ

To calculate the load multiplier at each integration point, the principal stresses must be calculated, and the maximum principal stress determined. The stresses at any integration point can be written as:

$$\begin{aligned}\sigma_{xx} &= \sigma_{xx,A} + \lambda\sigma_{xx,B} \\ \sigma_{yy} &= \sigma_{yy,A} + \lambda\sigma_{yy,B} \\ \sigma_{xy} &= \sigma_{xy,A} + \lambda\sigma_{xy,B}\end{aligned} \tag{4.2}$$

where $\sigma_{--,A}$ represent stresses resulting from the full application of load A, and $\sigma_{--,B}$ represent stresses resulting from the prescribed reference load B. For plane stress conditions, the principal stresses ($\sigma_{1,2}$) are described in the traditional manner using Equation (4.2):

$$\sigma_{1,2} = \frac{1}{2}\left[\left(\sigma_{xx,A} + \lambda_{1,2}\sigma_{xx,B}\right) + \left(\sigma_{yy,A} + \lambda_{1,2}\sigma_{yy,B}\right)\right] \pm \sqrt{\frac{1}{4}\left[\left(\sigma_{xx,A} + \lambda_{1,2}\sigma_{xx,B}\right) - \left(\sigma_{yy,A} + \lambda_{1,2}\sigma_{yy,B}\right)\right]^2 + \left(\sigma_{xy,A} + \lambda_{1,2}\sigma_{xy,B}\right)^2} \tag{4.3}$$

To determine the load multipliers ($\lambda_{1,2}$) for each integration point, the principal stresses ($\sigma_{1,2}$) are set equal to the current tensile strength, f_{ti}^{+}, and Eq. (4.3) is solved for $\lambda_{1,2}$. The closed form solution resembles the quadratic formula:

$$\lambda_{1,2} = \frac{1}{2A}\left(-B \pm \sqrt{B^2 - 4AC}\right) \tag{4.4}$$

where:

$$\begin{aligned}A &= {\sigma_{xy,B}}^2 - \sigma_{xx,B}\sigma_{yy,B} \\ B &= f_{ti}^{+}\left(\sigma_{xx,B} + \sigma_{yy,B}\right) + 2\sigma_{xy,A}\sigma_{xy,B} - \sigma_{xx,A}\sigma_{yy,B} - \sigma_{xx,B}\sigma_{yy,A} \\ C &= {\sigma_{xy,A}}^2 - \sigma_{xx,A}\sigma_{yy,A} + f_{ti}^{+}\left(\sigma_{xx,A} + \sigma_{yy,A}\right) - \left(f_{ti}^{+}\right)^2\end{aligned} \tag{4.5}$$

Note that when $\sigma_{xy,B} = \sqrt{\sigma_{xx,B}\sigma_{yy,B}}$ a singularity (A = 0) occurs in Equation (4.4), and the single solution becomes:

$$\lambda = -C/B \tag{4.6}$$

The principal stress directions, $\varphi_{1,2}$, corresponding to the load multipliers, $\lambda_{1,2}$, must be calculated to determine the orientation associated with each possible crack. Principal stress directions are again calculated in the traditional manner using Equation (4.2):

$$\varphi_{1,2} = \frac{1}{2}\tan^{-1}\left(\frac{2\left(\sigma_{xy,A} + \lambda_{1,2}\sigma_{xy,B}\right)}{\left(\sigma_{xx,A} + \lambda_{1,2}\sigma_{xx,B}\right) - \left(\sigma_{yy,A} + \lambda_{1,2}\sigma_{yy,B}\right)}\right) \tag{4.7}$$

Identification of the Critical Load Multiplier, λ_{crit}

In the case of proportional loading, λ_{crit} is simply selected as the minimum λ in the entire model, and the critical integration point is identified. Provided that after application of load A, the tensile stress does not exceed the tensile strength at any location in the entire model, this procedure of selecting the minimum λ is appropriate. This is often the case at the beginning of the analysis, but after damage, alternative criteria for selecting λ_{crit} are necessary. Furthermore, if load B is allowed to reverse direction, i.e. λ is allowed to become negative, the selection criteria must be defined more carefully. While lattice models also prescribe a damage increment, a relatively small amount of research has been devoted to lattice fracture under non-proportional loading. Schlangen (1993) applied a preliminary scheme for selecting the critical lattice element under non-proportional loading by breaking any element which violates the failure criteria after application of load A alone. This may be effective at times, but it can lead to incorrect results.

To exemplify the need for a more rigorous selection criterion, consider a pre-stressed unreinforced beam under four-point bending (Figure 4-2a). The beam is in pure bending (no shear) in the center between the point loads, so the principal stresses align exactly with the *x*- and *y*- directions in this region. Equation (4.4) becomes significantly simpler because $\sigma_{yy,A} = \sigma_{yy,B} = \sigma_{xy,A} = \sigma_{xy,B} = 0$, which yields a single load multiplier (λ) for each integration point, defined by Equation (4.6):

$$\lambda = -C/B = \frac{f_{ti}^{+} - \sigma_{xx,A}}{\sigma_{xx,B}} \tag{4.8}$$

This example illustrates that achieving convergence requires specialized iteration methods like arc-length control when using incrementally iterative analysis. It also tests the accuracy of the SLA procedure while illuminating the necessity for appropriate selection of λ_{crit}.

A course mesh was used to define the four-node linear-elastic finite elements with 2x2 Gauss integration used throughout the model, except at the center column (shown in grey in Figure 4-2b) where four-node elements with 4x1 Gauss integration were specified. At this center column of elements, a saw-tooth damage model was applied with a ripple enveloped defined by $p = 0.1$, which resulted in 16 saw-teeth per integration point. Sequentially linear analysis results were compared with nonlinear analysis based on an incrementally iterative Newton-Raphson scheme. This analysis utilized a total strain fixed crack model (Feenstra et al. 1998) for the center column elements, and crack mouth opening displacement (CMOD) arc-length control was necessary to achieve convergence. The crack bandwidth, *h*, was taken as the center column element width (20 mm) for both analyses, and the concrete material properties used are given in Table 4.1.

Table 4.1: Material properties used for the case studies in this section (§4.3).

Material	E [GPa]	ν	f_t [MPa]	G_f [N/mm]
Concrete	32	0.2	3.0	0.06

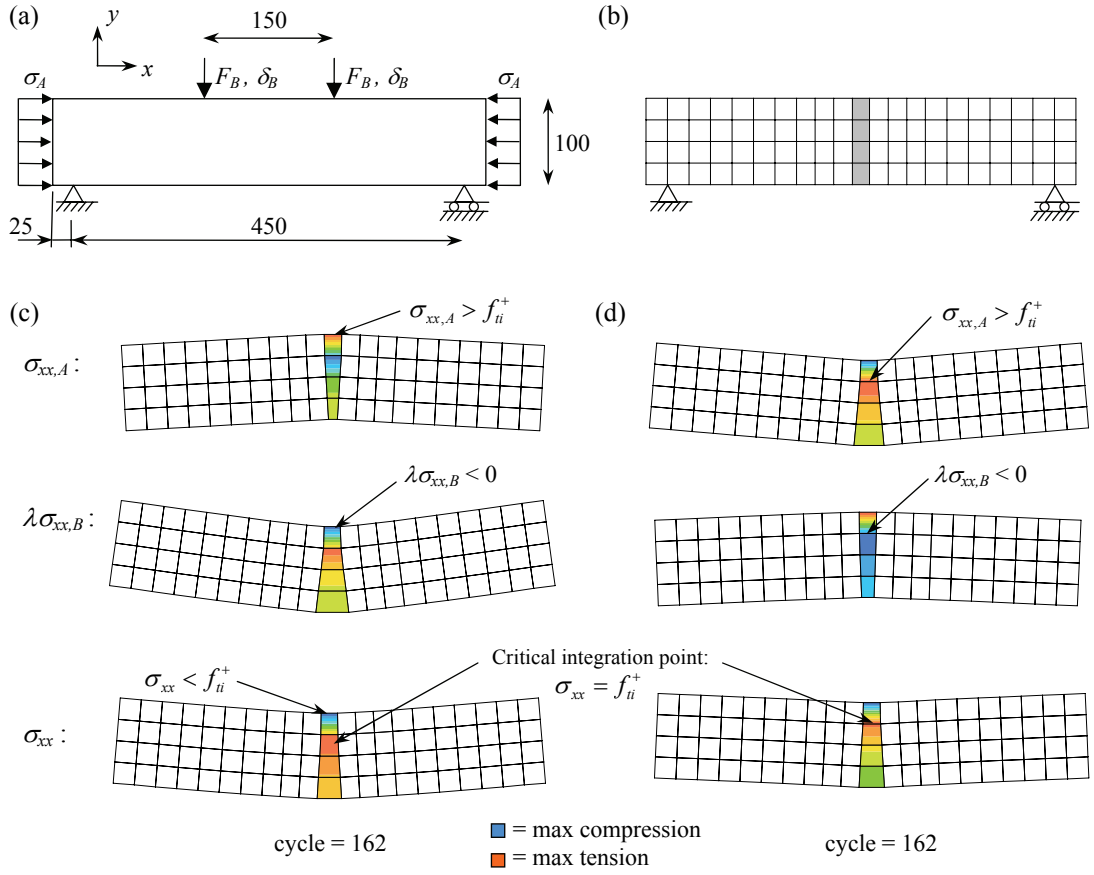

Figure 4-2: Four-point bending beam example: (a) geometry (dimensions in mm) and loading; (b) mesh with SLA elements shaded; stress results for (c) compressive pre-stress and (d) tensile pre-stress.

The four-point bending beam was analyzed with no pre-stress (σ_A = 0), a 1 N/mm^2 compressive pre-stress, and a 1 N/mm^2 tensile pre-stress:

1. Under no pre-stress, loading is proportional and $\lambda = f_{ti}^+ / \sigma_{xx,B}$ (see Equation 4.8). Since the numerator in this expression is always positive and at the top of the beam the denominator is negative, λ is negative at the top of the beam. However, selecting this negative λ as λ_{crit} would initiate cracking at the top of the beam and is not correct. Selecting λ_{crit} as the minimum positive λ in the model is appropriate.

2. Under a compressive pre-stress, the load A stresses ($\sigma_{xx,A}$) are initially compressive and uniform over the beam depth. Selection of λ_{crit} as the minimum positive λ in the model works successfully, and the beam begins cracking from the bottom up. However, as cracking propagates, the compressive pre-stress (load A) causes upward bending of the beam, and eventually the load A tensile stress exceeds the tensile strength at the top of the beam: $\sigma_{xx,A} > f_{ti}^{+}$ (Figure 4-2c). Now, both the numerator and the denominator in Equation (4.8) are negative at the top of the beam, leading to a positive λ. Selecting λ_{crit} as the minimum positive λ in the model, as was explained to be appropriate for proportional loading (i.e. no pre-stress, Case 1), would now initiate cracking at the top of the beam which is not correct. Thus, selecting λ_{crit} as the minimum positive λ in the model is not a robust solution.
3. Under a tensile pre-stress, load A stresses ($\sigma_{xx,A}$) are initially tensile and uniform over the beam depth. Selection of λ_{crit} as the minimum positive λ in the model again works successfully, and the beam begins cracking from the bottom up. However, as cracking propagates, the tensile pre-stress causes downward bending, and eventually $\sigma_{xx,A} > f_{ti}^{+}$ at the crack tip (Figure 4-2d). Now, at the crack tip the numerator in Eq. (4.8) is negative and the denominator is positive, leading to a negative λ. For simulating progressive cracking from the bottom up, it is crucial that the negative λ at the crack tip is identified as λ_{crit}. Thus, selecting λ_{crit} as the minimum positive λ in the model is again inappropriate.

A new procedure for selecting λ_{crit} is necessary for non-proportional loading, and is presented in Figure 4-3. The procedure works as follows:

- Load B stresses at each integration point are checked for either tension or compression in each principal stress direction (φ) resulting from each load multiplier (λ).
- All integration points in which load B causes *tension* are compared and the minimum λ_j^t is selected, λ_{min}^t, which represents the critical load multiplier (positive or negative) for which load B causes failure.
- Additionally, all integration points in which load B causes *compression* are compared and the maximum λ_j^c is selected, λ_{max}^c, which represents the minimum λ which will cause all points in which the tensile strength is exceeded after application of load A to "recover" due to compression in load B. Note that in the first cycle, before any damage has

occurred, care must be taken to ensure that the structure can resist load A without application of load B. However, after the first cycle this is not necessary, as loads A and B then act simultaneously.

- If $\lambda^t_{min} > \lambda^c_{max}$, all integration points recover by selecting $\lambda_{crit} = \lambda^t_{min}$, and the stress-strain results are output. However, if $\lambda^t_{min} < \lambda^c_{max}$, at least one integration point does not "recover", the worst case of which is selected as the critical integration point. No results are available for output because no unique λ_{crit} could be defined such that all integration points satisfy the tensile criterion. In other words, redistribution of stresses through cracking is necessary before the model can reach equilibrium and results can be obtained.

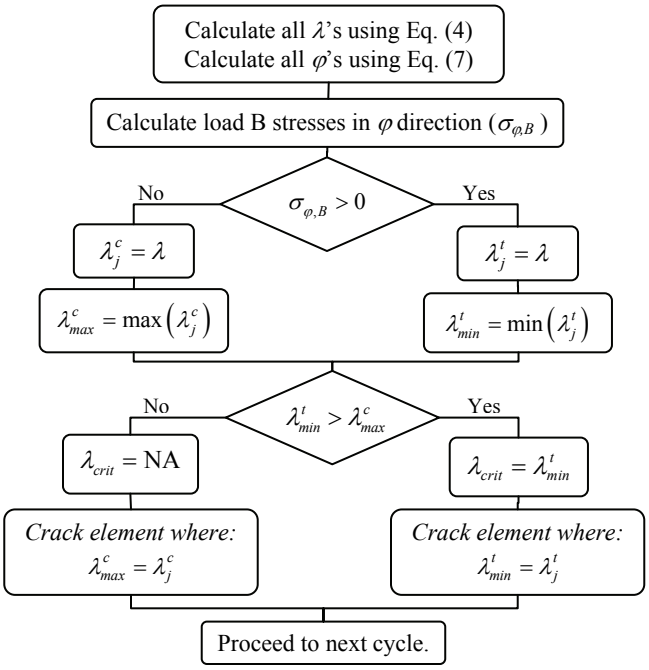

Figure 4-3: Flowchart for selection of the critical integration point and the critical load multiplier, λ_{crit}.

The selection criterion in Figure 4-3 was applied to the non-proportional loading cases of the four-point bending beam example above. Results compare well with incrementally iterative analysis (Figure 4-4), demonstrating the selection criterion to be effective. The selection process for λ_{crit} is illustrated in more detail in Figures 4-5 and 4-6. The shaded horizontal lines in these plots represent the λ values for which each integration point does not violate the tensile failure criteria, and is therefore in equilibrium. (Note: these shaded lines extend infinitely in the direction that they exit the plots.) There are 16 integration points over the depth of the beam, but some integration points at the bottom of the beam are not plotted because complete softening has

already occurred, i.e. the final saw-tooth has failed. In Figure 4-5, the vertical rectangular shaded regions represent λ values which can be sustained by the beam without further damage. Values of λ above this region would violate the tensile failure criterion due to load B. Values of λ below this region would violate the tensile failure criterion as a result of load A, due to insufficient compression from load B. Since $\lambda_{min}^{t} > \lambda_{max}^{c}$, the indicated critical integration points are selected and a damage increment is applied by progression to the next saw-tooth. Additionally, the maximum load that can be sustained before tensile damage occurs is determined. Note that λ_{crit} is selected correctly regardless of the sign of λ (positive for compressive pre-stress and negative for tensile pre-stress).

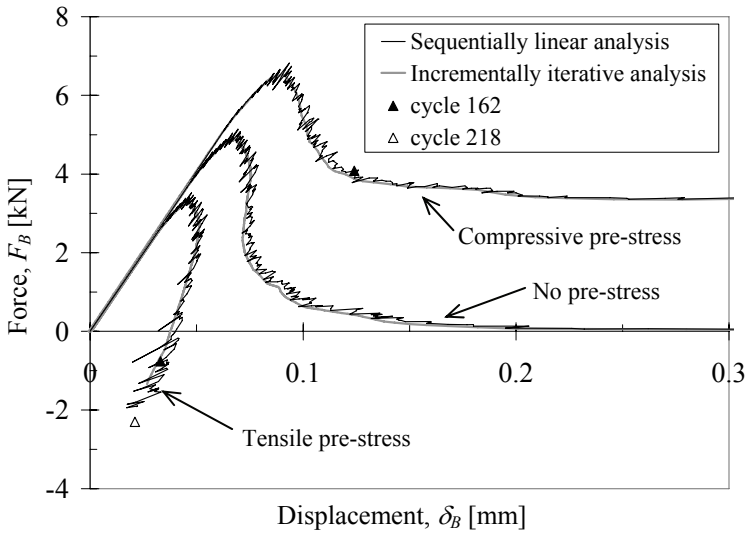

Figure 4-4: Four-point bending beam results.

Figure 4-6 illustrates two states for which equilibrium cannot be reached in all integration points simultaneously, i.e. $\lambda_{min}^{t} < \lambda_{max}^{c}$. This is visually evident in the fact that the shaded lines from all integration points do not overlap anywhere. In both of these cases, compression from load B is insufficient to counteract tension from load A. The critical integration points are selected (as indicated) in order to redistribute load A, and the model does not reach equilibrium prior to further cracking, so the results cannot be plotted as part of the beam response. This is apparent for cycle 218 (Figure 4-6b) which is plotted as an open triangle beyond the end of the load-displacement response in Figure 4-4. This point is evidence of the fact that the model continues running, and integration points continue to be damaged, but the model does not reach equilibrium. In fact, the model never reaches equilibrium again because there is not enough material strength remaining to sustain the fixed tensile pre-stress. Thus, collapse is imminent.

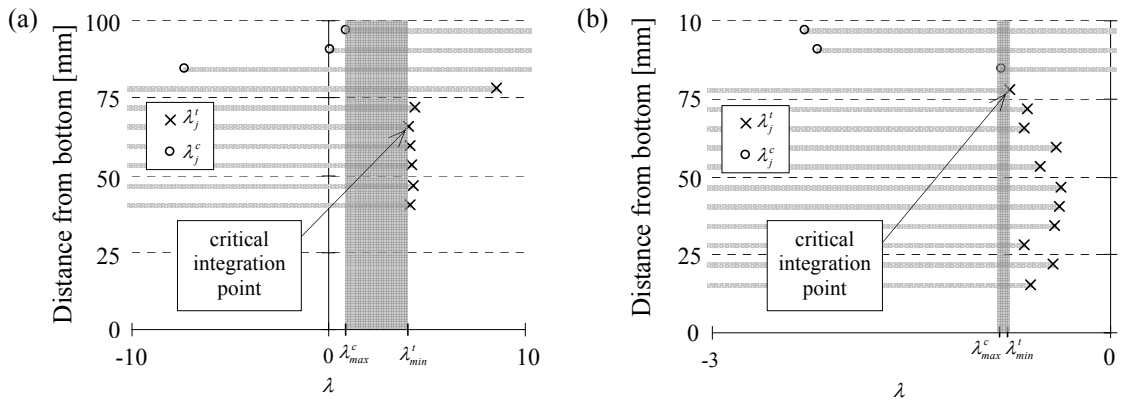

Figure 4-5: Lambda values which result in equilibrium (shaded lines) for each integration point plotted over the depth of the beam for cycle 162: (a) compressive pre-stress, and (b) tensile pre-stress. The shaded vertical rectangles represent the range of lambda values which result in equilibrium at all integration points without further damage.

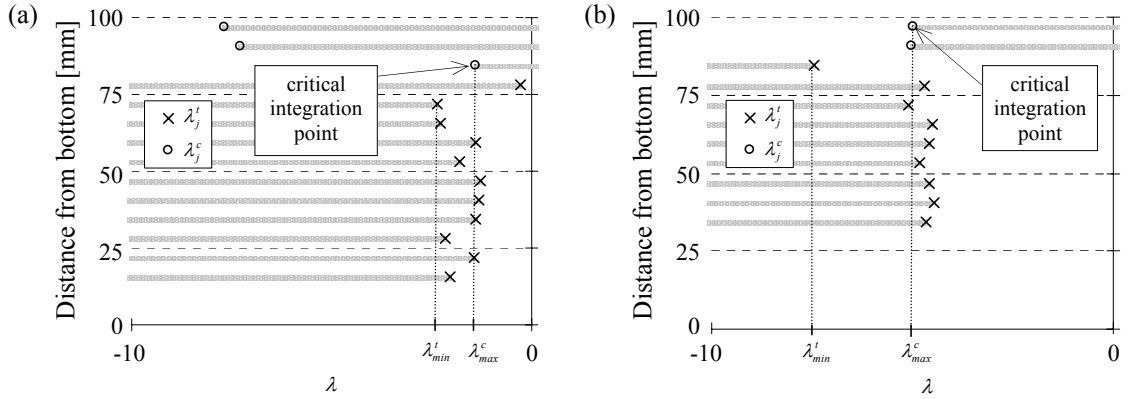

Figure 4-6: Lambda values which result in equilibrium (shaded lines) for each integration point plotted over the depth of the beam for the case of tensile pre-stress: (a) cycle 163, (b) and cycle 218. In both cases $\lambda_{min}^t < \lambda_{max}^c$, so equilibrium can not be reached without redistribution of load A.

4.3.2 Non-proportional Loading with Orthogonal Cracking

In the four-point bending example in §4.3.1, loading remains uni-axial and stress rotations do not occur. In most cases, non-proportional loads are applied in different directions and result in significant stress rotations, making orthotropic degradation appropriate.

Implementation of Secondary Cracking

Orthogonal secondary cracking for plane stress conditions is introduced into the sequentially linear framework to facilitate orthotropic degradation. The cracking model parallels the total strain fixed cracking model (Feenstra et al. 1998, de Borst 2002). After initiation of cracking, the

crack direction is fixed, and the stiffness perpendicular to the crack direction is reduced according to the saw-tooth curve. In subsequent linear analyses, a second saw-tooth constitutive relationship, identical to the first, is applied. This allows secondary cracking in the direction perpendicular to the initial crack. Therefore, the stresses and λ values for both crack directions of each integration point are calculated, and the global λ_{crit} is still selected according to the criteria outlined in Figure 4-3.

Orthotropic degradation necessitates the definition of the Poisson behavior during cracking. While the Poisson effect is often ignored completely at the initiation of cracking (de Borst 2002), the Poisson ratio is assumed to reduce at a similar rate as the modulus of elasticity:

$$\nu_{ns} = \nu_o \frac{E_n}{E_o}; \quad \nu_{sn} = \nu_o \frac{E_s}{E_o} \tag{4.9}$$

where the subscripts *n*- and *s*- refer to the initial and secondary crack directions, respectively, E_n and E_s are the reduced moduli of elasticity, and E_o and ν_o are the initial modulus of elasticity and Poisson's ratio, respectively. Thus, when a crack is completely open in the *n*- direction ($E_n = 0$), further crack strain in the *n*- direction creates no Poisson effect in the *s*- direction, while the Poisson effect in the *n*- direction is maintained for strain in the *s*- direction, and vice versa. Furthermore, reducing Poisson's ratio according to Equation (4.9) conveniently yields a symmetric reduced stress-strain relationship in which anisotropic degradation is solely dependent on the reduced moduli of elasticity:

$$\begin{bmatrix} \sigma_{nn} \\ \sigma_{ss} \\ \sigma_{ns} \end{bmatrix} = \frac{1}{1-\nu_o^2 \frac{E_n E_s}{E_o^2}} \begin{bmatrix} E_n & \frac{\nu_o}{E_o} E_n E_s & 0 \\ \frac{\nu_o}{E_o} E_n E_s & E_s & 0 \\ 0 & 0 & G_{red}\left(1-\nu_o^2 \frac{E_n E_s}{E_o^2}\right) \end{bmatrix} \begin{bmatrix} \varepsilon_{nn} \\ \varepsilon_{ss} \\ \gamma_{ns} \end{bmatrix} \tag{4.10}$$

where G_{red} is the reduced shear stiffness and is discussed in the next section. Implementation of orthogonal cracking, while being necessary for non-proportional loading, has the consequence of doubling the number of saw-teeth associated with each integration point, therefore increasing the number of linear analyses necessary for complete degradation.

Shear Stiffness Reduction during Cracking

Fixed orthogonal cracking also requires the specification of shear behavior, often implemented in the form of the shear retention factor, β_{sh}, which has been extensively discussed

in previous research (e.g. Kolmar and Mehlhorn 1984, Rots 1988, de Borst 2002). Although a constant shear retention factor is often specified (e.g. β_{sh} = 0.2), this leads to "stress locking" when large shear strains are present, allowing shear stresses to be transferred through a crack which is completely open. To prevent this, a shear retention factor of β_{sh} = 0 was initially attempted, but often led to convergence problems (Kolmar and Mehlhorn 1984). While immediate elimination of shear stiffness upon cracking is not advised because some shear stiffness is certainly retained until micro-cracks coalesce and due to aggregate interlock in concrete, these reported convergence problems are not an issue for the sequentially linear approach.

To prevent stress locking, the shear retention factor is often derived as a function of the crack normal strain, as this makes more physical sense. For example, Kolmar and Mehlhorn (1984) suggested several shapes for the shear retention curve, and concluded that a sharp initial drop followed by a continuous shear stiffness reduction to zero at the limit where the crack is completely open, is most appropriate.

Any shear retention factor could be readily implemented, but the reduced shear stiffness will be described using the isotropic definition of the shear stiffness, except using reduced elastic properties:

$$G_{red} = \frac{E_{\min}}{2(1+v_o \frac{E_{\min}}{E_o})} \tag{4.11}$$

where $E_{min} = \min(E_n , E_s)$. It is understood that the isotropic relation does not hold for anisotropic damage, but Equation (4.11) effectively relates the shear stiffness to a maximum of the orthotropic damage. The definition of G_{red} was observed to have an effect on crack propagation, and is the subject of continued research.

4.3.3 Nooru-Mohamed Test: Combined Shear and Tension

The experimental investigation by Nooru-Mohamed (1992) has served as a benchmark for many researchers modeling fracture under non-proportional loading (e.g. Schlangen 1993, Bolander and Saito 1998, di Prisco et al. 2000, Patzák and Jirásek 2004). The configuration of the double notched concrete test specimen is shown in Figure 4-7a. While Nooru-Mohamed (1992) tested several load paths, attention is focused on load paths 4a and 4b. These tests are characterized by an initial horizontal force (F_h = 5 kN and 10 kN for paths 4a and 4b, respectively), followed by a vertical force, F_v, applied until failure.

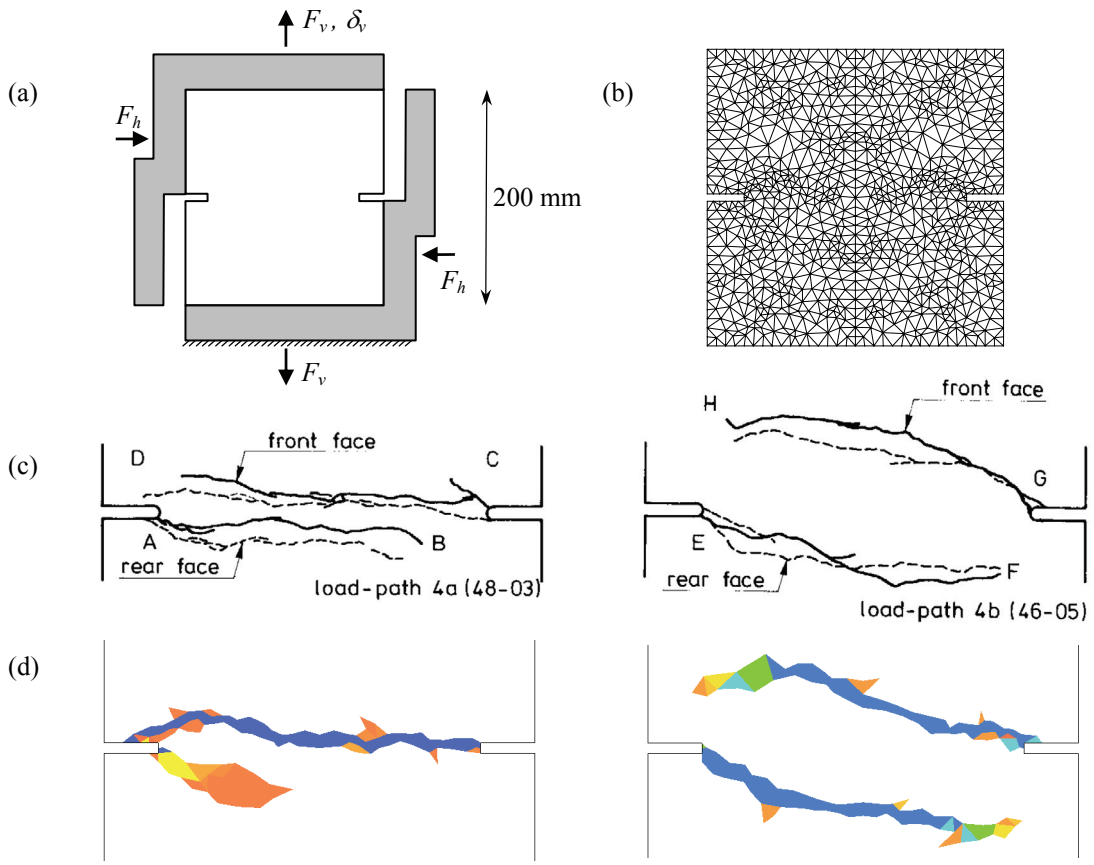

Figure 4-7: Nooru-Mohammed (1992) tests: (a) experimental setup; (b) triangular mesh used for SLA. Crack pattern for load paths 4a and 4b resulting from: (c) experimental tests by Nooru-Mohammad (1992), and (d) SLA.

The path 4a and 4b tests were simulated using the sequentially linear framework. Assumed concrete material properties are given in Table 4.1. The fracture energy is lower than that used in other studies (di Prisco et al. 2000) because linear softening is used and the fracture energy from the "tail" of the typical nonlinear softening curve is ignored. The bottom and bottom-right edges of the mesh were assumed fixed, while the top and top-left edges were required to remain planar. Mesh alignment, in which cracks tend to propagate along meshing lines (Rots et al. 1984, Rots 1988, Sluys 1992), was observed in preliminary analyses in which quadrilateral elements were defined by continuous meshing lines. As a result, a randomly generated triangular mesh (Figure 4-7b) was specified to minimize mesh alignment in the crack pattern. Further studies on mesh alignment were conducted as described in DeJong et al. (2009b).

The crack pattern was predicted well for both load paths, and crack curvature, which has proven more difficult to simulate (di Prisco et al. 2000), was predicted correctly (load path 4b, Figure 4-7d). Although the randomly generated mesh reduces the effects of mesh alignment,

crack propagation is still somewhat mesh dependent. This is evident for the presented mesh, which is symmetric about the vertical axis but not the horizontal. Therefore, "different meshes" produced the top and bottom cracks which are slightly different, but both close to the experimental result (Figure 4-7c). Mesh dependency is more evident for load path 4a (Figure 4-7d), in which the bottom crack does not propagate as far as expected, most likely due to larger elements in the random mesh for which the crack bandwidth is incorrectly estimated. While the current mesh should be refined so all elements are more uniform in size, the presented results demonstrate the occurrence of some mesh dependence which must be carefully considered, as in DeJong et al. (2009b).

The load-displacement responses for load paths 4a and 4b are shown in Figure 4-8. The simulation overestimated the ultimate load from experimental results; similar overestimation was reported by di Prisco et al. (2000). Overestimation could result from compliance in the loading frame and/or imperfection in the material, the effects of which are not captured by perfectly rigid model supports and a perfectly uniform material model. It is also notable that the employed linear softening model underestimates the post peak load for both load paths. This is expected, as the "tail" of the typical nonlinear concrete softening curve is neglected.

Regardless of these intricacies which are present for all orthotropic fixed cracking models, this example demonstrates that SLA can effectively model fracture under non-proportional loading, while demonstrating the sensitivity of results to modeling assumptions.

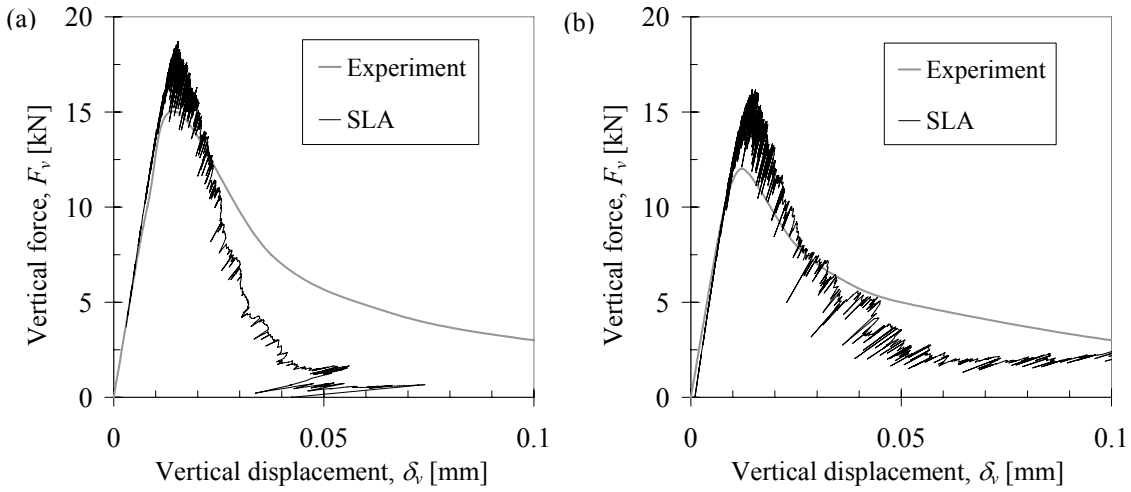

Figure 4-8: Load versus displacement plots for Nooru-Mohammed (1992) test paths (a) 4a and (b) 4b.

4.3.4 Swartz and Taha Test: Combined Shear and Compression

The experimental investigation by Swartz and Taha (1991) provides a second reference for checking model accuracy in which combined shearing and compression (instead of tension) causes failure. While there are clear limitations when trying to model compression-shear mixed-mode failure with a Mode I cracking criteria, the example is still instructive. Furthermore, some confidence in capturing this type of failure is desirable when modeling larger structures where multiple types of failure are present simultaneously, as is the case for the masonry building simulated in §4.4.2.

Swartz and Taha (1991) tested several beams with different geometries and levels of pre-stress. Attention is focused on Beam No. 24 which was pre-stressed with a 55.6 kN axial compressive force using the experimental setup in Figure 4-9a (see Swartz and Taha (1991) for more details). The test was modeled using displacement control after applying the initial compressive pre-stress, σ_A. The mesh consisted of randomly generated three-node triangular SLA elements with a single integration point in the center of the beam, with four-node 2x2 Gauss integration linear-elastic quadrilateral elements at the beam ends and at the four steel bearing pads (Figure 4-9b). Concrete properties are given in Table 4.1.

The resulting experimental crack pattern consisted of a pair of initial cracks (labeled 1 in Figure 4-9c), followed by a single secondary crack which originated at the center of the beam and then propagated outward towards the two bearing pads (labeled 2 in Figure 4-9c). The initial cracks and origin of the secondary crack are predicted well (cycle 715, Figure 4-9d). Through further damage, the secondary crack remains distinct from the initial cracks, although it does ultimately join the two notches instead of the two bearing pads (cycle 1500, Figure 4-9d).

The experimental test resulted in an ultimate shear load of F_{B2} = 171.8 kN, while SLA resulted in an ultimate shear load of F_{B2} = 170 kN. Therefore, SLA accurately predicts both the crack pattern and the ultimate load. While ultimate load prediction is possible, post peak behavior is not reported as it cannot be simulated with solely a tensile cracking model. This is qualitatively obvious through consideration of the failure mechanism. Ultimately, sliding will occur along a crack plane with a constant compressive normal stress. This can not be simulated in a model in which both the compressive stiffness and the tensile stiffness are reduced simultaneously, and the shear stiffness is zero once the crack is fully open. In other words, neither crack closure nor frictional sliding can be modeled at this point.

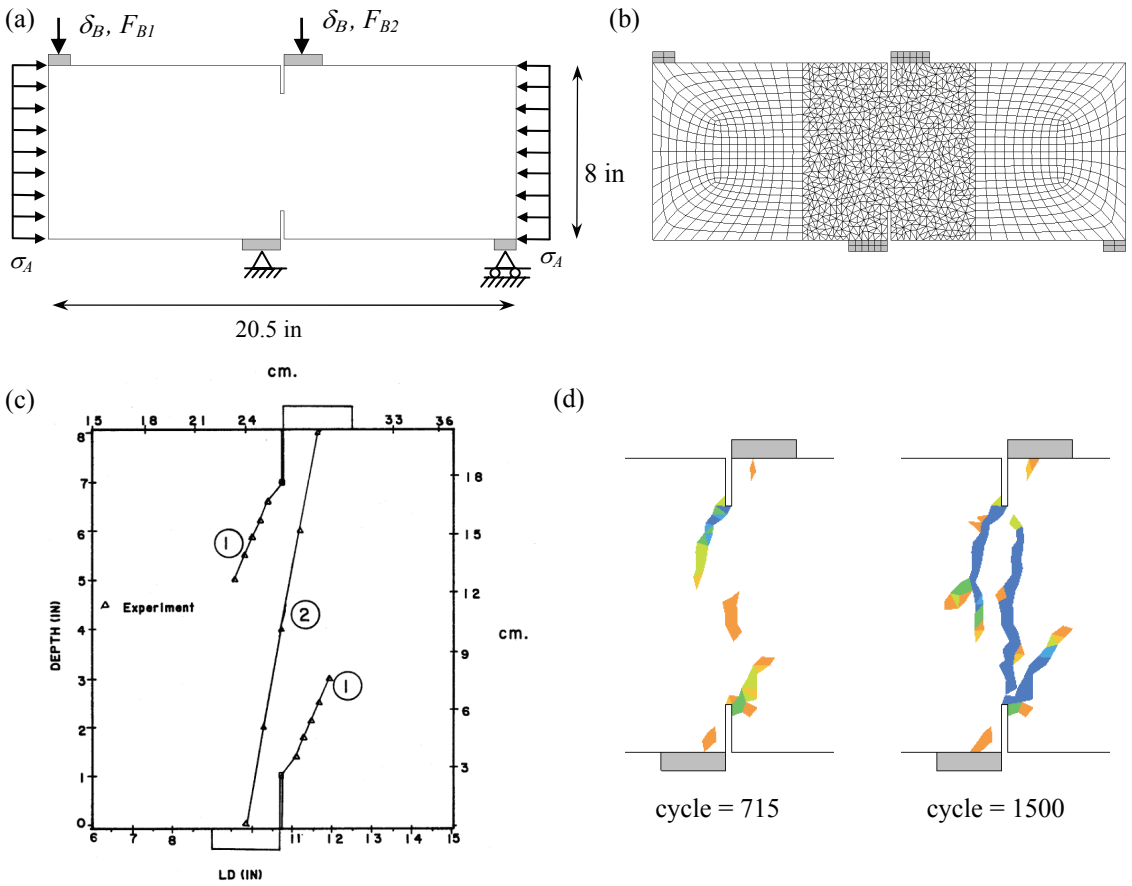

Figure 4-9: Swartz and Taha (1991) tests: (a) experimental setup; (b) mesh used for SLA. Resulting crack pattern for: (c) experimental test by Swartz and Taha (1991), and (d) SLA.

4.3.5 Discussion

The extension of this modeling framework to incorporate non-proportional loading makes it more applicable to real engineering problems, where non-proportional loading is almost always of interest. The previous examples illustrate the capabilities, benefits and challenges of SLA with non-proportional loading. In general, the following items are worth noting:

- The selection criterion for the critical integration point ensures that the model reaches equilibrium at the end of every cycle, effectively incorporating redistribution of an initial load (load A) through cracking during subsequent loading (load B).
- Both the mesh configuration and the prescribed shear retention after cracking were observed to have an effect on crack propagation. However, implementing a randomly generated mesh to limit mesh alignment and defining the shear retention as a function of the crack strain were effective in simulating experimental results. A critical evaluation of both of these effects can be found in DeJong et al. (2009b).

- The primary advantage of the SLA method is its ability to model brittle behavior without convergence problems. This benefit is particularly important when modeling fracture in large-scale structures where brittle snap-back behavior is amplified (DeJong et al. 2008).

While SLA is effective for many applications, clear limitations exist. For example, the inability to model crack closure and subsequent frictional sliding has not yet been addressed. Additionally, run-times can be long for models where a large number of integration points are present, especially if the modeling framework is extended to 3D brick elements in the future. However, more efficient solution techniques could be developed which significantly reduce run-times.

4.4 Shell Structures

The previous section has exemplified some of the intricacies of simulating brittle fracture under non-proportional loading using the SLA method. In fact, the method effectively matches the capabilities of total strain fixed crack models (e.g. Feenstra 1998), with the enormous benefit of eliminating convergence problems. Although many methods have been developed to deal with convergence issues, this primary advantage of the sequentially linear method is more evident when modeling fracture of full-scale structures. In this section, shell elements are incorporated into the sequentially linear analysis method to allow the modeling of three dimensional masonry structures under non-proportional loading. In the following sections, the shell element implementation is first presented and then applied to simulate a previous experimental test on a full-scale masonry structure under cyclic loading.

4.4.1 Implementation of Shell Elements in SLA

The capability of SLA is extended to three dimensional structures through the use of shell elements. While analysis with full 3D solid elements is possible, shell elements provide an efficient means of modeling many typical structures. The general solution procedure is the same as in two dimensions, as presented in the previous sections.

Shell elements are typically utilized in finite element analysis when structures are thin in one dimension, as is often the case in walls, floors, and roofs of buildings. They provide an efficient means of modeling 3D structures without 3D solid finite elements, which complicate and slow analyses if they are not necessary. In this formulation, Mindlin-Reissner shell theory is applied, in which the stress through the thickness (perpendicular to the mid-surface of the plate or shell) is

assumed to be zero, and material points normal to the shell mid-surface remain in a straight line after deformation (although they do not have to remain perpendicular to the shell mid-surface).

Considering a Cartesian coordinate system where the shell mid-surface is aligned with the *n*-*s* coordinate plane, and the *t*-coordinate describes the thickness direction normal to the shell mid-surface, the stress-strain relationship can be written as:

$$\begin{bmatrix} \sigma_{nn} \\ \sigma_{ss} \\ \sigma_{tt} \\ \sigma_{ns} \\ \sigma_{st} \\ \sigma_{tn} \end{bmatrix} = \begin{bmatrix} \frac{E_n}{1-\nu_{ns}\nu_{sn}} & \frac{\nu_{sn}E_n}{1-\nu_{ns}\nu_{sn}} & 0 & 0 & 0 & 0 \\ \frac{\nu_{ns}E_s}{1-\nu_{ns}\nu_{sn}} & \frac{E_s}{1-\nu_{ns}\nu_{sn}} & 0 & 0 & 0 & 0 \\ 0 & 0 & 0 & 0 & 0 & 0 \\ 0 & 0 & 0 & G_{ns} & 0 & 0 \\ 0 & 0 & 0 & 0 & G_{st} & 0 \\ 0 & 0 & 0 & 0 & 0 & G_{tn} \end{bmatrix} \begin{bmatrix} \varepsilon_{nn} \\ \varepsilon_{ss} \\ \varepsilon_{zz} \\ \gamma_{ns} \\ \gamma_{st} \\ \gamma_{tn} \end{bmatrix} \tag{4.12}$$

where $E_{\text{-}}$ is the modulus of elasticity, $\nu_{\text{--}}$ is the Poisson's ratio, and $G_{\text{--}}$ is the shear stiffness, in the indicated *n*-, *s*- and *t*- directions.

Initially, before any damage occurs, the material is assumed to be isotropic, which results in:

$$\nu_o = \nu_{ns} = \nu_{sn}; \quad E_o = E_n = E_s; \quad G_o = G_{ns} = G_{st} = G_{tn} = \frac{E_o}{2(1+\nu_o)} \tag{4.13}$$

where the subscript *o* refers to initial, undamaged material properties. Combining equations (4.12) and (4.13) yields the typical shell stiffness matrix for isotropic materials (see e.g. Bathe 2006):

$$\begin{bmatrix} \sigma_{nn} \\ \sigma_{ss} \\ \sigma_{tt} \\ \sigma_{ns} \\ \sigma_{st} \\ \sigma_{tn} \end{bmatrix} = \frac{E_o}{1-\nu_o^{\,2}} \begin{bmatrix} 1 & \nu_o & 0 & 0 & 0 & 0 \\ \nu_o & 1 & 0 & 0 & 0 & 0 \\ 0 & 0 & 0 & 0 & 0 & 0 \\ 0 & 0 & 0 & \frac{1-\nu_o}{2} & 0 & 0 \\ 0 & 0 & 0 & 0 & \frac{1-\nu_o}{2} & 0 \\ 0 & 0 & 0 & 0 & 0 & \frac{1-\nu_o}{2} \end{bmatrix} \begin{bmatrix} \varepsilon_{nn} \\ \varepsilon_{ss} \\ \varepsilon_{tt} \\ \gamma_{ns} \\ \gamma_{st} \\ \gamma_{tn} \end{bmatrix} \tag{4.14}$$

Following the procedure outlined in §4.3, the nonlinear behavior is modeled through application of a damage increment at the critical integration point in the model. When cracking is first implemented at any given integration point, the crack direction is fixed, and the crack normal elasticity, E_n, is reduced. At this point, the isotropic stiffness matrix no longer applies, and the

stiffness matrix in Equation (4.12) is applied. As introduced in §4.3, the Poisson's ratios in the *n-s* plane are reduced at the same rate as the corresponding elastic modulus values (Equation 4.9).

However, the Poisson's ratios in the other directions remain unchanged. Additionally, the shear modulus, which has a significant effect on crack propagation (DeJong et al. 2009b), is assumed to reduce according to:

$$G_{ns} = \frac{E_{\min}}{2(1+v_o \frac{E_{\min}}{E_o})}; \quad G_{st} = \frac{E_s}{2(1+v_o \frac{E_s}{E_o})}; \quad G_{tn} = \frac{E_n}{2(1+v_o \frac{E_n}{E_o})} \tag{4.15}$$

where $E_{min} = \min(E_n , E_s)$. These assumptions fix the crack plane to be perpendicular to the plane of the shell element.

Because the above formulation was implemented through adjusting the stiffness matrix between each linear elastic analysis, it is independent of the shell element characteristics. As a result, the typical suite of shell elements, with different numbers of nodes and integration points, are available.

Essentially, the shell element formulation is similar to layered membrane elements spaced over the thickness of the shell, introduced through a 2D mesh with additional integration points in the thickness direction. The number of integration points over the thickness is related to the number of analyses required to develop cracking through the entire shell, and should therefore be limited if possible. When out of plane bending is a concern, a higher number of integration points are necessary, but when in-plane loading is of interest, the number of integration points can be reduced.

The resulting framework can model the 3D failure of many typical buildings. The following example is intended to test the ability of the procedure to predict experimental results and to exemplify the benefits and weaknesses of the procedure through comparison with nonlinear finite element results. The example herein focuses on masonry structures, but the framework is generally applicable to shell structures. As a first approach, a simple isotropic tensile failure criterion is employed for masonry, but a more rigorous anisotropic failure criterion which takes into account the composite behavior of the brick and mortar could be implemented in the future.

4.4.2 Simulation of Tests on a Full-scale Masonry Structure

The shell element formulation is applied to model the full-scale masonry structure tested by Yi (Yi 2004, Yi et al. 2006a). In this experiment, a two-story masonry structure, approximately 7.5 m square by 7.1 m tall, was constructed and then tested under cyclic loading. Yi (2004) and Yi et al. (2006a) provide further details of the experimental procedure.

Testing and Simulation Procedure

The building is depicted in Figure 4-10. In the experiment, loading was first applied in-plane with walls 1 and 2. The building was then repaired and tested in the perpendicular direction. A post-tensioning force, P_t (Figure 4-10), was first applied, followed by horizontal cyclic loading, P_c (Figure 4-10). Cyclic loading was applied from one side of the structure via four hydraulic actuators, two located at the floor level, and two located at the roof level. Loading was applied in displacement control, with the two equal floor displacement being fixed at 80% of the two equal roof displacements.

The cyclic loading experiments were simulated in two separate analyses by applying monotonic loading in the positive and negative x-direction. Results from both analyses were then combined to get an envelope for comparison with cyclic loading curves. Simulation involved applying the self-weight and post-tensioning forces (load A), followed by the floor and roof displacements (load B). Initially, single wall simulations were carried out on walls 1 and 2, neglecting the rest of the building. For these simulations, both membrane and shell elements were used in the meshes shown in Figure 4-11a and 4-11b. These two meshes, with average edge lengths of 300 mm and 150 mm respectively, were used to check mesh dependence. Subsequently, the full structures were simulated in three dimensions using shell elements. The mesh used for full structure analyses (Figure 4-11c) is of the same density as the course 2D mesh. For all analyses, four point in-plane Gauss integration was used. For shell analyses, two integration points were specified over the thickness.

The material properties used to simulate the building response are given in Table 4.2. The density, ρ, elasticity, E_o, and Poisson's ratio, v_o, are the same as those used by Yi et al. (2006b), and were derived from experimental results. Additionally, the wood diaphragms at the floor and roof level were both assumed to have an elastic modulus of 0.02 MPa, also derived from experimental results and reasonable values for wood diaphragms (Yi et al. 2006b). An isotropic tensile strength is clearly a simplification of composite masonry behavior, and was particularly difficult to estimate because of the extremely weak mortar (Type K) used to simulate typical pre-1950 construction. The assumed value is slightly larger than the contact element normal tensile strength of 0.14 MPa assumed by Yi (2004). A linear softening material model was used with a ripple envelope defined by p = 20% and a crack bandwidth h = 424 mm for the course mesh and 212 mm for the fine mesh.

Table 4.2: Material properties used for simulation of the Yi et al. (2006a) test.

Material	ρ [kg/m^3]	E_o [GPa]	v_o	f_t [MPa]	G_f [N/mm]
Masonry	1920	6.9	0.25	0.2	0.05

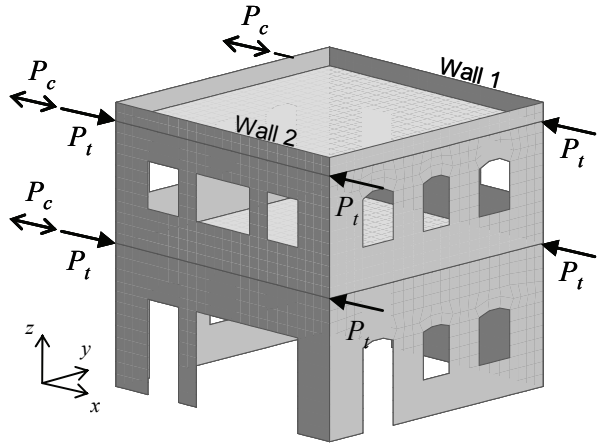

Figure 4-10: Geometry and loading conditions for the Yi et al. (2006a) test.

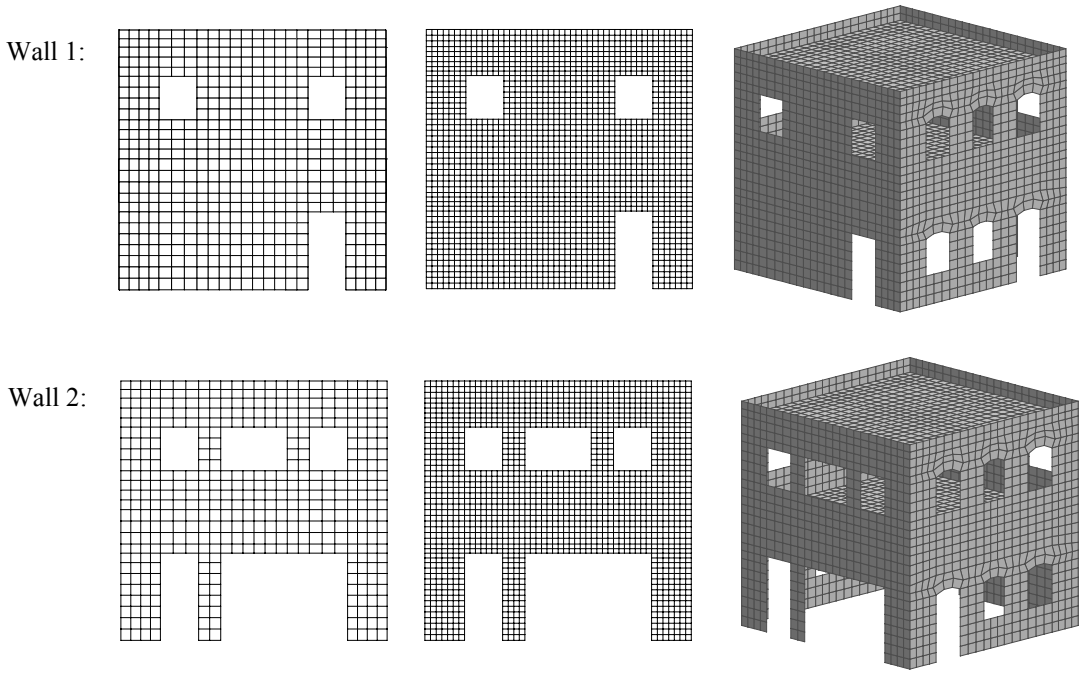

Figure 4-11: Meshes for simulation of the Yi et al. (2006a) test: (a) course 2D mesh, (b) fine 2D mesh, (c) 3D mesh.

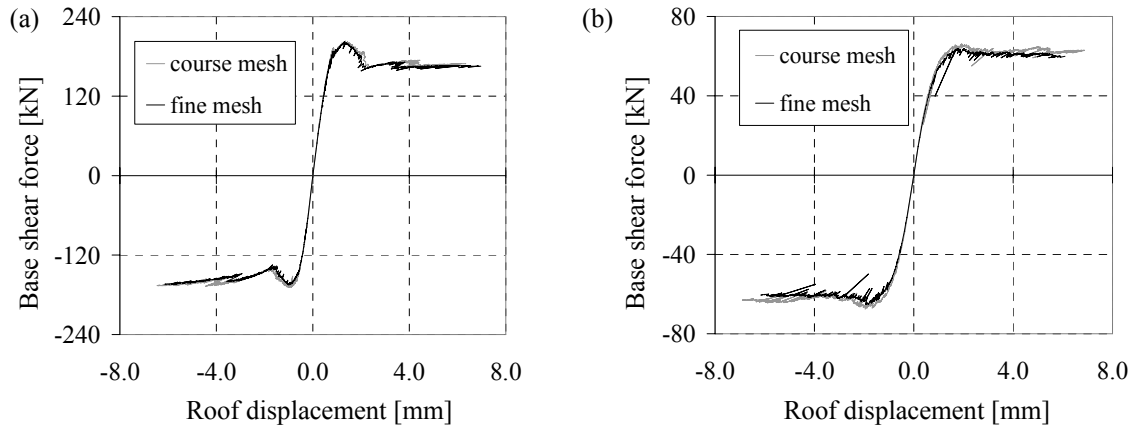

Figure 4-12: Base shear versus roof displacement for 2D membrane analysis with course and fine meshes: (a) wall 1, (b) wall 2.

Simulation Results

The 2D results for the course mesh and fine mesh are compared in Figure 4-12, and indicate no mesh density dependence. This is an important check, as other damage models have been observed to have strong mesh dependence in the post-peak range (Salonikios et al. 2003). The similar results for the course and fine meshes confirm the mesh-size objectivity of SLA demonstrated by Rots and Invernizzi (2004). As expected, results of shell element simulations (not shown) were the same as 2D membrane analyses, confirming the shell element implementation. However, shell elements provide no benefit for these 2D simulations, and twice as many cycles were necessary due to the two integration points over the depth.

The crack patterns for the fine mesh membrane analyses are shown in Figure 4-13, and were similar to crack patterns for the course mesh. The crack pattern indicates that rocking failure, not diagonal cracking, is occurring in the right pier of wall 1, and all piers in wall 2. This is expected due to the slender nature of the piers and compares well with the experimental result. Some mesh alignment is likely occurring, evidenced by the vertical cracks in the left portion of wall 1. These cracks would likely be diagonal, as in the experiment, but are slightly biased to propagate along meshing lines (DeJong et al. 2009b).

The results of 3D simulations using shell elements are shown in Figures 4-14 and 4-15. The cyclic experimental curves compare well with the 3D simulations (Figure 4-14). The maximum base shear force in both directions is predicted quite well for both cases, particularly for wall 2, and the initial stiffness of both walls also appears appropriate. The rather constant base shear capacity is predicted for wall 2, as is the reduction in base shear capacity after the maximum for wall 1, although this reduction is overestimated in the negative *x*-direction.

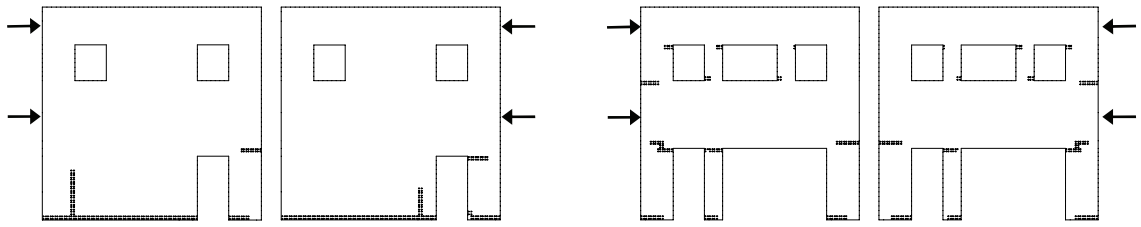

(a) (b)

Figure 4-13: Crack pattern for fine mesh membrane analysis for loading in each direction: (a) wall 1, (b) wall 2.

The results demonstrate the greater shear capacity of the full 3D structure when compared to the 2D walls alone. This is especially evident in Figure 4-14b, which indicates that wall 2 benefits more from the rest of the structure than wall 1, a logical result as wall 2 is weaker.

The experimental crack patterns are compared with the monotonic loading simulation results in Figure 4-15. The experimental result (Figure 4-15a) is to be compared with the combination of the two simulation results (Figures 4-15b and 4-15c). The 3D failure mechanism resulting from loading in the positive *x*-direction indicates a principle crack wrapping around the corner between wall 1 and wall A, a result supported by the experiment. Meanwhile, the 3D failure mechanism resulting from loading in the negative *x*-direction indicates diagonal cracking from the top left of the door in wall 1, while simulation results predict cracking initiating at the bottom center of wall 1 and propagating diagonally up and around the corner to wall B. This discrepancy is likely a result of the simplified monotonic loading.

In general, the results demonstrate the accuracy gained from simulating 3D instead of 2D failure. Clearly the 2D analyses could be improved by incorporating flange effects from walls A and B, as done by Yi et al. (2006b), but this requires flange assumptions which are avoided by modeling the entire structure, at the cost of increased computational effort. As mentioned in §2.2.2, Yi et al. (2006b) modeled the structural response to cyclic loading using contact elements at pre-defined crack locations (Figure 2-4). The SLA method avoids pre-defined crack locations, allowing determination of the cracking mechanism directly. If desired, one could use the two methods in series, first locating cracks using SLA and then simulating the cyclic response using contact elements at the determined locations, although this would require more computation time.

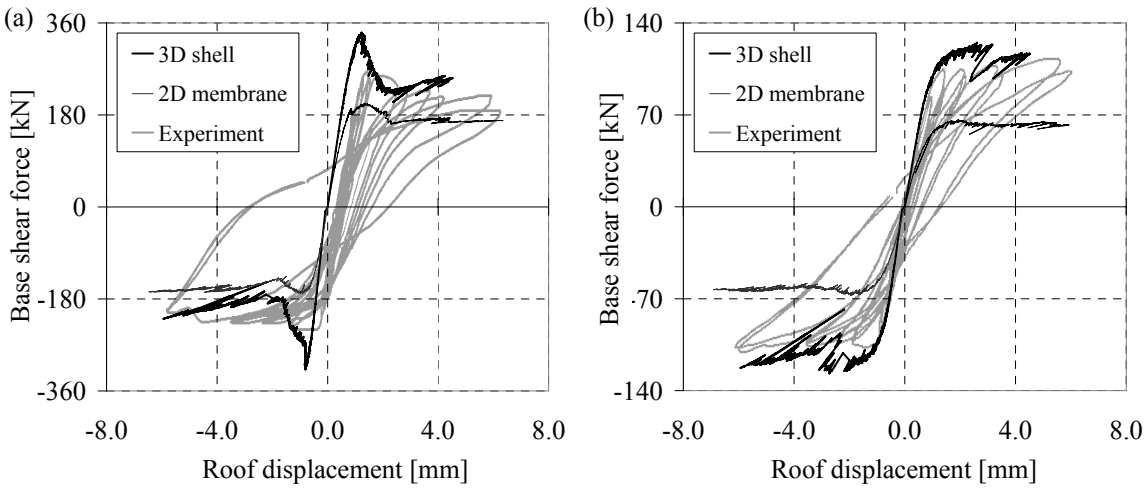

Figure 4-14: Base shear versus roof displacement: (a) wall 1, (b) wall 2.

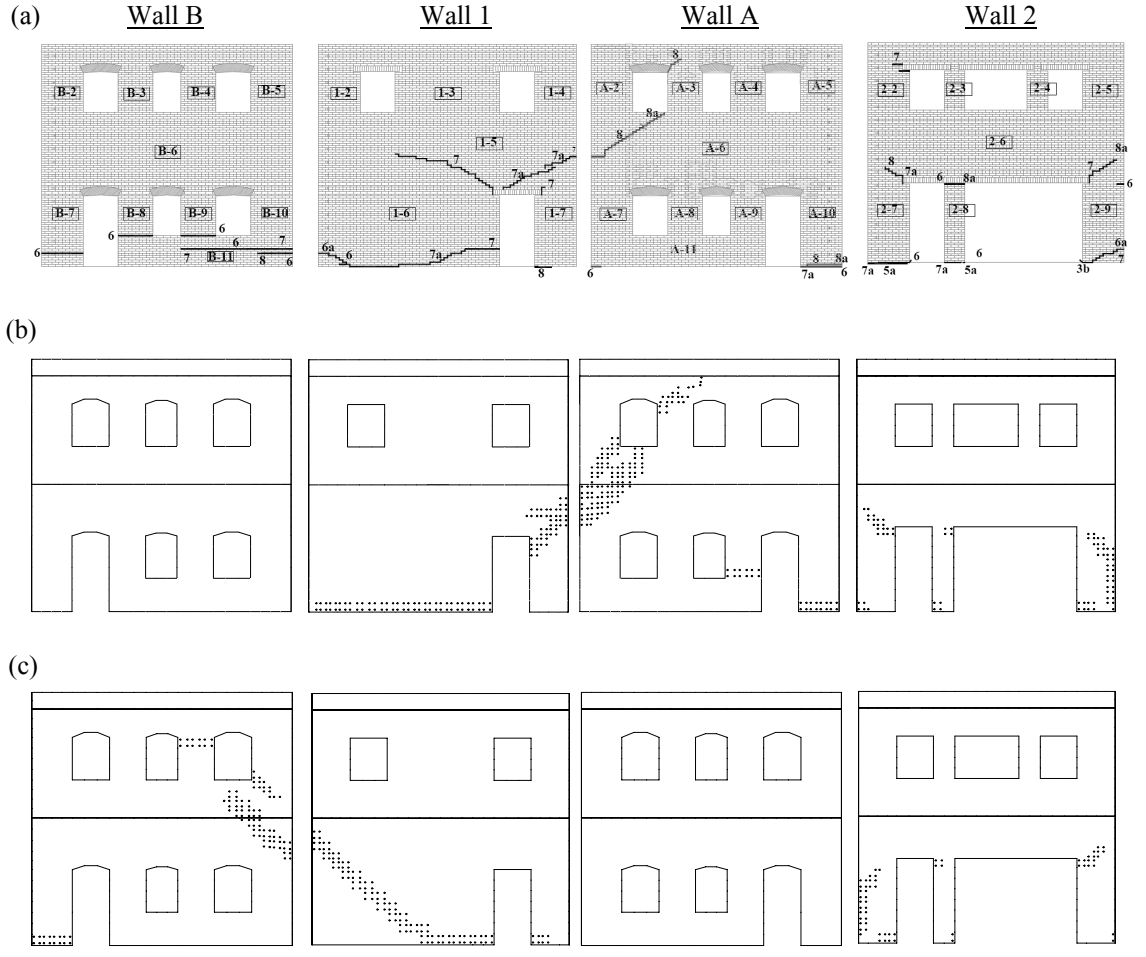

Figure 4-15: Crack patterns for: (a) experimental cyclic testing (Yi et al. 2006a); SLA with displacement loading in the (b) +*x*-direction and (c) –*x*-direction.

4.4.3 Discussion

In general, SLA effectively predicts the previous experimental results, while improvements in the modeling process could surely be made. In order to highlight the advantages and disadvantages of the method, the following items deserve further discussion: 1) comparison of SLA with non-linear finite element analysis, 2) the specific application of SLA to masonry structures, and 3) the ability of the SLA shell element implementation to capture 3D failure.

Comparison with Non-linear Analysis

The experimental tests by Yi et al. (2006a) have previously been simulated using nonlinear methods. Yi et al. (2006b) simulated their own experimental tests using 3D continuum elements with predefined crack locations to predict the cyclic response. While simulating the cyclic response is not possible using SLA, the post peak reduction (wall 1) or leveling (wall 2) of the cyclic envelope base shear capacity is better predicted using SLA than 3D FE, while the peak strength is slightly over predicted by both methods (Figure 4-16). Yi et al. (2006b) also carried out 2D nonlinear pushover analysis using their improved pier-spring model. Results compare well with SLA (Figure 4-16), but the roughly bilinear 2D pushover analysis cannot predict the post peak strength reduction. Additionally, the approximation of 3D perpendicular wall effects in the pier-spring model is avoided in the 3D SLA analysis.

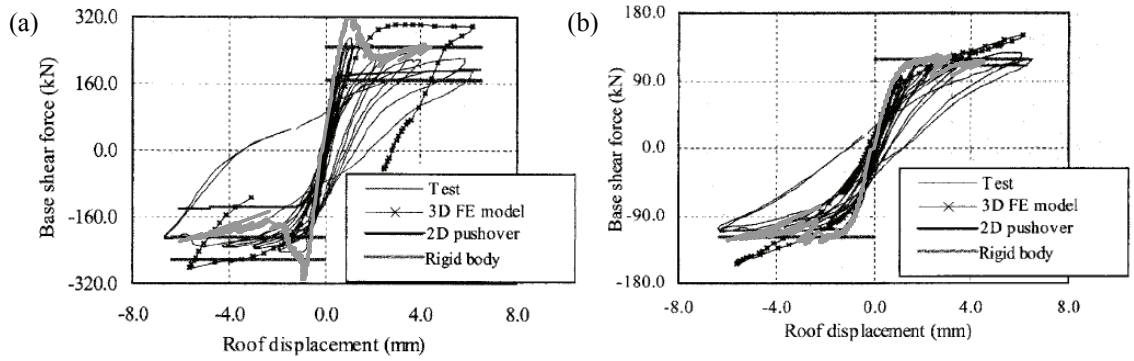

Figure 4-16: SLA results (colored grey) superimposed over the non-linear analysis results of Yi et al. (2006b): (a) Wall 1 and (b) Wall 2.

These studies demonstrate that nonlinear finite element methods are certainly capable of predicting the cyclic response of masonry walls. However, to highlight the benefits of SLA, it is useful to compare SLA with less sophisticated nonlinear finite element procedures. To this end, the experimental tests of Yi et al. (2006a) were also simulated using non-linear finite element

analysis with a total strain fixed crack model (Feenstra et al. 1998) available in typical commercial software. The meshes, shell element properties, and material properties used were consistent with SLA, with the exception of the default constant shear retention factor (β_{sh}) of 0.01 used for non-linear analysis (NLA). Load increments were automatically adapted to help convergence. Results are compared to SLA results in Figure 4-17.

The predicted load-displacement response is initially similar using both analysis methods and the initial crack patterns also compare well (not shown here). This provides further confidence in the solution algorithm implemented for simulating fracture under non-proportional loading (§4.3). However, although initial results compare well, the NLA simulations failed to converge at relatively low levels of displacement. Specifically, for loading in both the positive and negative *x*-directions, simulations of the Yi et al. (2006a) tests fail to converge close to when SLA indicates a sharp snap-back in the load-displacement response of wall 2 (Figure 4-17b). This lack of convergence under displacement control is expected because specifying displacements does not allow the utilization of arc-length methods which improve convergence during snap-back behavior. Certainly, an informed user could adjust the convergence criteria, attempt other load stepping procedures, or control crack opening displacements once crack locations are known, but all of these refinements are avoided using SLA.

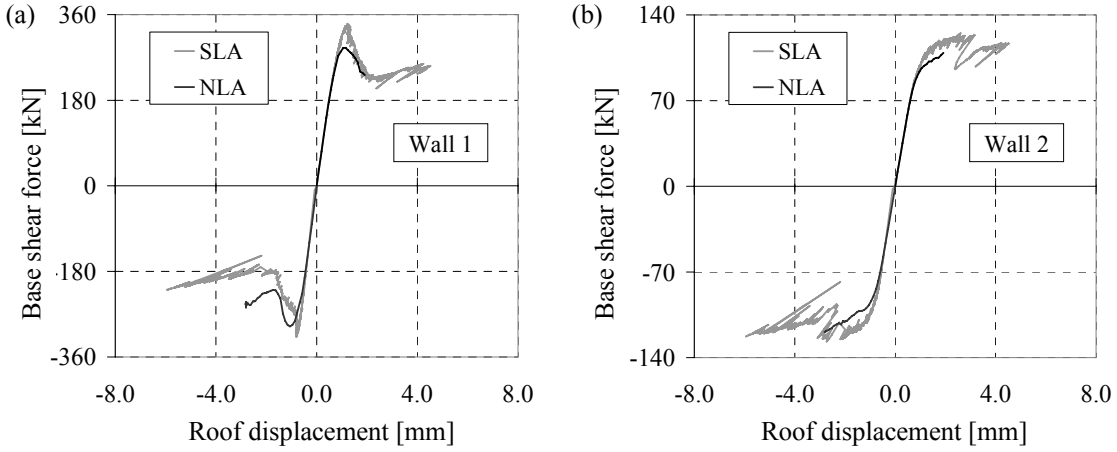

Figure 4-17: Comparison of non-linear analysis (NLA) and sequentially linear analysis (SLA) simulation results for the Yi et al. (2006a) test.

Modeling of Masonry

While the SLA framework is capable of modeling brittle fracture in general, results provide valuable insight into the ability of SLA to specifically capture masonry failure. It is known that pier failure mechanisms (rocking, shearing, and sliding) are dependent on pier aspect ratio and

axial load (Calvi et al. 1996). In §4.4.2, the building tested by Yi et al. (2006a) was subjected to low vertical loads (only self-weight) resulting in low axial loads in the piers. As a result, failure of wall 2 occurred through rocking of the slender piers (Yi 2004), and failure of wall 1 occurred through initial rocking followed by sliding of the stout, left pier. Shear failure in the piers, which typically occurs due to high axial loads (Calvi et al. 1996), was not observed. In contrast, SLA simulations of buildings subjected to large vertical loads resulted primarily in shear failure, followed by significant sliding failure (DeJong et al. 2009a).

In general, rocking failure is well predicted using SLA but the base shear tends to be overestimated when shear failure occurs (DeJong et al. 2009a). One primary reason for this is likely that a biaxial failure envelope for masonry has not been considered. The shear failure which occurs in the piers results from tensile stresses in the primary principle stress direction and compressive stresses in the secondary principle stress direction, which is currently neglected. When these secondary compressive stresses are large, a biaxial failure envelope would result in a reduction in the allowable tensile strength, and therefore a reduction in the base shear capacity.

It should also be noted that the failure mode, shear or rocking, is dependent on the material tensile strength, which is difficult to estimate. A larger tensile strength would cause a larger increase in shear capacity than rocking capacity. Therefore, a larger vertical tensile strength has a similar effect on the failure mode as a lower axial load. This effect was observed in other simulations of masonry failure using SLA for shell pushover studies (DeJong et al. 2009a), as doubling the tensile strength resulted in increased rocking failure and decreased diagonal pier cracking.

Finally, simulation results indicate that while rocking failure and shear failure can both be predicted using SLA, accuracy could be improved through a material model which incorporates the heterogeneous nature of masonry. However, large displacement sliding failure cannot be modeled at this point. If significant sliding failure is expected based on wall geometries and axial loads (Calvi et al. 1996), then care should be taken when using this model.

Three-dimensional Failure Mechanisms

In §4.4.2, the shell element implementation was shown to predict 3D failure mechanisms in which cracks propagate around building corners. This contribution is significant, as prediction of the failure mechanisms is achieved with a simple material model which requires relatively few material properties and no load stepping procedures or convergence criteria.

Simulation results exemplify the greater capacity of the entire structure with respect to a single wall. Clearly some effect of perpendicular walls must be included, and the 3D models

eliminate the need to estimate 3D wall corners effects. The simulated 3D capacity of the Yi et al. (2006a) structure is quite accurate, while the 2D membrane element models clearly underestimate the response (Figure 4-14).

4.5 Summary

The primary contributions herein are the extension of SLA to incorporate non-proportional loading, and the new framework by which shell structures can be effectively modeled under non-proportional loading. Application to a masonry structure under quasi-static lateral loading, a simplification of expected earthquake loading, has led to the following specific conclusions:

- SLA effectively predicts damage due to the brittle material failure of masonry, and requires a relatively small number of modeling parameters.
- Shell elements allow three dimensional collapse mechanisms to be directly predicted, eliminating the need to estimate the participating area of perpendicular walls when modeling in two dimensions.
- Monotonic loading provides an effective means of predicting experimental cyclic envelopes, although can result in slight overestimation of the maximum base shear. A safety factor should be applied to account for the simplified loading conditions.
- The simplified uni-axial tensile strength failure criterion reasonably predicts structural response. However, implementation of a more complex failure criterion which incorporates the heterogeneity of masonry is possible within the same framework.

In addition to these specific conclusions, the benefit of this improved brittle fracture modeling method must be reiterated within the context of this dissertation. The primary advantage of SLA when compared to equilibrium methods (e.g. Chapter 3) is its ability to model damage. The advantage of SLA when compared to other finite element brittle fracture models is its ability to model continued damage without convergence issues, thus being able to predict a greater extent of damage. Therefore, SLA provides a new useful tool for explaining existing crack patterns and predicting where damage might be expected during future earthquakes. Additionally, improved damage predictions can be used to better define possible collapse mechanisms. Predicted collapse mechanisms could then be used to inform quasi-static equilibrium analyses. Furthermore, while modeling the dynamic response of the structure is not possible using SLA, defined collapse mechanisms could also be used to inform dynamic analyses using the approaches discussed in Part III of this dissertation.

Part III

Dynamic Analysis

Chapter 5

Analytical Modeling: Dynamics of Arches

5.1 Introduction

Part III narrows the scope to dynamic assessment methods for masonry structures focused on stability, not strength. In effect, this means concentrating on the dynamics of discrete block structures. The majority of attention is paid to relatively simple structures, or structural components, whose dynamic behavior must be understood before using numerical tools to assess more complex structures.

Despite the prevalence of the masonry arch, its dynamic behavior under seismic loading has not been well-described. Therefore, a better understanding of the response of masonry arches (and vaults) to dynamic loading is necessary to develop tools which can be used to assess the safety of these structures.

In this chapter, an analytical model for the dynamics of masonry arches is first presented in §5.2 and the limitations of the model are discussed. Subsequently, in §5.3 an experimental program is presented which tests the stability of masonry arches under harmonic and seismic ground motion. Experimental results are compared with predictions from the analytical model. In §5.4, the analytical model is used to make steps towards a criterion for evaluating the safety of masonry arches in seismic regions. Although other assessment procedures have been developed (e.g. De Luca et al. 2004), they have been based on static analyses which do not incorporate the dynamics of the problem. Finally, results and conclusions are summarized in §5.5.

5.2 An Analytical Arch Model

As discussed in §2.3.1, Oppenheim (1992) developed an analytical model which describes the arch as a rigid body four-link mechanism and predicts failure of the arch in response to a given base impulse excitation. Although Oppenheim did not address the problem of what occurs if the arch recovers from the single impulse and 'rocks' in the other direction, his analytical model effectively poses the problem as a 'rocking arch' which is similar to the rocking block. Since these two systems are similar, the fundamental work on the rocking block (Housner 1963, see §2.3.1) will be used to guide the derivations herein.

The analytical model presented in this section builds upon the work by Oppenheim (1992) by addressing the impact which occurs if the arch recovers, and can therefore describe the motion of the arch through continued rocking cycles. Similar to rocking block models, the rocking arch model assumes rigid blocks and rigid supports and is therefore only dependent on geometric properties. For more details regarding the analytical model and its implementation in Matlab (2002), see De Lorenzis et al. (2007) and Appendix B. The model and the included impact formulation is a simplification of the actual response of the masonry arch under dynamic loading, but this chapter will attempt to illuminate the utility of such a model.

5.2.1 The Arch as a Four-hinge Mechanism

Following the work by Oppenheim (1992), the part-circular arch with center-line radius R_A, thickness t_A, and angle of embrace β_A, is modeled as a four-hinge mechanism. The four hinges which create the three-bar mechanism ABCD (Figure 5-1a) are assumed to form at the locations where they would form under equivalent static analysis, i.e. under a 'tilt test' where the base is quasi-statically tilted until collapse occurs (see Chapter 3). The minimum tilt angle at which collapse occurs in the quasi-static test correlates to the theoretical minimum base acceleration, γ, which would cause the four-link mechanism to form. (The arch would collapse if this horizontal base acceleration were applied for an infinite length of time.) The problem is purely geometrical; γ is a function of t_A, R_A, β_A, and the number of voussoirs, n_A.

The assumed single degree of freedom (SDOF) mechanism allows the response of the arch to a given ground acceleration, $\ddot{u}_g(t)$, to be described by the following equation of motion which can be derived using Hamilton's principle and Lagrange's equation:

$$M(\theta)R_A\ddot{\theta} + L(\theta)R_A\dot{\theta}^2 + F(\theta)g = P(\theta)\ddot{u}_g \tag{5.1}$$

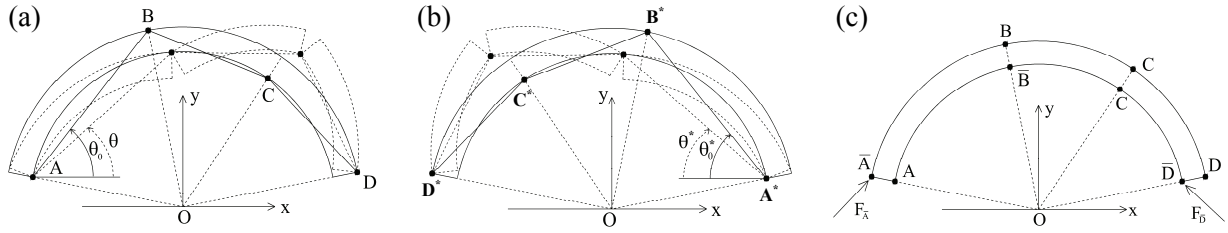

Figure 5-1: The four-hinge mechanism assumed by the analytical model: (a) during the first half cycle of motion, (b) during the second half cycle of motion, and (c) at the time of impact between (a) and (b).

where θ is the angle depicted in Figure 5-1a if $\ddot{u}_g(t)$ is initially negative (the ground moves to the left), and the coefficients *M(θ)*, *L(θ)*, *F(θ)*, and *P(θ)*, which are non-linear in θ, are described further by Oppenheim (1992). To solve Equation 5.1, initial conditions are necessary and can be defined as $\theta = \theta_0$ (Figure 5-1a) and $\dot{\theta} = 0$ at the onset of motion.

Equation 5.1 is only valid when $\theta < \theta_0$, i.e. before the arch recovers, impacts occur, and the arch 'rocks' in the other direction. If the arch does recover, the hinge locations are assumed to reflect about the vertical line of symmetry of the undeformed arch, the mechanism $A^*B^*C^*D^*$ is formed (Figure 5-1b), and motion continues as described by a similar equation of motion:

$$M\left(\theta^*\right)R_A\ddot{\theta}^* + L\left(\theta^*\right)R_A\dot{\theta}^{*2} + F\left(\theta^*\right)g = -P\left(\theta^*\right)\ddot{u}_g \tag{5.2}$$

where θ^* is the angle depicted in Figure 5-1b. Again, the equation of motion can be solved with the initial conditions $\theta^* = \theta_0^* = \theta_0$ and $\dot{\theta}^* = \dot{\theta}_{after}^*$, where $\dot{\theta}_{after}^*$ is the rotational velocity of link A^*B^* immediately after impact. At this point, the impact problem needs to be solved, i.e. $\dot{\theta}_{after}^*$ must be determined using the known rotational velocity immediately before impact, $\dot{\theta}_{before}$. Note that Equation 5.2 is only valid when $\theta^* < \theta_0^*$. If the arch recovers a second time, i.e. θ^* returns to θ_0^*, the impact problem is again solved and the initial mechanism is reformed (Figure 5-1a). This rocking motion continues and the arch alternates between the symmetric kinematical mechanisms until failure occurs or the arch returns to rest in its initial configuration.

5.2.2 The Impact Problem

Each time the arch recovers to its initial configuration and the symmetric mechanism is formed, impacts occur and energy is dissipated. To account for the energy dissipation at impact, the rotational velocity immediately after impact, $\dot{\theta}_{after}^*$, is calculated using the geometrical

properties of the arch, and the known rotational velocity immediately before impact, $\dot{\theta}_{before}$. Consistent with the rocking block formulation by Housner (1963), the impulsive forces are assumed to act at the opposite side of the arch thickness at the closing hinges, i.e. at points $\bar{A}$, $\bar{B}$, $\bar{C}$ and $\bar{D}$ (Figure 5-1c), inducing the external forces $F_{\bar{A}}$ and $F_{\bar{D}}$. Conservation of angular and linear momentum (five equations total) are used to solve for the five unknowns of the problem: $F_{\bar{A}x}$, $F_{\bar{A}xy}$, $F_{\bar{D}x}$, $F_{\bar{D}y}$, and $\dot{\theta}^{*}_{after}$ (see Appendix B). The resulting coefficient of restitution indicates the dissipation of energy induced by each impact:

$$c_v = \dot{\theta}^{*}_{after} \Big/ \dot{\theta}_{before} = \sqrt{E_{T,after} \Big/ E_{T,before}} \tag{5.3}$$

where $E_{T,after}$ and $E_{T,before}$ represent the total energy of the system immediately after and immediately before impact, respectively. Similar to γ, the resulting c_v is only a function of geometry (t_A, R_A, β_A, and n_A).

5.2.3 Predictions of the Analytical Model

The analytical model can now be used to predict the rocking response of an arch under a given ground motion. As a starting point, the arch geometry and the ground motion considered by Oppenheim (1992) will be employed. This will allow comparison with Oppenheim's results and verify the accuracy of the derivation. Subsequently, both the arch geometry and the ground motion will be adjusted in order to explore their effects on the stability of the masonry arch.

The arch analyzed by Oppenheim (1992) is defined by the following parameters: $t_A/R_A = 0.15$, $\beta_A = 157.5°$, $R_A = 10$ m, and $n_A = 7$. The ground motion applied by Oppenheim (1992) consists of a pulse of constant ground acceleration with duration t_p [seconds] and magnitude a_p [g], followed by a pulse in the opposite direction with half of the initial magnitude (a_p / 2) and with twice the duration ($2t_p$), producing zero terminal ground velocity.

Rocking Response

The rocking response of the arch is found as a function of time by repeatedly solving Equations (5.1) and (5.2), while applying the coefficient if restitution (Equation 5.3) when alternating between them. Results are plotted as a function of the rocking angle: $\phi = \theta_0 - \theta$ and $\phi = \theta^{*} - \theta^{*}_0$. Thus, $\phi > 0$ represents rocking to the right (Figure 5-1a), and $\phi < 0$ represents rocking to the left (Figure 5-1b). Failure is identified by an ever-increasing or an ever-decreasing ϕ during any given half cycle.

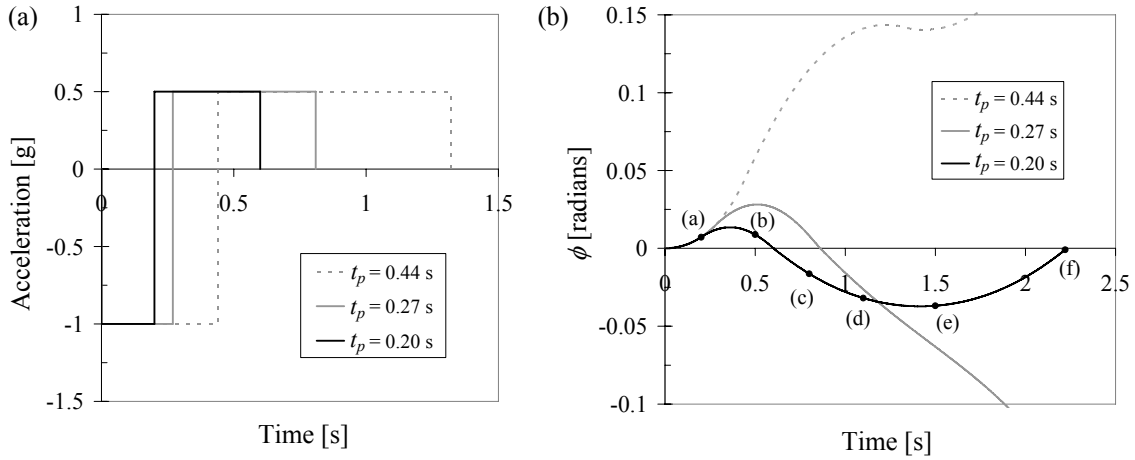

Figure 5-2: Rocking arch response: (a) applied ground motion impulses and (b) resulting rocking motion for a_p = 1.0 g and t_p = 0.44, 0.27, and 0.20 s.

Recall that the minimum ground acceleration (γ) necessary to transform the arch into a mechanism, and hence to initiate rocking motion, can be obtained through equivalent static analysis (e.g. Chapter 3). For the arch under investigation, γ = 0.37 g. Thus, ground motions which never exceed this level would cause the arch to move as a rigid body with the ground.

Figure 5-2 shows three impulses of magnitude a_p = 1.0 g with different durations, and the resulting arch response. For t_p = 0.44 s, the arch fails during the first half cycle of motion as ϕ, continuously increases. For t_p = 0.27 s, the arch recovers from the initial half cycle of motion, impact occurs at ~ 0.86 s (at which time the external excitation has ceased already), and failure occurs during the second half cycle of motion as ϕ decreases continuously. For t_p = 0.20 s, the arch initially recovers from the first half cycle of motion, impact occurs at ~ 0.6 s (at which time the external excitation has just ceased), the arch rocks in the other direction and recovers, and then would continue rocking back and forth until all the rocking energy is dissipated and the arch returns to rest. Note that successive half cycles would have decreasing amplitude and decreasing duration.

Failure Domains

The analysis above was repeated systematically to find the combinations of impulse magnitudes and durations leading to arch failure. Results for the arch under investigation are reported in Figure 5-3.

The arch can experience four general responses to the applied impulse. For an impulse with a large duration and magnitude, the arch fails immediately during the first half cycle of motion. This region is labeled “Mode II collapse”. For smaller impulses, the arch fails during the second

half cycle of motion. This region is labeled “Mode I collapse”. For even smaller impulses, the arch rocks back and forth until it recovers. This region is labeled “Recovery”. Finally for impulses of magnitude lower than γ, the rocking mechanism is not initiated. This region is labeled “No hinging”.

The Mode II failure curve is the same as was found by Oppenheim (1992), again confirming the accuracy of the model derivation. However, the new Mode I failure curve is significantly lower, and is therefore the critical failure curve. Design or assessment of the arch based on Mode II collapse would be unsafe. Since the Mode I failure curve governs, it is the analytical failure curve which will be plotted throughout this work (unless noted otherwise).

It is interesting to note that these possible responses parallel the possible responses of the single rocking block to a ground acceleration impulse found by Zhang and Makris (2001), who also concluded that the Mode I failure curve governs. It also should be mentioned that there is a very small region of impulses above the Mode I failure curve for which the arch would recover (depicted by Zhang and Makris (2001) for the rocking block), but this range is conservatively ignored when assessing masonry arches because expected ground motions cannot be identified with enough accuracy to rely upon this small safe region.

The three impulses in Figure 5-2 are also plotted as points on the failure domain plot in Figure 5-3. These three impulses exemplify behavior which results in the three possible rocking regions.

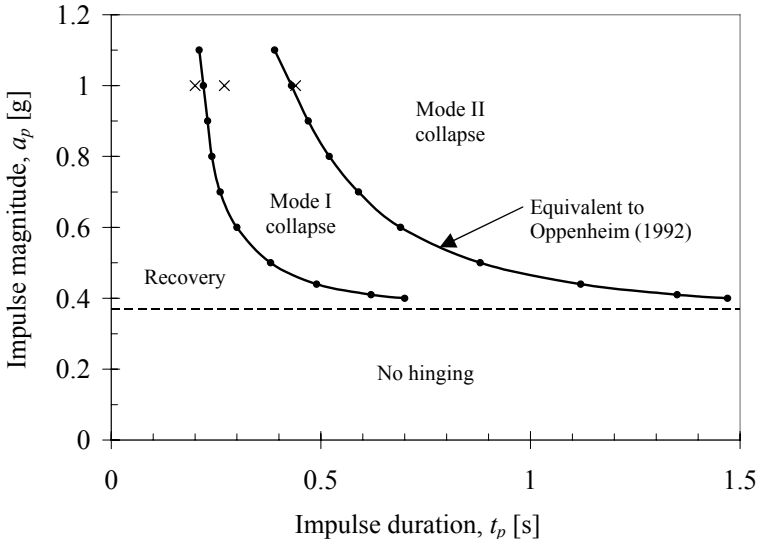

Figure 5-3: Analytical model prediction of the possible responses of a masonry arch to a step impulse of duration, t_p, and magnitude, a_p. (Note: the ‘x’ data points represent the impulses in Figure 5-2a.)

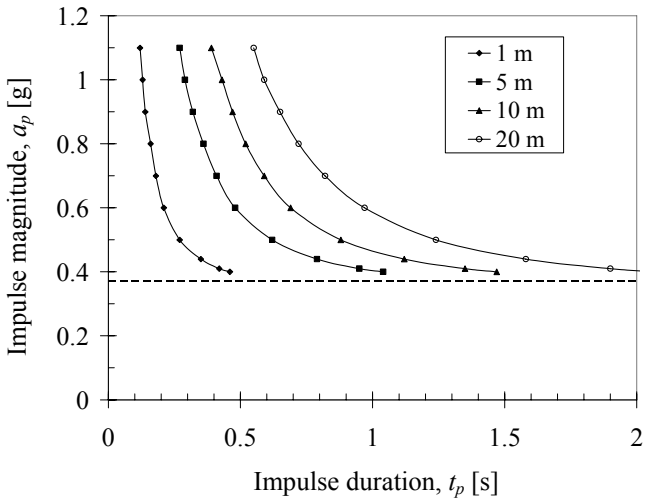

Figure 5-4: Analytical model predictions of the failure curves for masonry arches of different radii (R_A) but of the same proportions (t_A/R_A = 0.15 and β_A = 157.5º).

Scale Effect

The presence of the arch radius R in the differential equations of motion implies the existence of a scale effect, i.e. arches with the same proportions (t_A/R_A , β_A) but different sizes will have different dynamic response. This scale effect is illustrated in Figure 5-4, which shows the Mode I failure curves for similar arches (t_A/R_A = 0.15 and β_A = 157.5º) with different radii. The R_A = 10 m arch was analyzed in the previous section.

Figure 5-4 demonstrates that larger arches are clearly more stable than smaller ones with the same proportions. Furthermore, the failure domain curves are approximately scalable with the square root of the radius. For example, if one of the failure curves is taken as reference and the impulse magnitude corresponding to a given t_p is multiplied by the square root of the ratio of any desired radius R_A to the reference radius, the other failure domain curves are obtained. Thus, it is only necessary to compute rigorously the failure domain for an arbitrary reference radius. This confirms the findings of Housner (1963), and is explored further in §5.4.

Effect of Arch Geometry

Figure 5-5 illustrates the effect of the arch geometry, in terms of t_A/R_A and β_A, on the arch failure domains. As expected, increasing the t_A/R_A ratio and decreasing the angle of inclusion (β_A) increases the resistance of the arch to impulse ground motion, i.e. increasing its stability. These geometric changes also result in the assumption of slightly different four-hinge mechanisms (see Figure 5-5), which explains why the failure domains are not evenly distributed.

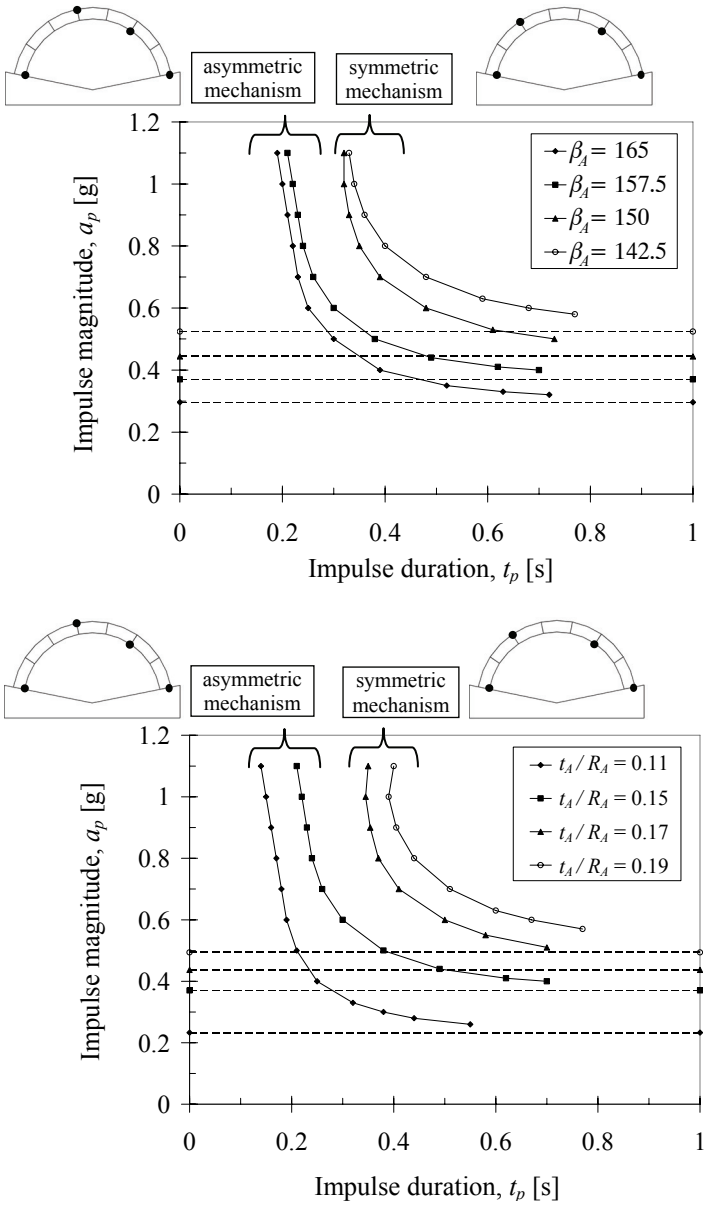

Figure 5-5: Analytical model predictions of the failure curves for masonry arches of the same radius (R_A = 10 m) but of different proportions (t_A / R_A and β_A).

The uneven distribution visible in Figure 5-5, suggests that the number of voussiors has an effect on the failure domains. More voussoirs would make the shift in mechanisms less drastic, and therefore the spacing of the failure curves would be more even. Thus, the effect of a greater number of voussoirs on the magnitude-duration failure domain was also investigated. As expected, increasing the number of voussoirs was found to effectively increase the resolution of the possible initial hinge locations which are found using equivalent static analysis. While this does change the four-link mechanism, it has a relatively small effect on the failure domains compared to a change in t_A/R_A or β_A.

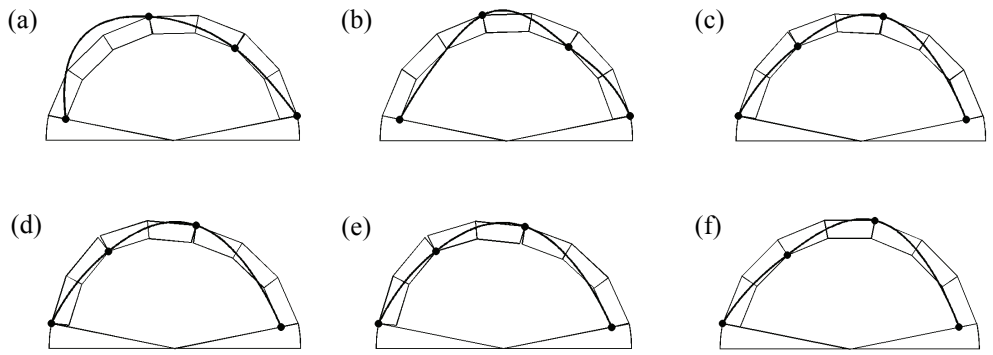

Figure 5-6: Arch hinge locations and dynamic thrust lines found using the analytical model for a step impulse of magnitude 1.0g and duration 0.20 seconds at times: (a) 0.20 s, (b) 0.50 s, (c) 0.80 s, (d) 1.10 s, (e) 1.50 s, and (f) 2.22 s.

Thrust Line during Motion

For static analysis, the support reactions and the resultant of the internal compressive forces were used to calculate the *thrust line* (Heyman 1966) of the arch. Similarly, at any instant during motion, the *dynamic thrust line* can be calculated by considering the inertial forces and moments acting on the individual arch links, in addition to their self-weight. The dynamic thrust line must be determined based on the deformed configuration of the arch, due to the significant effect of the displacements on the inertial forces and moments.

Drawing the dynamic thrust line can give useful information regarding the instantaneous equilibrium conditions of the arch. In particular, the hinge location assumptions of the analytical model can be checked. As mentioned previously, the hinge locations were determined through equivalent static analysis, and assumed to remain constant during motion, except at impact when hinges were assumed to reflect. However, a line of thrust exiting the thickness of the arch would signify the formation of a hinge at that location, suggesting that the actual hinge locations would be different than those assumed.

Figure 5-6 shows the dynamic thrust line for one of the arch responses shown in Figure 5-2 (a_p = 1.0 g and t_p = 0.20 s), in which the points corresponding to the snapshots of Figure 5-6 are also marked. The line of thrust exits the thickness of the arch in the first chosen instant of 0.20 s (Figure 5-6a), at which time the first pulse is still acting and the arch is undergoing the first half cycle of motion. Although it is not shown, the depicted the line of thrust is representative of the entire time interval during action of the first pulse ($0 < t < 0.2$ s). In the subsequent instants either during the return pulse (0.50 s, first half cycle of motion, Figure 5-6b) or after the excitation has ceased (second half cycle of motion, Figures 5-6c to 5-6f), the line of thrust exits the arch

thickness at limited locations and by a limited distance, indicating that the assumed hinge locations were reasonable.

In principle, the dynamic thrust line could be used to update the location of the hinges during the analysis, by placing the new hinges where the thrust line has the maximum distance from the axis of the arch. In the case reported in Figure 5-6a, the second hinge from the left would then be relocated between the second and third voussoirs. This would result in an iterative analysis which would be tedious for relatively minor benefits. Thus, the hinge locations were kept constant during motion, as initially assumed. This assumption will be further evaluated throughout this chapter, and will be further evaluated with discrete element modeling results in Chapter 7.

Sliding

The computed dynamic thrust line is also valuable for predicting whether sliding behavior might occur. This is done by comparing the angle of the line of thrust with respect to the tangential direction of the circular arch centerline. The minimum coefficient of friction (μ) required to prevent sliding can then be determined throughout the entire span of the arch at any time throughout motion. For the arch subjected to the impulses in Figure 5-2a, the maximum required coefficient of friction always occurs at the right springing (hinge D) at the onset of the impulse ($t = 0^+$). Thus, it does not depend on the duration of the impulse, but only on the magnitude. For an impulse magnitude of 1.0 g, sliding is prevented if the coefficient of friction is $\mu > 0.56$, which is less than the typical coefficients of friction for masonry. It should be noted that the thrust line at time $t = 0^+$ is not admissible because it exits the thickness of the arch (similar to Figure 5-6a), indicating that hinges initially form in different locations. If hinge locations were updated, the minimum coefficient of friction necessary to prevent sliding would be even lower than the one computed above, and hence even closer to the one computed with equivalent static analysis ($\mu = 0.50$). Regardless, sliding does not occur for the given arch geometry, and the dynamic thrust line is shown to be a valuable tool to check for possible sliding failure.

Effect of Impulse Shape

All results presented thus far have been in response to a step impulse of the form shown in Figure 5-2a. However, the same modeling framework can be used to determine the effect of other ground motions as well. For example, single cycle sinusoidal acceleration impulses of period, T_p, and acceleration amplitude, A_p, were applied to Oppenheim's arch, resulting in the analytical and numerical failure domains shown in Figure 5-7. The same four possible arch responses result, and the Mode I failure curve again governs.

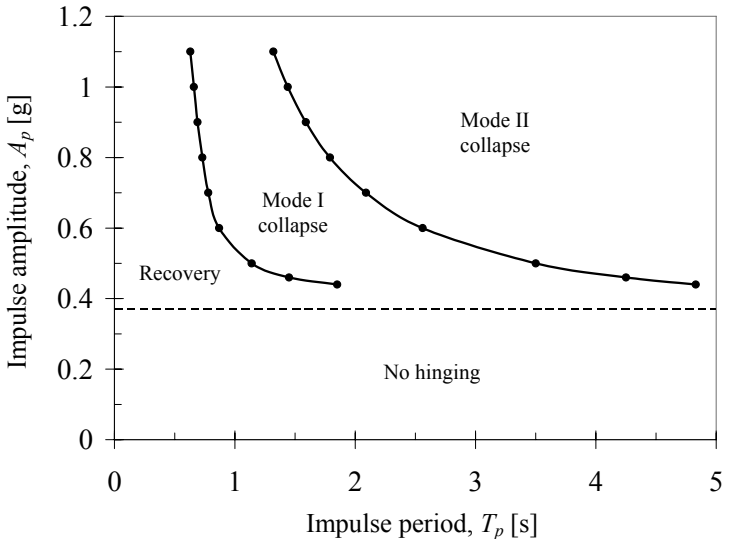

Figure 5-7: Failure domains of Oppenheim's arch in response to a single cycle sinusoidal impulse function of period, T_p, and amplitude, A_p.

5.3 Experimental Investigation of Arch Dynamics

This section is focused on an experimental investigation designed to obtain a better fundamental understanding of masonry arch dynamics, and to evaluate the analytical model presented in §5.2. Before the rigorous experimental results are presented, qualitative observations are described and used to evaluate the assumptions of the analytical model.

5.3.1 Evaluation of Analytical Model Assumptions

The assumptions included in the analytical model clearly lead to some limitations. First, the assumption of fixed hinge locations does not allow: (1) free initial hinge formation, (2) free hinge formation after impact, (3) opening at any non-hinged joint, or (4) sliding between blocks. Second, the assumption of rigid blocks does not allow elastic deformation, meaning that resonance cannot be modeled, and does not allow material failure during impact. Third, the assumption of perfectly rigid supports does not allow for support deformation which could reduce stability.

Although some of these limitations were discussed in §5.2.2, experimental tests were used to address them more completely. To this end, small scale arches were subjected to both a harmonic base motion with linearly increasing amplitude and a variety of earthquake time histories, and behavior was observed. The response of an arch made of aerated concrete blocks with a center-line radius of 15 cm and with 13 voussoirs is shown in Figures 5-8 and 5-9. Under harmonic base

motion, the arch initially moved as a rigid body with the base, with only minor vibration and no visible hinge mechanisms. As the amplitude increased, slight hinging occurred as the arch rocked back and forth. More visible hinging occurred in the final two rocking mechanisms which are shown in Figure 5-8. Under the El Centro earthquake time history in Figure 5-9a, four primary rocking mechanisms were formed before collapse (Figures 5-9b,c,d,e). The four corresponding rocking mechanisms predicted by the analytical model are also shown in Figure 5-9. The first two rocking mechanisms are less visible and result from the first smaller acceleration peaks in Figure 5-9a. The final mechanism (Figure 3e), which resulted in collapse, is induced by the first large negative peak and the large positive peak (the largest one) which immediately follows.

In Figures 5-8 and 5-9, the consecutive hinge mechanisms are shown at their maximum magnitude, and indicate that a four-hinge mechanism does form and that the hinges do approximately reflect. However, hinge mechanisms are not always exactly symmetric and the transition between these mechanisms does not occur in one distinct impact. In fact, hinge reflection is more fluent as hinges seem to 'migrate' instead of reflecting directly. Sliding was not observed, confirming the predictions of dynamic thrust line analysis presented in §5.2.2.

These observations indicate that through the first assumption mentioned above, that of fixed hinges, the analytical model describes a reasonable simplification of behavior. The second assumption, that of rigid blocks, is appropriate for the scale tested because negligible material failure occurred and the elastic resonant frequency of the first mode of the arch tested is over 300 Hz, well above the frequency content of the earthquake. However, the effects of the rigid block assumption are scale dependent. At larger scales, larger impact forces could cause material failure, especially at block corners, and the resonant frequency would be lower and could be excited. Regardless, it must be noted that resonance could only force hinges to occur at a lower acceleration than expected; resonance could not amplify the response until collapse because initial hinge formation immediately changes the resonant frequency. The third limitation, that of rigid supports, remains and is the subject of continued research.

Based on these observations, a more complete experimental investigation was conducted to test the ability of the analytical model to predict the collapse of arches under seismic loading.

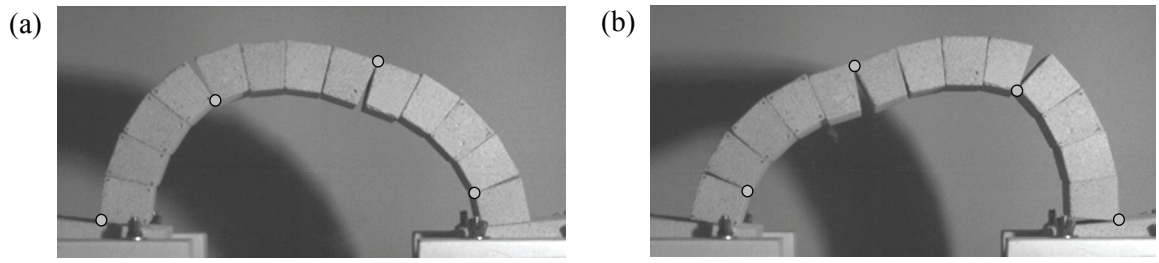

Figure 5-8: The final two mechanisms resulting from a harmonic base motion with linearly increasing amplitude: (a) the penultimate mechanism, and (b) the ultimate mechanism which resulted in collapse.

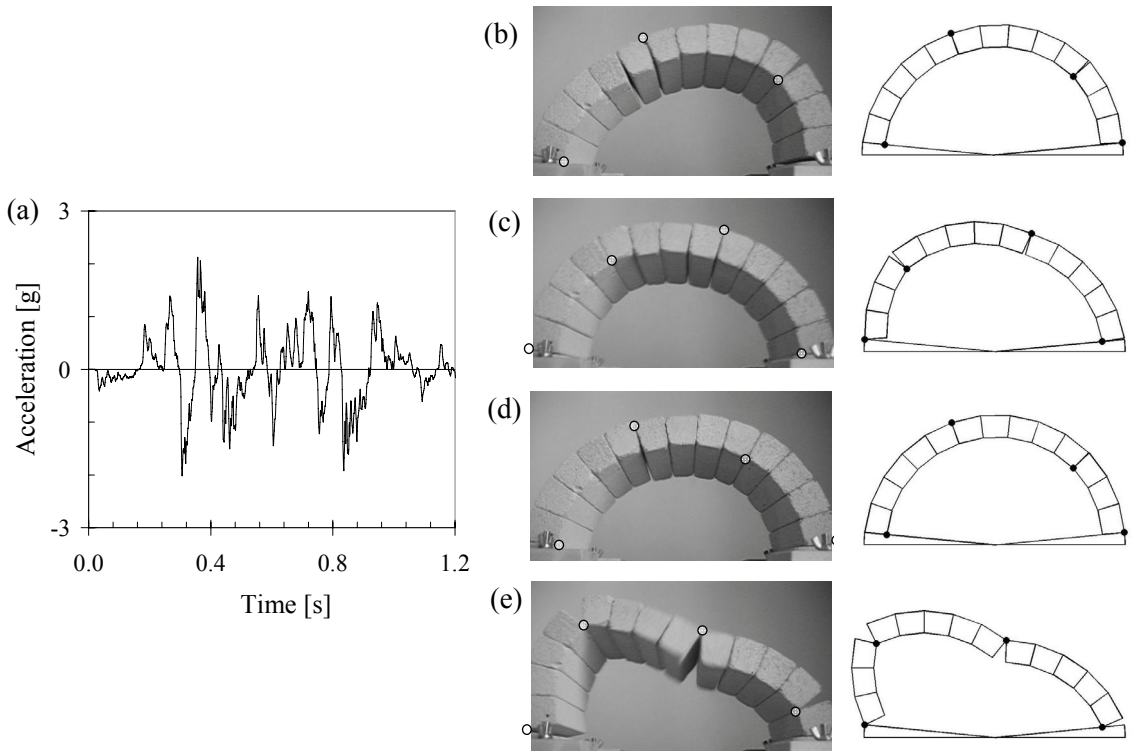

Figure 5-9: The four consecutive mechanisms resulting from the El Centro earthquake acceleration record shown in (a) as observed in the experiment and as predicted by the analytical model: the mechanisms are depicted in order from (b) first to (e) last.

5.3.2 Experimental Program

The primary focus of this experimental investigation is the application of five different earthquake time histories to two different arch geometries. The resulting state of the arch, failure or recovery, is compared with predictions using the analytical model. Prior to earthquake testing, harmonic testing with a continuously increasing amplitude was also conducted to determine the effect of a large number of consecutive impulses on the arch response.

Arch Characteristics

The characteristics of the two arches tested are given in Table 5.1. Arch voussoirs were cut from autoclaved aerated concrete (AAC) blocks to the required dimensions, including an out-of-plane thickness of ~ 10 cm. Base supports were also cut from AAC to maintain a consistent friction angle. Slight variations in the constructed geometry were inevitable as the arch collapsed and was reconstructed several times during testing. Padding was placed beneath the arch to limit damage to falling blocks during collapse.

Table 5.1: Test arch characteristics

Specimen	R_A [cm]	t_A [cm]	t_A/R_A [-]	β_A [degrees]	n_A [-]
Arch1	20	3	0.15	162	16
Arch2	20	3	0.15	152	15

Seismic Testing

Seismic shake table tests were performed using the commercially available Quanser Shake Table II at MIT. Time histories from the following earthquakes were used for testing: Parkfield 1966, El Centro 1940, Golden Gate 1957, Northridge 1994, and Helena 1935. These earthquakes were chosen because they differ considerably in their frequency content and maximum amplitude (Figure 5-10). Time scaling of all earthquake records was applied to comply with the maximum stroke of the table (±7.5 cm). While time scaling is often implemented to account for scale effects between the model and the represented structure, this was not necessary because analyzing a specific structure is not the goal. Instead, a suite of time histories with significantly different primary impulse characteristics is desired.

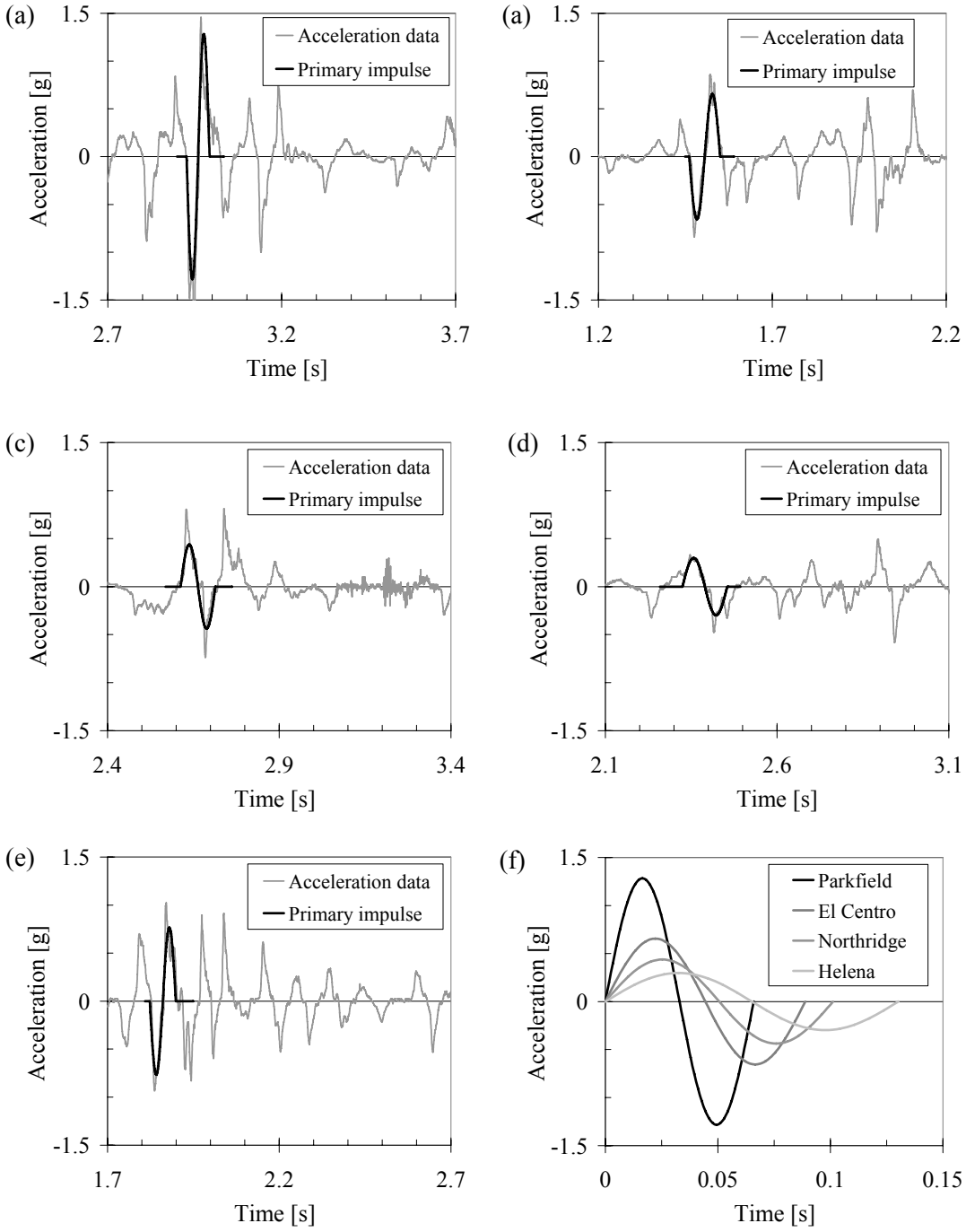

Figure 5-10: Recorded acceleration data for the minimum earthquake amplitude which caused collapse of Arch1: (a) Parkfield, (b) El Centro, (c) Northridge, and (d) Helena; (e) Golden Gate earthquake (100% amplitude) which did not cause collapse; (f) the primary impulses from (a)-(d).

The acceleration magnitude of each earthquake was scaled repeatedly so that an array of time histories was created consisting of even percentages (2%, 4%, …100%) of the full amplitude of the earthquake. Using these arrays, the earthquake magnitude was scaled down and then incrementally increased until failure occurred. When failure did occur, the earthquake magnitude was decreased slightly and then again incremented until failure. This process was repeated until a minimum of three failure points were obtained for each earthquake. The base motion during each test was obtained from an accelerometer mounted to the table and the tests were recorded on video so failure mechanisms could be observed. Approximately 70 tests were run on each arch to obtain the desired data.

While it would be possible to input the recorded earthquake time history directly into the analytical model and view the response, the exact behavior of a specific arch to a specific earthquake is not of much use for assessing arches of different geometries for which different types of ground motion are expected. Instead, the goal remains to develop a simplified method which can be broadly applied to predict the stability of masonry arches.

As mentioned in §2.3.1, discontinuous masonry structures, or rocking-type structures, are particularly susceptible to impulse loading as opposed to resonant frequency amplification as in the case of continuous structures governed by the elastic response. In particular, Zhang & Makris (2001) demonstrated that among several impulse types, the rocking block is most vulnerable to a single sinusoidal acceleration impulse. Additionally, they proposed that the response of a rocking block to a given earthquake could be effectively predicted by determining the response of the block to the primary impulse extracted from the earthquake. To test the hypothesis that the primary impulse of an acceleration time history is the governing factor affecting failure, the primary impulse characteristics (A_p, T_p) were extracted from the recorded table acceleration data for each test using a least-squares fitting method (Figure 5-10). These characteristics (A_p, T_p) were used for comparison with analytical sinusoidal impulse failure domains (see Figure 5-7). The robustness of this 'primary impulse method', extracting a primary impulse to represent a more complicated acceleration record, will be evaluated in later sections.

Harmonic Testing

Harmonic testing was performed using a shake table constructed in the Civil Engineering lab at MIT. The single-axis table rides on four Thomson self-aligning linear bearings and is driven by MTS model 506.00 pump which supplies an MTS model 204.08 hydraulic actuator. The actuator is controlled by a Moog model 760C260 servovalve with an MTS 406 Controller and an external HP 33120A function generator. The base motion was recorded using a Crossbow ± 4g LF series

accelerometer mounted to the table. The arch response was recorded on video. For more details and drawings of the shake table constructed for this work, see Appendix C.

The function generator was used to provide a harmonic excitation of constant frequency with a sinusoidal increase in acceleration magnitude (carrier wave). The carrier wave frequency was adjusted so that failure occurred within 60-90% of the peak carrier wave amplitude. Arch1 was tested at the following frequencies: 2, 4, 6, 8, and 10 Hz. Each frequency was tested a minimum of four times. Although the theoretical harmonic base motion is smooth, the actual recorded accelerations were not (Figure 5-11). Therefore, to obtain useful results, the primary impulse method was again used. The maximum acceleration impulse prior to collapse was fit with a single period sine wave using the least squares method (Figure 5-11b). The fitted impulse characteristics (A_p, T_p) were recorded as the impulse which caused collapse of the arch.

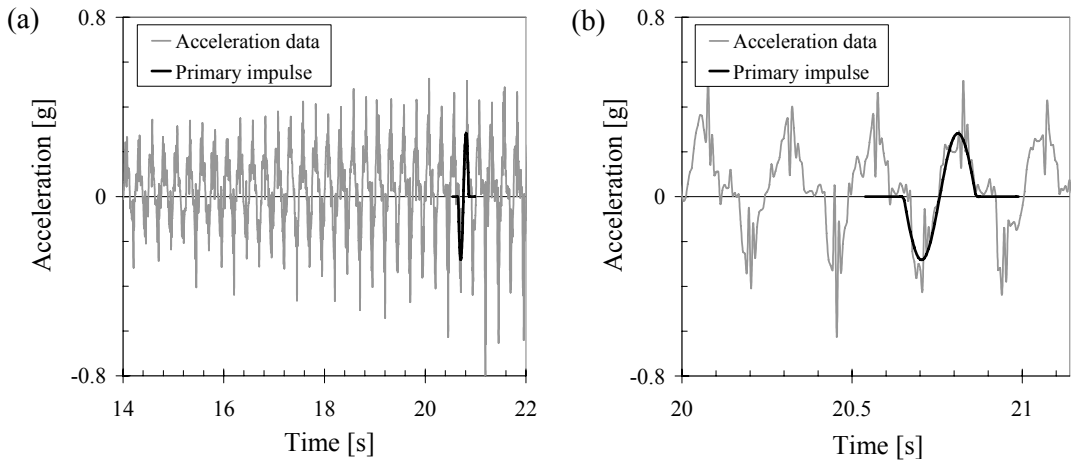

Figure 5-11: Recorded acceleration data for a 4 Hz harmonic loading test fitted with the maximum primary impulse prior to collapse (plotted at two different scales).

Tilt Testing

Although damage to the voussoirs was limited as much as possible, slight chipping at the sharp block corners was clearly visible after initial testing. Then, after the sharp corners were essentially rounded, little additional damage was observed. The slightly rounded corners of the arch cause the 'hinge locations', or rotation points between blocks, to move slightly within the thickness of the arch, essentially reducing the t_A/R_A ratio. In order to calibrate this reduction, tilt tests were performed by slowly rotating the base platform until failure occurs. The angle at which collapse occurs (α_{exp}) was recorded and the minimum horizontal acceleration (γ_{exp}) which caused collapse was determined:

$$\gamma_{exp} = \tan(\alpha_{exp}) \tag{5.4}$$

Tilt tests were performed between harmonic testing and seismic testing (after the block corners had effectively been rounded) and were repeated three times for each arch. As noted previously, γ is a function of t_A/R_A, β_A, and n_A, of which only t_A is affected by damage. Consequently, results were used to calculate an appropriate arch thickness (t_A) for analytical modeling predictions.

5.3.3 Experimental Results and Comparison with Analytical Model Predictions

Tilt Test Results

Tilt test results are presented first (Table 5.2), as they are required for accurate implementation of the analytical model. The measured tilt angle resulted in a minimum horizontal acceleration (γ_{exp}) lower than the theoretical value (γ) due to corner damage. However, the theoretical horizontal acceleration using 80% of the arch thickness (γ_{80}) compares well with the measured values (γ_{exp}).

Table 5.2: Tilt test results

Specimen	α_{exp} * [degrees]	γ_{exp} (Equation 5.4) [g]	γ (100% thickness) [g]	γ_{80} (80% thickness) [g]
Arch1	11.1 ± 0.3	0.20 ± 0.006	0.31	0.21
Arch2	17.5 ± 0.3	0.31 ± 0.004	0.41	0.30

* Tilt angle represents the average and standard deviation of three tilt tests for each arch.

Although measurements indicate that corner rounding caused a 10-15% decrease in thickness, the additional 5-10% decrease in effective thickness can be accounted for by slight variations in block size and imperfections in the constructed geometry. For example, if the blocks do not fit together perfectly or if the arch is not perfectly semi-circular, a reduction in stability would result. Notably, the appropriate reduction in arch thickness (20%) to account for corner rounding and imperfections was consistent for both arches.

Seismic Testing Results

In general, seismic testing confirmed the observations presented in the previous section. Rocking motion occurred through alternating four-hinge mechanisms. The hinge locations approximately matched those predicted by static analysis, but the transition between mechanisms again occurred more fluently through multiple impacts and mechanisms. Additional hinges and alternative mechanisms sometimes occurred, especially when clear four-hinge mechanisms were

interrupted by additional impulses that were out of phase with the rocking motion. Failure occurred as a result of hinging and rocking; sliding between blocks almost never occurred. However, minor sliding was occasionally observed at the arch supports during impact, which could have slightly reduced stability.

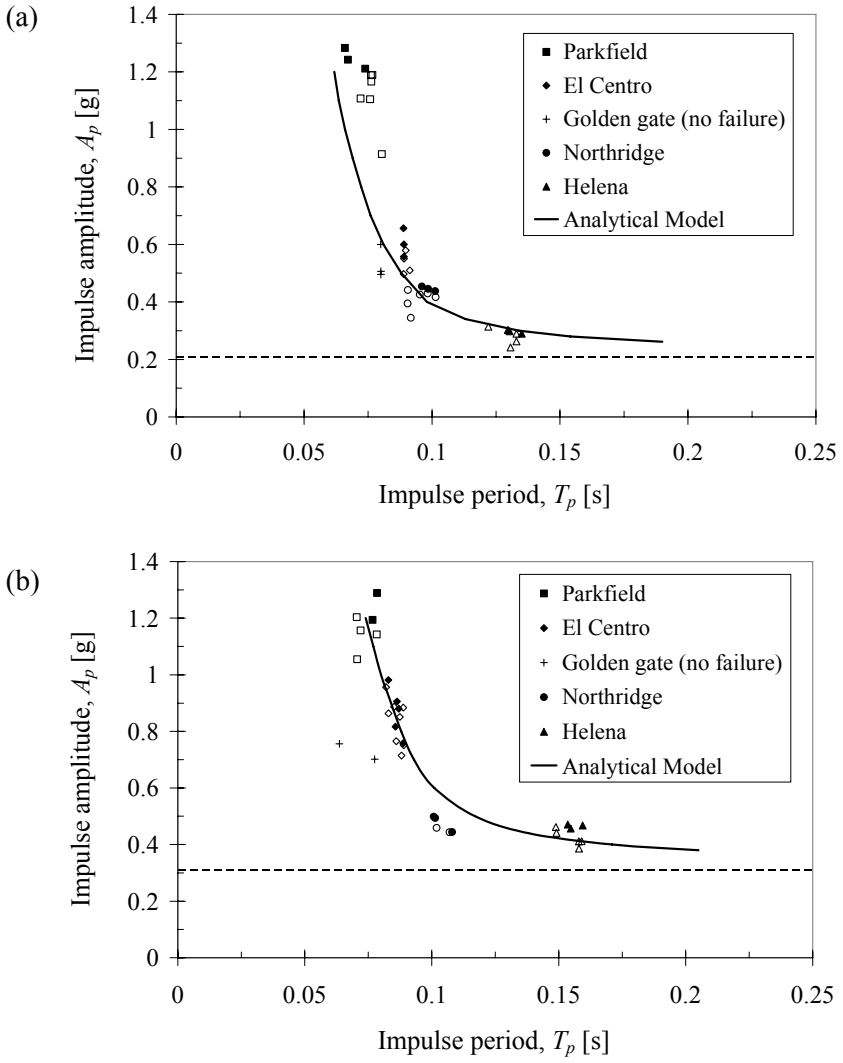

Figure 5-12: Comparison of experimental and analytical results for (a) Arch1 and (b) Arch2. Filled data points represent collapse and open data points represent recovery.

Results from seismic testing are presented in Figure 5-12, along with the analytical results assuming 80% of the arch thickness. The analytical curves represent the governing Mode I failure domain for a single period acceleration impulse of magnitude, A_p, and period, T_p, and the dashed lines represent γ_{80}. The primary impulse method is used to reduce each seismic test to a point representing the primary impulse characteristics (A_p, T_p). Ideally, all of the points representing

collapse (filled data points) would lie above the analytical curve, while all of the points representing recovery (open data points) would lie below. The maximum amplitude (100%) of the Golden Gate earthquake did not cause failure of either arch and could not be scaled up due to shake table stroke limitations, so no failure points are plotted.

Analytical and experimental results compare well for both arches. At first glance, it seems unlikely that plots (a)-(d) in Figure 5-10 represent the minimum amplitudes of each earthquake that would cause collapse of Arch1 (similar results could be plotted for Arch2). Failure is clearly dependent on both the amplitude and period of the primary impulse, exemplified by the four minimum primary impulses which caused failure of Arch1 plotted together in Figure 5-10f. Failure is clearly independent of elastic resonance, as the natural frequency of the first mode of both arches tested is over 300 Hz.

The scatter in the results in Figure 5-12 can be directly related to the earthquake time histories shown in Figure 5-10. The Parkfield earthquake resulted in the largest scatter, and also contains the largest number of significant peaks immediately before the primary impulse. The effect of these peaks was observed, as some chaotic rocking occurred prior to collapse. Despite this behavior, collapse still occurred through a distinct four-hinge mechanism and sliding was not observed. Very little scatter is observed for the Northridge and Helena earthquakes, which both have only one small peak before the primary impulse. Arches subjected to these earthquakes showed very little motion before the primary impulse caused clear rocking and collapse.

Of all results, the only one that was not predicted conservatively was the Northridge earthquake applied to Arch2. While possible explanations are numerous, the acceleration spike of considerable amplitude and duration immediately after the fitted primary acceleration impulse (Figure 5-10c) is likely the source of the slightly overestimated stability. Careful study of the collapse reveals that this second impulse occurs during the second half cycle of motion resulting from the primary impulse. This could amplify the response and cause failure at a lower acceleration than predicted. Similar overestimation did not occur for Arch1; apparently the impulse spacing was not exactly right in that case. Nevertheless, there is evidence that multiple impulses spaced at the correct frequency could cause this failure curve to be unconservative. While accounting for every possible intricacy in the acceleration record is unrealistic, the effect of multiple impulses will be addressed in the following harmonic testing results and in Chapter 6. Regardless, experimental observations and the accuracy of stability predictions indicate that the primary failure mechanism, that of rocking instability, is described by the analytical model despite its limiting assumptions.

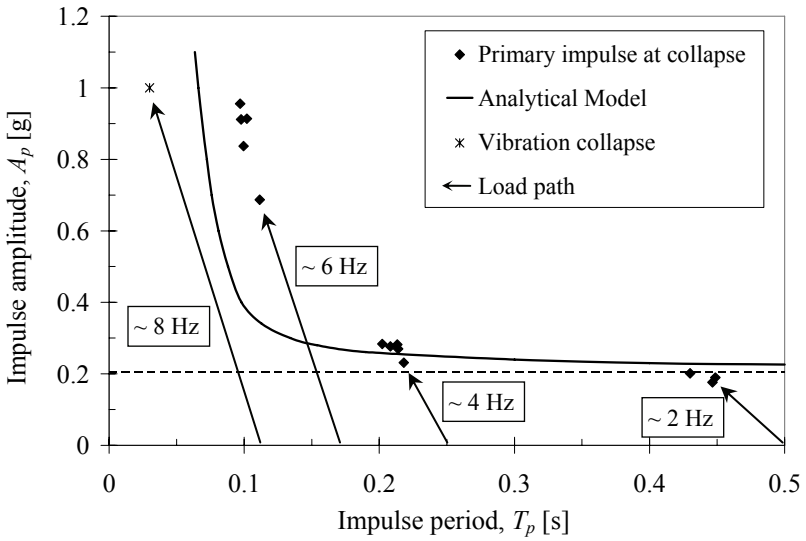

Figure 5-13: Comparison of experimental and analytical results for Arch1 subjected to harmonic loading. Filled data points represent collapse due to rocking and the arrows represent the approximate load paths during testing.

Harmonic Testing Results

Harmonic testing was conducted in order to evaluate the effect of repeated impulses on the arch response. Results for Arch1 are presented in Figure 5-13, again assuming 80% of the arch thickness for the analytical model. The filled data points again represent the characteristics of the primary impulse which caused collapse (A_p, T_p), and the dashed line again represents γ_{80}. The recorded acceleration data was not smooth and could better be described as a series of closely spaced impulses than a continuous harmonic loading (Figure 5-11b). The period of these impulses decreased with increasing acceleration amplitude, resulting in the load path approximately represented by the arrows. These load paths start at the prescribed frequency (or period) and then indicate the period reduction until failure occurs.

Failure is predicted well for low frequencies (2 Hz, 4 Hz), but arch stability is underestimated for higher frequencies (6 Hz). The results for each frequency range are interpreted as follows:

- *Low frequency (~ 2 Hz):* While the analytical model fits the data quite well, multiple impulses slightly lowered the acceleration amplitude (A_p) at which the arch fails. The results are just below the minimum predicted value at which collapse could occur (γ_{80}), which seems impossible. However, although the fitted primary impulse yielded an acceleration amplitude (A_p) below γ_{80}, the spikes in the recorded acceleration (Figure 5-11) easily exceeded γ_{80}. These spikes caused observed hinging of the arch, and the resulting momentum, although small, caused slight rocking at a lower acceleration than

expected. Failure ultimately occurred through a clear four-hinge mechanism and no sliding occurred.

- *Intermediate frequency (~ 6 Hz):* For this frequency, the analytical model significantly underestimates the stability of the arch, indicating that the arch is more resistant to multiple impulses than to one impulse. The source of this result is observed on video in which the arch hinges, blocks separate, and the arch rocks chaotically before collapse occurs. This parallels the behavior during seismic tests mentioned earlier, in which secondary impulses interrupt the formed four-hinge mechanism and cause additional hinges and alternative mechanisms. While one might expect this behavior to be detrimental, it seems to have a stabilizing effect in this case where the frequency of impulses is relatively high and the amplitude of consecutive impulses is slowly increased. The likely cause of this was observed: when any given impulse hits, hinges are present and some of the blocks are separated, so impacts immediately occur which dissipate energy. Impacts are closely spaced and increase slowly in magnitude, so the inertia necessary to cause rocking failure is not generated until higher accelerations than expected. In contrast, the analytical model assumes the arch to be perfectly intact when the primary impulse occurs, and that energy is only dissipated during the single impact in which the hinges reflect, causing the stability to be underestimated.
- *High frequencies (≥ 8 Hz):* At high frequencies the arch did not fail by hinging and rocking, but instead failed due to vibration displacements between the blocks, as described by Meyer et al. (2007). Essentially, no single impulse was large enough to create failure due to a hinging mechanism, but the arch instead vibrated apart. The lack of hinging failure is predicted by the analytical model, as the load path never intersects the analytically predicted failure domain (Figure 5-13), but illuminates the fact that the failure domain does not incorporate vibration collapse. Although several tests were run, only one representative failure point is plotted because vibration failure is dependent on the duration of the vibration which cannot be visualized in Figure 5-13.

In general, applying multiple impulses with increasing amplitudes and a constant frequency instead of a single impulse had either a stabilizing effect or very little effect at all. Although this result was unexpected, it does not mean that multiple impulses could not have a detrimental effect. The rocking arch parallels the rocking block, in which the natural frequency of rocking decreases with the rocking amplitude (Housner, 1963). Thus, multiple impulses spaced at a

decreasing frequency would be more likely to act together to amplify the response, and lower the impulse magnitude necessary to cause collapse. These concepts are explored further in Chapter 6.

5.4 Towards an Assessment Criterion for Arches

Although the analytical model has been shown to be effective in predicting collapse, it is of little use if a prohibitive amount of work is required to obtain a first-order failure curve for each possible arch geometry. Thus, working towards an applicable tool for assessment of existing arches, the analytical model is used as a basis to develop a suite of failure curves which predict the stability of a wide range of arch geometries.

5.4.1 Derivation of the Assessment Criterion

The analytical failure curves in Figures 5-12 and 5-13 were developed by repeatedly running the analytical model for a range of impulse accelerations and periods. Because this is time-intensive, fitting an equation to the failure curve is attractive for repeated use. While several fitting methods were attempted, the following power curve which asymptotically approaches the experimentally measured minimum acceleration necessary to cause collapse (γ_{exp}) was most effective:

$$\frac{A_p}{g} = C_1\left(T_p - T_{min}\right)^{C_2} + \gamma_{exp} \tag{5.5}$$

where C_1, C_2, and T_{min} are fitting coefficients. The fitted curves for the two arch geometries tested are shown in Figure 5-14. For Arch1, C_1 = 0.00252, C_2 = -1.51, and T_{min} = 0.044. For Arch2, C_1 = 0.00674, C_2 = -1.18, and T_{min} = 0.060.

Once the fitted failure domain is obtained, it is convenient to use dimensional analysis to extend the failure domain to any scale. Initially, the physical variables of the analytical model can be used to write an equation of the form: $F(A_p, T_p, g, R_A, t_A, \beta_A, n_A) = 0$, where F is a function of the m previously defined variables. Note that the physical variables exist in only two fundamental dimensions: length and time. Hence, two dimensionally independent variables (T_p, R_A) are used to create five (m - 2) dimensionless products (π-terms) which represent the complete set of physical variables. For the analytical model to remain dimensionally homogeneous:

$$G\left(\pi_1 = \frac{A_p T_p^{\,2}}{R_A}, \pi_2 = \frac{g T_p^{\,2}}{R_A}, \pi_3 = \frac{t_A}{R_A}, \pi_4 = \beta, \pi_5 = n\right) = 0 \tag{5.6}$$

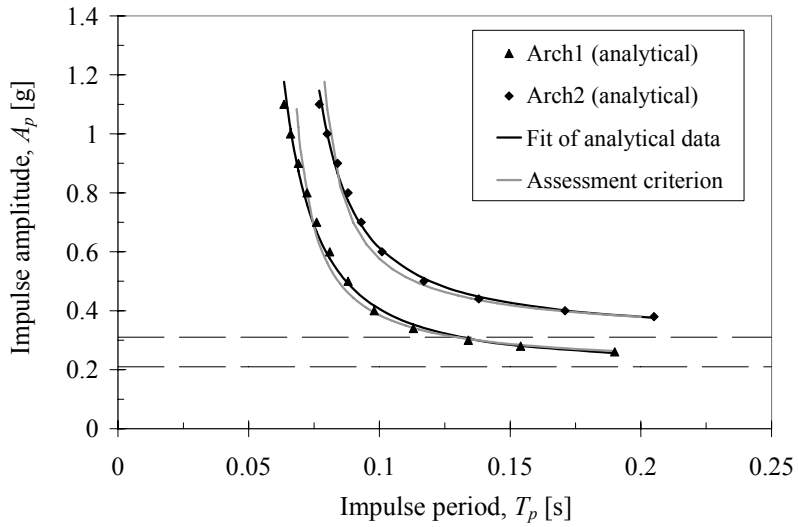

Figure 5-14: Comparison of the analytical failure points for Arch1 and Arch2 to the fitted failure curves (Equation 5.5) and the assessment criterion failure curves (Equation 5.8).

For complete similarity between scales, the dimensionless products in Equation 5.6 must remain constant at all scales. While π_3, π_4, and π_5 are unaffected by scale, π_1 and π_2 are affected. Using π_2, the known similitude requirement that the time must be scaled by the square root of the scale factor (Harris and Sabnis 1999) is derived:

$$T_{p,2} = T_{p,1}\sqrt{R_{A,2}/R_{A,1}} \tag{5.7}$$

where the subscript 1 indicates the original scale and the subscript 2 indicates the new scale. Note that Equation 5.7 also fulfills the similitude requirement for π_1. This scaling relation was also mentioned in §5.2.2, by Housner (1963) for the rocking block, and by Oppenheim (1992) for the arch. While this scaling relation is expected, dimensional analysis clearly demonstrates that material properties (density, elasticity, strength, etc.) do not enter the problem, so no other scaling relationship is necessary.

Failure curves can now be calculated and fit at a single scale (R_A = 1 m), and then easily extended to any other scale. The following failure curve results:

$$\frac{A_p}{g} = C_1\left(\frac{T_p}{\sqrt{R_A}} - T_{min}\right)^{C_2} + \gamma \tag{5.8}$$

where R_A is the centerline radius in meters, T_p is in seconds, and C_1, C_2, and T_{min} are fitting coefficients which need to be defined.

Table 5.3: Coefficients C_1, C_2, T_{min}, and γ for use in Equation 5.8.

t/R		β_A [degrees]				
		140	150	160	170	180
0.12	C_1	0.040	0.030	0.018	0.008	-
	C_2	-0.69	-0.80	-0.92	-1.20	
	T_{min}	0.20	0.17	0.14	0.11	
	γ	0.42	0.32	0.23	0.14	
0.15	C_1	0.061	0.048	0.032	0.018	0.008
	C_2	-0.54	-0.59	-0.76	-1.00	-1.31
	T_{min}	0.28	0.26	0.21	0.16	0.11
	γ	0.55	0.43	0.33	0.24	0.14
0.18	C_1	0.082	0.063	0.050	0.032	0.018
	C_2	-0.41	-0.51	-0.57	-0.79	-1.04
	T_{min}	0.39	0.33	0.30	0.23	0.17
	γ	0.69	0.54	0.43	0.33	0.23
0.21	C_1	0.101	0.080	0.063	0.047	0.028
	C_2	-0.41	-0.42	-0.50	-0.64	-0.89
	T_{min}	0.48	0.41	0.35	0.28	0.22
	γ	0.82	0.65	0.52	0.41	0.31

Assuming that each voussoir encompasses an angle of five degrees (i.e. $n_A = \beta_A/5$), the fitting coefficients are dependent only on t_A/R_A and β_A, and are presented in Table 5.3. In the analytical model the voussoirs only act to discretize the problem by defining the possible hinge locations. Assuming too few voussoirs typically causes an overestimation of stability, and vice versa. Additionally, if a sufficient number of voussoirs results in failure curves which are relatively insensitive to increased refinement, typical of many discretization problems. Therefore, a relatively large number of voussoirs were chosen as conservative.

The failure curves which result from Equation 5.8 and Table 5.3 are also plotted in Figure 5-14 for the arches which were experimentally tested. These curves compare well with the failure curves generated using Equation 5.5, indicating that the scaling relation and the assumption of the number of voussoirs ($n_A = \beta_A / 5$) are effective.

5.4.2 Application of the Assessment Criterion

Using Equation 5.8 and Table 5.3, the stability of a part-circular arch during an expected ground motion can be predicted through the following procedure:

1. Measure the arch geometry and reduce the arch thickness to account for geometrical imperfections. A 20% reduction in thickness is recommended but a larger reduction is recommended if the arch is significantly deformed.

2. Using the reduced thickness, extract the appropriate values from Table 5.3 (interpolate if necessary) and apply Equation 5.8 to obtain the predicted failure curve.
3. Extract the primary impulse from the expected ground motion and compare. If the primary impulse falls above the curve, failure is predicted, and vice versa.

To illustrate the value of an assessment criterion based on dynamics instead of statics, consider two arches with radii of 1m and 5m, respectively, both with the following characteristics: $t_A/R_A = 0.18$ and $\beta_A = 170$ degrees. Assuming 80% of the arch thickness ($t_A/R_A = 0.144$), the failure curves for the two arches are plotted in Figure 5-15. Primary impulses from several major earthquakes in Turkey are also plotted for comparison (data obtained from the PEER NGA Database). An assessment criterion based on statics would predict that both arches would fail under all of these seismic events, but the failure curves based on dynamics predict otherwise.

While the presented failure curves provide a valuable first-order evaluation of masonry arches in seismic areas, further research is necessary before a robust assessment criterion can be developed. Specifically, the following issues must be addressed:

- While failure prediction was effective for small scale models, higher stresses during impact could lead to material failure in full size structures. The effect of impact damage on collapse is uncertain as increased damage could obviously decrease stability, but could also increase stability by dissipating more energy.
- Extraction of the primary impulse is particularly appropriate for near-source earthquake loading which can be described by a primary acceleration pulse. While this study showed that primary impulse extraction is also effective for predicting rocking-type collapse resulting from a variety of earthquake time histories, further research is needed to confirm this. Specifically, the possible amplification of response through critically spaced impulses must be evaluated. This is the impetus for Chapter 6.
- For long duration, high frequency base motion, an additional failure criterion based on vibration displacements should be considered.
- In reality, arches do not rest on rigid supports and support deformation must be considered. Arches which rest on highly deformable supports (e.g. an arch on tall buttresses) could be of significantly lower stability (see §7.2.3).

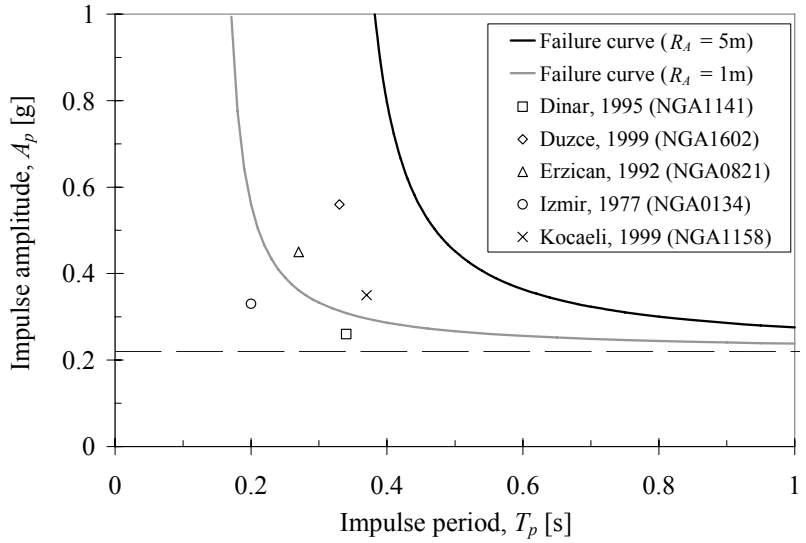

Figure 5-15: Predicted failure domains for two arches with radii (R_A) of 1m and 5m, both with $t_A / R_A = 0.18$ and β_A = 170 degrees, compared with primary impulses extracted from acceleration data from major earthquakes in Turkey (PEER NGA Database record number in parentheses).

5.5 Summary

The proposed analytical model presented in §5.2 and the experimental investigation discussed in §5.3 provide new insight into the dynamic behavior of masonry arches under base motion. Of primary importance, the rocking behavior of arches is described and modeled for the first time. Through this investigation, the following conclusions are drawn:

- For an arch subjected to a single horizontal base impulse, Mode I collapse governs, i.e. collapse during the second half cycle of motion, after a single impact has occurred. Therefore, the Mode `I failure curve should be used for design and assessment purposes.
- Larger scale arches are more resistant to ground motions than smaller arches with the same geometrical proportions. Additionally, for an arch of a given scale, the stability of the arch increases as t_A/R_A increases or β_A decreases.
- The minimum coefficient of friction theoretically required to prevent sliding is below the typical values of masonry joints, and hence the assumption of no sliding is reasonable.
- The primary impulse method, extracting the primary impulse of an acceleration record, provided accurate failure predictions for the arches tested. In the process, further evidence that rocking type structures are particularly vulnerable to impulse-type base motions was presented. Additionally, the acceleration magnitude and period of the

impulse were both shown to be critical in causing failure. Possible effects of multiple impulses were observed, and will be investigated further in Chapter 6.

The effectiveness of the analytical model in predicting experimental results led to the development of a suite of failure curves which predict the rocking stability of a range of masonry arch geometries (§5.4). While the failure curves accurately predicted failure of the small scale arches tested, application to full scale structures requires further research. Several areas of future research have been specifically identified, and could lead to a rapid assessment tool which would be of great utility for evaluating the safety of vaulted masonry structures around the world.

In conclusion, the characterization of rocking arch failure presented in this chapter exemplifies the merits of analytical dynamics as a tool for assessing masonry structures. If the essence of dynamic behavior can be captured by analytical models of reasonable complexity, then the method is appropriate and powerful.

Chapter 6

Analytical Modeling: Rocking Structures

6.1 Introduction

The rocking response to horizontal ground motion remains a concern in the seismic assessment of a variety of masonry structures: monuments, towers, statues, bridge piers, sculptures, etc. Chapter 5 adds the arch to this category, and inspires further investigation into the nature of rocking structures. Specifically, the evidence that the primary impulse is critically important for these structures beckons further inquiry into the ground motions to which rocking structures are most vulnerable. Despite a significant amount of research in this area, engineers still sometimes misunderstand the fundamental difference between the dynamic response of rocking structures and typical elastic structures, and therefore assess rocking from a flawed perspective. As a result, the fundamental behavior of rocking structures needs further clarification.

As mentioned in §2.3.1, the seminal work on the rigid rocking block by Housner (1963) first addressed the behavior of rocking structures, introducing a problem which has since attracted widespread interest. Housner (1963) showed that the natural rocking period increases with rocking angle, and evaluated the vulnerability of rocking structures to single square and sine pulses. He also demonstrated overturning through multiple successive pulses by generating earthquake motions as discrete step changes $\pm v$ in ground velocity and evaluating the probability

of collapse. He concluded that "…relatively small ground motion may fortuitously build up the amplitude… and lead to overturning the block."

This chapter addresses the response of rocking structures to horizontal ground motion from a similar rigid body dynamics perspective. Building on the work of Makris and Konstantinidis (2003), the goal is to further highlight the fundamental differences between rocking structures and typical elastic structures, and to explore ground motions which would cause the maximum amplification of rocking motion, or *rocking resonance*. To achieve this, an energy approach is taken, where the primary concern is the rate of energy input in the system.

In §6.2, the mathematical formulation for the rocking block is first presented, and the rate of energy input into the system is evaluated. Subsequently, the response of rocking structures which are not at rest but have some initial motion or energy is investigated. The motivation for this is twofold: 1) to explore the idea that at-rest stability is unconservative and unreliable if small initial motions are generated during earthquakes, an idea which has not been considered in the literature, and 2) to explore the ability of multiple impulses to amplify the rocking response, a behavior which has not been directly addressed since it was suggested by Housner (1963). In §6.3, a method of generating earthquake time histories using past earthquake data is presented and applied to statistically determine the probability of collapse of the rocking block and the rocking arch. In §6.4, conclusions are drawn.

6.2 An Energy Approach

Investigation of the fundamental behavior of rocking structures begins with the rocking block. Following the work of Housner (1963), it is assumed that a rigid block rocks back and forth about alternating bottom corner hinges (points O and O' in Figure 6-1). The resulting motion can be described by two dimensionless non-linear equations:

$$\begin{aligned} \theta'' + \sin\left(\theta_{cr} - \theta\right) &= -\left(\ddot{u}_g / g\right)\cos\left(\theta_{cr} - \theta\right) \quad for \quad \theta > 0 \\ \theta'' + \sin\left(-\theta_{cr} - \theta\right) &= -\left(\ddot{u}_g / g\right)\cos\left(-\theta_{cr} - \theta\right) \quad for \quad \theta < 0 \end{aligned} \tag{6.1}$$

where θ_{cr} and θ are defined in Figure 6-1, $\ddot{u}_g$ is the ground acceleration, g is the acceleration of gravity, and $\theta'' = d^2\theta / d\tau^2$ where $\tau = t\sqrt{3g/(4R_B)}$ is the dimensionless time. The transition between the equations of motion in Equation 6.1 occurs when the block passes through the rest position ($\theta = 0$) and the rotation point jumps to the opposing bottom corner. This transition is accompanied by a decrease in energy due to impact, often described by a coefficient of

restitution, defined with respect to the total energy (E_T) or the rotational velocity ($\theta' = d\theta / d\tau$) before and after impact:

$$c_v = \frac{\theta'_{after}}{\theta'_{before}} \quad \text{or} \quad c_E = \frac{E_{T,after}}{E_{T,before}}, \text{ where } c_E = c_v^2 \tag{6.2}$$

Housner (1963) estimated the amount of energy dissipated at impact by assuming conservation of angular momentum about the post-impact rotation point, yielding a coefficient of restitution dependent solely on geometry:

$$c_E = \left[1 - \frac{3}{2}\sin^2\theta_{cr}\right]^2 \tag{6.3}$$

While more complex impact formulations could be readily implemented into this framework, Equation 6.3 will be used throughout this study. The goal of this work is not to redefine impact but to understand the fundamental behavior of rocking structures. If the initial conditions are known, Equations 6.1 and 6.3 completely describe the motion of the rocking block. These nonlinear equations were solved numerically using Matlab (2002).

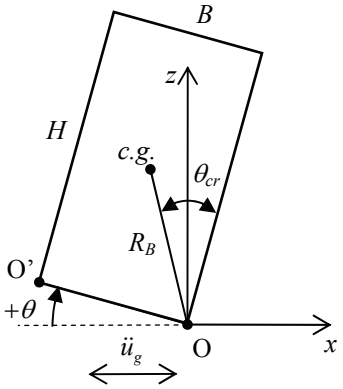

Figure 6-1: Rocking block geometry.

6.2.1 Rate of Energy Input

Using the rocking block formulation above, the fundamental behavior of rocking structures can be investigated. To start, failure is defined by rocking motion which causes overturning collapse. In order for this to occur, enough energy must be added to the system to make it unstable, so the rate of energy input is of fundamental interest. Starting from the equations of motion (Equation 6.1), the rate of energy input due to horizontal ground motion is derived as:

$$\frac{dE_T}{d\tau} = -m_B R_B \ddot{u}_g \theta' \cos(\theta_{cr} - \theta) \quad for \quad \theta > 0$$
$$\frac{dE_T}{d\tau} = -m_B R_B \ddot{u}_g \theta' \cos(-\theta_{cr} - \theta) \quad for \quad \theta < 0 \tag{6.4}$$

where m_B is the mass of the block and R_B is defined in Figure 6-1. Equation 6.4 reveals that the rate of energy input changes with $\ddot{u}_g$, θ', and θ. However, only $\ddot{u}_g$ and θ' can be negative, so the ground acceleration ($\ddot{u}_g$) must be of opposite sign as the current angular velocity (θ') for energy to be added to the system, otherwise energy is removed. This seemingly trivial solution has relevant implications.

To determine the types of ground motion to which rocking structures are most vulnerable, the ground motion will be optimized to maximize the energy input. Because all ground motions are not feasible, consider the single constraint that the absolute value of the ground acceleration cannot exceed a given value ($\pm a_g$). Optimization of the ground motion is achieved numerically in each time step, effectively solving:

$$\ddot{u}_g{}^{opt} = \max\left\{ \int_t^{t+\Delta t} -m_B R_B \ddot{u}_g \theta' \cos(\theta_{cr} - \theta)\, dt \right\} \quad for \quad \theta > 0 \tag{6.5}$$

For a given block geometry and initial conditions ($\theta_0 = \theta(0)$, $\theta_0' = \theta'(0)$), the optimized ground motion and the maximized *rocking resonance* response are shown in Figure 6-2. The optimized ground motion always has a magnitude equal to the constraint value (a_g), and is always opposite in sign to the angular velocity. The result is a step function which alternates between $\pm a_g$ at a time spacing which increases as the rocking angle increases. This is expected, as Housner (1963) showed that the free rocking period increases with increasing rocking angle.

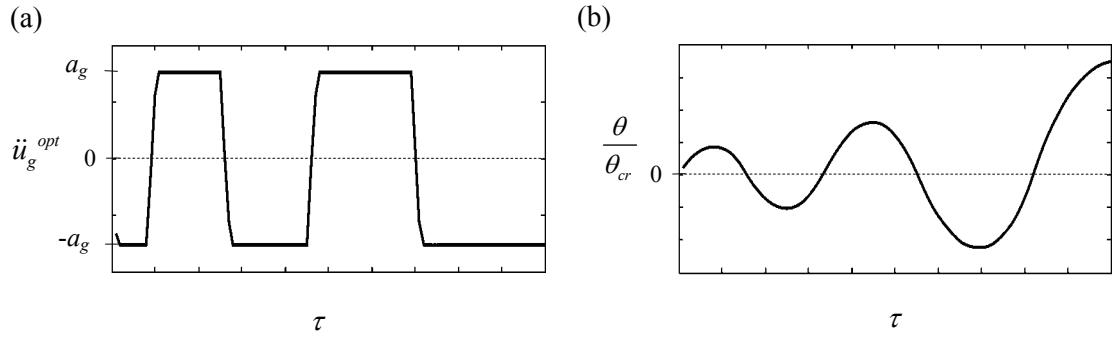

Figure 6-2: Results of maximizing energy input: (a) optimized ground motion and (b) resulting maximum block response.

Figure 6-2 depicts a fundamental difference between rocking structures and typical elastic structures: rocking structures don't have a fixed natural frequency and therefore cannot be forced at a single frequency which causes resonance and maximizes their response. Instead, rocking resonance would occur for sinusoidal ground motions with an optimized continuously increasing period. As a result, the response of rocking block structures to single frequency harmonic ground motions is somewhat irrelevant when trying to determine the worst case response to earthquake motion.

6.2.2 Initial Energy

From rest, rocking motion, and therefore rocking collapse, is typically assumed to be impossible if the horizontal ground acceleration remains below γ (Equation 3.2). This means that the inertial overturning moment must exceed the self-weight restoring moment for rocking to commence. Otherwise, the block translates laterally with the ground with no rotational energy, making rotational amplification impossible. While this is theoretically true, it may not be a conservative assumption. If the block or the ground is not perfectly rigid (in reality they are not), or if the block is not of perfect geometry (in reality it is not), then a slight amount of rocking motion could be generated at lower values of horizontal acceleration. Additionally, once rocking energy exists, rotational energy can be added to the system (Equation 6.4) by any magnitude of ground motion, including ground accelerations well below γ. As a result, it is worthwhile to investigate the effect of a slight amount of initial rotational energy on the response.

To begin, the minimum magnitude of ground acceleration necessary to cause collapse of a rocking structure is redefined as a function of the initial energy. To do this, an initial energy is prescribed and the ground motion is optimized to yield the maximum response, as demonstrated in §6.2.1 and Figure 6-2. The optimized ground motion always adds energy to the system and the rocking impact is the only source of energy dissipation. Therefore, provided that the total energy input between impacts exceeds the energy dissipated at impact, collapse will eventually occur.

The minimum ground acceleration for which rocking collapse is possible is plotted in Figure 6-3 as a function of the initial energy and block geometry. This plot was generated by repeatedly running the analytical model for an array of block aspect ratios (B / H) and initial energies (θ_o / θ_{cr}). For each pair of these variables, the constrained magnitude of acceleration ($\pm\ a_g$) was increased between individual analyses until the energy added between impacts is greater than the energy dissipated between impacts, indicating eventual overturning.

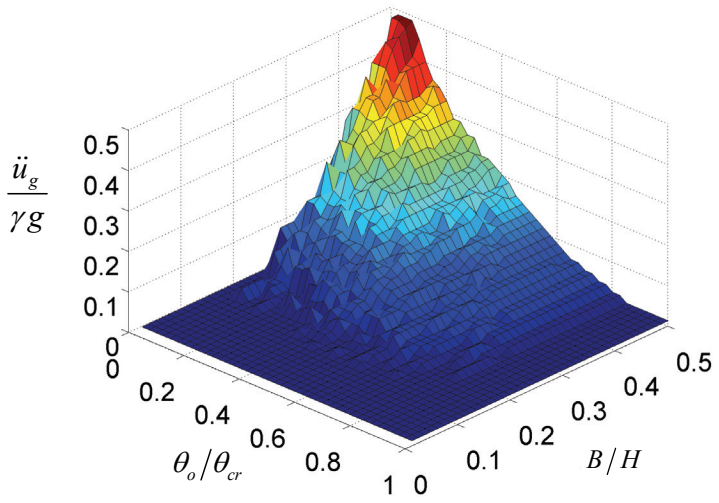

Figure 6-3: Minimum ground acceleration necessary for collapse through optimized rocking amplification.

Slender blocks dissipate less energy at impact than stocky ones, and the optimized ground motion always inputs energy into the system, so slender blocks could theoretically collapse at much lower acceleration magnitudes. Similarly, having more initial energy creates more time between impacts, and therefore more energy input between impacts, so a lower acceleration magnitude could cause collapse. However, notice that even for relatively stocky blocks (B / H = 0.5) with a relatively small amount of initial energy ($\theta_o / \theta_{cr} \approx 0.1$), the block could theoretically overturn at a value of $\ddot{u}_g/(\gamma g)$ of approximately 0.5. In other words, overturning could occur at 50% of the ground acceleration at which rocking is typically assumed to commence. In general, while ground motions which perfectly maximize rocking response are extremely unlikely, Figure 6-3 demonstrates that amplification of slight amounts of initial rotational energy can theoretically cause collapse for acceleration magnitudes lower than typically considered.

6.2.3 Multiple Sinusoidal Impulses

Prescribing initial energy can also give insight into the response of a rocking block to multiple impulses. The ability of a given impulse to add energy to a system already in motion is dependent on the relationship between the impulse duration, the current natural rocking period (T_n), and the time at which the impulse hits. The relative energy added to a rocking block ($B = H /$ 4 = 0.1m) by a single sinusoidal impulse is shown in Figure 6-4.

Figure 6-4a demonstrates that if the impulse period is significantly less than the current natural rocking period (T_n / 4), then there is approximately a 50% chance of either adding or subtracting energy from the system, depending on when the impulse hits with respect to the

rocking motion. However, longer period impulses nearly always add energy to the system, regardless of when they occur with respect to the rocking motion, indicating that the rocking response detrimentally aligns itself with the ground motion. Accordingly, the relative energy increase is much greater as the impulse period increases. Furthermore, Figure 6-4b shows that for initial maximum rocking angles from θ_{cr} /16 to θ_{cr} /2 (which correspond to different amounts of initial energy) the *relative* change in energy is approximately the same.

Based on these results, the effect of multiple impulses is qualitatively determined. If a sinusoidal impulse occurs which has a period much greater than T_n, then energy is injected and rocking increases. However, as the rocking period increases and becomes large with respect to the impulse period, the chance of future impulses removing energy from the system increases. Furthermore, as the natural rocking period increases with the maximum rocking angle, identical discrete impulses would have to be spaced at increasing time intervals to maximize amplification of motion, and the rate of energy input would decrease as amplification proceeds.

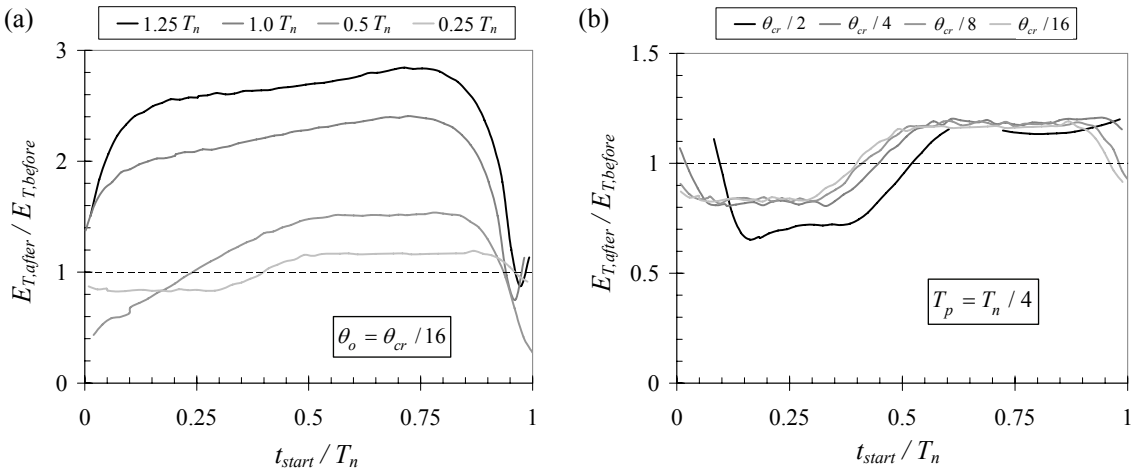

Figure 6-4: Change in energy with respect to the sinusoidal impulse start time normalized by the initial natural rocking period (t_{start} / T_n) for different: (a) impulse periods, T_p, and (b) initial rotation angles, θ_o.

6.3 A Statistical Approach

The previous section showed that the response of a rocking block to multiple impulses is extremely sensitive to the spacing and duration of each impulse. As a result, it is impossible to predict the exact response of a rocking block to a possible earthquake, which is essentially a collection of consecutive impulses with extremely different characteristics. Therefore, a statistical assessment method is necessary.

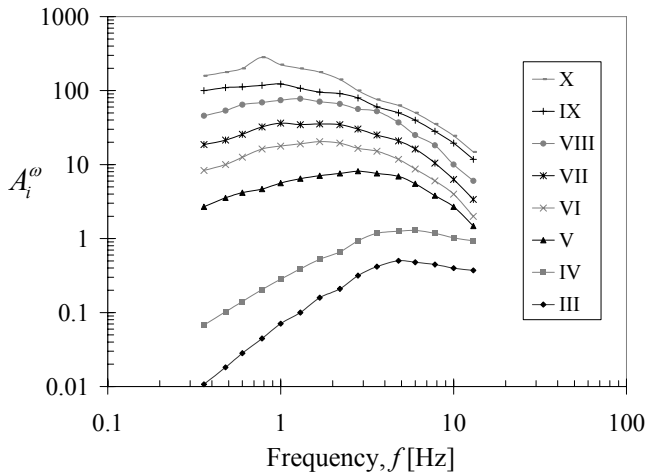

Figure 6-5: Mean spectral amplitude (A_i^ω) for different earthquake intensities (MMI) (after Sokolov 2002).

6.3.1 Earthquake Generation

For statistical assessment, an alternative method of generating expected ground motions will be presented and employed. Sokolov (2002) compiled data from about 1,150 earthquake records and developed frequency spectra for different earthquake intensities (MMI), as shown in Figure 6-5. It is interesting to note that increasing earthquake intensity yields a drastic increase in low frequency energy, to which rocking structures are particularly vulnerable.

The data presented by Sokolov (2002) allows the generation of acceleration time histories of expected intensity earthquakes:

$$a_{total}(t) = \sum_{i=1}^{15} A_i^\omega(\Delta\omega)\sin\left(\omega_i t + \phi_i^\omega\right) \tag{6.6}$$

where $\Delta\omega$ is the frequency step, A_i^ω is the mean spectral amplitude (see Figure 6-5), ω_i is the corresponding frequency, and ϕ_i^ω is the unknown corresponding phase angle. Using the data in Figure 6-5 and Equation 6.6 an earthquake is generated assuming: 1) a uniformly distributed random phase angle ($0 \le \phi_i^\omega \le 2\pi$) for each frequency in the spectrum, and 2) a specified earthquake duration (t_d) obtained using the following arctangent window:

$$P(t) = \frac{1}{\pi}\left[\arctan\left(\frac{t-t_0}{0.1}\right) - \arctan\left(\frac{t-t_{end}}{0.1}\right)\right] \tag{6.7}$$

where t_0 is the start time of the earthquake, t_{end} is the end time, and $t_d = t_{end} - t_0$. The earthquake ground motion then results from Equations 6.6 and 6.7:

$$\ddot{u}_g(t) = a_{total}(t)P(t) \tag{6.8}$$

While this relatively simple method of earthquake generation was developed independently, similar methods were subsequently found in the literature. In fact, a common group of methods for generating earthquakes is based on Equation 6.6 (Gasparini and Vanmarcke 1976). In these methods, the uniformly distributed random phase previously mentioned is also typically prescribed, but methods for estimating the intensity function, *P(t)* (i.e. the transient character of the earthquake), and the mean spectral amplitude (e.g. Figure 6-5), vary significantly. Gasparini and Vanmarcke (1976) provide a brief overview of other intensity functions, *P(t)*, and then discuss in detail a method for generating the 'spectral density function' (directly related to the 'mean spectral amplitude'). One of the intensity functions referenced was developed by Hou (1968). Hou estimated *P(t)* as a function of the earthquake magnitude, distance from the source, and the type of source (point -vs- line). This results in a trapezoidal intensity function which is site specific.

For the purpose of understanding fundamental behavior, Equations 6.6 to 6.8 will be used in the following sections. However, if this framework is to be applied for a specific application with specific site characteristics and different known measures of expected ground motion, then other methods for generating earthquakes might be appropriate (e.g. Gasparini and Vanmarcke 1976, Hou 1968), and could be directly implemented.

6.3.2 The Rocking Block

Example generated earthquakes and the resulting analytical model predictions of rocking motion are shown in Figure 6-6 for a block of geometry $B = H / 4 = 0.1$ m with initial conditions $\theta(0) = \theta_{cr} / 32$ and $\theta'(0) = 0$. While the generated earthquakes appear similar, they result in block overturning in two cases and block recovery in two cases, despite the fact that their source is the same frequency spectrum. Therefore, the random phase must yield the larger impulses observed in the first two earthquakes which appear to cause overturning. Furthermore, Figure 6-6 indicates significant amplification of rocking motion under accelerations less than $\gamma = 0.25$ g.

Extending these results, the stochastic response of a rocking block to an earthquake is obtained by determining the rocking response to 1000 generated earthquakes of a given intensity (MMI) and duration (t_d), which only differ in their randomly generated phase. The histograms in Figure 6-7 show the probable rocking response.

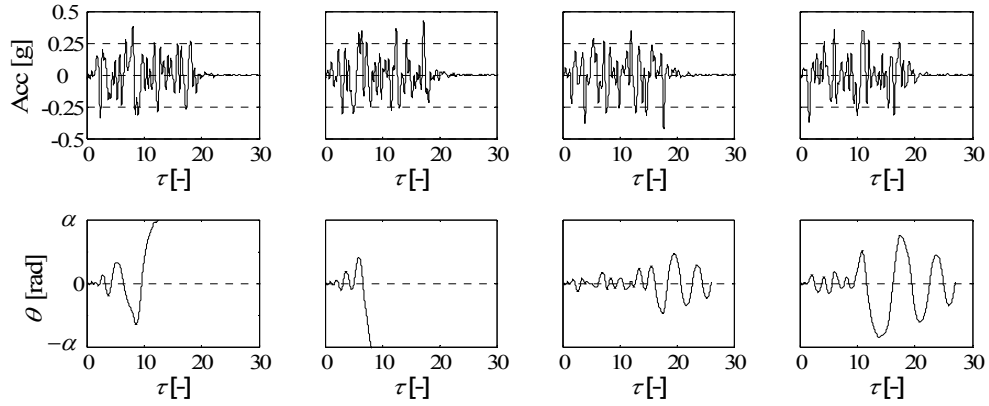

Figure 6-6: Generated earthquake ground motions (MMI = 6, t_d = 3 s) and the resulting rocking block responses ($B = H/4 = 0.1$ m, $\theta(0) = \theta_{cr} / 32$).

(a)

Property	Default value
B	0.1 m
B / H	1 / 4
θ_{cr}	0.245 rad
θ_o	$\theta_{cr} / 32$
t_d	6 s
MMI	5

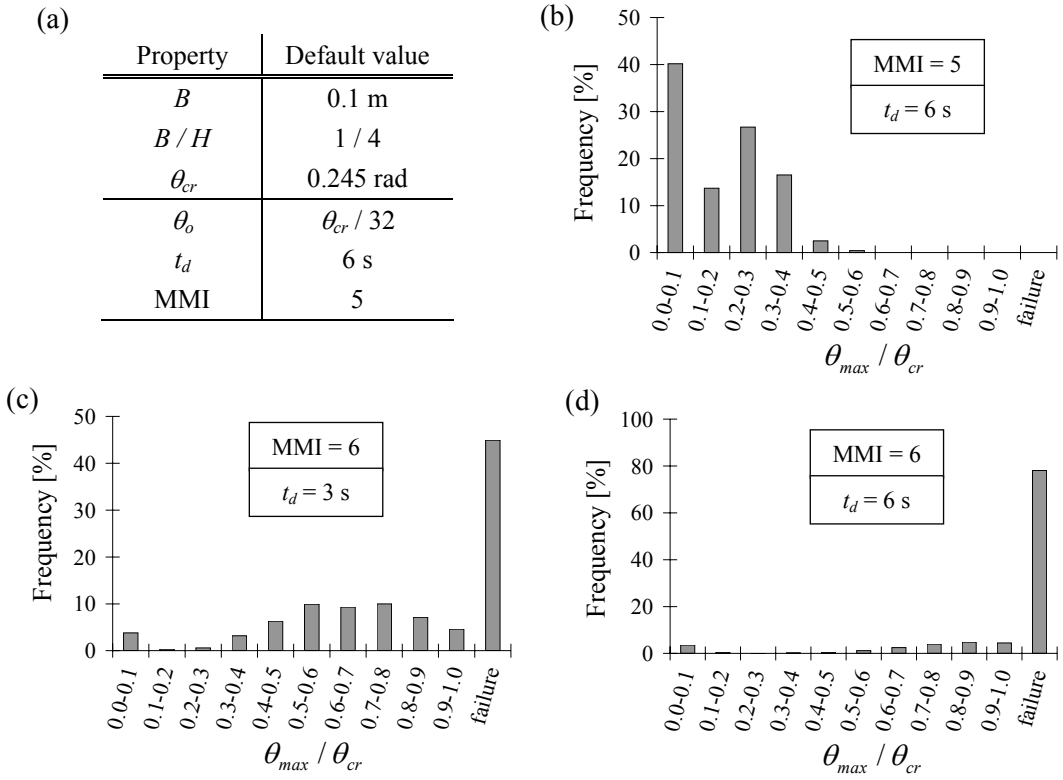

Figure 6-7: Histograms showing the probable maximum rotation angle for earthquakes of varying intensity (MMI) and duration (t_d).

In Figure 6-7, each histogram demonstrates the variability in rocking response to earthquakes with exactly the same frequency content. In Figure 6-7c, the maximum rotation angle varies from $\theta(0) = \theta_{cr} / 32$ to complete collapse. The sensitivity of the statistical response to different earthquake characteristics is also evident in Figure 6-7. As expected, increasing the earthquake

intensity from MMI = 5 to MMI = 6 causes a drastic increase in the probability of collapse. Perhaps less predictable, however, is the increase in failure probability from ~45% to ~80% when the earthquake duration (t_d) is increased from 3 to 6 seconds. It makes sense that a longer duration allows more impulses to amplify the response, further evidence of the time dependence of the response.

To more thoroughly evaluate the time dependence of the response, the average maximum rocking angle in response to an earthquake of intensity MMI = 5 is plotted as a function of t_d in Figure 6-8. Observe that $\theta_{max} / \theta_{cr}$ increases with the duration up to approximately 9 seconds, and then levels off. The impulses initially act to amplify the response because they are relatively long with respect to the current rocking period. However, after some amount of amplification has occurred and the impulses are short with respect to the rocking period, further increasing the duration has little effect.

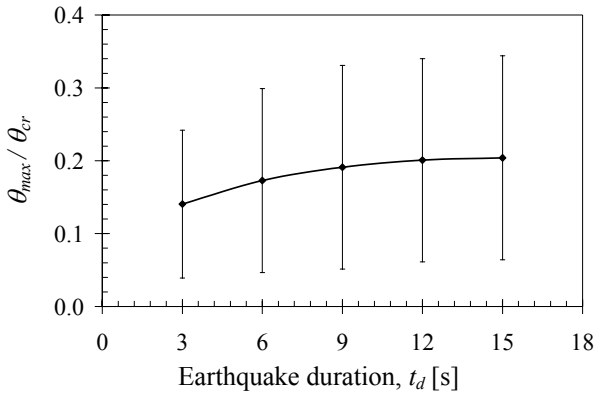

Figure 6-8. Average maximum rocking angle and standard deviation (1000 simulations / point) in response to an earthquake of intensity MMI = 5 ($B = H/4 = 0.1$ m, $\theta(0) = \theta_{cr} / 32$).

6.3.3 The Rocking Arch

To demonstrate how this work can be extended to predict rocking behavior of more complicated structures, consider the rocking arch model presented in §5.2. Using the procedure described above for the rocking block, the probable response of an arch can be calculated and is shown in Figure 6-10. (Note that ϕ_{cr} is the arch equivalent to θ_{cr} for the rocking block). Again, the extreme variability in response further demonstrates that the frequency content is not of primary interest for rocking structures. Instead, single large impulses or multiple amplifying impulses cause failure to occur. However, the frequency spectrum presented by Sokolov (2002) may still be useful for determining the likelihood of an earthquake of an expected intensity having an impulse signature capable of overturning a block.

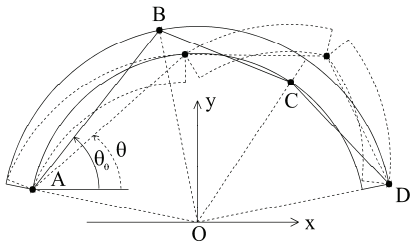

Geometry	R_A	1.0 m
	t_A/R_A	0.15
	n_A	14
	ϕ_{cr}	0.15 rad
Loading	MMI	7
	t_d	3 s
	ϕ_o	ϕ_{cr} / 16

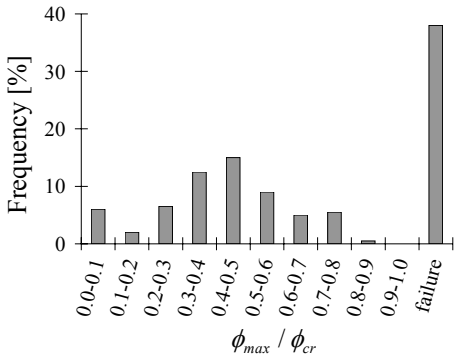

Figure 6-10. Rocking arch geometry and resulting probable maximum rotation angle ($\phi = \theta_o - \theta$) for an earthquake of MMI = 7.

6.4 Summary

This work demonstrates that the rocking response of structures under earthquake loading is fundamentally a time dependent problem. At least some consideration of the rocking response should be made when assessing historic masonry structures, statues, pedestals, and monuments, instead of solely considering a typical response spectrum analysis based on the elastic natural frequencies of the structure. More specifically, this work extends the understanding and assessment of rocking structures as follows:

- If a slight initial energy is considered, rocking collapse can occur under accelerations which are even lower than what is required to initiate rocking motion from the at-rest condition, and much lower than previous authors have considered.
- Multiple impulses can have an amplifying effect on the rocking motion. However, the amplifying capability is extremely sensitive to the spacing, magnitude, and duration of subsequent impulses.
- Generation of earthquake time histories using the wealth of past earthquake data collected by Sokolov (2002) provides an effective method to statistically determine the response of rocking structures to earthquakes of expected intensities. Such an approach is imperative when attempting to quantify possible amplification of motion due to chaotic earthquake ground motions which contain multiple consecutive impulses.

These conclusions, reached by considering the rate of energy input due to horizontal ground motion, provide a new perspective by which rocking structures can be better understood and assessed. Additionally, the framework of analytical dynamics illuminates characteristics of the rocking response which can be expected for dry-stone masonry structures. These characteristics should be kept in mind when applying the numerical modeling tools presented in Chapter 7.

Chapter 7

Discrete Element Modeling

7.1 Introduction

The previous two chapters have investigated the use of analytical models in assessing masonry structures under horizontal ground motion. While these analytical models are effective in predicting response, and provide valuable insight into the nature of the dynamics of rocking structures, they are rather involved for relatively simple structures and require significant simplifying assumptions. Developing similar models for more complex masonry structures would be unrealistic, signifying the need for computational tools which can accurately address problems involving multiple block dynamics.

Finite Element Modeling (FEM) is the computational tool of choice for most structural engineers, but it is optimal for problems of elasticity and strength, not stability. As a result, when linear elastic FEM is applied to masonry structures, results are often completely misinterpreted. High tensile stresses resulting from static loads or modal analysis are assumed to indicate cracking due to material failure, and the structure is determined to be unsafe. When, in reality, the structure might be perfectly stable, not relying on its tensile capacity for stability. Advances in finite element modeling have made them more appropriate for masonry structures (e.g. Chapter 4), but Discrete Element Modeling (DEM) inherently captures the discontinuous nature of masonry and allows for fully dynamic analysis with large displacements. As a result, DEM has the potential to provide greater insight into the collapse of masonry structures due to instability.

As discussed in Chapter 2, the application of DEM to masonry structures has increased in recent years. However, rigorous investigation into the accuracy of the method when applied to rigid body dynamics is still lacking. Further validation is necessary before these methods can be used with confidence. Thus, the primary goals of this chapter are to: 1) assess the ability of DEM to predict the analytical and experimental results presented previously in this work, and 2) propose a rational method for defining modeling parameters for DEM of masonry structures. Both verification of accuracy and a consistent approach to defining modeling parameters would allow the modeling technique to be more widely applied to masonry structures in the future.

In §7.2, DEM is first reviewed and then applied to masonry structures of increasing complexity. Previous modeling results are compared to DEM results, and the sensitivity of results to assumed input parameters is critically evaluated. In the process, the capabilities and shortcomings of analytical and numerical modeling are observed. In §7.3, equations for defining DEM parameters are derived. In §7.4, these equations are employed to predict experimental results. Finally, §7.5 summarizes findings.

7.2 Discrete Element Modeling Applications

In this study, masonry structures were modeled with the discrete element method using the commercial program UDEC (Itasca 2004). While developed for the field of rock mechanics, UDEC is applicable to discontinuous systems in general. It allows finite displacements and rotations of discrete bodies, including complete detachment, and recognizes new contacts during progression of the analysis. Constitutive properties of blocks and contacts must be defined. Contact forces on each block are assumed to be proportional to the inter-penetration between blocks, which is determined using the input contact stiffness. The out-of-balance force after each time step is applied to the equations of motion in the next time step. UDEC uses an explicit, time-domain solution of the governing equations of motion (Cundall and Strack 1979, Itasca 2004).

Although deformable blocks could be considered, the masonry structures herein are modeled as assemblages of rigid blocks with frictional joints. The joint properties required for analysis are the shear stiffness, normal stiffness, cohesion, friction angle, tensile strength, and dilatancy angle. To be consistent with previous chapters in which analytical models and experiments dealt with dry-stone masonry, mortar will be neglected (i.e. the tensile strength, cohesion, and dilatancy angle of all joints was specified as zero). Additionally, a large coefficient of friction was initially specified to prevent any sliding and allow comparison with analytical modeling results. Subsequently, a more realistic friction angle was specified and sliding evaluated.

The joint stiffness properties are critical to this modeling framework, and correlating real material properties to joint stiffness properties can be challenging. Generally, two approaches are accepted. First, if deformable blocks are specified for modeling, the elasticity of the blocks is already taken into account, and the joint stiffness should be specified to represent actual joint properties. When mortar is present, the joint stiffness should approximate mortar properties; when mortar is not present, the joint stiffness should approximate the compliance of the asperities of the contacting surfaces. Second, if rigid blocks are specified for modeling, then the elasticity of all material should be lumped in the joints. This approach is taken in §7.3 and §7.4.

In this section, discrete element modeling results are compared to analytical modeling results for verification. Recall that the analytical models are purely based on rigid body dynamics and do not incorporate elasticity. Therefore, the joint stiffness necessary for DEM has no correlate in the analytical model, and is purely a "penalty stiffness". As a result, the joint stiffness should be specified to be as large as possible to minimize joint deformations and allow comparable results. Thus, when comparing DEM to analytical modeling results, the joint normal stiffness and shear stiffness were assumed to be 10^{12} Pa/m. The sensitivity of results to this assumption will be investigated.

When modeling dynamics, the damping properties are also critical. In UDEC, damping is applied in the form of Rayleigh damping:

$$\mathbf{C} = \alpha_R \mathbf{M} + \beta_R \mathbf{K} \tag{7.1}$$

where $\mathbf{C}$, $\mathbf{M}$, and $\mathbf{K}$ are the damping, mass, and stiffness matrices, respectively, α_R is the mass-proportional damping constant, and β_R is the stiffness-proportional damping constant. Rayleigh damping results in a critical damping ratio (ξ) which is dependent on frequency (ω):

$$\xi(\omega) = \frac{1}{2}\left(\frac{\alpha_R}{\omega} + \beta_R \omega \right) \tag{7.2}$$

Specifying appropriate damping can be difficult. Some damping must be specified in order to limit extremely high frequency vibrations which are typically damped out in real materials and can cause unrealistic bouncing in numerical simulations. At the same time, over-damping the response is typically unconservative, and should be avoided. Thus, in this section a minimal amount of damping is initially specified, and then the effect of both the mass-proportional and stiffness-proportional damping on results is investigated. The damping specified in this chapter, unless noted otherwise, is α_R = 6.28x10^{-5} and β_R = 1.59x10^{-4}. This results in a minimum damping ratio (ξ_{min}) of 0.01% at a frequency (f_{min}) of 0.1 Hz. These damping parameters result in

a damping ratio of less than 0.5% in the frequency range from 0.001 Hz to 10 Hz. A consistent way of specifying the damping is discussed in §7.3. Finally, although the material density is not necessary in the analytical models, it is necessary for DEM. A default material density of 2,000 kg/m^3 is assumed to approximate the density of masonry, but the material density is insignificant for the stability of rigid block structures under horizontal ground motion.

7.2.1 The Rocking Block

The first masonry structure addressed is the single rocking block on a rigid foundation. This problem serves as a good starting place for comparison of DEM and analytical modeling results. Block dimensions were 1 m wide by 4 m tall, resulting in a constant horizontal acceleration necessary for collapse of 0.25 g (Equation 3.2). The following horizontal harmonic ground acceleration was applied:

$$\ddot{u}_g = A_h \cos(\omega t) \tag{7.3}$$

where the acceleration amplitude A_h = 0.5 g, and the frequency ω = 10.88 rad/s (f = 1.72 Hz).

For analytical modeling, Equations 6.1 and 6.3 are used to determine the response of the rigid rocking block to the harmonic ground motion. Results are compared with DEM in Figure 7-1, where the block rotation angle θ (Figure 6.1) is plotted in the time domain. The results compare quite well, giving some confidence in the method. Note that while bouncing is prevented in the analytical model, it is possible using DEM and it can be difficult to detect from the rotation angle plot in Figure 7-1. However, bouncing did not occur in this simulation.

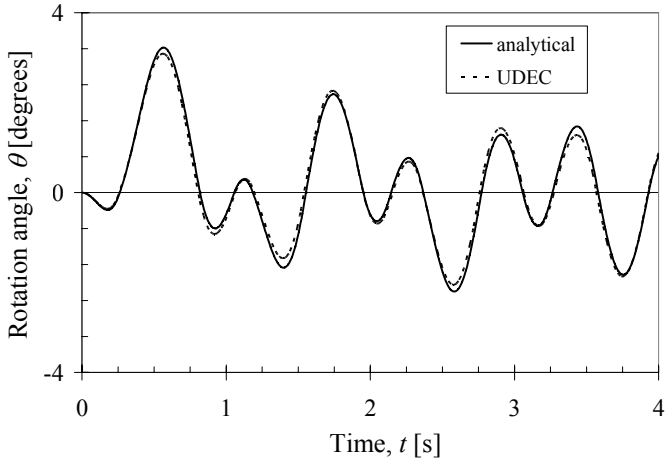

Figure 7-1: Comparison of the predicted rotation angle (θ, see Figure 6-1) of a rocking block on a rigid foundation using both UDEC and analytical rigid body dynamics.

Similar effectiveness of DEM was reported by Papantonopoulos (1997), who demonstrated good correlation between the solutions yielded by UDEC and analytical rigid body dynamics for a rocking block subjected to simulated earthquake ground motion. The results of Papantonopoulos (1997) show an independent verification for a similar problem. With good initial agreement for this problem, the robustness of the solution with respect to the input parameters can be investigated.

Effect of Damping

A range of different mass- and stiffness-proportional damping constants were applied (Table 7.1, Figure 7-2) and the rocking responses were compared. First, the mass-proportional damping was increased, which increases low frequency damping but has an extremely small effect on the high frequency damping, as shown in Figure 7-2. In Figure 7-3, a slight increase in mass proportional damping (UDEC II) shows a negligible difference in response with respect to the initial analysis (UDEC I). However, a further increase in damping (UDEC III) causes a noticeable difference in rocking response, and the highest level of damping (UDEC IV) causes a significant decrease in rocking amplitude (Figure 7-3), indicating that the response is over-damped.

The minimal mass-proportional damping initially specified had negligible effects on the results, but the over-damped response (UDEC IV) causes unconservative results. Additionally, mass-proportional damping is velocity dependent, and therefore does not make physical sense for rocking systems. Furthermore, it is not necessary for numerical stability or to prevent strange numerical behaviors in the rocking responses. Therefore, mass-proportional damping should either be extremely small or eliminated entirely.

Table 7.1: Different damping parameters used for rocking block simulations.

	Damping Constants		ξ_{min}	f_{min}	f_{crit}
	α_R	β_R	[%]	[Hz]	[Hz]
UDEC I	6.28×10^{-5}	1.59×10^{-4}	0.01	0.1	2,000
UDEC II	6.28×10^{-3}	"	0.1	1	2,000
UDEC III	0.628	"	1	10	2,000
UDEC IV	15.7	"	5	50	2,000
UDEC 1	6.28×10^{-5}	1.59×10^{-4}	0.01	0.1	2,000
UDEC 2	"	3.98×10^{-5}	0.005	0.2	8,000
UDEC 3	"	6.37×10^{-6}	0.002	0.5	10,000

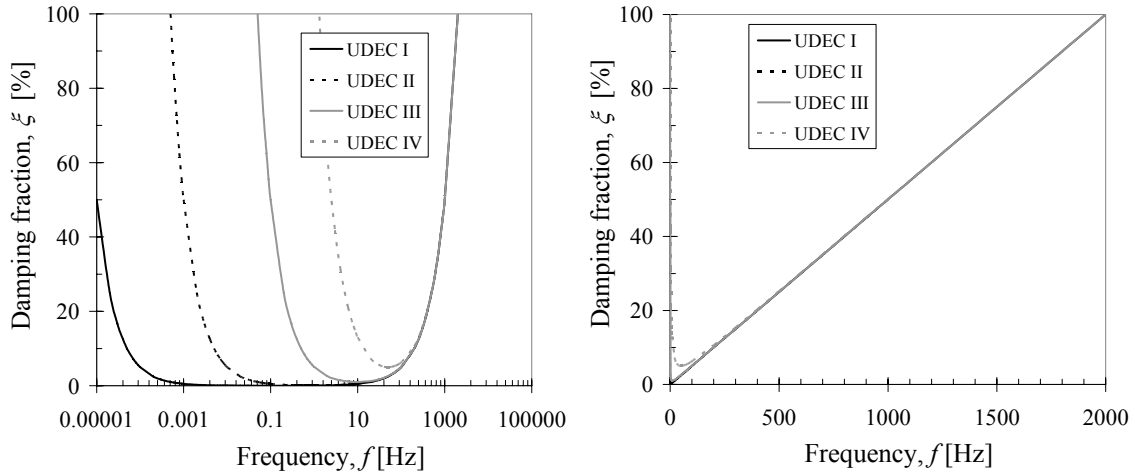

Figure 7-2: Frequency dependence of the fraction of critical damping (ξ) for a range of different mass-proportional damping constants (see Table 7.1).

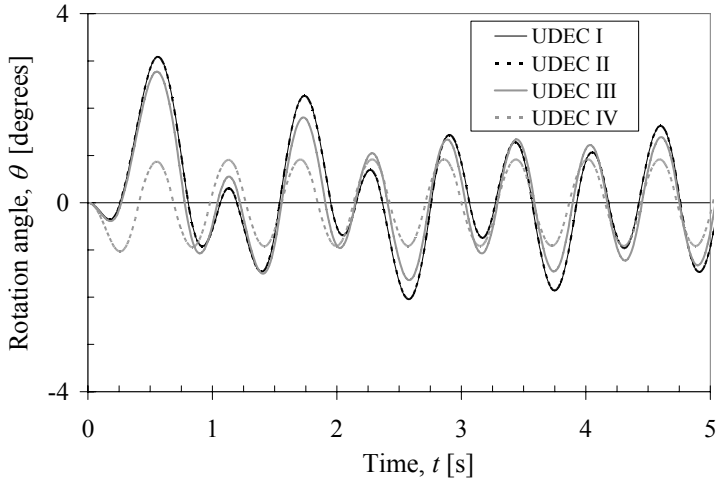

Figure 7-3: Comparison of the simulated rotation angle (θ) of a rocking block using UDEC with a range of mass-proportional damping constants (see Table 7.1).

Second, stiffness-proportional damping was decreased, which has no effect on low frequency damping but causes a decrease in high frequency damping, as shown in Figure 7-4. This causes a corresponding increase of the critical frequency (f_{crit}) at which the system is critically damped ($\xi = 100\%$). In Figure 7-5, comparison of the rocking response demonstrates that a slight decrease in stiffness-proportional damping (UDEC 2) causes the system to be under-damped. A further decrease in stiffness-proportional damping (UDEC 3) caused the block to bounce back and forth on its corners, evidenced by the sharp spikes in the rocking response (Figure 7-5). While airborne between bounces, the block translated large horizontal distances until ultimately overturning.

The results indicate that decreasing the stiffness-proportional damping too much prevents rocking-only motion. While bouncing may be realistic in some cases (e.g. short blocks, rubber blocks), it is not expected for tall slender blocks made of brick or stone. Thus, eliminating the stiffness-proportional damping entirely causes unrealistic numerical bouncing. This is supported by a wide range of research which has demonstrated that high-frequencies must be damped out to get physically reasonable results.

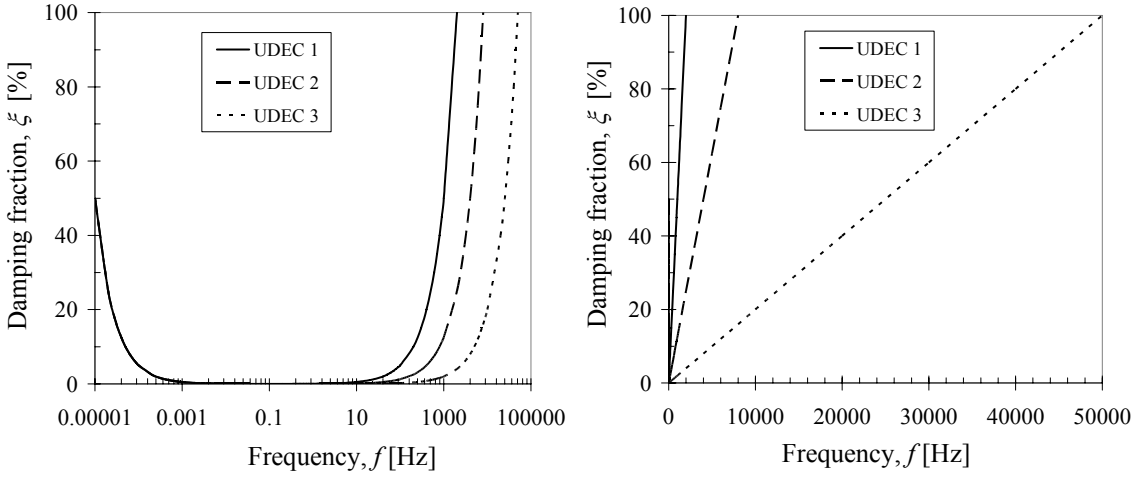

Figure 7-4: Frequency dependence of the fraction of critical damping (ξ) for a range of different stiffness-proportional damping constants (see Table 7.1).

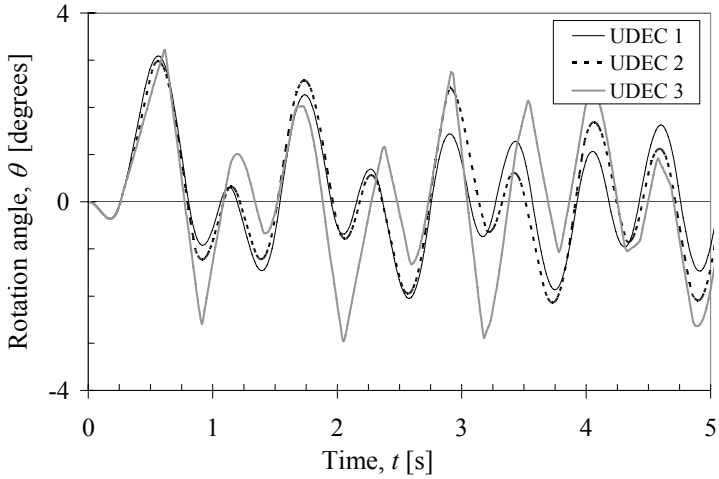

Figure 7-5: Comparison of the simulated rotation angle (θ) of a rocking block using UDEC with a range of stiffness-proportional damping constants (see Table 7.1).

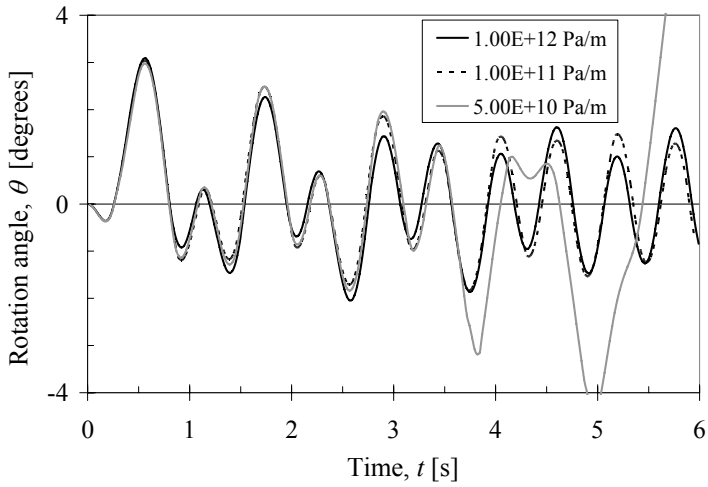

Figure 7-6: Comparison of the simulated rotation angle (θ) of a rocking block using UDEC with a range of joint stiffness values.

Effect of Joint Stiffness

A range of different joint stiffness values were also applied and the rocking responses were compared. The default damping parameters (UDEC I) were used. In Figure 7-6, the effect of reducing the joint stiffness is demonstrated (recall that the original joint stiffness used was 1.0 x 10^{12} Pa/m). For the initial reduction in joint stiffness (1.0 x 10^{11} Pa/m), very little difference in response is initially visible, but the rocking response is slightly over-estimated as rocking continues. For the lowest joint stiffness (5.0 x 10^{10} Pa/m), the rocking response is further over-estimated. The block begins bouncing and ultimately it overturns; the system is again under-damped.

The effective reduction in damping can be explained by the fact that Rayleigh damping is frequency dependent. The natural frequency of the system is dependent on the relationship between the mass and the stiffness. Reducing the stiffness decreases the amount of damping at the natural frequency. Thus, the relationship between the joint stiffness, damping, and mass of the system must be defined carefully to result in an appropriate level of damping. This concept will be more thoroughly addressed in §7.3.

7.2.2 The Arch

The arch analytical model presented in §5.2 is also used for comparison with DEM results. The same geometry (t_A/R_A = 0.15, β_A = 157.5º, R_A = 10 m, n_A = 7) and step impulse (see Figure 5-2 or Figure 7-7) investigated in §5.2 will be used. The rocking angles predicted by the two

modeling techniques are compared, followed by a comparison of the predicted failure domains. Finally, DEM modeling is used to re-evaluate the hinge assumptions of the analytical model, and investigate whether sliding failure is likely. Subsequently, the sensitivity of the results to the prescribed modeling parameters is investigated.

Predicted Rocking Motion

In Figure 7-7, the predicted DEM and analytical modeling rocking motions are compared. The applied impulses are shown in Figure 7-7a. The numerical (UDEC) results in Figure 7-7b are for a three-voussoir arch with the same hinge locations assumed for the analytical model. This was done to verify the accuracy of the analytical and numerical solutions for an identical geometry, and the results show excellent agreement. In Figures 7-7c and 7-7d, the numerical results for the actual seven-voussoir arch are plotted, and the agreement between the two curves is reasonably good, especially during the pre-impact phase.

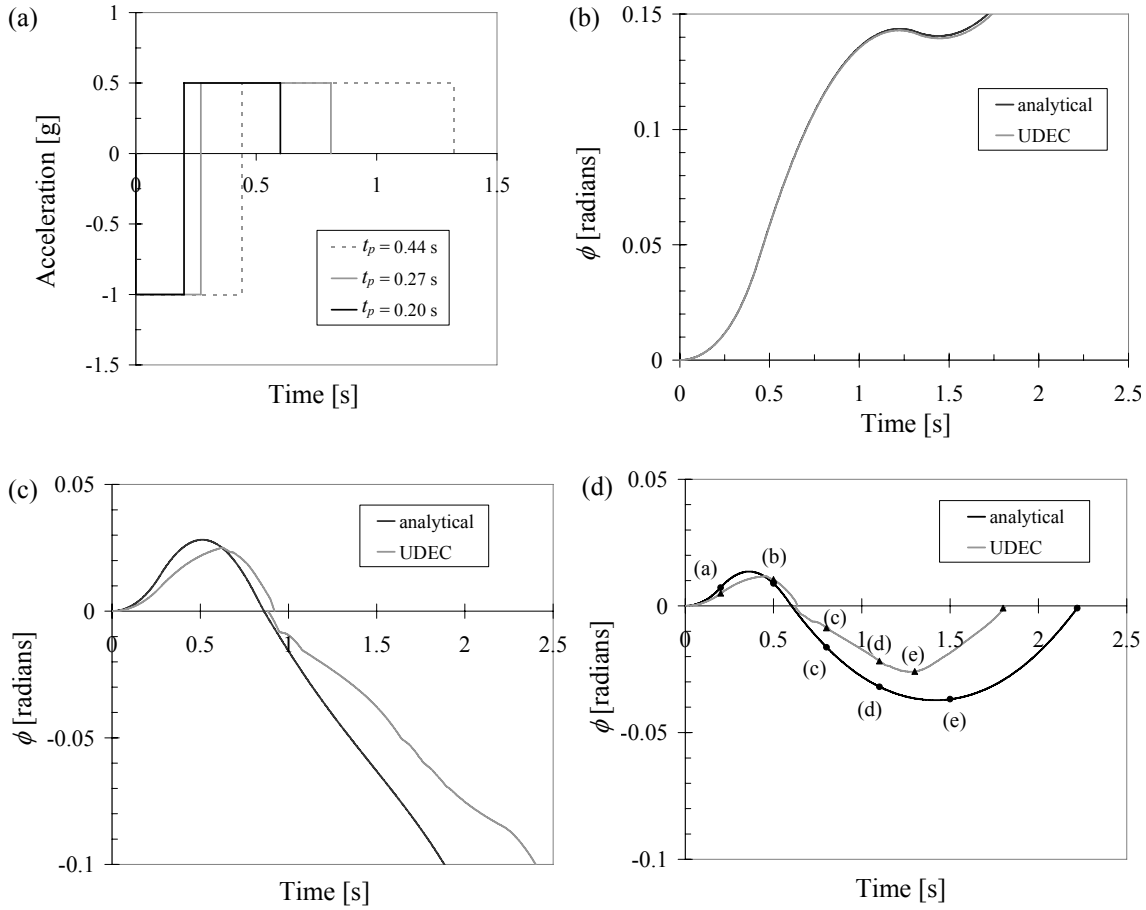

Figure 7-7: Predicted arch response using UDEC and analytical rigid body dynamics: (a) applied impulses; (b), (c), (d) rocking response, ϕ, for a_p = 1.0 g and t_p = 0.44 s, 0.27 s, and 0.20 s, respectively.

The discrepancy between analytical and numerical results comes from two primary sources. First, the hinge locations are not always the same in the two models due to the fact that hinge locations change more fluently in the numerical model. As a result, the location of the first hinge, which is used to measure ϕ, is not the same in both models. Therefore, the curves in Figures 7-7c and 7-7d do not provide a direct comparison between the methods, but rather an approximate comparison. Second, treatment of the impact conditions by the analytical and numerical models is based on different assumptions. The analytical model assumes a single distinct impact and is based on pure rigid body mechanics, whereas numerical modeling results in several impacts, which occur over a finite contact area having a finite stiffness. The energy dissipated during each of these impacts is governed by the specified Rayleigh damping.

Hinging and Impact Behavior

The two sources of discrepancy just mentioned, differing hinge mechanisms and damping properties, can be further evaluated by careful consideration of a single impulse test. In the process, the hinge assumptions of the analytical model can be further evaluated.

The predicted rocking angle to the impulse used for comparison (a_p = 1.0 g, t_p = 0.2 s) is shown in Figure 7-7d, where the points corresponding to the snapshots in Figures 7-8 and 7-9 are marked. Figure 7-8 shows the deformed configuration and the hinge locations using DEM, and Figure 7-9 shows the deformed configuration, the hinge locations, and the dynamic thrust line for analytical modeling (same as Figure 5-6).

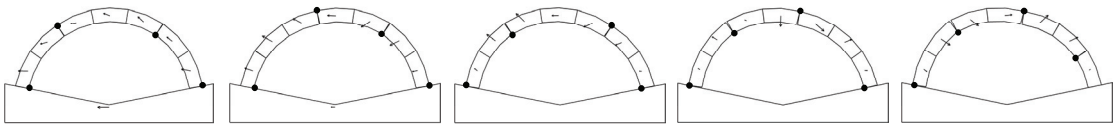

(a) (b) (c) (d) (e)

Figure 7-8: Hinge locations and block velocity vectors found using UDEC for a step impulse of magnitude 1.0g and duration 0.20 seconds at times (a) 0.20 s, (b) 0.50 s, (c) 0.80 s, (d) 1.10 s, and (e) 1.30 s.

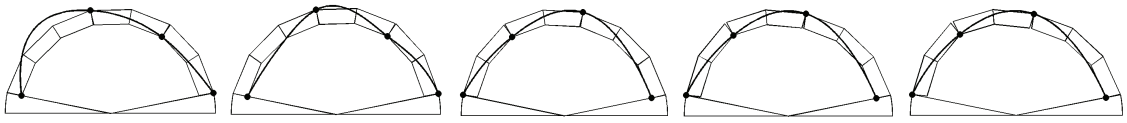

(a) (b) (c) (d) (e)

Figure 7-9: Hinge locations and dynamic thrust lines found using the analytical model for a step impulse of magnitude 1.0g and duration 0.20 seconds at times (a) 0.20 s, (b) 0.50 s, (c) 0.80 s, (d) 1.10 s, and (e) 1.50.

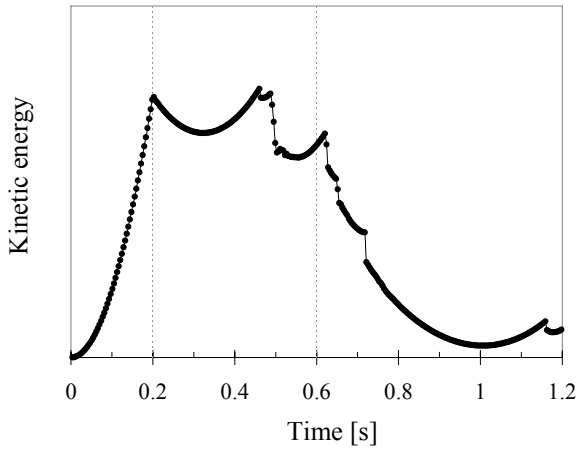

Figure 7-10: Kinetic energy in the arch for numerical modeling (UDEC) of the response to a step impulse (a_p = 1.0 g, t_p = 0.20 s).

In general, the arch motion predicted by UDEC (Figure 7-8) agrees with the basic rocking and hinging behavior predicted by the analytical model (Figure 7-9). In the first half cycle of motion during the first pulse (Figures 7-8a and 7-9a), the location of the second hinge given by the numerical model differs from that given by the analytical model. It is interesting to note that the dynamic thrust line drawn in Figure 7-9a exits the thickness of the arch at this time, predicting the location of the second hinge given by UDEC. On the other hand, in the first half cycle of motion but during the return pulse (Figures 7-8b and 7-9b), the hinge locations from the two models are the same. After impact, one of the hinges predicted by UDEC initially forms at a different location than predicted by the analytical model (0.80 s, Figures 7-8c and 7-9c), then all locations become identical (1.10 s, Figures 7-8d and 7-9d), and finally one hinge in the UDEC model changes location again (Figures 7-8e and 7-9e). This demonstrates that while the hinge locations change several times in the UDEC model, the hinge locations assumed in the analytical model appear to be appropriate "average" estimates of the hinge locations.

Investigation of the total kinetic energy of the arch further demonstrates the migration of hinges, and the corresponding dissipated energy. For the impulse response depicted in Figures 7-8 and 7-9, the total kinetic energy of the arch is plotted in Figure 7-10. The sharp drops reveal dissipated energy when blocks impact each other. The amount of energy dissipated by each impact is a function of the Rayleigh damping.

Failure Domains

For practical purposes, the most useful predictions are those concerning failure of the arch. Thus, discrete element modeling was repeated systematically to reproduce the Mode I and Mode

II failure domains previously discovered for the rocking arch (Figure 5-3). In Figure 7-11, the predicted analytical and numerical (UDEC) failure domains are compared. The agreement is excellent for the Mode II failure domain, where a three-voussoir arch is again used for UDEC modeling and no impacts occur. For Mode I failure, a seven-voussoir arch was again specified. The agreement between Mode I failure domains is also quite good considering the simplifications and assumptions which have been made. Moreover, predictions of the analytical model are conservative, primarily because DEM predicts that more kinetic energy is dissipated due to multiple impacts which occur during hinge location changes.

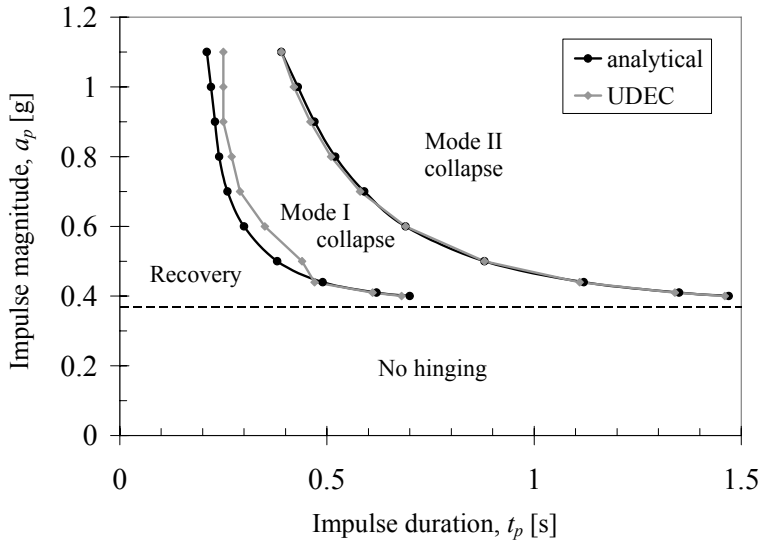

Figure 7-11: Resulting failure domains of Oppenheim's arch in response to an impulse function of duration, t_p , and magnitude, a_p , using both analytical and numerical (UDEC) modeling.

The slight divergence of the analytical and numerical Mode I failure domains (at an impulse magnitude of ~0.5 g in Figure 7-11) was similarly observed for several different arch geometries. This divergence is due to the fact that the number of different first half-cycle mechanisms, and therefore the amount of energy dissipated by first half-cycle hinge transitions, are limited for lower acceleration values, and therefore match analytical results better. However, for larger impulse magnitudes, UDEC predicts more significant first-half cycle hinge migration resulting in more energy dissipation, and therefore a higher failure domain.

Effect of Damping

The sensitivity of the Mode I failure domain (Figure 7-11) with respect to damping was evaluated with the damping parameters shown in Table 7.2 and Figure 7-12 (UDEC B represents

the initial damping ratio used in previous sections). Results are shown in Figure 7-13. In general, increased damping caused an increase in arch stability, especially for impulses of larger magnitude. For the three larger damping ratios tested (UDEC B-D), the damping had a relatively small effect on the failure domain, while the minimum damping ratio tested (UDEC A) caused a more pronounced decrease in stability.

Table 7.2: Different damping parameters used for rocking arch simulations.

	Damping Constants		ξ_{min}	f_{min}	f_{crit}
	α_R	β_R	[%]	[Hz]	[Hz]
UDEC A	3.14×10^{-6}	3.18×10^{-5}	0.001	0.05	10000
UDEC B	6.28×10^{-5}	1.59×10^{-4}	0.01	0.1	2000
UDEC C	6.28×10^{-4}	1.59×10^{-3}	0.1	0.1	200
UDEC D	6.28×10^{-2}	1.59×10^{-3}	1.0	1.0	50

The inset snapshot (Figure 7-13a) shows that decreased damping (UDEC A) caused relative displacements between stones which did not occur for the larger damping ratios tested. These relative displacements can not be a result of sliding because the specified friction was very large. The explanation is rather found in the fact that high frequency excitations can cause small inter-stone separations due to vibration that result in irreversible relative displacements of the stones (Meyer et al. 2007), i.e. *vibration displacements*. This behavior is similar to the bouncing behavior observed for the rocking block. However, instead of bouncing, each impact that occurs when hinge locations change causes a vibration response (which is restrained due to the thrust in the arch) at the natural frequencies of the system. The reduction in damping (UDEC B to UDEC A) causes vibrations large enough that blocks separate and impact each other. Thus, an increase in the critically damped frequency range from >2,000 Hz to >10,000 Hz appears to prevent the higher natural frequencies of the arch from being critically damped.

These high frequency vibration displacements could be physically realistic in certain cases, just as block bouncing could sometimes occur. However, in masonry structures, where high frequency vibrations are typically damped, vibration displacements are unlikely unless there is a significant high frequency component in the ground acceleration time history, and hence unlikely for the assumed impulse excitation. Regardless, the failure domain was not radically affected for the impulse which was applied, and the analytical model still provides an appropriate lower bound estimate of the failure domain.

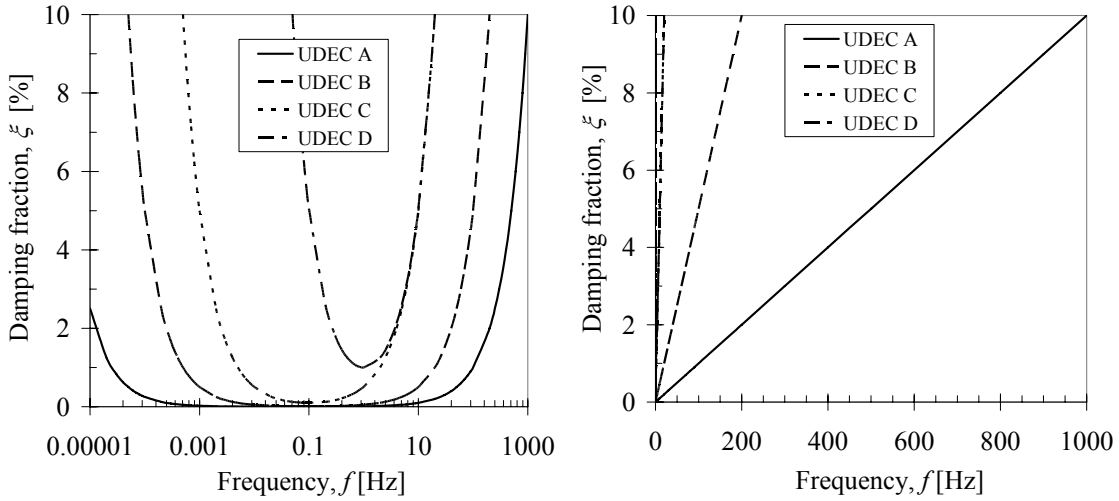

Figure 7-12: Frequency dependence of damping parameters used for rocking arch simulations (see Table 7.2).

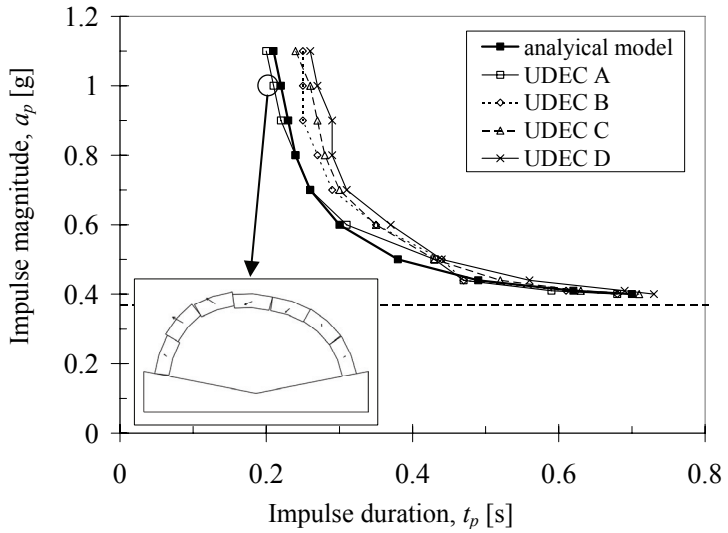

Figure 7-13: Effect of Rayleigh damping constants (Table 7.2) on the Mode I failure domain. Inset: Snapshot of an arch subjected to an impulse (a_p = 1.0 g, t_p = 0.22 s) at t = 1.29 s with UDEC A damping.

Effect of Joint Stiffness

The sensitivity of the Mode I failure domain (Figure 7-11) with respect to the joint stiffness is shown in Figure 7-14. A variation in stiffness of two orders of magnitude ($1x10^{11}$ - $1x10^{13}$ Pa/m) had a relatively small effect on the failure domain results. In general, a decrease in the joint stiffness caused a slight decrease in the stability resulting from impulses of larger magnitude. Although this trend is not definitive, it could perhaps be explained by the existence of larger joint contact overlaps between blocks, which effectively move the hinge locations slightly within the thickness of the arch, reducing stability.

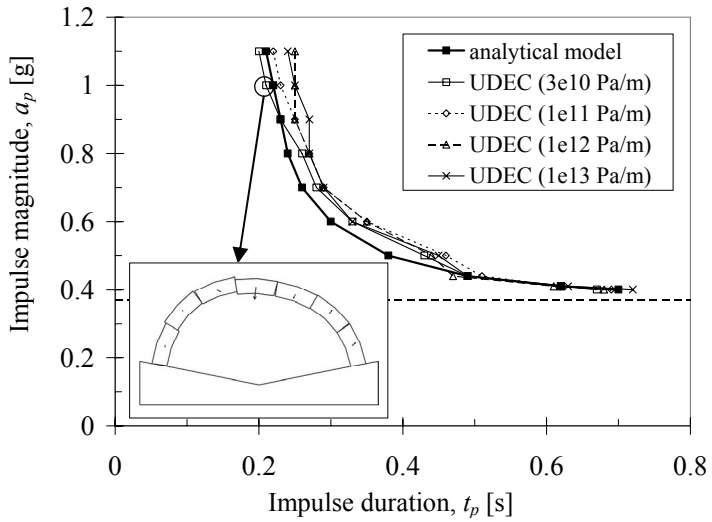

Figure 7-14: Effect of the joint stiffness (shown in parentheses) on the Mode I failure domain. Inset: Snapshot of arch subjected to an impulse (a_p = 1.0 g, t_p = 0.21 s) at t = 1.29 s with a joint stiffness of 3.0×10^{10} Pa/m.

Increasing stiffness values further (> 1×10^{13} Pa/m) requires excessively small time steps for the solution to remain stable and had little effect on the results. However, lower stiffness values (≤ 3×10^{10} Pa/m) reduced stability more noticeably, again causing the vibration displacements discussed previously (Figure 7-14 inset). Due to the reduction in stiffness, the natural frequencies decrease, higher natural frequencies are no longer critically damped, and vibration displacements occur. This re-emphasizes the fact that the joint stiffness, density, and frequency dependent damping parameters are interrelated, making their accurate definition even more delicate.

Fortunately, the failure domains were found to be relatively insensitive to a large range in both damping and joint stiffness. As a result, numerical modeling has the potential to determine the stability of historic URM structures where material properties are not precisely known. However, a consistent method for approximating material properties is still necessary.

Effect of Friction

As discussed in §5.2.2, the dynamic thrust line is also valuable for determining the minimum coefficient of friction (μ) required to prevent sliding. Recall that for the arch under investigation, the maximum required coefficient of friction occurs at the right springing (hinge D) at the onset of the impulse ($t = 0^+$), and hence does not depend on the duration of the impulse, but only on the magnitude. For an impulse magnitude of 1.0 g, sliding was predicted to be prevented if $\mu \geq 0.56$.

For numerical modeling, the effect of friction was investigated by gradually lowering the coefficient of friction until the threshold below which sliding occurs was identified. Results were

in excellent agreement with predictions of the analytical model. For example, for an impulse magnitude of 1.0 g, the threshold was $\mu = 0.55$, as opposed to the value of 0.56 given by the analytical model. For an impulse magnitude of 0.5 g, the threshold was also the same ($\mu = 0.51$) for both the numerical and the analytical models. This friction check confirms that sliding does not govern failure in this case.

7.2.3 The Buttressed Barrel Vault

The final problem addressed in this section is the buttressed barrel vault. To allow comparison with equivalent-static results presented in §3.4, the same geometry was specified. This problem was only investigated using tilting thrust line analysis and discrete element modeling because a single degree of freedom analytical model would limit the motion of the arch on buttresses unrealistically.

The UDEC material properties stated at the beginning §7.2 were again specified. Both tilting thrust line analysis and UDEC modeling resulted in a constant horizontal acceleration necessary to cause collapse of 0.13 g. The hinge locations at collapse compared well (Figure 7-15).

The effect of a step impulse (see Figure 7-7a) on the buttresses barrel vault was also investigated using UDEC. For this analysis the joint stiffness was increased to 5×10^{12} Pa/m, and the Rayleigh damping was adjusted to $\alpha_R = 6.28 \times 10^{-4}$ and $\beta_R = 1.59 \times 10^{-5}$ ($\xi_{min} = 0.01\%$, $f_{min} = 1.0$ Hz). This allowed the solution to be obtained more rapidly while still preventing vibration displacements. Collapse occurred in the following progression: tilting of both buttresses slightly to left, tilting of both buttresses to the right, tilting of the left buttress to the left, collapse of the arch, and recovery of both buttresses. The final collapse mechanism is shown in Fig. 7-16a with both buttresses leaning outward while the arch collapses.

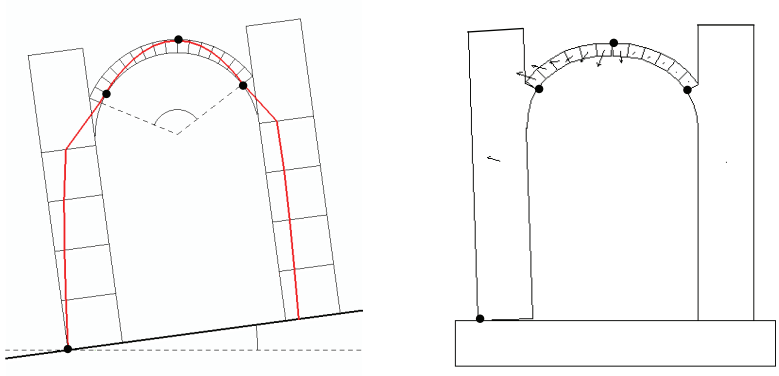

Figure 7-15: Results for a buttressed barrel vault subjected to constant horizontal ground acceleration: (a) tilting thrust line analysis, and (b) UDEC collapse mechanism.

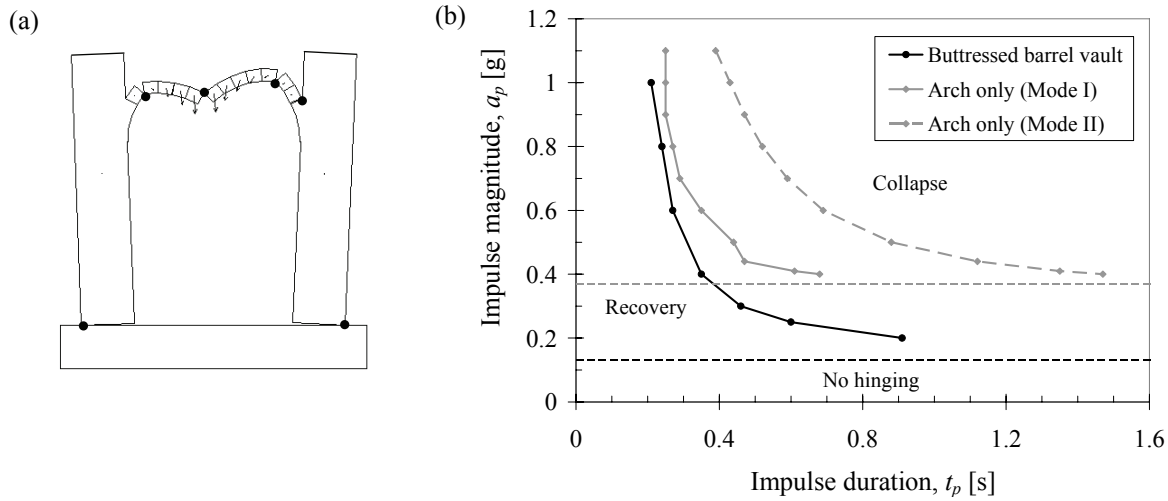

Figure 7-16: Results for a buttressed barrel vault subjected to a step impulse of duration, t_p, and magnitude, a_p: (a) UDEC collapse mechanism, and (b) failure domain.

The governing failure domain for the buttressed barrel vault is plotted in Figure 7-16b, along with the Mode I and II failure domain results from §5.2.2 for comparison. For all impulse durations, the addition of the buttresses causes the structure to collapse at lower magnitudes of acceleration, effectively weakening the structure. It should be mentioned that the assumption of monolithic buttresses is a non-conservative one, as they have been observed to fracture under lateral loading due to the low tensile strength of masonry (Ochsendorf 2002). Buttress cracking could be included by discretizing the buttresses in the UDEC model.

7.3 Defining Modeling Parameters

The trial and error approach to defining modeling parameters demonstrated in the previous section is typical of many studies involving the dynamics of masonry structures using DEM. While adjustment of the parameters can yield the desired response, a more robust way of defining damping parameters is necessary. Then, after an educated estimate of damping parameters is applied, the sensitivity of results to the applied damping should still be evaluated.

In §7.2, high frequency damping is shown to prevent bouncing and vibration displacements. In this section, the amount of high frequency damping will be determined through consideration of the natural frequencies of individual blocks, whether alone or as part of a complete structure. Specifically, the aim is to determine the frequency at which the structure should be critically damped, and then to define the stiffness-proportional damping constant accordingly. The single rocking block is first addressed, followed by extension to multiple block systems.

7.3.1 The Rocking Block

For the single rocking block, three different types of impact between the block and the base were observed in numerical modeling: vertical translational corner impact, vertical translational edge impact, and rotational impact. The first two are self-explanatory, but rotational impact involved rotation about one corner of the block, impact, and then rebound rotation about the same corner. The natural frequencies of the block related to these three types of impulses first need to be estimated. This will be done by determining the natural frequency of the block as if it is always in contact with the base. In reality, the block is only in contact for a short time, during which the natural frequency holds. In other words, impact is approximated by one half cycle of motion at the natural frequency of the system. If the system is critically damped at this frequency, it will not rebound.

In UDEC, block contacts are modeled with a spring-dashpot element at each corner-edge or corner-corner contact. Thus the single rocking block has a vertical spring with stiffness, k_s, at each of its bottom corners. The natural frequencies of the first two types of impact are straightforward:

$$\begin{aligned} &\text{Corner impact:} \quad \omega_c = \sqrt{\frac{k_s}{m_B}} \\ &\text{Edge impact:} \quad \omega_e = \sqrt{\frac{2k_s}{m_B}} \end{aligned} \tag{7.4}$$

where m_B is the mass of the block.

To determine the natural frequency of rotational impact, the single rocking block problem depicted in Figure 7-17 is considered. If the rocking block rotating about point O impacts the spring support (assume $c = 0$) at point X, the equation of motion for the system can be written:

$$J\ddot{\theta} + k_s B^2 \sin\theta = 0 \tag{7.5}$$

where J is the mass moment of inertia about point O, and θ is the rotation about point O (assuming $\theta = 0$ at the at-rest rotational displacement, θ_s). For a rectangular block:

$$J = \frac{m_B}{3}\left(B^2 + H^2\right) = \frac{\rho BH}{3}\left(B^2 + H^2\right) \tag{7.6}$$

Additionally, for small rotation angles:

$$\theta_s = \frac{m_B g B}{2B^2 k_s - m_B g H} \tag{7.7}$$

Note that for a very stiff spring, mgh is negligible with respect to $2B^2k_s$, and the at-rest rotational displacement reduces to:

$$\theta_s = \frac{m_B g}{2Bk_s} \tag{7.8}$$

From Equations 7.5 and 7.6, the natural frequency associated with rocking impact is determined:

$$\omega_r = \sqrt{\frac{k_s B^2}{J}} = \sqrt{\frac{3k_s B^2}{m_B\left(B^2+H^2\right)}} = \sqrt{\frac{3k_s B}{\rho H\left(B^2+H^2\right)}} \tag{7.9}$$

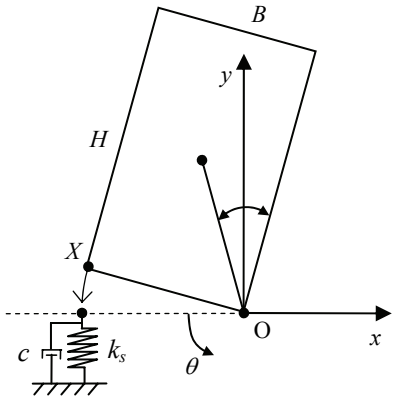

Figure 7-17: Definition of the rotational impact problem.

Joint Stiffness

To calculate the impact frequencies, the joint stiffness needs to be defined. For rigid blocks, it is assumed that the deformation is concentrated in the joints. The joint stiffness, k_j, is then defined using the material properties of the blocks:

$$k_j = \frac{EA}{L} \tag{7.10}$$

where E is the modulus of elasticity of the masonry blocks, A is the area of contact between the blocks, and L is the length of rigid material represented in the direction perpendicular to the joint, as mentioned in §7.1. For the rocking block in question, this reduces to:

$$k_j = \frac{EB}{H} \tag{7.11}$$

The joint stiffness has been determined but must be translated into a spring stiffness, k_s. Since the stiffness is lumped to springs at the corners of the blocks, and the spring stiffness is defined as:

$$k_s = \frac{k_j B}{2} = \frac{EB^2}{2H} \tag{7.12}$$

The impact frequencies of the system (Equations 7.4 and 7.9) are:

$$\text{Corner impact:} \quad \omega_c = \sqrt{\frac{k_j B}{2m_B}} = \sqrt{\frac{EB^2}{2Hm_B}}$$

$$\text{Edge impact:} \quad \omega_e = \sqrt{\frac{k_j B}{m_B}} = \sqrt{\frac{EB^2}{Hm_B}} \tag{7.13}$$

$$\text{Rotational impact:} \quad \omega_r = \sqrt{\frac{k_j B^3}{2J}} = \sqrt{\frac{EB^4}{2HJ}} = \sqrt{\frac{3EB^3}{2\rho H^2\left(B^2+H^2\right)}}$$

Selection of the Critical Frequency

To select which impact frequency should be specified as the critical frequency, it is useful to compare the rotational impact (Equation 7.9) and bouncing impact (Equation 7.4) frequencies:

$$\frac{\omega_c}{\omega_r} = \sqrt{\frac{1+\left(\frac{H}{B}\right)^2}{3}} \quad ; \quad \frac{\omega_e}{\omega_r} = \sqrt{\frac{2\left(1+\left(\frac{H}{B}\right)^2\right)}{3}} \tag{7.14}$$

The relationships in Equation 7.14 are plotted in Figure 7-18. Provided that $H/B > \sqrt{2}$, one finds that $\omega_r < \omega_c$. Likewise, provided that $H/B > 1/\sqrt{2}$, one finds that $\omega_r < \omega_e$. Thus, provided that $H/B > \sqrt{2}$:

$$\omega_r < \omega_c < \omega_e \tag{7.15}$$

Therefore, specifying critical damping (ξ = 100%) at ω_r will cause ω_c and ω_e to be over-damped (ξ > 100%), and would be least conservative. Alternatively, specifying critical damping at ω_e would cause ω_r and ω_c to be under-damped (ξ < 100%), and would be most conservative but might not ensure that rocking and bouncing do not occur. Either choice is reasonable, but both extremes should be checked to determine the sensitivity of results.

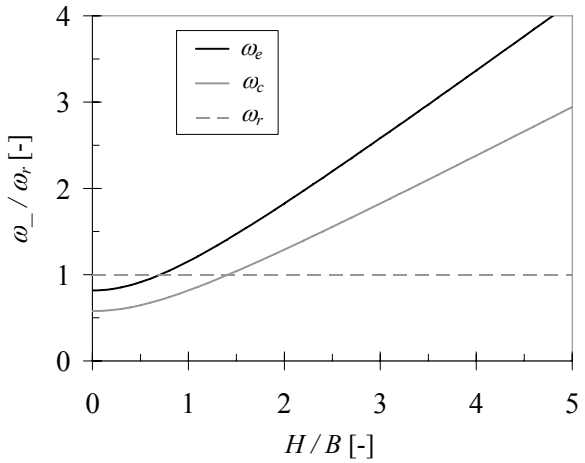

Figure 7-18: Relationship between block aspect ratio and the ratio of natural frequencies associated with different types of impact.

Damping Parameters

Once the critical damping frequency (ω_{crit}) is selected, the damping parameters can be defined accordingly. Mass-proportional damping will be avoided ($\alpha_R = 0$), as it is not physically realistic and is not needed to prevent unrealistic behavior (see §7.2), and only stiffness-proportional damping is employed. Thus, Equation 7.1 reduces to $\mathbf{C} = \beta_R \mathbf{K}$, and Equation 7.2 reduces to:

$$\xi = \frac{1}{2}\beta_R \omega = \pi \beta_R f \tag{7.16}$$

Using Equation 7.16, the desired damping at the critical impact frequency can be specified:

$$\beta_R = \frac{2\xi}{\omega_{crit}} = \frac{\xi}{\pi f_{crit}} \tag{7.17}$$

7.3.2 Multiple Rocking Blocks

To extend to multiple block systems, only the two extreme frequencies will be considered: ω_e and ω_r (Equation 7.15). To extend the edge impact frequency to multiple block systems ($\omega_{e,m}$), consider a single block vibrating vertically in the middle of a column of stacked blocks. Lumping the tributary stiffness to the corners of the block results in a vertical spring at each corner with stiffness k_s. Thus, the stiffness is effectively doubled, and the natural vibrating frequency is:

$$\omega_{e,m} = \omega_e \sqrt{2} \tag{7.18}$$

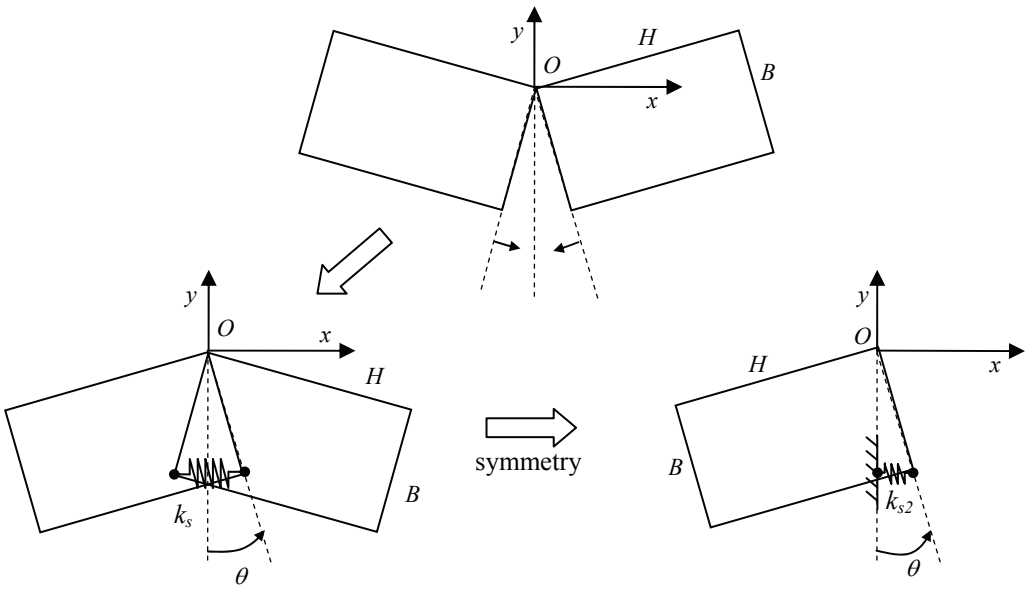

Figure 7-19: Definition of the rotational impact problem for two rocking blocks.

To extend the rotational impact frequency of multiple blocks, consider the two rocking blocks depicted in Figure 7-19. The problem can be simplified using symmetry, where $k_{s2} = 2k_s$. Therefore, the problem reduces to a single rocking block with twice the spring stiffness, thus:

$$\omega_{r,m} = \omega_r \sqrt{2} \tag{7.19}$$

Furthermore, consider the rotational frequency of the different sized blocks depicted in Figure 7-20. In this case, the problem must be solved as a two degree of freedom system. Two natural frequencies exist, one relating to a combined pendulum motion of the two blocks, and the other relating to a symmetric mode, the mode of interest for impact. The natural frequency of the pendulum-type mode is dependent on gravity, but the symmetric mode is independent of gravity (using small angle approximations). The natural frequency for the symmetric mode is:

$$\omega_{r,m2} = \sqrt{k_s B_1^{\,2} \left(\frac{1}{J_1} + \frac{1}{J_2} \right)} \tag{7.20}$$

where J_1 is the mass moment of inertia of the smaller block and J_2 is the mass moment of inertia of the larger block.

In the limit where J_2 approaches infinity, Equation 7.20 yields $\omega_{r,m2} = \omega_r$. At the other limit, $J_2 = J_1$ (note that J_2 can't be less than J_1 as J_1 is defined as the smaller of the two blocks), the problem reduces to the symmetric problem in Figure 7-19, and Equation 7.20 yields $\omega_{r,m2} = \omega_{r,m}$.

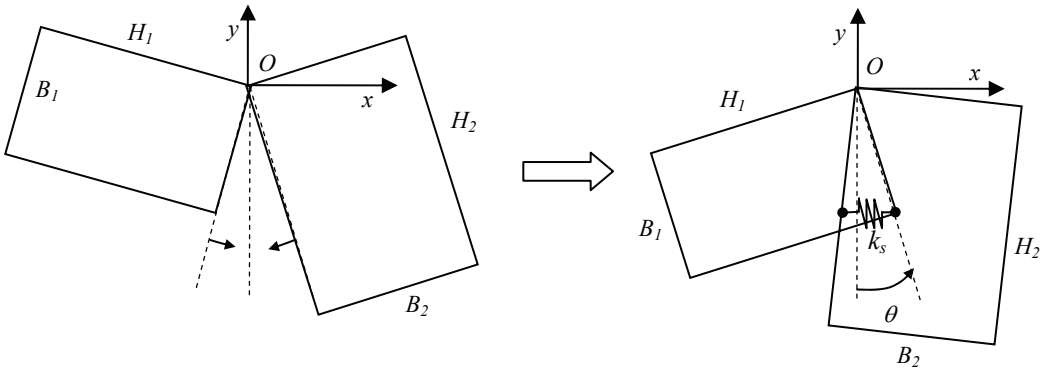

Figure 7-20: Definition of impact problem for two different sized blocks.

Therefore, for multiple block systems, the critical frequency is bounded by:

$$1 \le \frac{\omega_{crit,m}}{\omega_{crit}} \le \sqrt{2} \tag{7.21}$$

For a system of multiple blocks of approximately the same size, the critical frequency can be estimated by $\omega_{crit,m} = \omega_{crit}\sqrt{2}$.

Although these are clearly simplifications of the behavior, they provide order-of-magnitude estimates for determining damping properties. Ideally, one would determine the highest vibration frequencies of the entire system, and define critical damping according to which modes would likely be critically damped in the actual system. However, this is prohibitively complicated in systems with numerous blocks, and would not necessarily provide greater accuracy because approximation of the actual damping is inevitable.

7.4 Evaluation of Modeling Parameter Derivation

The approach to defining modeling parameters presented in §7.3 is evaluated in this section. First, a simple example is used to demonstrate how the derived modeling parameters are implemented in DEM. Second, the framework presented in §7.3 is used to predict the bouncing and vibration displacements observed in §7.2. Finally, the derivation in §7.3 is used to assess other studies involving discrete element modeling.

7.4.1 Example Application

To exemplify how §7.3 can be implemented, DEM is used to predict the rocking response of a single block tested on a shake table. The block ($E \approx 1\text{x}10^{10}$ Pa/m, $\rho \approx 500$ kg/m^3, $B = 0.05$ m, H

= 0.2 m) was tested under harmonic motion with the following specified characteristics: A_h = 0.4 g, ω = 10π rad/s (Equation 7.3). The actual acceleration of the base was recorded with an accelerometer and the motion of the block was recorded using high speed video. Point tracking software was used to calculate the rocking angle.

For simulations, the recorded base acceleration was input into UDEC. The joint stiffness was specified using Equation 7.11 (k_j = 2.5x10^9 Pa/m), and the stiffness-proportional damping was specified using Equation 7.17. Simulations were carried out with each of the impact frequencies (ω_r, ω_c, ω_e) specified as the critical damping frequency (ω_{crit}). Additionally, other damping parameters were also specified to evaluate the sensitivity of results. The specified damping and the calculated damping fractions for each simulation are presented in Table 7.3.

The results are plotted in Figures 7-21a and 7-21b. Specifying critical damping at ω_c (UDEC Y) and ω_e (UDEC Z) caused nearly identical responses, and gave the best prediction of the experimental result. Specifying critical damping at ω_r (UDEC X) gave a very similar result, but slightly over-damped the response. Regardless, all simulations predicted the response quite well, indicating that the rocking response is not overly sensitive to the selection of which impact frequency to critically damp. Thus, the minimum damping (UDEC Z) should be selected as conservative.

To further evaluate the sensitivity of results, additional simulations were carried out with less damping. Starting from UDEC Z, the damping was divided by two (UDEC Z1) and four (UDEC Z2). Simulation UDEC Z1 was slightly under-damped, but still predicted a similar response. Simulation UDEC Z2 was significantly under-damped, and slight bouncing occurred resulting in a poor prediction. Thus, the results are relatively insensitive to damping, as roughly an order of magnitude of damping (UDEC Z1 to UDEC X) had a relatively small effect on the rocking response. Furthermore, the damping parameters defined using §7.3 successfully avoid unobserved bouncing behavior.

Table 7.3: Different damping parameters used for rocking block simulations.

	Damping Constants		ξ at ω_r	ξ at ω_c	ξ at ω_e
	α_R	β_R	[%]	[%]	[%]
UDEC X	0.0	1.3 x 10^{-3}	100	240	340
UDEC Y	"	5.7 x 10^{-4}	42	100	141
UDEC Z	"	4.0 x 10^{-4}	30	71	100
UDEC Z1	"	2.0 x 10^{-4}	15	36	50
UDEC Z2	"	1.0 x 10^{-4}	7.6	18	25

Note: The shaded row represents a simulation in which bouncing occurred.

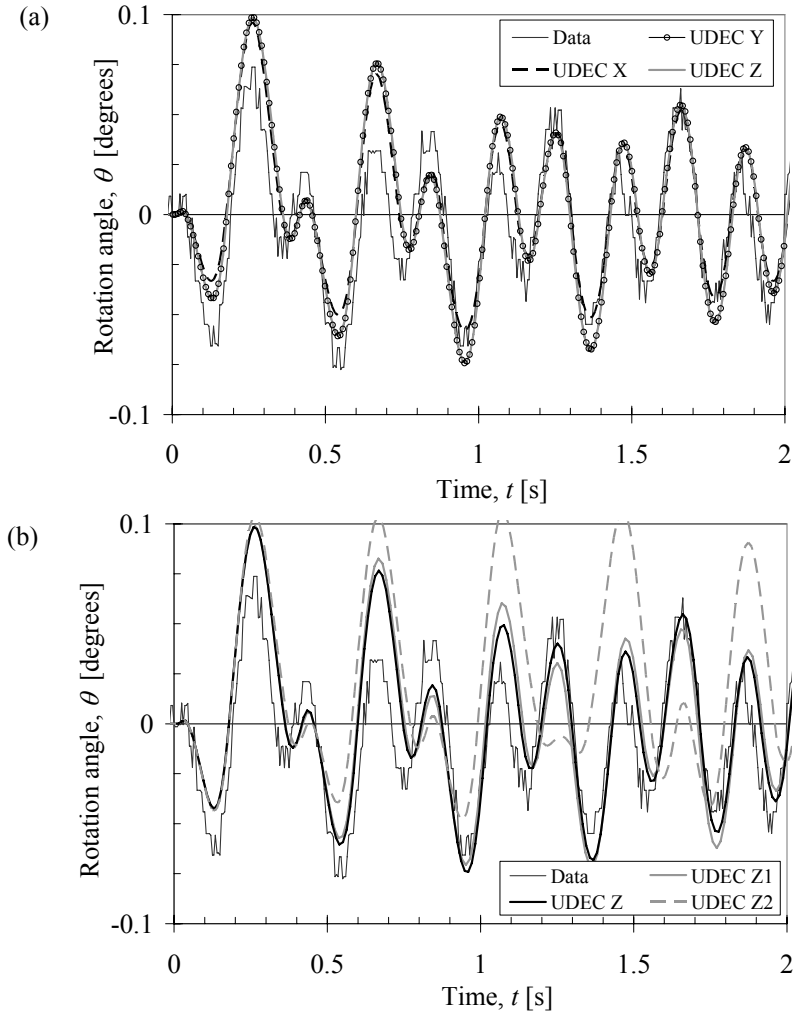

Figure 7-21: Comparison of experimental and simulated response for a rocking block subjected to harmonic ground motion.

This example shows how the procedure for defining modeling parameters can be applied. Results give confidence in the effectiveness of the method, but clearly further verification is necessary.

7.4.2 Evaluation of DEM Simulations in §7.2

Using the framework presented in §7.3, the bouncing and vibration displacement responses observed in §7.2 can be evaluated. In Tables 7.4, 7.5, 7.6, and 7.7, the damping constants, joint stiffness, and damping fractions at the impact frequencies are presented. The shaded rows demonstrate when simulations were observably under-damped, and when bouncing or vibration displacements occurred.

Table 7.4: Range of damping parameters used for rocking block simulations.

	Damping Constants		k_j	ξ at ω_r	ξ at ω_e
	α_R	β_R	[Pa/m]	[%]	[%]
UDEC 1	6.28×10^{-5}	1.59×10^{-4}	1.0×10^{12}	26	89
UDEC 2	"	3.98×10^{-5}	"	6.6	22
UDEC 3	"	6.37×10^{-6}	"	1.1	3.6

Note: Light shading indicates an under-damped simulation.
Dark shading indicates a simulation in which bouncing occurred.

Table 7.5: Range of stiffness parameters used for rocking block simulations.

Damping Constants		k_j	ξ at ω_r	ξ at ω_e
α_R	β_R	[Pa/m]	[%]	[%]
6.28×10^{-5}	1.59×10^{-4}	1.0×10^{13}	84	280
"	"	1.0×10^{12}	27	89
"	"	1.0×10^{11}	8.4	28
"	"	5.0×10^{10}	5.9	20

Note: Light shading indicates an under-damped simulation.
Dark shading indicates a simulation in which bouncing occurred.

Table 7.6: Range of damping parameters used for rocking arch simulations.

	Damping Constants		k_j	ξ at $\omega_r\sqrt{2}$	ξ at $\omega_e\sqrt{2}$
	α_R	β_R	[Pa/m]	[%]	[%]
UDEC A	3.14×10^{-6}	3.18×10^{-5}	1.0×10^{12}	11	18
UDEC B	6.28×10^{-5}	1.59×10^{-4}	"	56	91
UDEC C	6.28×10^{-4}	1.59×10^{-3}	"	560	900
UDEC D	6.28×10^{-2}	1.59×10^{-3}	"	560	900

Note: Shading indicates a simulation in which vibration displacements occurred.

Table 7.7: Range of stiffness parameters used for rocking arch simulations.

Damping Constants		k_j	ξ at $\omega_r\sqrt{2}$	ξ at $\omega_e\sqrt{2}$
α_R	β_R	[Pa/m]	[%]	[%]
6.28×10^{-5}	1.59×10^{-4}	3.0×10^{10}	10	16
"	"	1.0×10^{11}	18	29
"	"	1.0×10^{12}	56	91
"	"	1.0×10^{13}	180	286

Note: Shading indicates a simulation in which vibration displacements occurred.

All four tables indicate that under-damped behaviors occur beneath a similar threshold: $\xi \approx$ 10% at ω_r and $\xi \approx 25\%$ at ω_e. Furthermore, specifying $\xi \approx 100\%$ at ω_e successfully avoids under-damped behavior. Thus, this seems to be an appropriate starting point for DEM.

7.4.3 Evaluation of Previous Research Results

The framework presented in §7.3 can be used to explain modeled behavior in previous studies. As mentioned in §2.3.2, damping parameters in the majority of previous studies have been specified at random or have been applied based on numerical modeling constraints. For example, stiffness-proportional damping is sometimes neglected entirely because it can extend computational run-times, and mass-proportional damping is substituted simply because the system should have some minimal damping. Furthermore, UDEC (Itasca 2004) and 3DEC (Itasca 2003) have been applied in numerous studies, but damping parameters are rarely given, and sometimes barely discussed. Thus, it was difficult to find a study for comparison in which the damping was actually specified.

Mouzakis et al. (2002) tested the earthquake response of a 1:3 scale replica of a column of the Parthenon on the Acropolis of Athens. The classical marble column was tested under several earthquake ground motions. Additionally, Papantonopoulos et al. (2002) modeled the response using 3DEC. Rigid blocks were employed, and joint stiffness and friction properties were approximated for marble. Mass-proportional damping was neglected on the basis that it has no physical meaning, and a sensitivity study of stiffness-proportional damping was carried out. Figure 7-22 displays the experimental and simulated displacements in the transverse and longitudinal directions, using three different stiffness-proportional damping constants (β_R = 0.0, 0.005, and 0.010). Based on this study, the authors conclude that during strong shaking, zero damping gives the best results, while towards the tail of the response, the response is under-damped. Thus, the authors rightly conclude that zero stiffness-proportional damping is appropriate, since the response during strong shaking is more important.

Applying the concepts presented in §7.3 to this problem, the impact frequencies of the system can be used to evaluate the damping constants specified. Edge impact in two-dimensions becomes surface impact in three-dimensions, and the frequency associated with this impact is only a function of the height of the drums. Using the material properties specified by Papantonopoulos et al. (2002) and assigning critical damping to the surface impact frequency yields an estimated stiffness-proportional damping constant of β_R = 0.0016. Additionally, an approximation of the rotational impact frequency of the individual column drums yields an estimated stiffness-

proportional damping constant of β_R = 0.002. Thus, while the minimum damping (β_R = 0.005) was thought to be very small, it may have been too large. Specifying zero damping did predict the critical response during strong shaking quite well, but perhaps a smaller amount of damping would have worked better, and could have been prescribed directly using this method.

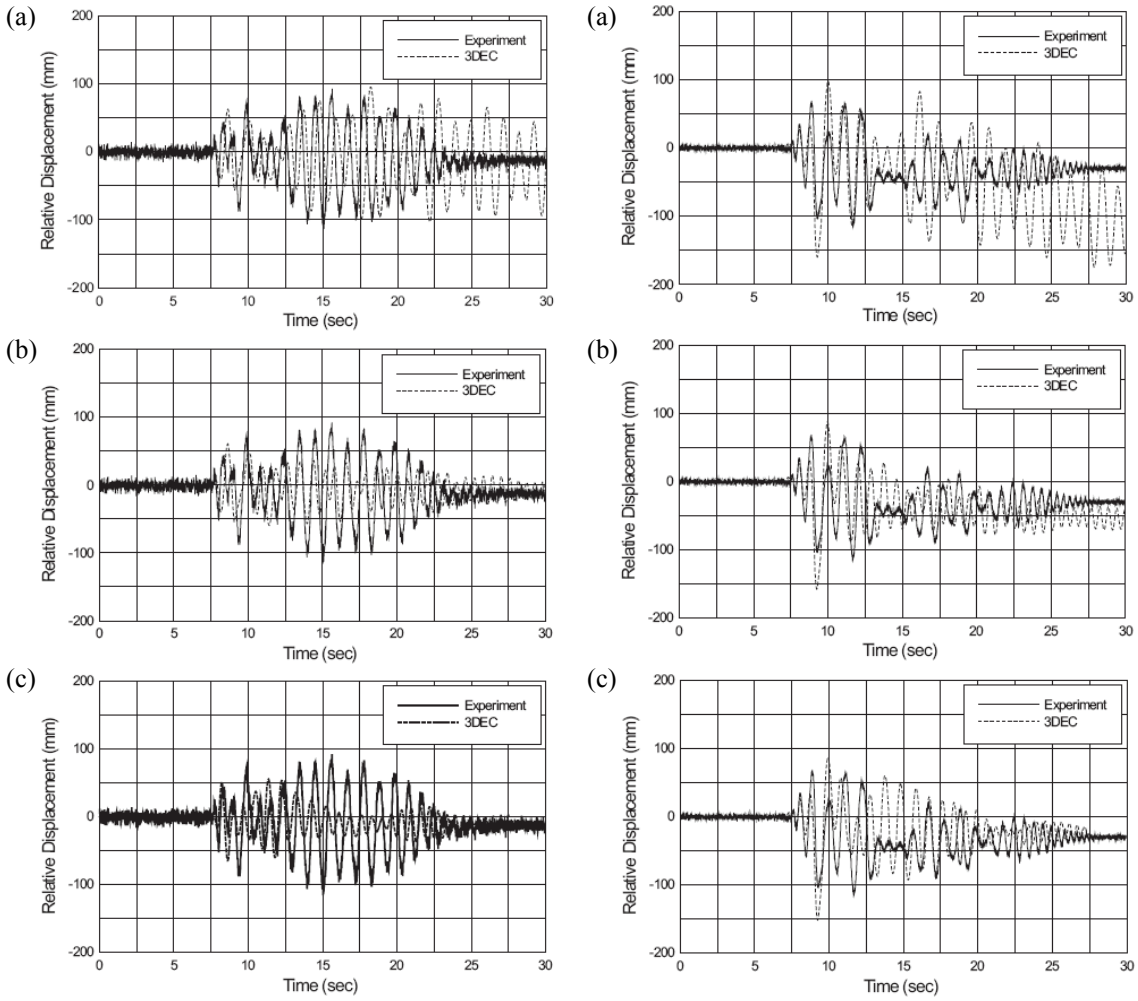

Figure 7-22: Displacement of the column capital in the longitudinal (left plots) and transverse (right plots) directions for the Kalamata record: (a) zero damping, (b) stiffness-proportional damping, β_R = 0.005, and (c) stiffness-proportional damping, β_R = 0.010. (after Papantonopoulos et al. 2002)

7.4.4 Discussion

The method for defining modeling parameters presented in §7.3 is certainly a first order approach. However, only one other study (Peña at al. 2007) has attempted the derivation of appropriate modeling parameters for rocking structures using DEM. Peña at al. (2007) focused specifically on the single rocking block, and used a frequency parameter associated with rocking

motion to define the joint stiffness properties. Thus, the joint stiffness was tailored to produce the appropriate rocking response instead of being specified according to the expected deformation in the system. The extremely soft joints which result have no physical basis and cause the block to never lose contact with the ground during the simulated rocking response. The derived DEM parameters are then adjusted by a fitting procedure to produce the experimentally measured rotation angle of the block. While this fitting provides extremely accurate results, it approximates the measured energy dissipation at impact with an equivalent viscous damping over the entire rocking motion. Thus, this approach is not realistic for assessment of masonry structures in general.

The presented method fills a critical gap in the process of applying DEM to assess masonry structures under dynamic loading, by providing a rational basis from which to assign parameters and begin modeling. Without such a basis, researchers have typically tested a random range of parameters and determined the sensitivity of results (as in §7.2), but have risked the possibility of missing the appropriate range of parameters entirely. Furthermore, the method presented in §7.3 has the benefits of being simple and easily applicable, while effectively explaining the results presented throughout this chapter. However, there are clear limitations:

- The method provides a physical basis for the joint stiffness, but only provides an order of magnitude estimate of appropriate damping for the system. Thus, informed by the derived impact frequencies, a sensitivity analysis for a range of frequencies is still necessary.
- The method specifies critical damping to the impact frequency, thus producing plastic impact. While this seems to be effective for masonry, further validation is necessary. This is certainly not realistic for materials which behave more elastically during impact. However, using this method, the fraction of damping during impact for a given material could be measured and then directly specified at the approximated impact frequency.
- The derivation is based on relatively low frequency ground motions, for which vibration displacements are unlikely. However, for ground motions with a significant high frequency component, vibration displacements would likely occur. The effectiveness of this method for those situations must be investigated.
- When the system consists of multiple blocks of vastly different size, defining modeling parameters is more involved. The joint stiffness and damping of every joint could be described individually, but would be quite tedious. Alternatively, one damping level could be prescribed for the entire model. In this case, deriving damping properties using the smallest block in the system would produce the largest impact frequencies, the least

amount of damping, and thus conservative results. However, sensitivity studies would be even more important in this case.

In addition to these limitations, it must be stated that it is impossible to predict exact response of any structures using DEM, especially multiple block systems under complex loadings. This is evident in the fact that experiments themselves are often not reproducible due to tiny imperfections in the geometry and minor differences in the ground motion (e.g. Yim et al. 1980, Mouzakis et al. 2002, Peña et al. 2007). Thus, while these methods effectively improve results, DEM must be applied with this in mind. Furthermore, this highlights the importance of understanding structural behavior, and using DEM accordingly. A good example of this is the approach taken to arch assessment in this dissertation. Using DEM to predict the exact displacement of every block in the arch during an earthquake is unrealistic. However, first understanding that the arch is fundamentally vulnerable to impulse loading, allows utilization of DEM for a much simpler load case. Thus, applying DEM in simpler situations, for example the dynamic collapse of a buttressed barrel vault under impulse loading (§7.3.4), can provide insight into specific modes of collapse. Subsequently, behavior under more complex ground motions can be attempted. Comparison of results can then lead to a determination of what is fundamentally important in assessing structures.

7.5 Summary

Discrete element modeling is a powerful method with potential for capturing the dynamic response of masonry structures. The detailed comparisons with analytical modeling, the method for deriving input parameters, and the sensitivity studies herein allow the following conclusions to be drawn:

- For the rocking block, DEM results compared well with both the analytical and experimental rocking block response.
- For the rocking arch, results of numerical modeling are in good agreement with analytical results, both in terms of behavior and the predicted failure domain.
- Both analytical modeling and numerical modeling provide a means for determining the minimum coefficient of friction theoretically required to prevent sliding. For the arches investigated, the coefficient of friction required is below the typical values of masonry joints, and hence the assumption of no sliding is reasonable.

- Specifying a desired damping at the critical frequencies of the system effectively prevents erroneous numerical prediction of bouncing behavior and vibration displacements. Accordingly, the proposed method provides an effective basis from which to specify modeling parameters.
- The sensitivity of numerical modeling results to input parameters is integral to the confidence in results and to the potential of DEM. Therefore, a sensitivity analysis is essential. The predicted rocking block response and rocking arch failure domains were shown to be relatively insensitive to the parameters specified.

Part IV

Conclusions

Chapter 8

Conclusions

8.1 Summary of Main Findings

The primary objective of this research, as stated in §1.3, is twofold: (1) To increase fundamental understanding of the dynamic behavior of masonry structures under eathquake loading, and (2) to develop tested analysis methods that allow appropriate assessment of masonry structures which might be subjected to earthquake loading. While working towards these objectives, new and existing analysis methods were created or improved, and applied and tested. The main findings are as follows:

- *Tilting Thrust-Line Analysis*: Tilting thrust-line analysis provides a graphical evaluation of stability under constant horizontal acceleration. The parametric and visual characteristics are particularly useful for understanding the behavior of vaulted masonry structures, and exploring the interaction of structural components (e.g. arches, buttresses, vaults). Stability during earthquakes, approximated by the tilt capacity, was found to be highly dependent on the spatial relationship of these components. Furthermore, tilting solutions identified geometries which optimize the interaction of components. The framework predicted collapse mechanisms which were not initially intuitive and could not be easily predicted.

- *Sequentially Linear Analysis*: The extension of sequentially linear analysis to include non-proportional loading allows the self-weight of the structure to be included, enabling its application to masonry structures under quasi-static seismic loading. This extension was verified through comparison of SLA results with incrementally iterative non-linear analysis results. The new framework accurately predicted experimental results involving brittle fracture of concrete blocks. Additionally, experiments involving horizontal cyclic loading of a full-scale two-story masonry structure were effectively simulated using SLA with shell elements. Thus, the method was shown to have potential for predicting damage to masonry structures during earthquakes.

- *Dynamics of Arches:* A SDOF analytical model with a reflecting four-hinge mechanism qualitatively describes the behavior of a rocking arch under horizontal ground motion. This analytical model was successfully used to predict the collapse of experimentally tested masonry arches. Results show that the primary impulse within the ground motion is critical in causing collapse. A single impulse can cause two modes of arch collapse which parallel the collapse modes of a single rocking block.

- *Rocking Structures:* The natural rocking period increases with the magnitude of rocking motion, so constant frequency rocking resonance can not occur. Instead, rocking resonance is identified for ground motions with constantly increasing periods. Furthermore, if likely imperfections in the rocking system are included, overturning of a single rocking block is possible at lower ground accelerations than previously considered. Although the primary impulse of the ground motions is crucial in causing collapse, it is possible that multiple distinct impulses could act together to amplify motion. Considering the uncertain characteristics of possible ground motions and the sensitivity of the rocking response, a statistical approach is necessary to assess this possibility of multiple impulse amplification. Results from a statistical analysis showed a wide range in possible responses for earthquakes of exactly the same frequency content, demonstrating the time dependence of rocking motion.

- *Discrete Element Modeling:* Discrete element modeling can effectively predict the response of rocking structures, but damping must be defined appropriately and the sensitivity of the results to the assigned damping must be investigated. Mass-proportional damping is not realistic and should not be used. Stiffness-proportional damping, while not being physically accurate, should be prescribed to damp unrealistic high frequency vibrations which occur during numerical modeling. The proposed method for defining

stiffness-proportional damping proved a functional approach when simulating experimental and analytical results. Finally, DEM was found to be useful in predicting general behavior, but not the exact displacement of an individual block within a large system. The unknowns of the problem are too many to expect this kind of accuracy.

8.2 Primary Contributions

Based on the main findings above, the two aspects of the primary objective in §1.3 have been addressed. This dissertation has provided: (1) an increased understanding of the stability and fundamental behavior of masonry structures under both static and dynamic loading, and (2) new and improved tools for assessing masonry structures. Specifically, the primary contributions are as follows:

- *Development of tilting thrust-line analysis*: This graphical equilibrium tool allows first-order assessment and a new perspective regarding the stability of vaulted structures under lateral loading.
- *Extension of SLA to non-proportional loading:* This extension allows the inclusion of self-weight in analysis, which is critical for the prediction of damage under simplified quasi-static seismic loading. This improvement provides a practical tool for assessing and predicting damage to masonry structures.
- *Characterization of the rocking of arches under horizontal ground motion:* A new analytical tool and an experimental program involving small-scale arches describe and evaluate the rocking behavior of arches for the first time. Additionally, the first seismic assessment criterion for masonry arches which considers dynamic rocking behavior is presented.
- *Redefinition of the vulnerability of rocking structures to horizontal ground motion:* An energy approach was applied which provides a fresh perspective to an old problem, and reveals the possibility of rocking resonance. This motivated a new statistical approach which incorporates past earthquake data and analytical models into a tool for predicting the probability of rocking collapse during an earthquake of an expected intensity.
- *Improved application of discrete element modeling*: The evaluation of DEM through comparison with experimental and analytical results provides confidence in, and a

perspective of, modeling capabilities. A method for defining discrete element modeling parameters is proposed, allowing a more informed application of this tool.

These contributions can lead to more informed assessment of the safety of masonry structures throughout the world.

8.3 Future Research

The development and application of seismic assessment tools and the experimental investigations herein contribute towards better assessment of masonry structures in seismic regions, but also motivate numerous areas of continued research:

- *Graphical methods:* First, tilting thrust-line analysis could be applied to assess multiple structures with similar cross-sections, with the goal of pinpointing the least stable. An ideal resource for such a study would be the database of Bourbonnais churches assembled by researchers at Columbia University (Murray 2009). Second, this graphical method could be made more powerful by implementation in a more flexible geometric computing environment, e.g. Generative Components. This would also allow more adaptability after constructions have been made, and could facilitate some inclusion of three-dimensional effects. Finally, the concept of tilting could be implemented in three-dimensions, but this would require a completely different graphical framework, such as that proposed by Block and Ochsendorf (2007).

- *Strength methods:* First, SLA currently employs a uni-axial failure criterion, which should be improved to a bi-axial failure criterion to better capture failure under non-proportional loading. Second, the computational solution procedure is currently quite inefficient and should be improved to account for the fact that only a single element is updated between each linear analysis. This could significantly shorten run-times. Third, the algorithm developed for non-proportional loading could be implemented in lattice modeling frameworks. Finally, with these improvements, SLA could be applied to better understand and predict damage to shell structures such as vaults and domes.

- *Analytical modeling:* With a better understanding of rocking behavior and the analytical models developed herein, optimized methods for structural retrofit could be investigated. Specifically, the effect of adding damping and stiffness on the rocking response is of interest, and could explain past destructive interventions to historic masonry structures. Additionally, the analytical arch model motivates similar simplification of other

structures to SDOF systems which could be modeled analytically. New analytical models could be verified experimentally and numerically through the methods applied in this dissertation.

- *Discrete element modeling:* First, further experimental evaluation of discrete element modeling is necessary, particularly in three-dimensions. Second, the method for defining damping parameters should be further evaluated and improved. This could be done by measuring experimentally determining energy dissipation at impact as a material property, and then prescribing the damping accordingly. Additionally, the effect of damping parameters on experimentally realized vibration displacements should be investigated.

In addition to these areas of future research which directly relate to the contributions herein, one final comment must be made. There is a definite need to identify what information can be drawn from computer modeling of historic masonry structures, especially under earthquake loading. The unknowns (e.g. earthquake characteristics, material properties, damage, geometry, etc.) often do not warrant the extremely complex analyses employed, which perhaps confuse the evaluation of masonry structures rather than clarify it. The primary challenge is to utilize the tools which are available, while maintaining a realistic perspective on what can be determined.

Part V

Appendices

Appendix A

Notation

The following notation is used in this dissertation:

a_p = magnitude of a step impulse of ground acceleration

a_g = ground acceleration constraint used for optimization

A_i^{ω} = mean amplitude for spectral frequency ω

A_h = amplitude of harmonic motion

A_p = amplitude of a single sinusoidal ground acceleration impulse

B = block width

c_v = coefficient of restitution with respect to the rotational velocity

c_E = coefficient of restitution with respect to the total energy

$\mathbf{C}$ = damping matrix

E = elastic modulus

E_T = total energy in a system

f = frequency [Hz]

f_{crit} = frequency at which the system is critically damped ($\xi = 100\%$)

f_{min} = frequency at which Rayleigh damping has a minimum

f_t = material tensile strength

f_{ti}^{+} = current tensile strength used in Sequentially Linear Analysis

F = applied force

G = shear modulus

G_f = material fracture energy

G_{red} = reduced shear modulus after cracking for Sequentially Linear Analysis

h = crack bandwidth

H = block height

j = integration point identifier

J = mass moment of inertia of a rectangular block about its corner

k_j = joint stiffness

k_s = spring stiffness

$\mathbf{K}$ = stiffness matrix

$L_{\_}$ = angular momentum about point _

m_B = mass of a block

$\mathbf{M}$ = mass matrix

n- = primary crack normal direction in the plane of the finite element

n_A = number of voussoirs in a part-circular arch

p = parameter which modulates the fineness of the saw-tooth constitutive model

p_x , p_y = linear momentum in the x- and y- directions

$P(t)$ = intensity function used for earthquake generation

R_A = center-line radius of a part-circular arch

s- = secondary crack normal direction in the plane of the finite element

t = time

t- = thickness direction (normal to the mid-surface of the finite element)

t_A = thickness of a part-circular arch

t_d = generated earthquake duration

t_p = duration of a step impulse of ground acceleration.

T_n = natural rocking period

T_p = period of a single sinusoidal ground acceleration impulse

$\ddot{u}_g$ = horizontal ground acceleration

$\ddot{u}_h$ = horizontal acceleration

$\ddot{u}_v$ = vertical acceleration

α = ground surface tilt angle

α_{cr} = critical ground surface tilt angle

α_{exp} = experimentally measured critical ground surface tilt angle

α_R = mass-proportional constant of Rayleigh damping

β_A = angle of embrace of a part-circular arch

β_R = stiffness-proportional constant of Rayleigh damping

β_{sh} = shear retention factor

γ = minimum horizontal acceleration which causes collapse [g]

γ_{80} = theoretical γ using 80% of the arch thickness

γ_{exp} = value of γ calculated from the measured critical ground surface tilt angle

γ_{ns} , γ_{st} , γ_{tn} = shear strain in the subscript directions

δ = displacement

ε = strain

ε_{nn} , ε_{ss} , ε_{tt} = normal strain in the subscript directions

ε_u = ultimate normal strain for the linear softening constitutive model

θ = rotation angle of the rocking arch or the rocking block

θ_{cr} = critical rotation angle of a rocking block

θ_s = static (at-rest) rotational displacement

$\dot{\theta}$ = rotational velocity

$\dot{\theta}^*_{after}$ = rotational velocity immediately after impact

$\dot{\theta}_{before}$ = rotational velocity immediately before impact

θ' = derivative of the rocking angle with respect to the dimensionless time τ

θ'' = derivative of θ' with respect to the dimensionless time τ

λ = load multiplier for Sequentially Linear Analysis

λ_1, λ_2 = load multipliers for each integration point under non-proportional loading

λ_{crit} = critical load multiplier for Sequentially Linear Analysis

λ_j^c = load multiplier for integration point j which causes a compressive stress $\sigma_{\varphi,B}$

λ_j^t = load multiplier for integration point j which causes a tensile stress $\sigma_{\varphi,B}$

μ = coefficient of friction

ν = Poisson's ratio

ξ = fraction of critical damping

ξ_{min} = minimum fraction of critical damping at f_{min} for Rayleigh damping

ρ = material density

σ = stress

σ_1, σ_2 = principal stresses

σ_A , $\sigma_{--,A}$ = stress due to application of load A

σ_B , $\sigma_{--,B}$ = stress due to application of load B

σ_t = maximum principal tensile stress at each integration point

$\sigma_{\varphi,B}$ = stress in the principal stress direction due to application of load B

τ = dimensionless time

ϕ = rotation angle of the rocking arch

ϕ_{cr} = critical rotation angle of a rocking arch

ϕ_i^{ω} = phase angle for spectral frequency ω

φ_1, φ_2 = principal stress directions

ω = frequency [radians]

$\Delta\omega$ = frequency step used for earthquake generation

ω_c = natural frequency associated with corner impact

ω_{crit} = frequency at which the system is critically damped (ξ = 100%) [radians]

ω_e = natural frequency associated with edge impact

ω_r = natural frequency associated with rotational impact

Appendix B

Implementation of the Analytical Arch Model in Matlab*

B.1 Introduction

In §5.2, the presentation of the analytical model was relatively brief. This appendix is intended to provide additional information about the model. First, further details of the derivation of the model are presented, followed by a discussion regarding implementation of the model in Matlab.

B.2 Additional Details of the Analytical Model

As shown in Figure B-1, the mechanism motion is completely described by the rotations of the links θ_{AB}, θ_{BC}, and θ_{CD}, measured counterclockwise from the horizontal. Because the planar four-link mechanism is a single degree of freedom (SDOF) system, one of these rotations (namely $\theta_{AB} = \theta$) is arbitrarily chosen as the Lagrange parameter of the system. Figure B-1 marks the link rotations in the initial (undisplaced) configuration of the arch, θ_0, θ_{0BC} and θ_{0CD}. In the displaced configuration $\theta < \theta_0$, and the variable $\phi = (\theta_0 - \theta) > 0$ is used to denote rotation with respect to the original geometry.

* The analytical arch model was derived and implemented in Matlab in collaboration with Laura De Lorenzis, Assistant Professor, University of Lecce, Italy.

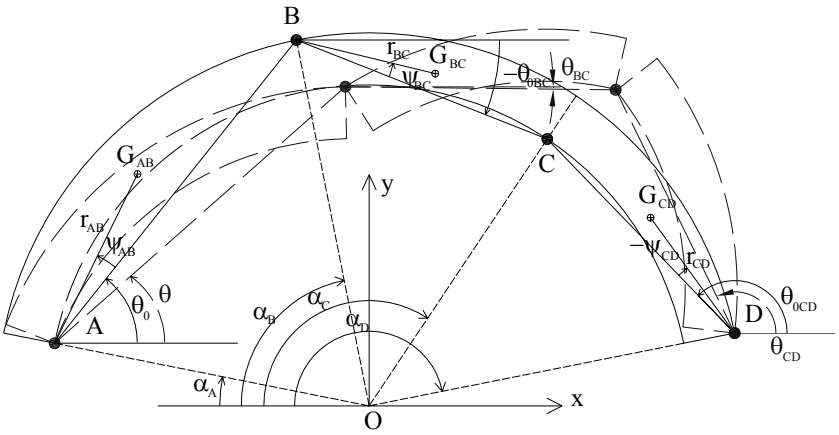

Figure B-1: The arch as a four-link mechanism during rocking motion.

Displacement analysis and velocity analysis are used to describe the link rotations and rotational velocities, respectively, in terms of θ and $\dot{\theta}$, i.e. to obtain functions $\theta_{BC}(\theta)$, $\theta_{CD}(\theta)$ and $\dot{\theta}_{BC}(\theta,\dot{\theta})$, $\dot{\theta}_{CD}(\theta,\dot{\theta})$. The latter two functions can be expressed as follows:

$$\dot{\theta}_{BC}(\theta,\dot{\theta}) = \frac{d\theta_{BC}}{d\theta}\dot{\theta} = f_{BC}(\theta)\cdot\theta \tag{B.1a}$$

$$\dot{\theta}_{CD}(\theta,\dot{\theta}) = \frac{d\theta_{CD}}{d\theta}\dot{\theta} = f_{CD}(\theta)\cdot\theta \tag{B.1b}$$

For more details, see a standard text on mechanism design and analysis (e.g. Erdman and Sandor 1984). Recall that the differential equation of motion of the system (Equation 5.1) is written:

$$M(\theta)R_A\ddot{\theta} + L(\theta)R_A\dot{\theta}^2 + F(\theta)g = P(\theta)\ddot{u}_g \tag{B.2}$$

Solving this equation, the rotation of link AB is found. The rotation of either of the two other links is also known using Equation B.1. Recall also that when the arch rocks in the other direction, a symmetric mechanism is assumed to form. Equations for all the links in this symmetric mechanism could be found in a similar manner.

Modeling of Impact

At the transition between the symmetric mechanisms, impact occurs. Figure A-2 illustrates the arch at this instant. Recall that the primary goal of solving the impact problem is to determine the initial conditions for post-impact motion, using the final conditions (positions and velocities) of the pre-impact motion. For this purpose, suitable simplifying assumptions must be introduced.

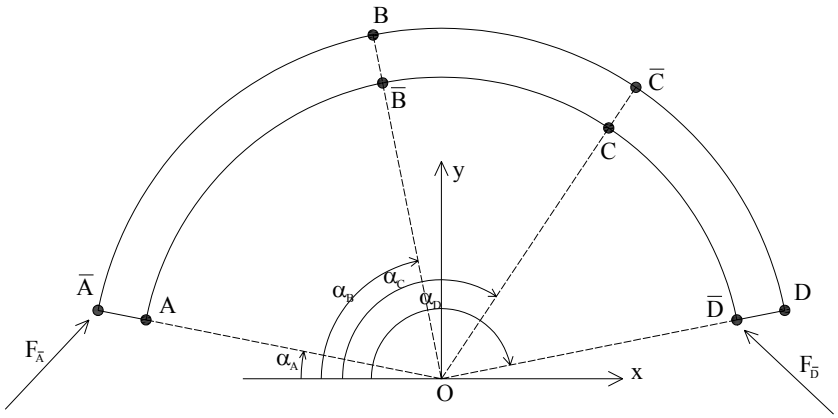

Figure B-2: The arch at the instant of the impact.

It is assumed that the position of the system does not vary during impact, while its velocities are subjected to an instantaneous variation due to the action of impulsive forces. Impact occurs at the hinge sections, where contact generally involves a finite area which is *a priori* unknown. In analogy with Housner's treatment of impact of the single rocking block (Housner 1963), the impulsive force at each hinge section is assumed to be located on the opposite side of the hinge across the arch thickness, i.e. at points $\overline{A}$, $\overline{B}$, $\overline{C}$ and $\overline{D}$ (Figure B-2).

At the location of the internal hinges *B* and *C*, the impact generates internal impulsive forces which balance each other. At the locations of the extreme hinges *A* and *D*, external impulsive forces $F_{\overline{A}}$ and $F_{\overline{D}}$ arise. The problem can be formulated considering five unknowns, namely: the *x*- and *y*- components of $F_{\overline{A}}$ and $F_{\overline{D}}$ ($F_{\overline{A}x}$, $F_{\overline{A}y}$, $F_{\overline{D}x}$, $F_{\overline{D}y}$), plus the rotational velocity of link A^*B^* (see Figure 5-1) immediately after impact, $\dot{\theta}^*_{after}$. The five equations used to determine these unknowns are:

The equation of linear momentum in the *x*-direction for the whole arch:

$$F_{\overline{A}x}\Delta t - F_{\overline{D}x}\Delta t - k^*_x\dot{\theta}^*_{after} = -p_{x,before} \tag{B.3a}$$

The equation of linear momentum in the *y*-direction for the whole arch:

$$F_{\overline{A}y}\Delta t + F_{\overline{D}y}\Delta t - k^*_y\dot{\theta}^*_{after} = -p_{y,before} \tag{B.3b}$$

The equation of angular momentum about *O* for the whole arch:

$$-F_{\overline{A}x}\Delta t\cdot y_{0\overline{A}} + F_{\overline{A}y}\Delta t\cdot x_{0\overline{A}} + F_{\overline{D}x}\Delta t\cdot y_{0\overline{D}} + F_{\overline{D}y}\Delta t\cdot x_{0\overline{D}} - k^*_O\dot{\theta}^*_{after} = -L_{O,i} \tag{B.3c}$$

The equation of angular momentum about $\overline{B}$ for the portion of the arch to the left of $\overline{B}$:

$$F_{\overline{A}x}\Delta t\cdot\left(y_{0\overline{B}}-y_{0\overline{A}}\right)-F_{\overline{A}y}\Delta t\cdot\left(x_{0\overline{B}}-x_{0\overline{A}}\right)-k^{*}_{\overline{B}}\dot{\theta}^{*}_{after}=-L_{\overline{B},before} \tag{B.3d}$$

The equation of angular momentum about $\overline{C}$ for the portion of the arch to the right of $\overline{C}$:

$$-F_{\overline{D}x}\Delta t\cdot\left(y_{0\overline{C}}-y_{0\overline{D}}\right)+F_{\overline{D}y}\Delta t\cdot\left(x_{0\overline{D}}-x_{0\overline{C}}\right)-k^{*}_{\overline{C}}\dot{\theta}^{*}_{after}=-L_{\overline{C},before} \tag{B.3e}$$

where Δt is the duration of the impact, the $k^{*}_{\_}$ terms are known geometric coefficients, the $p_{\_,before}$ and $L_{\_,before}$ terms are known quantities of linear and angular momentum immediately before impact, and the $x_{0\_}$ and $y_{0\_}$ terms are known *x*- and *y*- coordinates of points in the initial (undisplaced) configuration of the arch. In writing the equations, self-weights are neglected because they are small compared to impulsive forces, as is normally assumed for impact problems. By solving the system of equations, the angular velocity immediately after impact ($\dot{\theta}^{*}_{after}$) is computed.

B.3 Implementation in Matlab

The differential equations of motion (Equations 5.1 and 5.2) were solved using the ode45 algorithm in Matlab. This algorithm is based on an explicit Runge-Kutta (4,5) formula (Dormand and Prince 1980). It is a one-step solver, and therefore needs only the results from the previous time step to solve the equation of motion in the current time step.

The entire Matlab code is not included herein, but a graphical user interface (GUI) was built to provide a tool which can be used to predict the response of arches to any ground motion. This allowed the model to be run repeatedly to obtain the results included in this dissertation.

Figure B-3 is a screen image of the GUI. The top section of the GUI allows the input of the desired arch geometry. Using this information, the constant horizontal acceleration which would cause collapse (γ) is determined (in this case 0.33g), and the hinge locations of the corresponding collapse mechanism are plotted. This static problem is solved numerically using Matlab, but gives an equivalent result to the graphical method of tilting thrust-line analysis presented in §3.3.

The middle section of the GUI allows the input of the desired horizontal ground acceleration. The ground acceleration can be input as either a single impulse or an acceleration time history. For a single impulse, the impulse characteristics are input directly into the GUI, and solving commences when the appropriate button is clicked. For an acceleration impulse, a data file with an acceleration time history is placed in the same directory as the GUI, and is read as input. In Figure B-3, a time history was applied and the resulting rocking angle is plotted. In this case, the

arch rocked back and forth and failed after three impacts. The time at which the impacts occurred are given as output in the GUI, and the scale of the output plots can be directly adjusted.

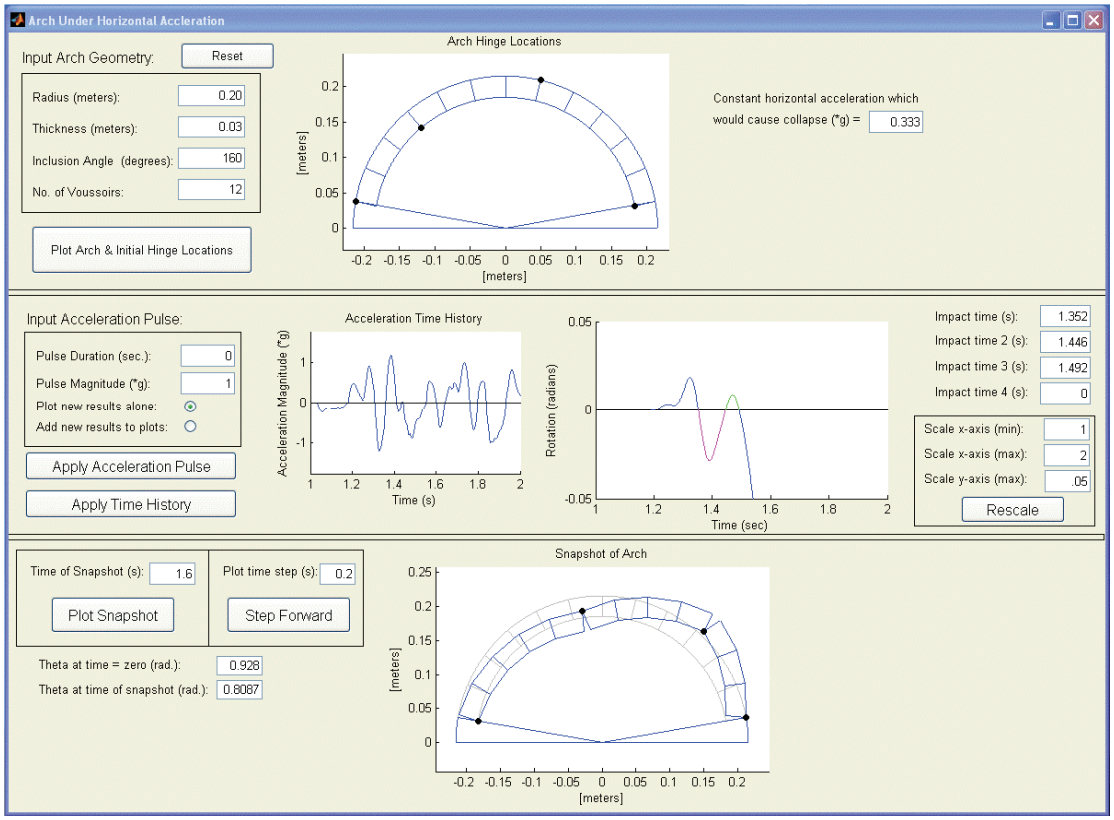

Figure B-3: A screen image of the graphical user interface after application of an earthquake acceleration time history.

The bottom section of the GUI is devoted to visualizing the response. The user can input the time at which to plot the deformed arch, or the rocking motion can be visualized by stepping through the response. In Figure B-3, the arch is plotted at t = 1.6 seconds. Based on the plotted rotation angle response, failure is imminent.

In an updated version of the graphical user-interface, some additional features were added. Figure B-4 depicts this updated version, in which an arch is tested under a sinusoidal impulse. In this figure, the current impulse (the longest one) and the current response (the one in which failure occurs) are superimposed on previous results. The bottom section of the user interface again plots the deformed arch at the desired time, but the dynamic line of thrust is now added. As discussed in §5.2.3, this line of thrust can be used to evaluate the accuracy of hinge locations, and to determine the friction angle necessary to prevent sliding. In Figure B-4, the deformed arch and the line of thrust is plotted at t = 2.5 seconds; failure is again imminent. The line of thrust is

outside of the arch geometry at one block interface (second from the left), indicating that the left hinge would actually move up as failure occurs. This behavior was observed in experimental results. The line of thrust is also used to calculate the friction angle necessary to prevent sliding at all points in the arch. In Figure B-4, the plot at the bottom right corner of the GUI depicts the required friction angle along the length of the arch. This plot is updated according to the current time of the snapshot (in this case t = 2.5 seconds).

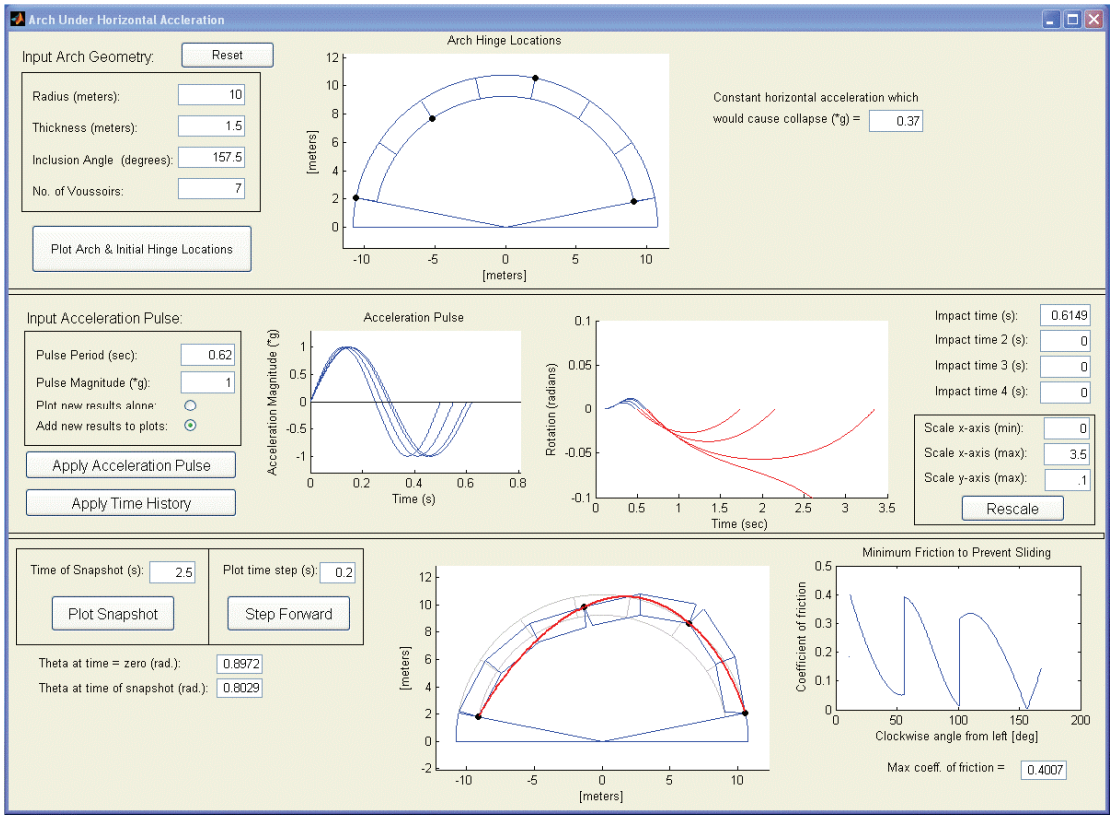

Figure B-4: A screen image of the graphical user interface after application of a sinusoidal acceleration impulse.

Appendix C

Shake Table Design*

C.1 Introduction

In order to test the response of masonry structures to horizontal ground motion, a single axis shake table was designed and constructed in the Civil Engineering Laboratory at MIT. The table was used for part of the experimental program presented in §5.3. In this appendix, the design and specifications of the table are presented.

In general, the table incorporated an existing pump, actuator, and controller. This system was attached to a new single axis sliding table, and an external function generator was employed to produce the desired input.

C.2 Power, Control, and Data Recording

The table is driven by an MTS model 506.00 pump with a maximum flow rate of 0.75 gallons/minute at a continuous operating pressure of 3000 psi. The pump drives an MTS model 204.08 hydraulic actuator with a piston area of 0.40 in^2, a dynamic stroke of ±2 inches, and an allowable force of 1.1 kips. The actuator is controlled by a Moog model 760C260 servovalve with a capacity of 1 gallon/minute.

* The shake table was designed with the assistance of Dr. John T. Germaine, Research Scientist, MIT, and constructed with the assistance of David Lallemant, undergraduate student, MIT.

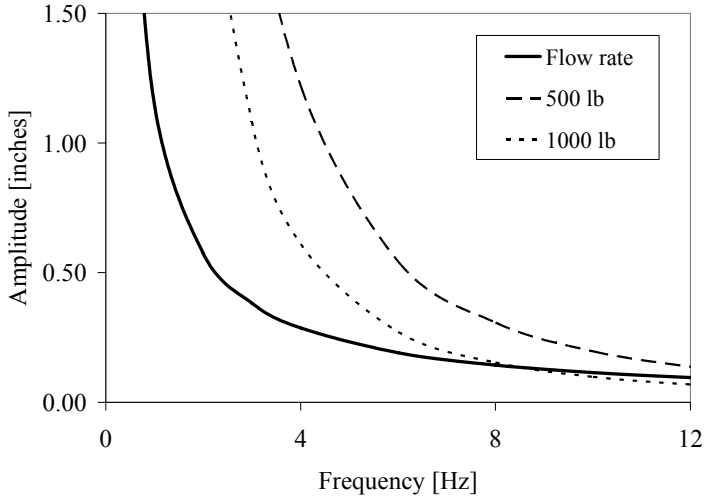

Figure C-1: Capacity of the table as a function of amplitude and frequency of harmonic motion.

Based on the specifications above, the capacity of the system can be determined as a function of the amplitude and frequency of harmonic table motion. In Figure C-1, the pump flow rate capacity curve is compared to two actuator force capacity curves for activated weights of 500 lbs and 1000 lbs. The plot indicates that for an activated weight of less than 1000 pounds, the pump is the governing factor which limits the capacity of the system. The possibility of adding an accumulator to increase the flow rate was investigated, but this could only improve the table capacity by 33% due to the servovalve flow rate capacity.

The servovalve is controlled with an MTS 406 Controller. In order to allow greater flexibility of input options, an external HP 33120A function generator was added. The base motion was recorded using a Crossbow CXL04LP1 accelerometer mounted to the table. The accelerometer has an input range of ±4 g, a sensitivity of 500 mV/g, and requires a supply voltage of 5 V. Data was acquired with a Crossbow CXLDK Digital Interface Card, which connects to a laptop or PC with an RS-232 cable. The CXLDK has a maximum sampling rate of 200 Hz, and a voltage range of 0-4 V with a 1 mV resolution.

C.3 General Layout and Construction Drawings

A drawing and a picture of the constructed system without the table deck are shown in Figures C-3 and C-4, respectively. The table was designed out of aluminum to limit the weight, allowing it to be disassembled and moved easily. The general layout consists of two I-beams on which continuously supported Thomson 60 Case LinearRace Support Rails (0.75 inch diameter)

were mounted. The table slides on these rails on four Super Smart Ball Bushing Pillow Blocks (Model number TSSUPBO-12).

The actuator is mounted on a plate which spans between the bottom flanges of the aluminum I-beams. The actuator piston is connected to the table using a rod alignment coupler to compensate for possible misalignment of the piston axis with the rail axes. The table was tested with and without the rod alignment coupler to ensure that it did not cause any slip in the system when the table changes directions.

The table deck itself was constructed of a composite of solid insulation foam and plywood. Specifically, a two inch thick piece solid foam insulation was glued between two ¼-inch thick plywood sheets. This resulted in a table deck which was fairly large (approximately 3 feet wide by 6 feet long), but extremely lightweight. Thus, the weight which the system has to drive was minimized while the necessary flexural stiffness and strength of the table was maintained.

The remainder of the table was constructed of aluminum plates, angles, and beams. Drawings of these components are shown in Figures C-5 to C-12.

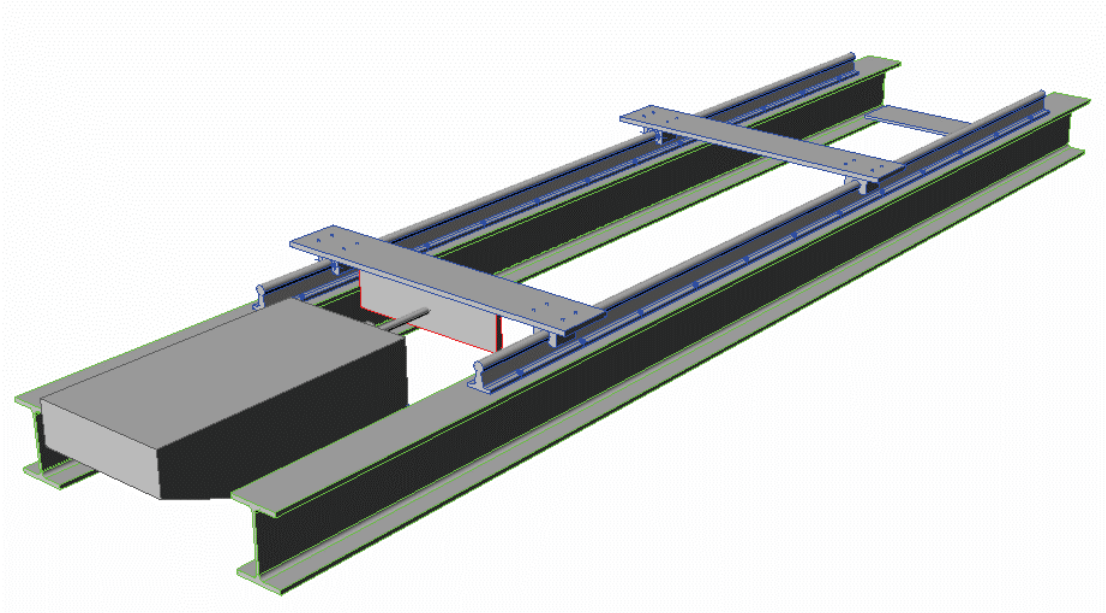

Figure C-3: Drawing of the system without the table deck.

Figure C-4: Image of the constructed system without the table deck.

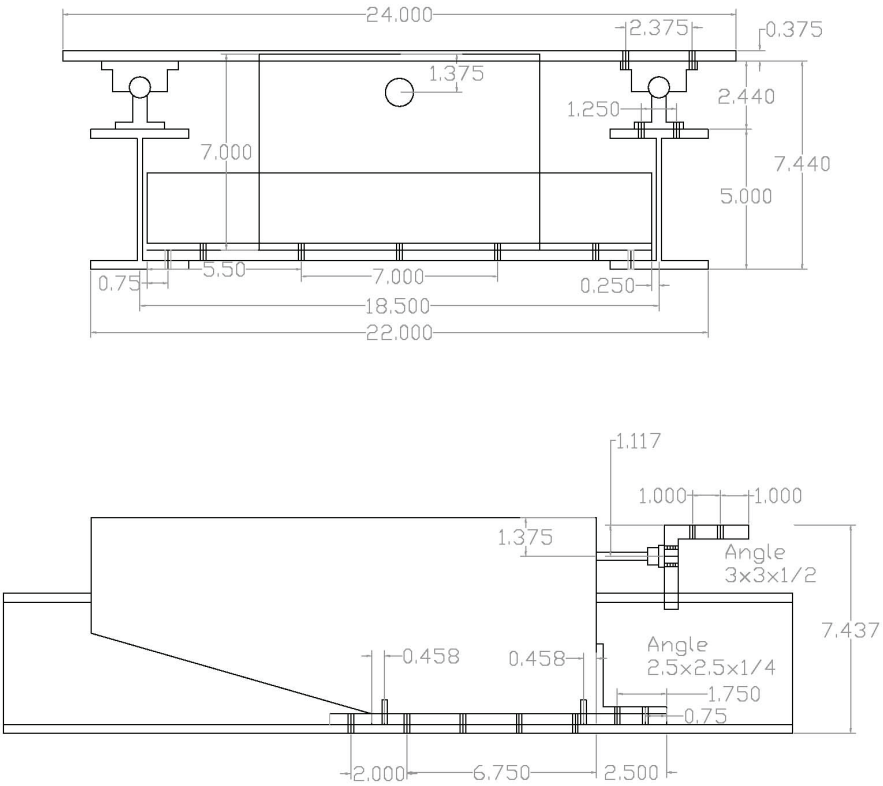

Figure C-5: Actuator and attached plates and angles.

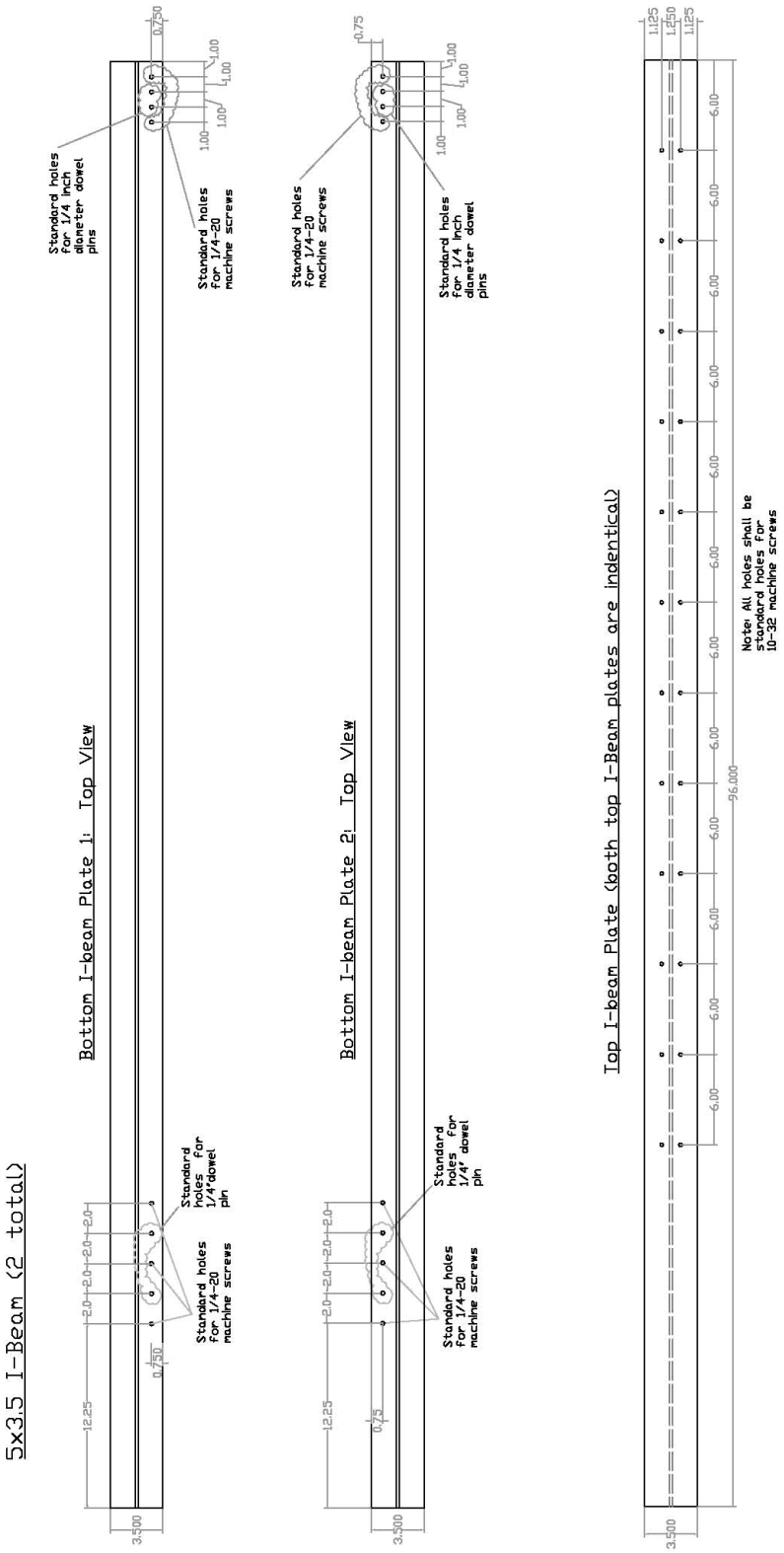

Figure C-6: I-beams on which the rails and sliders are mounted.

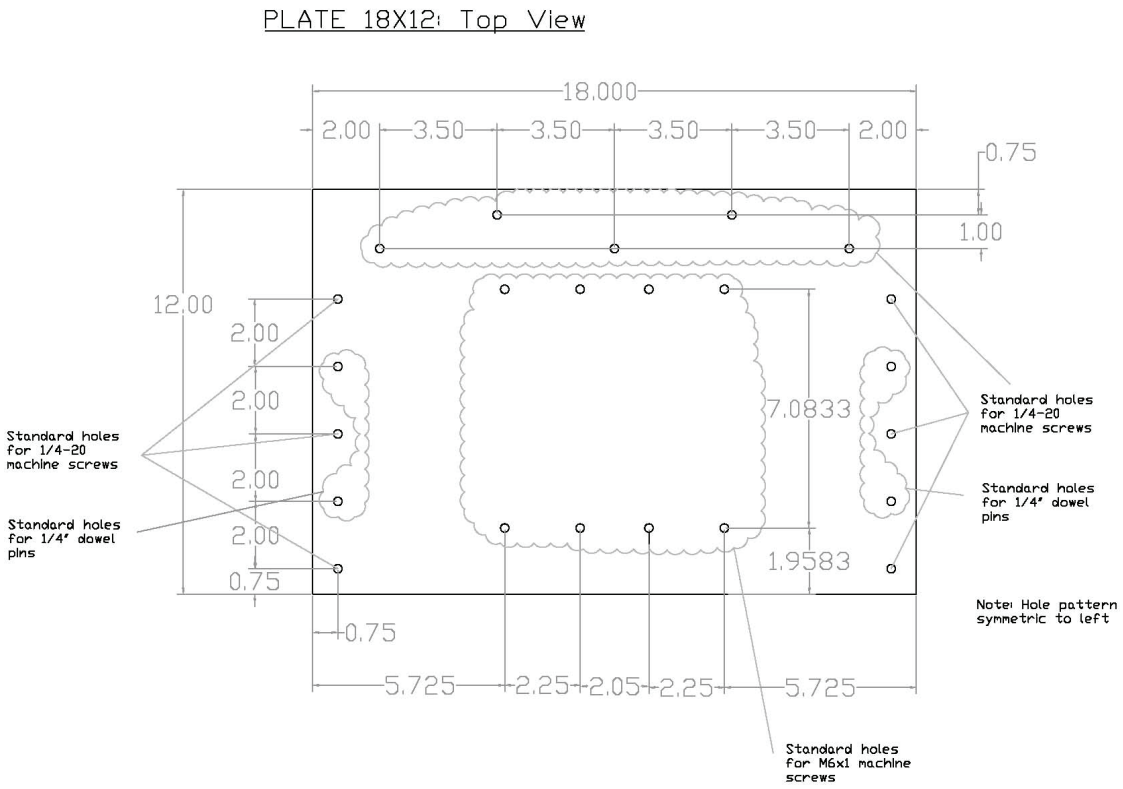

Figure C-7: Plate on which the actuator is mounted.

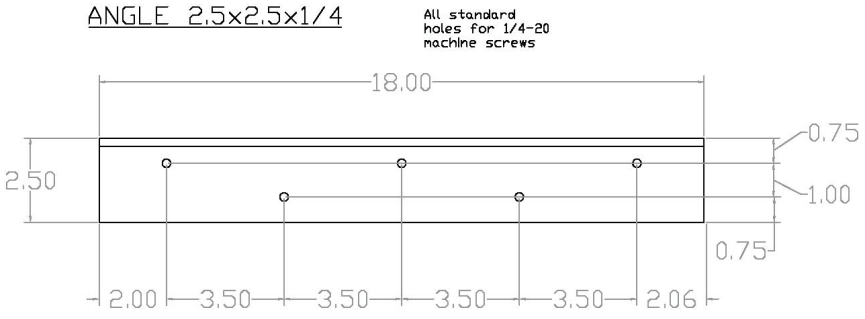

Figure C-8: Angle at the front base of the actuator.

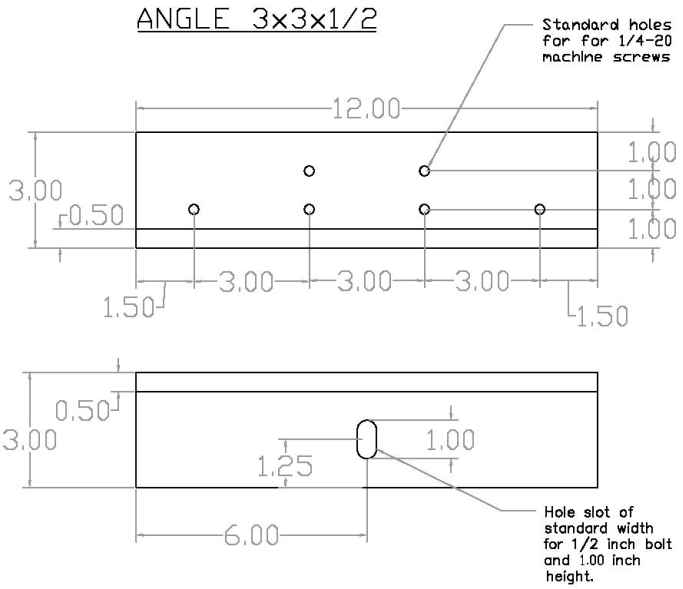

Figure C-9: Angle to which the actuator piston is attached.

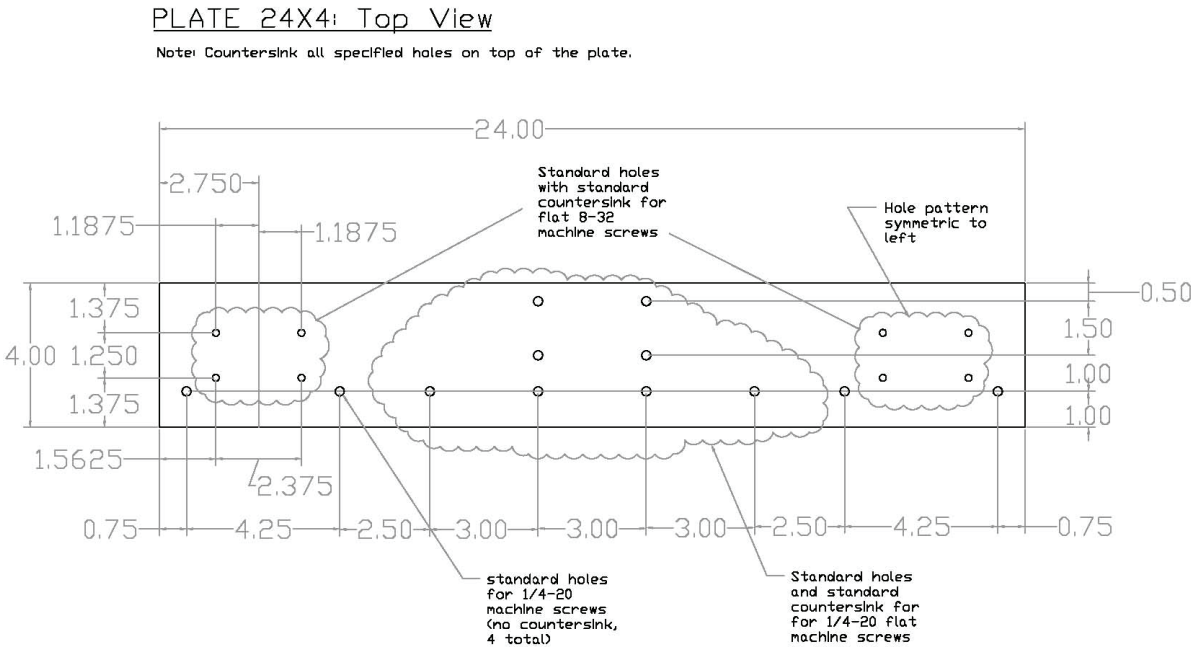

Figure C-10: Plate which rides on the bearings and attaches to the 3x3 angle.

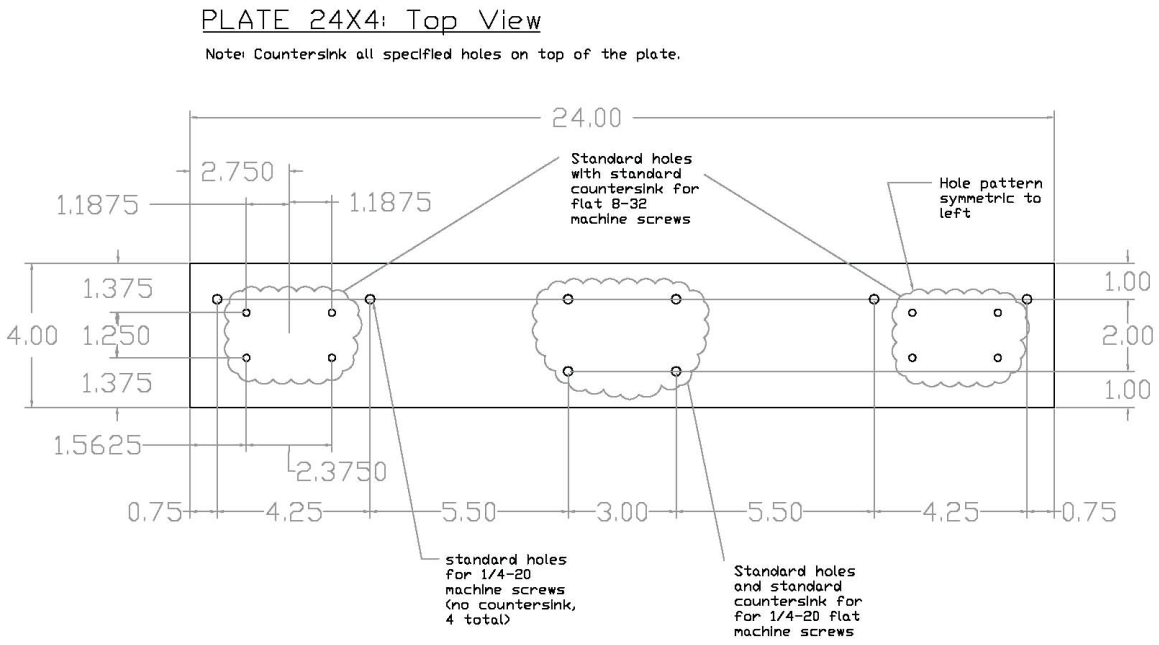

Figure C-11: Plate which rides on the bearings.

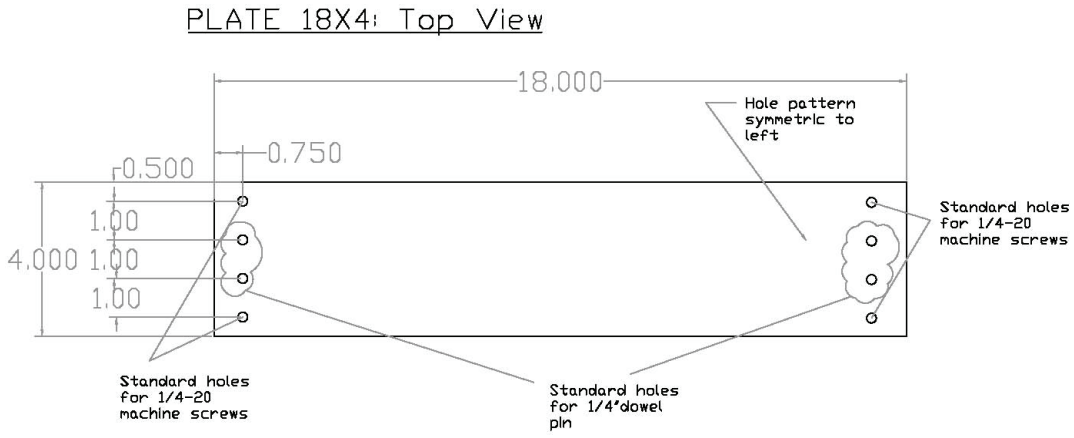

Figure C-12: Plate which attaches the I-beam bottom flanges.

Bibliography

Allen, E. and Zalewski, W. (2009). *Form and forces: Designing efficient, expressive structures*. New York: John Wiley and Sons.

American Society of Civil Engineers (2000). *Prestandard and commentary for the seismic rehabilitation of buildings, FEMA-356*.

Appleton, J. (1999). *Earthquake response of arches*. Fourth-year undergraduate project, University of Cambridge. Cambridge, UK.

Augusti, G. and Sinopoli, A. (1992). Modeling the dynamics of large block structures, *Meccanica*, 17, 195-211.

Azevedo, J., Sincraian, G. and Lemos, J.V. (2000). Seismic behavior of blocky masonry structures, *Earthquake Spectra*, 16(2), 337-365.

Bathe, K.J. (2006). *Finite element procedures*. New Jersey: Prentice Hall.

Block, P. (2005). *Equilibrium systems: Studies in masonry structure*. S.M. Thesis, Massachusetts Institute of Technology. Cambridge, Massachusetts.

Block, P. and Ochsendorf, J. (2007). Thrust network analysis: a new methodology for three-dimensional equilibrium, *Journal of the International Association for Shell and Spatial Structures*, 48(3), 167-173.

Bohlen, C. (1997, October 25). Assisi holds its breath and rebuilds treasures, *The New York Times*, p. A5.

Bolander, J.A. and Saito S. (1998). Fracture analyses using spring networks with random geometry, *Engineering Fracture Mechanics*, 61, 569-591.

Boothby, T.E. (2001). Analysis of masonry arches and vaults, *Progress in Structural Engineering and Materials*, 3, 246-256.

Brasile, S., Casciaro, R. and Formica, G. (2007). Multilevel approach for brick masonry walls - Part I: A numerical strategy for the nonlinear analysis, *Computer Methods in Applied Mechanics and Engineering*, 196, 4934-4951.

Calvi, M.G., Kingsley, G.R. and Magenes G. (1996). Testing of masonry structures for seismic assessment, *Earthquake Spectra*, 12(1), 145–162.

Chetouane, B., Dubois, F., Vinches M. and Bohatier, C. (2005). NSCD discrete element method for modeling masonry structures, *International Journal for Numerical Methods in Engineering*, 64, 65–94.

Clemente, P. (1998). Introduction to the dynamics of stone arches, *Earthquake Engineering and Structural Dynamics*, 27, 513-522.

Culmann, K. (1866). *Die graphische Statik*. Zürich: Meyer und Zeller.

Cundall, P.A. (1971). A computer model for simulating progressive large-scale movements in blocky rock systems, *Proceedings of the Symposium of the International Society of Rock Mechanics*, 1, 132-150.

Cundall, P.A. and Strack, O.D.L. (1979). A discrete numerical model for granular assemblies, *Geotechnique*, 29, 47-65.

de Borst, R. (2002). Fracture in quasi-brittle materials: a review of continuum damage-based approaches, *Engineering Fracture Mechanics*, 69, 95-112.

DeJong, M.J., Hendriks, M.A.N. and Rots, J.G. (2008). Sequentially linear analysis of fracture under non-proportional loading, *Engineering Fracture Mechanics*, 75, 5042-5056.

DeJong, M.J., Belletti, B., Hendriks, M.A.N. and Rots, J.G. (2009a). Shell elements for Sequentially Linear Analysis: Lateral failure of masonry structures, *Engineering Structures* (in press).

DeJong, M.J., Hendriks, M.A.N. and Rots, J.G. (2009b). Shear retention and mesh alignment during fracture using sequentially linear analysis, *Proceeding of the 12th International Conference on Fracture* (available July, 2009).

De Luca, A., Giordano, A. and Mele, E. (2004). A simplified procedure for assessing the seismic capacity of masonry arches, *Engineering Structures*, 26, 1915-1929.

De Lorenzis, L., DeJong, M.J. and Ochsendorf, J. (2007). Failure of masonry arches under impulse base motion, *Earthquake Engineering and Structural Dynamics*, 36(14), 2119–2136.

di Prisco, M., Ferrara, L., Meftah, F., Pamin, J., de Borst, R., Mazars, J. and Reynouard J. (2000). Mixed mode fracture in plain and reinforced concrete: some results on benchmark tests, *International Journal of Fracture*, 103, 127-148.

Drei, A. and Fontana, A. (2003). Response of multiple-leaf masonry arch-tympani to dynamic and static loads, In C.A. Brebbia (Ed.), *Structural Studies, Repairs, and Maintenance of Heritage Architecture VIII* (pp. 267-276). Boston: WIT Press.

Dormand, J.R. and Prince, P.J. (1980). A family of embedded Runge-Kutta formulae, *Journal of Computational and Applied Mathematics*, 6, 19-26.

EERI (2005). Learning from Earthquakes: First Report on the Kashmir Earthquake of October 8, 2005, *EERI Special Earthquake Report – December 2005*. Retrieved March 13, 2009, from EERI Online: [http://www.eeri.org/lfe/clearinghouse/kashmir/observ1.php].

Erdman, A. and Sandor, G. (1984). *Mechanism Design: Analysis and Synthesis*. New Jersey: Prentice-Hall.

Fallahi, A. (2007). Lessons learned from the housing reconstruction following the Bam Earthquake in Iran, *The Australian Journal of Emergency Management*, 22(1), 26-35.

Feenstra, P.H., Rots, J.G., Arnesen, A., Teigen, J.G. and Høiseth, K.V. (1998). A 3D constitutive model for concrete based on a co-rotational concept. In R. de Borst et al. (Eds.), *EURO-C 1998: Computational Modelling of Concrete Structures* (pp. 12-22). Rotterdam: Balkema.

Gambarotta, G. and Lagomarsino, S. (1997a). Damage models for the seismic response of brick masonry shear walls - Part I: The mortar joint model and its applications, *Earthquake Engineering and Structural Dynamics*, 26, 423-439.

Gambarotta, G. and Lagomarsino, S. (1997b). Damage models for the seismic response of brick masonry shear walls - Part II: The continuum model and its applications, *Earthquake Engineering and Structural Dynamics*, 26, 441-462.

Gasparini, D.A. and Vanmarcke, E.H. (1976). *Simulated earthquake motions compatible with prescribed response spectra*. MIT Department of Civil Engineering Research Report R76-4. Cambridge, Massachusetts.

Gaß, S. (1990). *IL 25: Experiments*. University of Lightweight Structures, Germany: Institute for Lightweight Structures.

Harris, H.G. and Sabnis, G.M. (1999). *Structural modeling and experimental techniques (2nd edition)*. Boca Raton, Florida: CRC Press, Inc.

Herrmann, H.J., Hansen, A. and Roux, S. (1989). Fracture of disordered, elastic lattices in two dimensions, *Physical Review B*, 39(1), 637-648.

Heyman, J. (1966). The stone skeleton, *International Journal of Solids and Structures*, 2, 249-279.

Heyman, J. (1995). *The Stone Skeleton: Structural engineering of masonry architecture*. Cambridge: Cambridge University Press.

Heyman, J. (1998). *Structural Analysis: A Historical Approach*. Cambridge: Cambridge University Press.

Hogan, S.J. (1990). The many steady state responses of a rigid block under harmonic forcing, *Earthquake Engineering and Structural Dynamics*, 19, 1057–71.

Hooke, R. (1675). *A description of helioscopes, and some other instruments*. London.

Hou, S. (1968). *Earthquake simulation models and their applications*. MIT Department of Civil Engineering Research Report R68-17. Cambridge, Massachusetts.

Housner, G.W. (1963). The behavior of inverted pendulum structures during earthquakes, *Bulletin of the Seismological Society of America*, 53(2), 403-417.

Huerta, S. (2004). *Arcos bóvedas y cúpulas. Geometría y equilibrio en el cálculo tradicional de estructuras de fábrica*. Madrid : Instituto Juan de Herrero.

Itasca Consulting Group (2003). *3DEC Version 3.0: User's Guide*, Minneapolis, Minnesota.

Itasca Consulting Group (2004). *UDEC Version 4.0: User's Guide*, Minneapolis, Minnesota.

Jean, M. (1999). The non-smooth contact dynamics method, *Computer Methods in Applied Mechanics and Engineering*, 177(3-4), 235-257.

Kappos, A.J., Penelis, G.G. and Drakopoulos, C.G. (2002). Evaluation of simplified models for lateral load analysis of unreinforced masonry buildings, *ASCE Journal of Structural Engineering*, 128(7), 890-897.

Kolmar, W. and Mehlhorn, G. (1984). Comparison of shear stiffness formulations for cracked reinforced concrete elements. In F.B. Damjanić, E. Hinton, D.R.J. Owen, N. Bićanić, V. Simović (Eds.), *International Conference on Computer Aided Analysis and Design of Concrete Structures, Volume 1* (pp. 133-147). Swansea: Pineridge Press Ltd.

Lemos, J.V. (1998). Discrete elemente modeling of the seismic behaviour of stone masonry arches. In G. N. Pande, J. Middleton, B. Kralj (Eds.), *Proceedings of the Fourth International Symposium on Computer Methods in Structural Masonry* (pp. 220-227). London: E and FN Spon.

Lemos, J.V. (2007). Numerical issues in the representation of masonry structural dynamics with discrete elements. In M. Papadrakakis, D.C. Charmpis, N.D. Lagaros, Y. Tsompanakis (Eds.), *ECCOMAS Thematic Conference on Computational Methods in Structural Dynamics and Earthquake Engineering*. Crete, Greece.

Lenci, S. and Rega, G. (2006). A dynamical systems approach to the overturning of rocking blocks, *Chaos, Solitons and Fractals*, 28, 527–542.

Lipscombe, P.R. and Pellegrino, S. (1993). Free Rocking of Prismatic Blocks, *ASCE Journal of Engineering Mechanics*, 119(7), 1387-1410.

Lourenço, P.B. (1996). *Computational strategies for masonry structures*. Ph.D. dissertation, Delft University of Techonology. Delft, The Netherlands.

Lourenço, P.B. and Rots, J.G. (1997). A multi-surface interface model for the analysis of masonry structures, *ASCE Journal of Engineering Mechanics*, 123(7), 660–668.

Lourenço, P.B. and Rots, J.G. (1998). Continuum model for masonry: Parameter estimation and validation, *ASCE Journal of Engineering Mechanics*, 124(6), 642-652.

Magenes, G. and Calvi, G.M. (1997). In-plane seismic response of brick masonry walls, *Earthquake Engineering and Structural Dynamics*, 26, 1091-1112.

Magenes, G. and Della Fontana, A. (1998). Simplified non-linear seismic analysis of masonry buildings. In H.W.H. West (Ed.), *Proceedings of the British Masonry Society No.8* (pp. 190-195).

Makris, N. and Konstantinidis, D. (2003). The rocking spectrum and the limitation of practical design methodologies, *Earthquake Engineering and Structural Dynamics*, 32, 265-289.

Mallardo, V., Malvezzi, R., Milani, E., and Milani, G. (2008). Seismic vulnerability of historical masonry buildings: A case study in Ferrara, *Engineering Structures*, 30, 2223-2241.

masonry. (2009). In *Encyclopædia Britannica*. Retrieved March 13, 2009, from Encyclopædia Britannica Online: http://www.britannica.com/EBchecked/topic/368060/masonry.

Matlab (2002). *High-performance Language Software for Technical Computation*. Natick, MA: The MathWorks, Inc.

Meyer, P., Ochsendorf, J., Germaine, J. and Kausel, E. (2007). The impact of high-frequency/low energy seismic waves on unreinforced masonry, *Earthquake Spectra*, 23(1), 77–94.

Milani, E., Milani, G. and Tralli, A. (2008). Limit analysis of masonry vaults by means of curved shell finite elements and homogenization, *International Journal of Solids and Structures*, 45, 5258-5288.

Milani, G., Lourenço, P.B. and Tralli, A. (2006a). Homogenised limit analysis of masonry walls, Part I: Failure surfaces, *Computers and Structures*, 84, 166-180.

Milani, G., Lourenço, P.B. and Tralli, A. (2006b). Homogenised limit analysis of masonry walls, Part II: Structural examples, *Computers and Structures*, 84, 181-195.

Milani, G., Lourenço, P.B. and Tralli, A. (2007). 3D homogenized limit analysis of masonry buildings under horizontal loads, *Engineering Structures*, 29, 3134-3148.

Moon, F.L., Yi, T., Leon, R.T. and Kahn, L.F. (2006). Recommendations for the seismic evaluation and retrofit of low-rise URM structures, *ASCE Journal of Structural Engineering*, 132(5), 663-672.

Moreau, J.J. (1985). Standard inelastic shocks and the dynamics of unilateral constraints. In G. Del Piero, F. Maceri (Eds.), *Unilateral Problems in Structural Analysis, CISM Courses and Lectures No. 288* (pp. 173-221). Wien, New York: Springer-Verlag.

Moreau, J.J. (1988). Unilateral contact and dry friction in finite freedom dynamics. In J.J. Moreau, P.D. Panagiotopoulos (Eds.), *Nonsmooth Mechanics and Applications, CISM Courses and Lectures No. 302* (pp. 1-82). Wien, New York: Springer-Verlag.

Mouzakis, H., Psycharis, I.N., Papastamatiou, D.Y., Carydis, P.G., Papantonopoulos, C. and Zambas C. (2002). Experimental investigation of the earthquake response of a model of a marble classical column, *Earthquake Engineering and Structural Dynamics*, 31, 1681-1698.

Murray, S. (2009). Romanesque Churches of the Bourbonnais [http://www.learn.columbia.edu/bourbonnais/].

Nikolinakou, M.A., Tallon, A.J. and Ochsendorf, J.A. (2005). Structure and form of early Gothic flying buttresses, *Revue Européenne de Génie Civil*, 9(9-10), 1191-1217.

Nooru-Mohamed, M.B. (1992). *Mixed mode fracture of concrete: an experimental approach*. Ph.D. Dissertation, Delft University of Technology. Delft, The Netherlands.

Nooru-Mohamed, M.B., Schlangen, E. and van Mier, J.G.M. (1993). Experimental and numerical study on the behavior of concrete subjected to biaxial tension and shear, *Advanced Cement Based Materials*, 1, 22-37.

Ochsendorf, J.A. (2002). *Collapse of Masonry Structures*, Ph.D. Dissertation, University of Cambridge. Cambridge, UK.

Ochsendorf J.A. and De Lorenzis, L. (2008). Failure of rectangular masonry buttresses under concentrated loading, *Proceedings of the Institution of Civil Engineers - Structures and Buildings*, 161(5), 265-275.

Oppenheim, I.J. (1992). The masonry arch as a four-link mechanism under base motion, *Earthquake Engineering and Structural Dynamics*, 21, 1005-1017.

Papantonopoulos, C., Psycharis, I.N., Papastamatiou, D.Y., Lemos, J.V. and Mouzakis, H. (2002). Numerical prediction of the earthquake response of classical columns using the distinct element method, *Earthquake Engineering and Structural Dynamics*, 31, 1699-1717.

Patzák, B. and Jirásek M. (2004). Adaptive resolution of localized damage in quasi-brittle materials, *ASCE Journal of Engineering Mechanics*, 130(6), 720-732.

Peña, F., Prieto, F., Lourenço, P.B., Campos Costa, A. and Lemos, J.V. (2007). On the dynamics of rocking motions of single rigid-block structures, *Earthquake Engineering and Structural Dynamics*, 36(15), 2383-2399.

Poleni, G. (1748). *Memorie istoriche della gran cupola del Tempio Vaticano*. Padua: Nella Stamperia del Seminario.

Pompei, A., Scalia, A. and Sumbatyan, M.A. (1998). Dynamics of rigid blocks due to horizontal ground motion, *ASCE Journal of Engineering Mechanics*, 124(7), 713-717.

Povoledo, E. (2007, September 4). Italy, a land of earthquakes, works to protect the priceless from the unexpected, *The New York Times*, p. E1.

Priestley, M.J.N., Evison, R.J. and Carr A.J. (1978). Seismic response of structures free to rock on their foundations, *Bulletin of the New Zealand National Society for Earthquake Engineering*, 11(3), 141-150.

Psycharis, I.N., Lemos, J.V., Papastamatiou1, D.Y., Zambas, C. and Papantonopoulos, C. (2003). Numerical study of the seismic behaviour of a part of the Parthenon Pronaos, *Earthquake Engineering and Structural Dynamics*, 32, 2063-2084.

Psycharis, I.N., Papastamatiou, D.Y. and Alexandris, A.P. (2000). Parametric investigation of the stability of classical columns under harmonic and earthquake excitations, *Earthquake Engineering and Structural Dynamics*, 29, 1093-1109.

Rafiee, A., Vinches, M. and Bohatier C. (2008a). Application of the NSCD method to analyse the dynamic behaviour of stone arched structures, *International Journal of Solids and Structures*, 45, 6269-6283.

Rafiee, A., Vinches, M. and Bohatier C. (2008b). Modelling and analysis of the Nîmes arena and the Arles aqueduct subjected to a seismic loading, using the Non-Smooth Contact Dynamics method, *Engineering Structures*, 30, 3457-3467.

Romano, A. (2005). *Modelling, Analysis and Testing of Masonry Structures*. Ph.D. Disseration, Università degli Studi di Napoli Federico II. Naples, Italy.

Rots, J.G. (1988). *Computational modeling of concrete fracture*. Ph.D. Dissertation, Delft University of Technology. Delft, The Netherlands.

Rots, J.G. (2001). Sequentially linear continuum model for concrete fracture. In R. de Borst, J. Mazars, G. Pijaudier-Cabot, J.G.M. van Mier, A.A. Balkema (Eds.), *Fracture Mechanics of Concrete Structures* (pp. 831-839). Lisse, The Netherlands: Balkema.

Rots, J.G., Belletti, B., Boonpichetvong, M. and Invernizzi, S. (2006). Event-by-event strategies for modeling of Amsterdam masonry structures. In P.B. Lourenço, P. Roca, C. Modena, S. Agrawal (Eds.), *Proceedings of the Fifth International Conference on Structural Analysis of Historical Constructions* (pp. 1195-1203). New Delhi: Macmillan India.

Rots, J.G., Belletti, B. and Invernizzi, S. (2008). Robust modeling of RC structures with an "event-by-event" strategy, *Engineering Fracture Mechanics*, 75, 590-614.

Rots, J.G. and Invernizzi, S. (2004). Regularized sequentially linear saw-tooth softening model. *International Journal for Numerical and Analytical Methods in Geomechanics*, 28, 821-856.

Rots, J.G., Nauta, P., Kusters, G.M.A. and Blaauwendraad, J. (1984). Smeared crack approach and fracture localization in concrete, *HERON*, 30(1), 1-48.

Salonikios, T., Karakostas, C., Lekidis, V. and Anthoine A. (2003). Comparative inelastic pushover analysis of masonry frames, *Engineering Structures*, 25, 1515-1523.

Scalia, A. and Sumbatyan, M.A. (1996). Slide rotation of rigid bodies subjected to a horizontal ground motion, *Earthquake Engineering and Structural Dynamics,* 25, 1139-1149.

Schlangen, E. (1993). *Experimental and numerical analysis of fracture processes in concrete.* Ph.D. Dissertation, Delft University of Technology. Delft, The Netherlands.

Shenton, H.W. (1996). Criteria for initiation of slide, rock, and slide-rock rigid-body modes, *ASCE Journal of Engineering Mechanics*, 122(7), 690-693.

Shenton, H.W. and Jones, N.P. (1991a). Base excitation of rigid bodies, I: Formulation, *ASCE Journal of Engineering Mechanics*, 117(10), 2286-2306.

Shenton, H.W. and Jones, N.P. (1991b). Base excitation of rigid bodies, II: Periodic slide-rock response, *ASCE Journal of Engineering Mechanics*, 117(10), 2307-2328.

Sinopoli, A. and Sepe V. (1993). Coupled motion in the dynamic analysis of a three block structure, *Applied Mechanics Reviews*, 46(11), 185-197.

Sluys, L.J. (1992). *Wave propagation, localisation and dispersion in softening solids.* Ph.D. Dissertation, Delft University of Technology. Delft, The Netherlands.

Snell, G. (1846). On the stability of arches, *Minutes and Proceedings of the Institution of Civil Engineers*, 5, 439-476.

Sokolov, V.Y. (2002). Seismic intensity and Fourier acceleration spectra: Revised relationship, *Earthquake Spectra*, 18(1), 161-187.

Spanos, P.D. and Koh A. (1984). Rocking of rigid blocks due to harmonic shaking, *ASCE Journal of Engineering Mechanics*, 110(11), 1627-1642.

Spanos, P.D., Roussis, P.C. and Politis, N.P.A. (2001). Dynamic analysis of stacked rigid blocks, *Soil Dynamics and Earthquake Engineering*, 21, 559-578.

Swartz, S.E. and Taha, N.M. (1991). Crack Propagation and fracture of plain concrete beams subjected to shear and compression, *ACI Structural Journal*, 88(2), 169-177.

Tso, W.K. and Wong, C.M. (1989). Steady state rocking response of rigid blocks, Part I: Analysis, *Earthquake Engineering and Structural Dynamics*, 18(106), 89-106.

Unesco (1984). *Montenegro Earthquake: The Conservation of the Historic Monuments and Art Treasures*. Paris: UN Educational, Scientific and Cultural Organization.

Uniform Building Code (1997). Volume 2. USA: International Conference of Building Officials.

Valente, G. (2003). Fracture mechanics for the reconstruction of Noto Cathedral, *Construction and Building Materials*, 17, 579-593.

Viollet-le-Duc, E. (1860). *Dictionnaire Raisonné de L'Architecture Française du XI^{e} au XVI^{e} Siècle, Volume 4: Construction*. Paris: Librairie-imprimeries réunies.

Winkler, T., Meguro, K. and Yamazaki, F. (1995). Response of rigid body assemblies to dynamic excitation, *Earthquake Engineering and Structural Dynamics*, 24, 1389-1408.

Yi, T. (2004). *Large-scale testing of a two-story URM structure*. Ph.D. Dissertation, Georgia Institute of Technology. Atlanta, Georgia.

Yi, T., Moon, F.L., Leon, R.T. and Kahn, L.F. (2006a). Lateral load tests on a two-story unreinforced masonry building, *ASCE Journal of Structural Engineering*, 132(5), 643–652.

Yi, T., Moon, F.L., Leon, R.T. and Kahn, L.F. (2006b). Analyses of a two-story unreinforced masonry building, *ASCE Journal of Structural Engineering*, 132(5), 653-662.

Yim, C., Chopra, A.K. and Penzien J. (1980). Rocking response of rigid blocks to earthquakes, *Earthquake Engineering and Structural Dynamics*, 8(6), 565-587.

Yim, S.C.S. and Lin, H. (1991). Nonlinear impact and chaotic response of slender rocking objects, *ASCE Journal of Engineering* Mechanics, 117(9), 2079-2100.

Zalewski, W. and Allen, E. (1998). *Shaping Structures: Statics*. New York: John Wiley and Sons.

Zhang, J. and Makris, N. (2001). Rocking response of free-standing blocks under cycloidal pulses, *ASCE Journal of Engineering Mechanics*, 127(5), 473–483.

Related publications by the author

DeJong, M.J. and Ochsendorf J.A. (2006). Analysis of vaulted masonry structures subjected to horizontal ground motion. In P.B. Lourenço, P. Roca, C. Modena, S. Agrawal (Eds.), *Proceedings of the Fifth International Conference on Structural Analysis of Historical Constructions, Volume 2* (pp. 973-980). New Delhi: Macmillan India.

Block, P., DeJong, M.J. and Ochsendorf, J. (2006) As Hangs the Flexible Line: Equilibrium of Masonry Arches, *The Nexus Network Journal*, 8(2), 13-24.

De Lorenzis, L., DeJong, M.J. and Ochsendorf, J. (2007). Failure of masonry arches under impulse base motion, *Earthquake Engineering and Structural Dynamics*, 36(14), 2119–2136.

DeJong, M.J., De Lorenzis, L. and Ochsendorf, J.A. (2007). Numerical modelling of masonry arch stability under impulse base motion. In M. Papadrakakis, D.C. Charmpis, N.D. Lagaros, Y. Tsompanakis (Eds.), *ECCOMAS Thematic Conference on Computational Methods in Structural Dynamics and Earthquake Engineering*. Crete, Greece.

DeJong, M.J., De Lorenzis, L. and Ochsendorf, J. (2008). Rocking stability of masonry arches in seismic regions, *Earthquake Spectra*, 24(4), 847–865.

DeJong, M.J., Hendriks, M.A.N. and Rots, J.G. (2008). Sequentially linear analysis of fracture under non-proportional loading, *Engineering Fracture Mechanics*, 75, 5042-5056.

DeJong, M.J., Belletti, B., Hendriks, M.A.N. and Rots, J.G. (2009). Shell elements for Sequentially Linear Analysis: Lateral failure of masonry structures, *Engineering Structures*, (in press).

DeJong, M.J., Hendriks, M.A.N. and Rots, J.G. (2009). Shear retention and mesh alignment during fracture using sequentially linear analysis, *Proceeding of the 12th International Conference on Fracture* (July, 2009).

DeJong, M.J. (2009). Redefining the Vulnerability of Rocking Structures to Horizontal Ground Motion, *Proceedings of the 2009 Earthquake Engineering Research Institute (EERI) Annual Meeting*.